Università degli Studi di Torino
Scuola di Dottorato in Scienza ed Alta Tecnologia

Identified hadron distributions in p–Pb collisions at $\sqrt{s_{NN}} = 5.02$ TeV with the Inner Tracking System of ALICE at the LHC

Yasser Corrales Morales

Supervisor: Prof.ssa Elena Botta, Dr. Francesco Prino
External reviewer: Dr. Guillaume Batigne

Tesi di Dottorato di Ricerca in Scienza ed Alta Tecnologia
Indirizzo di Fisica ed Astrofisica
Ciclo XXVII

A mi familia, por muchas razones
A mi esposa, entre tanto por su sacrificio
y en especial a Fabio, por todo el tiempo
alejado de él.

Abstract

Le collisioni di ioni pesanti offrono la possibilità di studiare in laboratorio le proprietà delle materia fortemente interagente in condizioni estreme di pressione, densità di energia e temperatura. In particolare, l'obiettivo è di caratterizzare lo stato di Plasma di Quark e Gluoni (QGP), previsto dalla Cromodinamica Quantistica (QCD), in cui i partoni sono deconfinati e liberi di muoversi in volumi più ampi di quelli degli adroni. Le misure effettuate in collisioni protone–protone e protone–nucleo sono importanti perché forniscono i dati di riferimento per l'interpretazione dei risultati ottenuti in collisioni di ioni. In particolare, una inattesa struttura a "double-ridge" è stata osservata negli studi di correlazioni angolari tra coppie di particelle in collisioni p–Pb ad alta molteplicità al Large Hadron Collider (LHC). Le caratteristiche di questa "ridge" sono qualitativamente, e in qualche misura anche quantitativamente, simili a quelle osservate in collisioni di ioni pesanti, dove sono comunemente interpretate come effetti dell'espansione collettiva (*flow*) del mezzo denso creato nella collisione. Una descrizione soddisfacente delle correlazioni angolari misurate in collisioni p–Pb può essere ottenuta sia dai modelli teorici basati sul "Colour Glass Condensate" (CGC), cioè su una evoluzione non lineare delle densità dei gluoni nello stato iniziale, sia da modelli di tipo fluidodinamico che includono un moto collettivo delle particelle prodotte nella collisione.

Le distribuzioni di impulso trasverso (p_{T}) degli adroni identificati, come pioni, kaoni e protoni, in collisioni di ioni contengono informazioni cruciali sull'espansione collettiva del sistema e sulle condizioni termiche del sistema al momento del "freeze-out". Pertanto, la misura delle distribuzioni di p_{T} di pioni, kaoni e protoni in collisioni p–Pb può fornire un'ulteriore verifica della possibile interpretazione delle misure di correlazioni angolari in termini di espansione collettiva.

La caratteristiche uniche di ALICE (A Large Ion Collider Experiment) nel tracciare e identificare particelle cariche fino a basso p_{T} consentono la misura delle distribuzioni di adroni carichi su un ampio intervallo di p_{T}. In particolare, per estendere l'analisi degli spettri di pioni, kaoni e protoni a bassissimo p_{T}, si utilizza l'Inner Tracking System (ITS) di ALICE come uno spettrometro in modalità stand-alone, con uno specifico algoritmo di tracciamento e di identificazione di particelle.

Questa tesi è focalizzata sulla misura delle distribuzioni di impulso di pioni, kaoni, protoni in collisioni p–Pb all'LHC nella regione di rapidità centrale usando l'informazione del rivelatore ITS per coprire la regione di basso p_{T}. L'identificazione degli adroni con l'ITS é basata su un approccio Bayesiano con una parametrizzazione della risposta ($\mathrm{d}E/\mathrm{d}x$) dei rivelatori in funzione dell'impulso e della specie della particella. I risultati ottenuti con l'analisi ITS sono poi combinati con quelli di altre analisi, per ricavare distribuzioni di impulso su un intervallo di p_{T} più esteso.

L'analisi è stata effettuata in sette classi di molteplicità dell'evento, definita in base all'ampiezza dei segnali nel rivelatore VZERO, che copre una regione di alta rapidità nella direzione del nucleo di piombo. Infine, la tesi si conclude con una discussione sulla dipendenza dalla molteplicità delle distribuzioni di p_{T} misurate per pioni, kaoni e protoni e sul confronto tra i risultati ottenuti in collisioni con alta molteplicità e le predizioni di modelli teorici di tipo fluidodinamico, che includono un'espansione collettiva delle particelle prodotte nella collisione.

Abstract

Heavy-ion (A–A) collisions offer a unique possibility to study in the laboratory the properties of the strongly-interacting matter under extreme conditions of pressure, energy density and temperature. In particular, the deconfined quark-gluon plasma (QGP) system which is predicted by quantum chromodynamic (QCD) calculations can be investigated. The measurements performed in smaller systems, such as proton–proton (pp) and proton–nucleus (p–Pb) collisions, provide the reference data for the interpretation of the A–A collision results. In addition, an unexpected "double-ridge" structure in two particle correlation measurements in high multiplicity p–Pb collisions at the Large Hadron Collider (LHC) has been observed. The features of this ridge are qualitatively, and to some extent also quantitative, similar to those observed in heavy-ion collisions where they are commonly explained in term of collective expansion (flow) of the high density medium created in the collision. Both a Colour Glass Condensate (CGC) description, based on initial state non-linear gluon interactions, as well as a model based on hydrodynamic flow can give a satisfactory description of these observed correlations in p–Pb collisions.

The transverse momentum p_{T} distributions of identified hadrons, such as pions, kaons and protons, in Pb–Pb collisions encode crucial information about the transverse "collective" expansion of the system and the thermal conditions at the freeze-out. Therefore, measuring the p_{T} distributions of π, K and p in p–Pb collisions can provide a further test of the possible hydrodynamic expansion that is suggested by the two-particle correlation results.

The tracking of low p_{T} charged particles and the good particle identification (PID) capability of the ALICE (A Large Ion Collider Experiment) detectors, allow the measurement of the identified hadron distributions over a broad p_{T} range. In order to extend the π, K and p spectra analysis to very low p_{T}, the ALICE Inner tracking System (ITS) can be used as a stand-alone tracker with dedicated tracking algorithm and exploiting at maximum its PID capabilities.

This thesis is focused on the measurement of the pion, kaon and proton momentum distributions at low p_{T} and at mid-rapidity in p–Pb collisions at $\sqrt{s_{\mathrm{NN}}} = 5.02$ TeV using

only the information from the ITS detector. The π, K and p identification with the ITS is based on a Bayesian approach using a dedicated parametrization of the detector response. The results are then combined with results from other analyses, which cover higher transverse momentum ranges, in order to obtain spectra extending to a broad p_{T} range.

The analysis has been performed in seven multiplicity classes based on the amplitude of the signals in the VZERO detector, located away from mid-rapidity, in the Pb-going direction. In addition, the multiplicity dependence of the pion, kaon and proton p_{T} distributions is discussed and the results for the highest multiplicity collisions are compared to productions of models including a hydrodynamic expansion of the system.

Contents

1 Quark-Gluon Plasma

The goal of high-energy physics (HEP) is to study the nature of matter at the most fundamental level, i.e. to understand its elementary-components and the interactions that rule them. In particular, heavy-ion collisions at ultra-relativistic energies are aimed at studying the properties of strongly-interacting matter under extreme conditions of pressure and temperature, as those assumed to have existed during the first moments after the Big Bang. The gauge theory of strong interaction, Quantum-Chromo-Dynamics (QCD), predicts that when high enough temperatures and energy densities are achieved, e.g. in ultra-relativistic heavy-ion collisions at the Relativistic Heavy-Ion Collider (RHIC) or at the Large Hadron Collider (LHC), strongly-interacting matter undergoes a phase transition from normal confined state (i.e. hadrons) to almost free quarks and gluons, creating a weakly interacting matter called the Quark-Gluon Plasma (QGP) [1]. Over the past 30 years, the QGP phase transition has been studied by heavy-ion fixed target experiments at the Alternate Gradient Synchrotron (AGS) and at the Super Proton Synchrotron (SPS) accelerators [2, 3], with heavy-ion collisions at centre-of-mass energies per nucleon varying from 5 and 17 GeV. Extra studies were then performed at RHIC [4] colliding Au and Cu nuclei at $\sqrt{s_{NN}} = 200$ GeV. Further insight into the QGP physics was achieved in 2010 when the LHC at the European Organization for Nuclear Research (CERN) started to collide Pb ions nuclei at $\sqrt{s_{NN}} = 2.76$ TeV. In this chapter I survey the strong interaction theory and the study of the phase diagram of strongly-interacting matter with heavy-ion collisions.

1.1 QGP: A QCD signature

Our world, according to the Standard Model (SM), is composed of two kinds of particles: the matter components and the particles responsible of the interaction among them [5–8]. The components of matter are *fermions*, particles with spin 1/2. There are two types of these particles: *quarks q* with *flavours u, d, s, c, b, t* and their *anti-particles*, all with fractional charge $\pm 1/3e$ or $\pm 2/3e$; and *leptons*, $e^{\pm}$, $\mu^{\pm}$, $\tau^{\pm}$, $\nu_{e,\mu,\tau}$ and $\bar{\nu}_{e,\mu,\tau}$. The particles carrying the interaction are *bosons*, with spin 0 or 1. Photons (γ) carry electromagnetic

force, weak bosons ($W^{\pm}$ and Z^0) carry the weak force and gluons g carry the strong interaction. The weak bosons acquire a mass through the Higgs mechanism [9, 10], and in the minimal SM formulation there should exist at least one neutral Higgs* boson. The grouping of elementary particles of the SM and the force mediating gauge bosons are shown in Fig. 1.1.

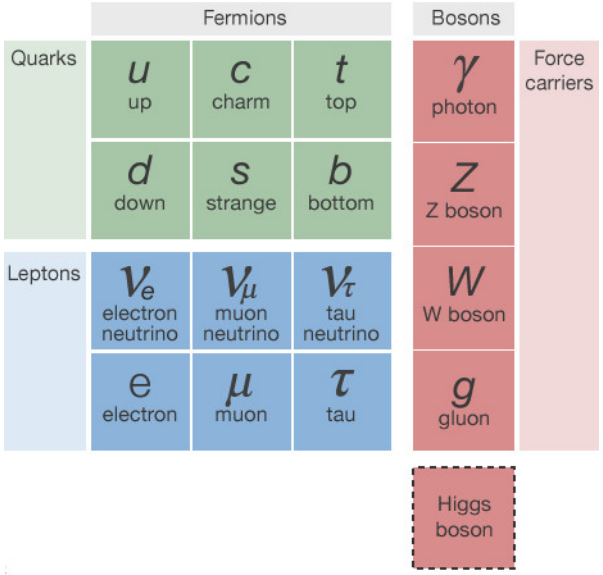

Figure 1.1: The fundamental particles of the standard model and the force mediating gauge bosons.

Quantum Chromodynamics (QCD) is the gauge theory, in the SM [13], which describes the strong interaction (i.e. the fundamental force that keeps quarks confined into hadrons). In QCD, the charges responsible for strong interaction are called *colour charges*, with gluons as the carriers that bind quarks together. There are two features of QCD which can be understood from the expression of the strong interaction coupling constant, α_s, given by:

$$\alpha_s(Q^2) = \frac{12\pi}{(33 - (2N_f)\ln(Q^2/\Lambda^2_{QCD}))} \tag{1.1}$$

where Q^2 is the momentum transfer, N_f is the number of quark flavours and Λ_{QCD} is the scale parameter. The typical value of Λ_{QCD}, obtained from scattering experiments is about 200 MeV. The value of α_s has been extracted from different experimental results and compared with perturbative QCD (pQCD) predictions [14]. The pQCD has been very successful in predicting and describing various processes at high Q^2 observed in different experiments as illustrated in Fig. 1.2.

*Higgs boson was recently discovered by the ATLAS and CMS experiments at the LHC [11, 12]

At large distances or small Q^2, α_s is large and increases as the distance between two quarks is increased. This property is called *Confinement* and is the reason why quarks are never seen alone but are instead always bound together in groups of three, in the form of baryons, or as quark-antiquark pairs in the form of mesons. For large momentum transfers (short distances), α_s tends to vanish and quarks behave as free non-interacting particles. As a consequence, a QCD medium at very high temperature is predicted to be a gas of free quarks and gluons. This property, the fact that the interactions between the quarks become arbitrarily weak at length scales that asymptotically go to zero, is known as *Asymptotic Freedom* [15,16]. In this regime, perturbative calculations can be performed and the experimental data are well described.

On the other hand, for small Q^2 values, which correspond to distances of the order of the hadron size (1 fermi), a non-perturbative approach is mandatory. The main tool to investigate the non-perturbative region of QCD are calculation on the Lattice [17]. In this framework, the QCD equations are solved using Monte Carlo simulations in a discrete four dimensional space-time. The challenge for these calculations is to reduce the lattice space in order to approach the continuum. In addition, models such as the *MIT Bag Model* [18] provide a qualitative understanding of the mechanism of confinement and of the phase transition to the deconfined state. This model assumes that massless quarks move freely within a spherical hadron of radius R, but are prevented to move outside it by the vacuum pressure. QCD predicts that the ground-state energy expectation value of vacuum is not zero but $\langle \psi\bar{\psi} \rangle \approx -(250\ \text{MeV})^3$, leading to the *chiral symmetry breaking*.

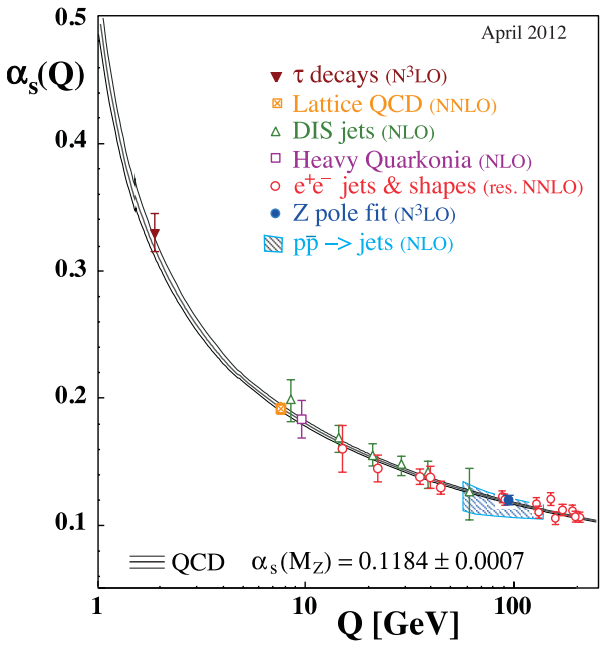

Figure 1.2: Summary of measurements of α_s(Q) as a function of the energy scale Q. The curves are the QCD predictions [14].

Chiral symmetry implies that if quarks were massless, they would exist only in one of the two possible *helicity* eingenstates $h = 1/2$[†]. However, quarks moving in the bag have a *bare mass* and only for the lighter ones, u and d, chiral symmetry is an approximated symmetry. In normal nuclear matter, quarks are in a superposition of both helicity eigenvalues due to the vacuum pressure, which gives an additional mass to the quarks[‡] [19, 20].

In the MIT Bag model, the transition to the deconfined state is achieved when the internal pressure of the system overcomes the critical bag pressure B. A transition temperature $T = 144$ MeV is obtained if the system is considered in the high temperature limit, as a non interacting massless quarks, antiquarks and gluons ensemble with zero net baryon number [21].[§]

1.1.1 QGP from lattice QCD

Lattice QCD calculations predict a phase transition from hadron matter to a deconfined state of quarks and gluons at a critical temperature of $T_c \sim 170$ MeV, which corresponds to an energy density of $\epsilon_c \sim 1$ GeV/fm^3 [1, 19, 20]. This deconfined system of weakly interacting quarks and gluons is called the Quark-Gluon Plasma (QGP) [1]. This system is believed to have existed a few microseconds after the creation of the universe in the Big Bang. Moreover, it's also assumed that the dense nuclear matter at the centre of a neutron star could consist of a plasma of quarks and gluons at low temperature with high baryon density [22].

Figure 1.3 shows the pressure (p) and the energy density (ϵ) as a function of the temperature for strongly-interacting matter obtained from lattice QCD calculations [23]. These calculations are performed for non-zero temperatures and non-zero chemical potentials. The ratio ϵ/T^4 is proportional to the number of degrees of freedom in the thermodynamics system. The sharp increase of ϵ/T^4 around T_c indicates a transition in the system to a state where the quarks and gluons have become the relevant degree of freedom. The pressure changes slowly at T_c compared to the rapid increase of the energy density, which means the pressure gradient is significantly reduced during the phase transition. When the QGP is formed, the vacuum pressure vanishes and the chiral symmetry is approximately restored, so quarks in the plasma have their bare masses [24].

[†] $h = \vec{s} \bullet \vec{k}/|k|$, where $\vec{s}$ and $\vec{k}$ are the spin and the momentum of the particle.

[‡] Quarks u and d have small bare mass of about ~ 5 MeV, but due to chiral symmetry breaking their mass is increased to ~ 350 MeV inside hadrons.

[§] This result only holds if the quark and gluon system has no boundary and $N_f = 2$.

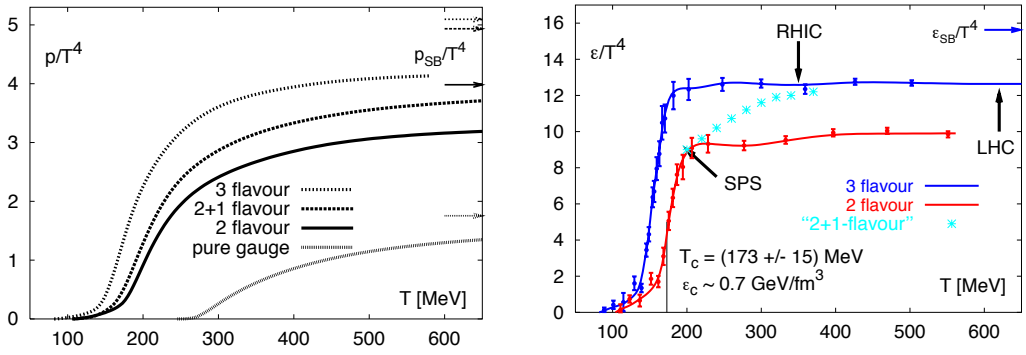

Figure 1.3: Pressure (left) and energy density (right) in units of T^4 as a function of the temperature from lattice QCD calculations. The curves labeled "2 flavours" and "3 flavours" were calculated for two and three light quark flavours of mass $\frac{m_q}{T} = 0.4$, respectively. "2+1 flavour" indicates a calculation for two light quarks and one heavier (strange) quark of mass $\frac{m_q}{T} = 1$. The arrows indicate the Stefan-Boltzmann limit.

Both deconfinement and chiral symmetry restoration are phenomenologically important. Deconfinement leads to the production of a large number of gluons which can produce extra quark-antiquark pairs and drive the system towards chemical equilibrium among quarks, antiquarks and gluons. The melting of the dynamical quark masses (chiral symmetry restoration) above T_c makes the quarks lighter and lowers the quark-antiquark pair production threshold. This is particularly important for strange quarks whose constituent quark mass is much higher than the critical temperature while its current mass is comparable with T_c. Leading to an enhancement in the production of strange particles in heavy-ion collisions; further details in Sec. 2.1.2.

1.1.2 QGP and the QCD phase space diagram

Interactions between single coloured objects (quarks and gluons) are well described by the QCD theory. However, thermodynamics principles are needed to understand the properties of a large system composed of elementary particles, such as a strongly-interacting medium composed of quarks and gluons. In thermodynamics, the properties of the system are often presented in form of *phase diagram*[¶]. In the case of strongly-interacting matter, the control parameters for the phase diagram displayed in Fig. 1.4 are the temperature T and the *baryo-chemical potential* μ_B. The baryo-chemical potential

[¶]A phase diagram is a plot in function of some *control parameters*, where the different phases of a substance occupy different regions. The common example is the phase diagram of water, whose control parameters are the temperature T and the pressure P. Water is commonly described having three phases, liquid, gas and solid.

is defined as the energy needed to increase by one unity the total number of baryons and anti-baryons, $\mu_B = \partial E/\partial N_B$, and it is directly related to the baryonic density.

Strongly-interacting matter may pass through several phases as the temperature and energy density (ϵ) raise. Low temperatures and $\mu_B \simeq m_p \simeq 940$ MeV characterize ordinary nuclear matter. Increasing the temperature or the energy density leads to a hadronic gas, mainly constituted of pions. If T and ϵ are further increased, a transition to a deconfined QGP is expected (Fig. 1.4). Phase transitions are characterized by the *order of transition*, corresponding to the order of the derivative of the *grand potential* Ω[‖] diverging at the critical point. The order of the transition to the QGP is not known. Lattice QCD tells us that even for realistic small up and down quark masses the transition for small $\mu_B \sim 0$ is most likely a not first-order phase transition but a rapid crossover. Furthermore, there might be a second-order critical point in the phase diagram connecting a first-order transition at high baryon density to this crossover, as shown in Fig. 1.4 [25]. At low temperatures and asymptotically large baryon densities quarks are also deconfined, although not in a quark-gluon plasma state but in a color superconductor [26].

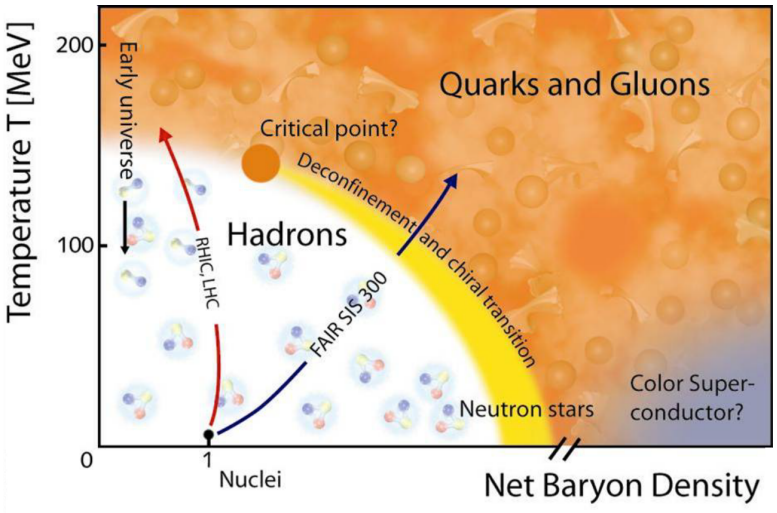

Figure 1.4: A qualitative view of the QCD phase space diagram.

1.2 Ultra-relativistic heavy-ion collisions

To explore experimentally the properties of the QGP, it is necessary create a strongly-interacting system which satisfies some conditions:

[‖]For open systems for which the baryon number B is allowed to vary, the most relevant thermodynamics potential is the grand potential $\Omega(T, \mu_B) = E - T \bullet S - \mu_B \bullet B$.

- It must be "Big", i.e. dimensions larger than the typical scale of the strong force ($>>$ 1 fm), in order to use macroscopic variables.
- Its lifetime has to be larger than the typical relaxation times ($\tau >> 1$ fm/c). Since thermodynamics language can be used only if is verified that the system is in (or near) equilibrium.
- The energy density ϵ or the equivalent temperature must exceed the critical values needed for QGP formation (see Sec. 1.1.1), or a baryonic density $\rho_c \approx$ 5–10 times the nuclear matter density.

The request of equilibrium implies that a sufficiently interacting system must be created in the experimental setup; therefore, the number of collisions suffered by each medium constituent has to be greater than one, which means that the mean free path of the constituents must be smaller than the system dimensions, so that several collisions per particle can occur.

In high-energy nucleus-nucleus (A–A) collisions, all these requirements are expected to be fulfilled mainly because of the high multiplicity of produced particles due to the presence of *multiple collisions* between nucleons of the colliding nuclei. For example, the system created in a Pb–Pb collisions can reach a volume of the order of 1000 fm^3, consisting of $\approx$ 1000 hadrons and, already at SPS energies, can reach an energy density $\approx$ 200 times larger than that of a nucleus. Moreover, at LHC energies, the nucleons that suffer collisions have enough energy to continue travelling far from the interaction zone and thus the system created is characterized by a large energy density but a small net baryon content (*transparency*). Therefore, if the temperature of the medium is larger than T_c, defined in Sec. 1.1.1, the formation of a deconfined system of quarks and gluons in the region of vanishing μ_B of the QCD phase diagram is expected.

Since nuclei are extended objects, the centrality of the collision is a key parameter in the study of the properties of the QGP because it is related directly to the overlap region of the colliding nuclei. Geometrically, it is defined by the impact parameter, b[**](see Fig. 1.5). The collision centrality is also characterized in terms of the number of participants (N_{part}), i.e. the number of nucleons that undergo at least one collision, or in terms of the number of binary collisions among nucleons from the two nuclei (N_{coll}). The nucleons that do not participate in any collision, the spectators, essentially keep travelling undeflected, close to the beam direction. Unfortunately, the impact parameter b, N_{part} and N_{coll} are not directly measurable. Hence, the centrality of the collision is

[**]the distance between the centres of the two colliding nuclei in a plane transverse to the collision axis.

determined by measuring the multiplicity of produced particles or the transverse energy, assuming that they are a monotonic function of b, or by measuring the energy in the detector at forward rapidity (see Appendix A for rapidity definition), which is related to the number of spectator nucleons [27].

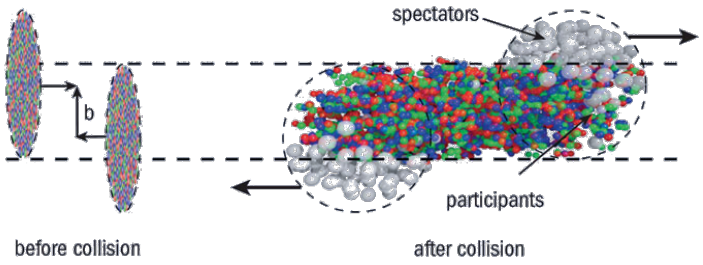

Figure 1.5: Left: Two heavy ions before collision with impact parameter b. Right: Spectator nucleons remain unaffected while particles are produced in the interactions between participant nucleons [28].

1.2.1 Time evolution of a heavy-ion collision

All our basic understanding about the space-time evolution of a heavy-ion collision is depicted in Fig. 1.6. In relativistic heavy-ion collisions, two nuclei (normal nuclear matter) are accelerated to nearly the speed of light in opposite directions. Due to their relativistic velocities both ions are Lorentz contracted along the beam axis (z-axis).

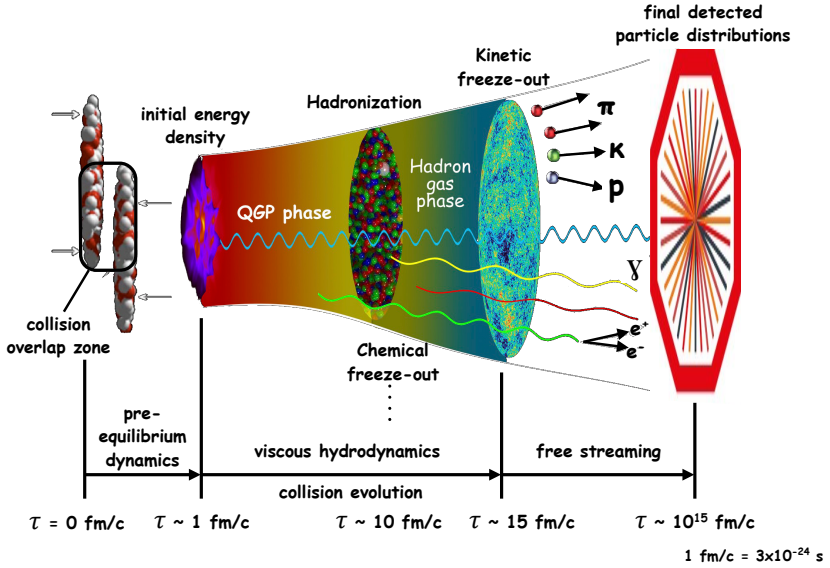

Figure 1.6: Sketch of a heavy-ion collision evolution. The values of τ are the indicative values expected at the LHC.

If we define the time of the collision between the nuclei as $\tau = 0$, then different stages can be distinguished:

- $\tau \leq \tau_0 \sim 1$ fm/c. **Pre-equilibrium:** Nucleons pass through each other (*collision overlap zone*), several nucleon-nucleon interactions occur. The nucleons lose part of their initial energy in the interacting region and a high-density system, usually called fireball, is formed. The *fireball* of interacting quarks and gluons expands at mid-rapidity (y $\simeq$ 0), where μ_{B} vanishes, while forward and backward regions (|y| $>$ 0), are relatively rich in baryons corresponding to the remnants of the nuclei (spectators in Fig. 1.5). Hard partons[††] with $p_{\mathrm{T}} >> 1$ GeV/c are created in partonic scattering processes with large momentum transfer, occurring on short time scales. The fireball reaches (or quasi-)equilibrium at a proper time τ_0 through parton re-scatterings in the medium. After this point the temperature of the system can be defined and a thermodynamics description becomes applicable. If temperature exceeds $\mathrm{T_c}$, the system is expected to be in a QGP phase.

- $\tau_0 \leq \tau \leq 10$ fm/c. **QGP phase:** The system expands due the pressure gradients[‡‡] and, as a consequence, gradually cools down. When the critical temperature $\mathrm{T_c}$ is reached α_s becomes large enough to confine the quarks and gluons inside hadrons. A transition from QGP to hadron gas occurs. From this point onward the degrees of freedom of the system are hadrons instead of free quarks and gluons.

- 10 fm/c $\leq \tau \leq$ 15 fm/c. **Hadron gas:** Below $\mathrm{T_c}$, the system is composed of hadrons which interact both elastically and inelastically. The system keeps expanding and cooling down. This leads as a consequence, to a decrease of the density and an increase of the mean free path of hadrons.

    . At a certain moment, the inelastic interaction rate becomes too small to keep up with the system expansion and the hadron abundances freeze-out. This moment is the so-called *Chemical freeze-out*, and the corresponding temperature is $\mathrm{T_{ch}}$.

    . After the chemical freeze-out, hadrons continue expanding and interacting elastically. When the system reaches the temperature $\mathrm{T_{kin}}$ elastic interactions cease and p_{T}-distributions of hadrons are frozen: this is the *Kinetic freeze-out*.

[††]point-like particles responsible of strong interaction (as a quark or gluon) that are held to be constituents of hadrons

[‡‡]Difference between the thermal pressure at the medium boundaries and the vacuum one.

- $\tau \geq 15$ fm/c. **Free hadron stream:** Both elastic and inelastic interactions no longer play a role in the system evolution. Hadrons freely stream to the experimental apparatus where they are detected. Nevertheless, short-lived particles decays produce daughter particles with, on average, smaller p_{T} that can modify the p_{T} spectra of long-lived species (e.g. resonance decay products dominate pion spectrum at low p_{T}).

Any information about the QGP or the hadron gas at thermal equilibrium must be inferred from the properties e.g. momentum spectra, relative abundance of different hadron species, azimuthal distributions etc., of the particles remaining after the thermal freeze-out.

2

QGP signatures and heavy-ion observables

As discussed in Sec. 1, the hot and dense medium created in heavy-ion collisions is extremely short-lived ($\sim$ 1–15 fm/c) and only the final state particles are measured in the detectors of the experiments. Various experimental observables are used to characterize the properties of the system created in these collisions. In the following sections, some experimental measurements used to probe the QGP formation and study its properties are summarized. The first part is dedicated to the description of hard probes like the nuclear modification factor of high-p_{T} particle yields which allow to understand the mechanism of in-medium parton energy loss, expected to be relevant in presence of a hot and dense deconfined medium. An overview of quarkonium measurements in heavy-ion collisions will also be presented: quarkonium suppression was been considered for more than twenty years a smoking-gun proof of the presence of a deconfined state. Moreover, in the second part of this chapter, soft particles which define the collective and thermal properties of the medium created in the collisions are briefly reviewed. Hadron yields and the thermodynamic models used to reproduce them are discussed. On the other hand, measurements of particle spectra, which are the main objective of this thesis, and azimuthal distributions allow us to identify and characterize the collective motion (flow) emerging from hydrodynamic behaviour of the system. Finally, some considerations about Cold Nuclear Matter (CNM) effects and surprising results observed in p–Pb collisions at $\sqrt{s_{\mathrm{NN}}} = 5.02$ TeV at the LHC are reported.

2.1 Observables related to QGP formation

The goal of heavy-ion collisions is to study the properties of strongly-interacting matter at high temperatures and energy densities. The ephemeral medium under study hadronizes in a relative short time and the final particles arriving to the detectors are the only sources of information available. There are several observables that have been studied in heavy-ion experiments and some of them suggest that in heavy-ion collisions at BNL and at CERN laboratories a new state of strongly interacting matter has been produced.

In this section, a review of the most important observables used to study the medium created in heavy-ion collisions and the most relevant experimental results from SPS, RHIC and LHC are provided.

2.1.1 Hard probes of the QGP

High-p_{T} particles provide information about the propagation of hard partons* in the medium. Hard processes are characterized by a large momentum transfer Q^2 and an associated QCD coupling constant α_s small enough that a perturbative QCD approach is possible. If a strongly interacting medium is created, the scattered partons propagating through the medium lose energy due to elastic collisions with the medium constituents and medium induced gluon radiation. In order to test that A–A collisions are not a simple uncorrelated superposition of nucleon–nucleon collisions, a comparison between A–A and pp results is performed. The number of particles produced in A–A collisions are expected to be proportional to $\mathrm{N_{part}}$ at low p_{T} and to the number of nucleon–nucleon collisions $\mathrm{N_{coll}}$ at high p_{T}.

In order to show the existence of parton energy-loss induced by the QGP presence it is useful to define the *nuclear modification factor* $\mathrm{R_{AA}}$ as,

$$\mathrm{R_{AA}}(p_{\mathrm{T}}) = \frac{d^2\mathrm{N_{AA}}/dp_{\mathrm{T}}d\mathrm{y}}{\langle \mathrm{N_{coll}} \rangle \; d^2\mathrm{N_{pp}}/dp_{\mathrm{T}}d\mathrm{y}} \tag{2.1}$$

where $\mathrm{N_{AA(pp)}}$ is the particle spectra in A–A(pp) collisions.

From this definition, one expects a value $\mathrm{R_{AA}} = 1$ at high p_{T} (i.e. in the region where hadron production is dominated by hard process) if A–A is an incoherent superposition of $\mathrm{N_{coll}}$ nucleon–nucleon collisions.

Initial state effects, such as Cronin enhancement [29] or nuclear modifications of the parton distribution functions (PDF), such as shadowing, could modify this behaviour [25]. In order to separate the initial state effects from the "hot" nuclear matter effects due to the QGP, nucleon–nucleus (p–A) collisions are studied and compared to results from pp collisions, see Sec. 2.2.

In particular, the nuclear modification factor is measured for different centralities in A–A collisions to study the dependence of energy loss on the medium density and size. The size and density of the QGP fireball are smaller in peripheral collisions with respect to central collisions. Therefore, $\mathrm{R_{AA}}$ is smaller in central than in peripheral collisions.

*High-*pt* partons are generated in scattering processes with large momentum transfer occurring the first stages of the collision.

Suppression of high-p_{T} hadron yield

The first evidence of a suppression of high-p_{T} hadrons was observed at RHIC in Au–Au collisions. In the left panel of Fig. 2.1 the $\mathrm{R_{AA}}$ of charged hadrons measured by ALICE, in the 5% most central Pb–Pb collisions at $\sqrt{\mathrm{s_{NN}}}$ = 2.76 TeV [30], is compared to PHENIX results in the centrality range 0–10% [31] and STAR results in 0–5% [32] for Au–Au collisions at $\sqrt{\mathrm{s_{NN}}}$ = 200 GeV at RHIC. At $p_{\mathrm{T}} \approx 1$ GeV/c the magnitude of the suppression measured at LHC energies is similar to that observed at RHIC. In the intermediate p_{T} region, a strong dependence on p_{T} is seen with a maximum $\mathrm{R_{AA}}$ around $p_{\mathrm{T}} = 2$ GeV/c for all measurements. For $p_{\mathrm{T}} = 6$–7 GeV/c, where the effects of in-medium energy loss start to be dominant, the ALICE result indicates a stronger suppression ($\mathrm{R_{AA}} \approx 0.13$) with respect to the one observed at RHIC energies. This evidence suggests an enhanced energy loss at LHC respect to RHIC, which can be a consequence of different relative abundance of quarks-jet and gluons-jet in a larger medium density. However, since the $\mathrm{R_{AA}}$ is also sensitive to the steepness of the spectrum, the energy loss (ΔE) can be the same in both collision systems, but the steeper spectrum at LHC gives a smaller $\mathrm{R_{AA}}$. A considerably rise of the nuclear modification factor by a factor of two is observed at higher momenta. This trend of the $\mathrm{R_{AA}}$ has been predicted by various theoretical calculations based on in-medium energy loss[†]. The $\mathrm{R_{AA}}$ reported by CMS [33] is fully in agreement with the ALICE results within the uncertainties.

In addition, right part of Fig. 2.1 shows the $\mathrm{R_{AA}}$ measured by ALICE in central collision superposes to the results from peripheral (70–80%) Pb–Pb collisions at $\sqrt{\mathrm{s_{NN}}}$ = 2.76 TeV and non-single diffractive (NSD) p–Pb collisions at $\sqrt{\mathrm{s_{NN}}}$ = 5.02 TeV in $|\eta_{cms}| < 0.3$[‡]. In peripheral Pb–Pb collisions the suppression is significantly smaller than in central Pb–Pb collisions. If a QGP is created in peripheral Pb–Pb collisions, the QGP phase is expected to be shorter and the system size to be smaller. Hence, if the suppression is produced by parton energy loss in the QGP medium, a smaller suppression in peripheral collisions is expected. The interpretation of the Pb–Pb results in term of in-medium energy loss is also confirmed by the $\mathrm{N_{coll}}$-scaling of the nuclear modification factor in p–Pb collisions at high p_{T} ($\mathrm{R_{pA}} \approx 1$). In proton–nucleus (p–A) collisions, an extended QGP phase is not expected to be formed, and therefore no medium effects are expected. In the intermediate p_{T} region a hint to a Cronin enhancement[§] can be observed.

[†]see [30] and references therein

[‡]Due to the absence of pp measurement at $\sqrt{\mathrm{s}}$ = 5.02 TeV, the reference pp spectrum is obtained by interpolating or scaling data measured at $\sqrt{\mathrm{s}}$ = 2.76 and 7 TeV [34]

[§]Not relevant considering the error bars

The interaction of the hard jets with the deconfined medium leads also to a suppression in the production of jet pairs (di-jet). This effect can be studied from angular correlation of high-p_{T} particles on events, in which one requires the presences of a high-p_{T} hadron (or an energetic jet). A hadron pair drawn from a single jet generate an enhanced correlation at $\Delta\phi \approx 0$. In contrast, a hadron pair drawn from back-to-back di-jets will generate an enhanced correlation at $\Delta\phi \approx \pi$, with a broader width than the near-side correlation peak. Measurements of high-p_{T} hadron correlations in pp collisions show two peaks at zero and 180 degrees (back-to-back). In A–A collisions, energetic jet is likely to come from a hard scattering that occurred on the surface of the collision volume (surface emission), therefore, one of the produced partons traversed a very short distance, inside the medium, while its partner goes through a longer path. As a consequence, if a dense deconfined medium is formed, the latter loses its energy interacting with the medium and it is not detected. In Fig. 2.2 this observable as observed by STAR at RHIC is shown [35]. Similar result has been obtained at LHC, using the ATLAS detector [36].

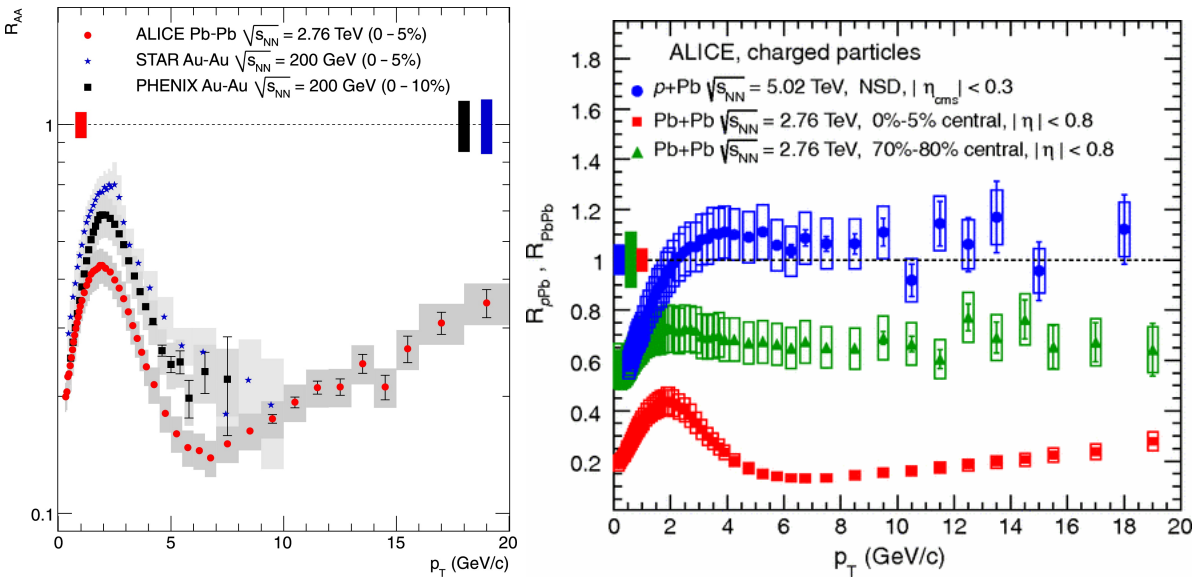

Figure 2.1: The nuclear modification factor of charged hadrons for central (0–5%) Pb–Pb collisions at $\sqrt{s_{\mathrm{NN}}} = 2.76$ TeV measured by ALICE [30] compared to: left, the results observed in Au–Au collisions at $\sqrt{s_{\mathrm{NN}}} = 200$ GeV at RHIC [31, 32]; right, peripheral (70–80%) Pb–Pb collisions at $\sqrt{s_{\mathrm{NN}}} = 2.76$ TeV [34] and non-single diffractive (NSD) p–Pb collisions at $\sqrt{s_{\mathrm{NN}}} = 5.02$ TeV in $|\eta_{cms}| < 0.3$. The statistical errors are represented by vertical bars, the systematic ones by shaded (left) and empty (right) boxes and the relative systematic uncertainties on the normalization are shown as boxes around unity.

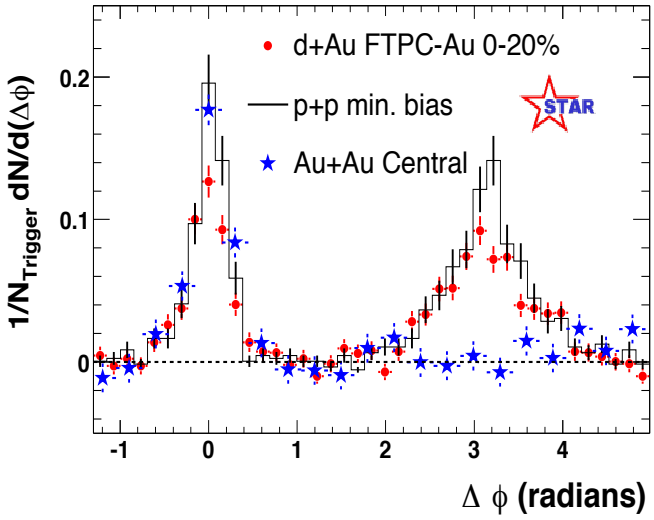

Figure 2.2: Azimuthal distributions measured by STAR in central Au–Au collisions at $\sqrt{s_{NN}}$ = 200 GeV with results obtained in pp and central pA collisions [35].

Heavy flavours

Heavy quarks (i.e. charm and beauty), owing to their large mass, can only be produced in the initial phase of the collision in the scattering of partons with high enough Q^2 to create a pair (quark-antiquark) of them. Since heavy flavour production is characterized by large energy transfer, the production rate can be computed with a perturbative approach to QCD. As these particles are produced at the beginning of the collision, they experience all the stages of the QGP evolution and finally hadronize forming heavy flavour hadrons. These hadrons carry a large fraction of the parton momentum, because the fragmentation function is much harder for b and c quarks than for light quarks and gluons. Heavy quark energy loss can be estimated by measuring the nuclear modification factor of heavy flavour hadrons, reconstructed from their decay products. This is shown in Fig. 2.3 where the average R_{AA} of D^0, D^+ and D^{*+} mesons is compared to that of charged particles for Pb–Pb collisions at $\sqrt{s_{NN}}$ = 2.76 TeV in the centrality interval 0–20%. The R_{AA} shows a suppression by a factor 3–4, for transverse momenta larger than 5 GeV/c in the 20% most central collisions. The suppression is almost as large as that observed for charged particles (mainly light-flavour hadrons). However data seem to suggest, even through it is not fully significant with the present level of experimental uncertainties, that the suppression for D mesons is smaller that the one for charged hadrons. In the same figure is also shown the R_{AA} for non-prompt J/ψ mesons (from B decays) with $p_T > 6.5$ GeV/c measured by the CMS Collaboration [37]. Their sup-

pression is clearly weaker than that of charged particles, while the comparison with D mesons is not conclusive and would require more differential and precise measurements of the transverse momentum dependence. Energy loss models predict the R_{AA} value to be larger (i.e. a smaller suppression) when going from the mostly gluon-originated light-flavour hadrons (e.g. pions) to D and B mesons, i.e. ${R_{AA}}^{\pi} < {R_{AA}}^{D} < {R_{AA}}^{B}$, due to the colour-charge and quark mass dependence of parton in medium energy loss (see e.g. [38, 39]).

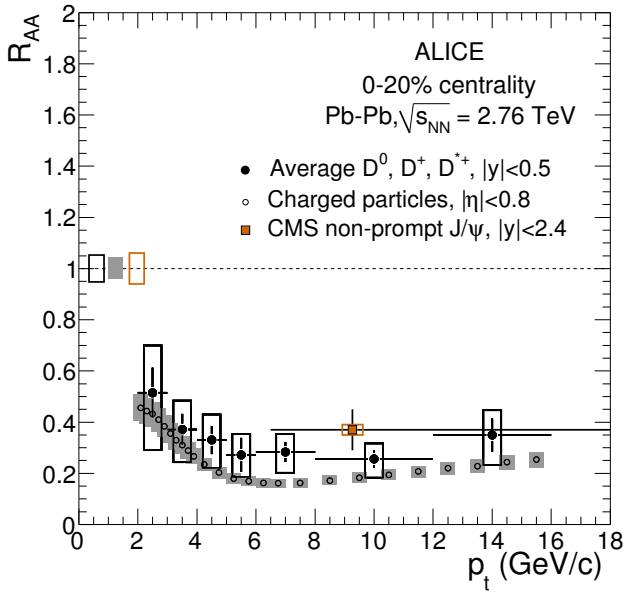

Figure 2.3: Average R_{AA} of D^0, D^+ and D^{*+} mesons compared to the nuclear modification factors of charged particles [30] and non-prompt J/ψ from B decays [37] for Pb–Pb collisions at $\sqrt{s_{NN}} = 2.76$ TeV in the centrality range 0–20%. The charged particle R_{AA} is shown only for $2 < p_T < 16$ GeV/c. The three normalization uncertainties shown in the right-hand panel are almost fully correlated.

Quarkonium production

In 1986, Matsui and Satz predicted that the suppression of quarkonium production in ultra-relativistic heavy-ion collisions was expected to be an unambiguous signature for the formation of QGP [40]. The interaction between c and $\bar{c}$ (or b and $\bar{b}$) quarks, can be expressed as:

$$V(r) = -\frac{\alpha(r)}{r} + kr \tag{2.2}$$

where the first term is the *Coulomb* term given by gluon exchanges between the quark and the antiquark and the second term represents the confinement term. In presence of

a deconfined state, the effect of confinement term vanish and the long-range Coulomb part of the potential is screened. In these conditions, the quark-antiquark potential is described by a short-range Yukawa interaction, $V(r) = -\frac{\alpha(r)}{r}e^{-r/\lambda_D}$, where λ_D is called *Debye screening length* and defines the range of the interaction; it is expected to decrease with increasing temperature. In presence of a "hot" medium, thus, quarkonium states are not formed or they dissociate into separate quark and antiquark pair in the plasma, and then eventually hadronize at the phase boundary combining predominantly with light quarks. According to the colour-screening model [41], quarkonium states with different binding energies are expected to melt at different temperatures. Therefore, the measurement of the suppression of these states can provide an estimation of the medium temperature. Other effects can modify the quarkonium production in heavy-ion collisions: shadowing of the PDF, quarkonium suppression by hadronic matter (so called *hadronic co-movers*) and regeneration given by statistical recombination of $c\bar{c}$ (and $b\bar{b}$) pairs in the medium. In the left panel of Fig. 2.4, the inclusive J/ψ $\mathrm{R_{AA}}$ reported by ALICE in Pb–Pb collisions at $\sqrt{\mathrm{s_{NN}}} = 2.76$ TeV as a function of number of participating nucleons $\langle \mathrm{N_{part}} \rangle$ is shown [42]. The J/ψ $\mathrm{R_{AA}}$ was measured at central rapidity $|\mathrm{y}| < 0.8$ in the $\mathrm{e^+e^-}$ decay channel and at forward rapidity $2.5 < \mathrm{y} < 4$ via the reconstruction of the $\mu^+\mu^-$ decay channel. The measurement at forward rapidity is lower than unity, pointing to a clear suppression of the J/ψ production in central Pb–Pb collisions ($\langle \mathrm{N_{part}} \rangle > 70$). A similar suppression is observed in the central rapidity region although with larger uncertainties. In the right panel of Fig. 2.4, the $\mathrm{R_{AA}}$ as a function of p_T measured by ALICE for Pb–Pb collisions at $\sqrt{\mathrm{s_{NN}}} = 2.76$ TeV in the centrality interval 0–20% and rapidity region $2.5 < \mathrm{y} < 4$ is compared to results obtained by PHENIX [43] in 0–20% most central Au–Au collisions at $\sqrt{\mathrm{s_{NN}}} = 200$ GeV. At the LHC the $\mathrm{R_{AA}}$ is larger than the one measured for most central collisions at RHIC. This can be interpreted as an increasing regeneration of J/ψ at the LHC with respect to RHIC due to the larger number of $c\bar{c}$ pairs at higher $\sqrt{\mathrm{s}}$. The ALICE measurement, indeed, is well described by theoretical calculations which include a relevant component of J/ψ production via charm recombination in the medium [44, 45].

2.1.2 Soft probes of the QGP

Low transverse momentum hadrons ($p_\mathrm{T} < 2$ GeV/c) represent more than 99% of particles produced in heavy-ion collisions. These hadrons are mainly created by the hadronization of soft[¶] partons in the QGP, which are in thermal equilibrium in the deconfined phase. A thermalized system has a thermal pressure which, when acting against

[¶]The production of soft partons is usually non-perturbative and requires phenomenological models.

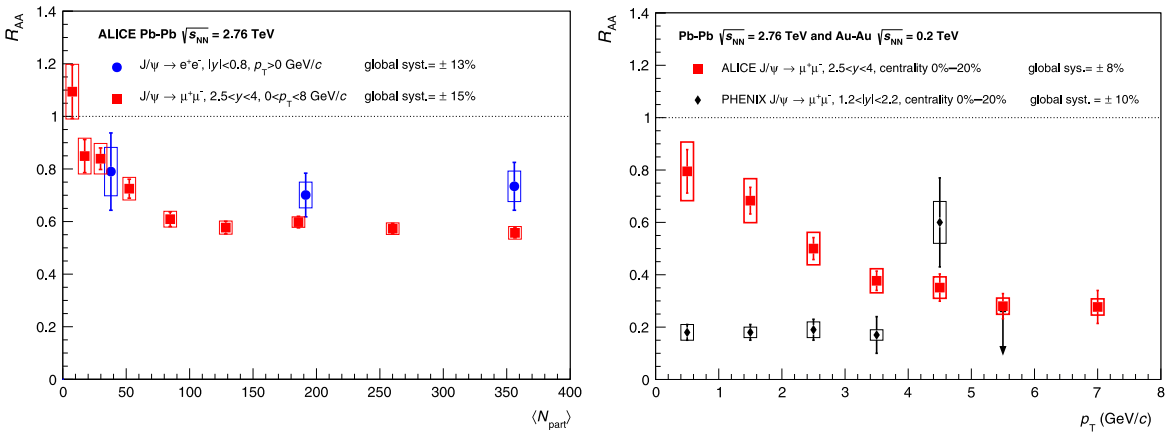

Figure 2.4: Left: Centrality dependence of the R_{AA} of inclusive J/ψ measured by ALICE in Pb–Pb collisions at $\sqrt{s_{NN}}$ = 2.76 TeV at mid-rapidity ($|y| < 0.8$) and at forward-rapidity ($2.5 < y < 4$) [42]. Right: Inclusive J/ψ R_{AA} measured by ALICE in the 0–20% most central Pb–Pb collisions at $\sqrt{s_{NN}}$ = 2.76 TeV compared to PHENIX [43] results in the 0–20% most central Au–Au collisions at $\sqrt{s_{NN}}$ = 200 GeV.

the surrounding vacuum, leads to collective (hydrodynamical) expansion of the collision fireball. While expanding, the fireball cools down and its energy density decreases. When the latter reaches the critical energy for the phase transition $\epsilon \approx 1$ GeV/fm^3, the partons convert into hadrons. After hadronization, the hadrons keep re-scattering with each other for a while, continuing to build up the expansion flow. These hadrons are strongly interacting particles which cannot decouple from the fireball before the system is so dilute that interactions cease. First, their abundances freeze-out at T_{ch} when the rates for inelastic collisions become too small to keep up with the expansion. Below T_{ch} hadrons still suffer elastic[‖] scatterings until the kinetic freeze-out temperature T_{kin} is reached, at this point hadrons decouple from the fireball and they are detected by the experiments. Their observed momentum distributions thus provide a *snapshot* of the kinetic decoupling stage (*thermal freeze-out*), which carry thermal information about the prevalent temperature at chemical respect to thermal freeze-out, folded with (i.e. blueshifted by) the collective expansion flow. The reconstruction of the global space-time evolution of the fireball from initial stages until the finally observed soft hadrons is the basis on which other rarer observables, in particular the "deep" or "hard" probes, can be interpreted. This illustrates the network-like interdependence between soft and hard observables in their role for studying heavy-ion collision.

[‖]What it is called "elastic" includes resonance processes such as $\pi + N \to \Delta \to \pi + N$, which do not change chemical composition, but contribute to the thermalization of the momenta.

Particle multiplicity and energy density

Charged particle pseudo-rapidity density at mid-rapidity $d\mathrm{N_{ch}}/d\eta|_{\eta=0}$ depends on the parton density of the medium and it allows an estimation of the energy density which is an important observable to characterize the system produced in heavy-ion collisions. For example, jet quenching and quarkonium suppression cannot be quantitatively interpreted without knowledge of the fireball density and its space-time evolution. The particle pseudo-rapidity density normalized to the number of participant nucleon pairs as a function of the centre-of-mass energy for different colliding systems is presented in the left panel of Fig. 2.5 [46]. The energy dependence of the charged multiplicity for central heavy-ion collisions is steeper than for pp and $\mathrm{p\bar{p}}$ collisions and exhibits a power-law scaling, which was confirmed by the ALICE, CMS and ATLAS measurements at the LHC in central Pb–Pb collisions at $\sqrt{\mathrm{s_{NN}}} = 2.76$ TeV [46–48]. A strong increase, by a factor 2.2, in the pseudo-rapidity density is observed at the LHC compared to the STAR results from Au–Au collisions at RHIC at $\sqrt{\mathrm{s_{NN}}} = 200$ GeV [49]. The right panel of Fig. 2.5 shows the dependence of $d\mathrm{N_{ch}}/d\eta/(0.5\langle \mathrm{N_{part}}\rangle)$ as a function of $\langle \mathrm{N_{part}}\rangle$ measured with ALICE: the charged-particle density per participant pair increases with centrality from 4.4 ± 0.4 for most peripheral to 8.3 ± 0.3 for most central events. In the same plot, the results obtained at RHIC (averaged among all the experiments) are shown after being scaled by a factor 2.1. The centrality dependence of the two measurements is very similar [50]. This is described in models including saturation effects in which the geometry and energy dependence factorize.

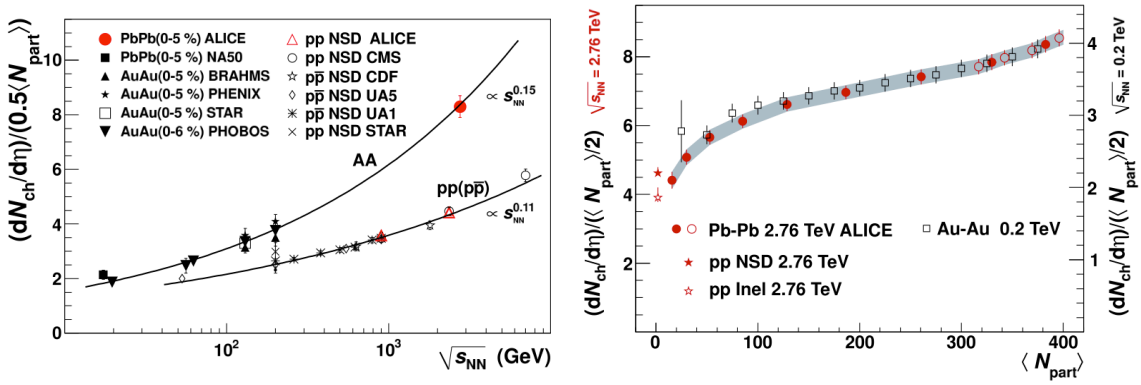

Figure 2.5: Left: Charged particle pseudo-rapidity density per participant pair for central A–A collisions as a function of the centre-of-mass energy for different colliding systems [46]. Right: Centrality dependence of $d\mathrm{N_{ch}}/d\eta/(0.5\langle N_{part}\rangle)$ for Pb–Pb collisions at $\sqrt{\mathrm{s_{NN}}} = 2.76$ TeV measured with ALICE and Au–Au collisions at $\sqrt{\mathrm{s_{NN}}} = 200$ GeV obtained with an average of RHIC results. The latter measurement is scaled by a factor 2.1 [50].

An approach to estimate the energy density of the QGP from the particle multiplicity was proposed by Bjorken in the '70s [51]. In his approach, the energy density of the medium can be estimated from the transverse energy density per rapidity unit, $d\mathrm{E_T}/d\mathrm{y}$.

It can be found that:

$$\epsilon_{\mathrm{Bj}} = \frac{1}{\tau_0 \mathrm{A}} \frac{d\mathrm{E_T}}{d\mathrm{y}}\bigg|_{\mathrm{y}=0} \tag{2.3}$$

where A is the transverse overlapping area in the collision of the nuclei and τ_0 is the formation time of the QGP. At mid-rapidity (y = 0) it is possible to approximate the transverse energy density as follows:

$$\frac{d\mathrm{E_T}}{d\mathrm{y}}\bigg|_{\mathrm{y}=0} \sim \langle \mathrm{E_T} \rangle \frac{d\mathrm{N}}{d\mathrm{y}}\bigg|_{\mathrm{y}=0} \sim \langle \mathrm{E_T} \rangle \frac{d\mathrm{N}}{d\eta}\bigg|_{\mathrm{y}=0} \tag{2.4}$$

where $d\mathrm{N}/d\mathrm{y}$ and $d\mathrm{N}/d\eta$ are the particle rapidity and pseudo-rapidity densities respectively and $\langle \mathrm{E_T} \rangle$ is the average hadron transverse energy which can be obtained experimentally e.g. by measuring the energy of charged hadrons with the tracking detectors.

Using Eq. 2.3 and 2.4, the energy density ϵ_{Bj} at mid-rapidity can be estimated starting from the measured $d\mathrm{N}/d\eta$ and $\langle \mathrm{E} \rangle$. ALICE obtained for Pb–Pb collisions in the centrality range 0–5% $\epsilon_{\mathrm{Bj}} \approx 16$ GeV/fm^3, about a factor 3 larger than the corresponding one at RHIC in the same centrality range. For both the estimations, the QGP formation time considered was $\tau_0 = 1$ fm/c**. The energy density measured at LHC and at RHIC is well above the critical density $\epsilon_c \sim 1$ GeV/fm^3 expected for the phase transition according to lattice QCD calculations (Section 1.1.1).

Hadron species abundance and Statistical Hadronization Model

Hadron abundances are expected to provide information on properties of the system at the moment of the chemical freeze-out since hadronic yields are fixed when inelastic interactions cease. The proper approach to study a non-perturbative, multi-channel and multi-particle problem, e.g. multi-particle production in heavy-ion collisions, is a statistical one (as was already recognized by Fermi, Landau and Hagedorn more than a half century ago).

Several thermal models, also called Statistical Hadronization Model (SHM), have been able to reasonably reproduce particle abundances in both hadron-hadron and A–A collisions [52–55]. The SHM assumes that hadronic matter is in chemical and kinetic equilibrium at the moment of the chemical freeze-out. Thus, this model does not require

** $\tau_0 = 1$ fm/c is larger than the equilibration time estimated from hydrodynamic calculations, so it makes sense to assume that at such times a thermalized QGP state exists

any assumption on the characteristics of the system in previous stages of the collision and the hadron abundances can be obtained from the principle of maximum entropy.

In heavy-ion collisions, the system can be considered in equilibrium with an external source with which it can exchange particles and energy. For this reason, the partition function for a given particle species i can be calculated in the grand-canonical ensemble as:

$$\ln \mathrm{Z}_i = \frac{\mathrm{V g}_i}{2\pi^2} \int_0^\infty \pm p^2 dp \ln[1 \pm \mathrm{e}^{-\frac{\mathrm{E}_i - \mu_i}{\mathrm{T_{ch}}}}] \tag{2.5}$$

where V is the system volume, $\mathrm{T_{ch}}$ is the temperature at the chemical freeze-out, $\mathrm{E}_i = \sqrt{p^2 + m_i^2}$ is the energy of the particle, $\mathrm{g}_i = (2\mathrm{J}_i + 2)$ is the spin degeneracy factor and μ_i is the chemical potential for the considered species i. In the expression above, the sign $-$ is valid for fermions while $+$ for bosons. The chemical potential μ_i can be expressed in terms of the baryon number B_i, the third component of the isospin I_{3i}, the strange and charm content S_i and C_i of the hadron species and the corresponding chemical potentials μ_B, μ_{I_3}, μ_s and μ_c:

$$\mu_i = \mu_\mathrm{B}\mathrm{B_i} + \mu_{\mathrm{I}_3}\mathrm{I_{3i}} + \mu_\mathrm{s}\mathrm{S_i} + \mu_\mathrm{c}\mathrm{C_i} \tag{2.6}$$

The density of particles of species i can be derived from Eq. 2.5 as:

$$n_i = \frac{\mathrm{N}_i}{\mathrm{V}} = -\frac{\mathrm{T}}{\mathrm{V}} \frac{\partial \ln \mathrm{Z}_i}{\partial \mu_i} = \frac{\mathrm{g}_i}{2\pi^2} \int_0^\infty \frac{p^2 dp}{e^{-\frac{\mathrm{E}_i - \mu_i}{\mathrm{T}}} \pm 1} \tag{2.7}$$

Imposing the charge conservation (I_3) and the strangeness and charm conservation ($\mathrm{V}\sum_i n_i \mathrm{S}_i{=}0$ and $\mathrm{V}\sum_i n_i \mathrm{C}_i{=}0$ for heavy-ion collisions) the only free parameters are the temperature $\mathrm{T_{ch}}$, the baryo-chemical potential μ_B and the volume of the system V. The values of these parameters can be obtained via a fit to the measured p_T-integrated yields of the different hadron species using a χ^2 minimization procedure:

$$\chi^2 = \sum_i \frac{(\mathrm{N}_i^{measured} - \mathrm{N}_i^{model})^2}{\sigma_i^2} \tag{2.8}$$

In case ratio of particle yields are used, the volume V cancels out in the fit leaving only $\mathrm{T_{ch}}$ and μ_B as free parameters. A good description of the experimental data by SHM is only achieved if the model considers the contribution from decays of short-lived particles to the thermal production of species i when particle yields are estimated.

For small systems (such as peripheral A–A or pp collisions) a canonical treatment, instead of a grand canonical one, is essential. Differences from the (grand canonical) equilibrium case can be restored through empirical under(over)-saturation parameters for strange, charm or light quarks (γ_s, γ_c and γ_q).

The need for γ_s is because a fluctuation from the equilibrium abundances by a factor which depends on the strangeness content is expected for strange particles [56, 57]. Nevertheless, it is already established, for central collisions at RHIC, that $\gamma_s \approx 1$ [58]. Another approach consists in the implementation of a "canonical suppression" mechanism (i.e. strangeness are forced to conserve locally and not on average) [57] on a smaller volume than the overall size of the system, determined by a "canonical radius" parameter, R_c. The parameter γ_c is introduced because charm can only be created in the initial stages of the collisions (it is too heavy to be created thermally) [59] and it is thus expected to be significantly out of equilibrium. While the usage of γ_s and γ_c is common to most implementations of the statistical model [52–54], γ_q is only found in the non-equilibrium model SHARE [55]. The physical picture in this model is that of an expanding, super-cooled quark-gluon plasma which undergoes a sudden hadronization without further re-scattering. Hence the thermal parameters of the quark-gluon plasma are frozen, leading to out-of-equilibrium hadron abundances. From the point of the fit, γ_q allows the relative abundance of mesons and baryons to vary (as it is determined by the number of valence light quarks).

Thermal fits were found to give an excellent description of particle yields in A–A collisions over a broad range of energies. A comparison of data in Au–Au collisions at top RHIC energy ($\sqrt{s_{NN}} = 200$ GeV) with equilibrium thermal model is shown in Fig. 2.6 [60]. The data are very well reproduced by SHM predictions[††] with a temperature of chemical freeze-out of $T_{ch} \approx 160$ MeV and a small baryo-chemical potential, μ_B.

The analysis of data as a function of $\sqrt{s_{NN}}$ allows to extrapolate the parameters to the case of very high collision energy. The values of T_{ch} and μ_B as a function of the centre-of-mass energy of the collisions $\sqrt{s_{NN}}$ are reported in Fig. 2.7 [61]. A flat behaviour of the chemical freeze-out temperature, T_{ch}, as a function of $\sqrt{s_{NN}}$ above ≈ 10 GeV is observed. This saturation of the chemical freeze-out happens close to the critical temperature, T_c, where a phase transition is predicted. This might suggest a similar T_{ch} value for RHIC and the LHC. On the other hand, μ_B decreases asymptotically to zero for high $\sqrt{s_{NN}}$. Hence, a vanishing baryo-chemical potential is suggested at the LHC.

An anomalously low $p/\pi = 0.046 \pm 0.003$ ratio (a factor of ~ 1.5 lower than SHM expectation based on $T_{ch} = 164$ MeV[‡‡]) was observed by ALICE [62, 63] in central collisions at the LHC. A thermal model fit to the ALICE data measured in central Pb–Pb collisions at $\sqrt{s_{NN}} = 2.76$ TeV at the LHC is shown in the left panel of Fig. 2.8.

[††] A better fit is obtained when analysing data from the same experiment.

[‡‡] Chemical freeze-out temperature expected at the LHC from the extrapolation including SHM reults on RHIC data.

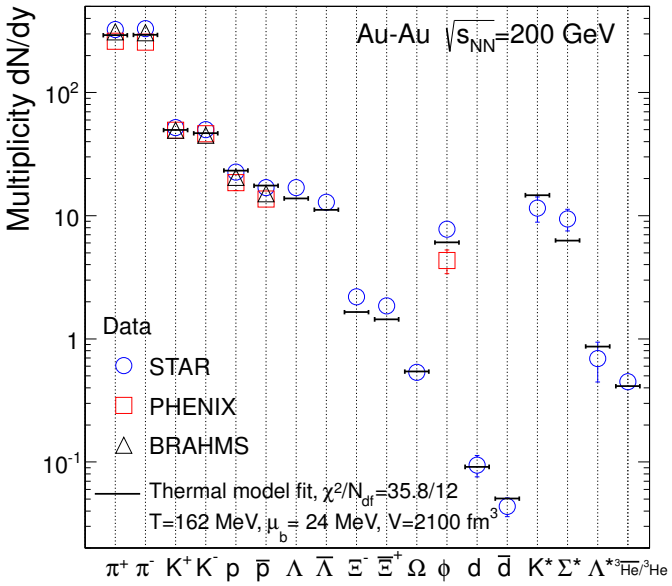

Figure 2.6: Comparison of thermal model predictions with RHIC data [60] for hadron abundances.

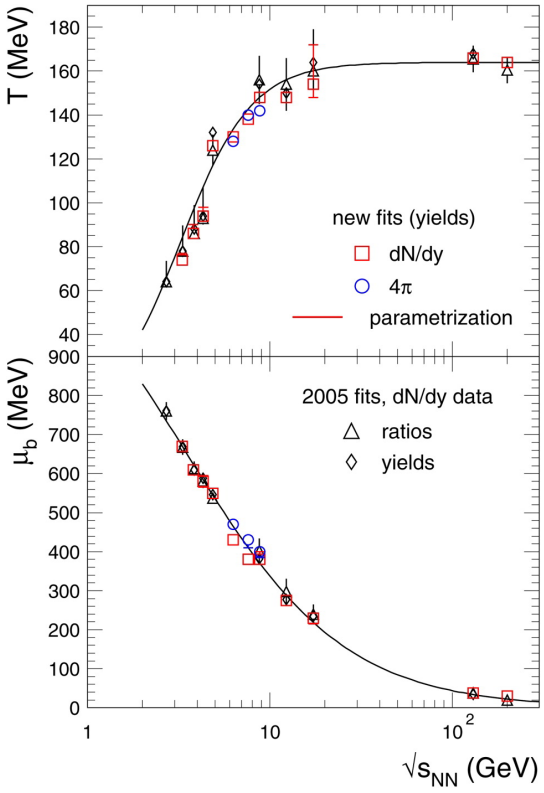

Figure 2.7: Energy dependence of temperature and baryo-chemical potential at chemical freeze-out. The lines are parametrizations for T_{ch} and μ_B [61].

A lower chemical freeze-out temperature, $T_{ch} \approx 156$ MeV, than at RHIC is obtained with a reduced χ^2 of 2.4 (slightly worse than expected from fit quality at RHIC) [60]. The largest contribution to χ^2/NDF comes from the low yield of protons relative to pions. Results for a statistical model calculation using $T_{ch} = 164$ MeV and $\mu_B = 1$ MeV are also shown. The deviations between fit and data are shown in the right panel. The (anti-)proton yields are bellow the model expectation by 18.0(19.4) % which, due to the small experimental errors, amounts to a deviation of 2.7(2.9) sigma. The cascade yields, on the other hand, are above the model by about 2 sigma. Otherwise the agreement of data and fit is excellent.

Already for the RHIC data there is some indication of lower proton yields as compared to the statistical model calculations (Fig. 2.6). But due to the larger uncertainties in removing the contributions from feeddown from Λ and Σ weak decays* there are deviations among different experiments and no clear picture emerges.

Different explanations such as *Incomplete hadron list*, *Non-equilibrium thermal model*, *Hadronic interactions* and *Flavour hierarchy at freeze-out* (See. Ref. [64] for more details of each mechanism) have been proposed to explain the yields measured at the LHC. Additional experimental constraints could help to determine which is the correct one and how the T_{ch} relates to the phase transition temperature.

Strangeness enhancement

It was long ago argued that an enhancement of the production of strange particles in A–A collisions, relative to pp or to p–A collisions, could be a signal of QGP formation [56]. As discussed in Sec. 1.1.1, when a deconfined system of quarks and gluons is created the chiral symmetry is partially restored and the dynamical mass of the strange quark reduces to the current value of ≈ 150 MeV/c^2. This leads to an abundant production of strange quark and antiquark pairs by gluon fusion ($gg \rightarrow s\bar{s}$), also because of the large gluon density of the system. During the hadronization, the larger amount of strange quarks in the QGP turns to an increased production of strange hadrons with respect to pp collisions. The magnitude of the strangeness enhancement is usually estimated in experiments using the enhancement factor $E(X) = \frac{(N_X^{A-A}/\langle N_{part}\rangle)}{N_X^{pp}}$ of a given specie X. Inelastic scattering between hadrons like $\pi + \pi \rightarrow K + K$ or $\pi + N \rightarrow \Lambda + K$ could also enhance the measured amount of strangeness. For this reason, it is predicted that $E(X)$ depends on the strangeness content of the particles [65] and a hierarchy, $E_\Lambda < E_\Xi < E_\Omega$, for strange and multi-strange hyperon and anti-hyperons is expected in case of QGP formation.

*The published hadron yields at RHIC were obtained without vertex detectors

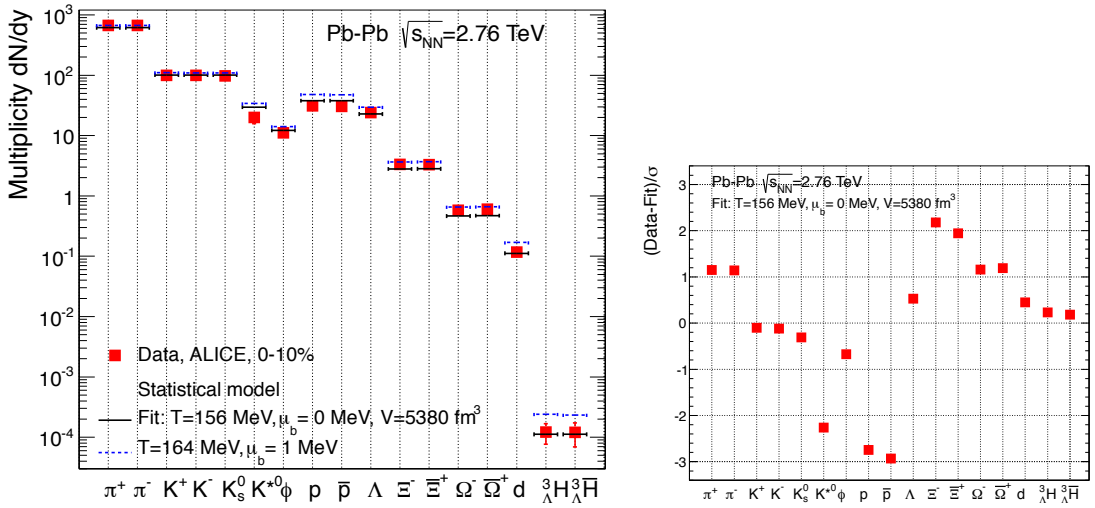

Figure 2.8: Left: Hadron yields from ALICE at the LHC and fit with the statistical hadronization model. In addition to the fit, yielding T = 156 MeV, also results of the model for T = 164 MeV are shown, normalized to the value for π^+. The data point for the K_0^* is not included in the fit because as a strongly decaying resonance, its yield can be significantly modified after chemical freeze-out. Right: Deviations between thermal fit and data normalized to the errors on the data points [60].

The enhancement factor for Ξ^-, $\bar{\Xi}^+$ and $\Omega^{\pm} = \Omega- + \bar{\Omega}^+$ in Pb–Pb collisions at $\sqrt{s_{NN}}$ = 2.76 TeV as a function of $\langle N_{part} \rangle$ have been measured by ALICE at the LHC, Fig 2.9 [66]. Enhancements larger than unity for all particles are observed. They increase with the strangeness content of the particle, showing the hierarchy mentioned above and already observed at lower energies. In addition, the same trend and scale are observed for baryons and anti-baryons (shown for Ξ^- and $\bar{\Xi}^+$ in Fig. 2.9), as expected because of the vanishing net-baryon number at LHC energies. The centrality dependence shows that the multi-strange particle yields grow faster than linearly with $\langle N_{part} \rangle$[†], at least up to the three most central classes (N_{part} > 100–150), where there are indications of a possible saturation of the enhancement. Comparing the ALICE measurements with those from the experiments NA57 at the SPS (Pb–Pb collisions at $\sqrt{s_{NN}}$ = 17.2 GeV) and STAR at RHIC (Au–Au collisions at $\sqrt{s_{NN}}$ = 200 GeV), open symbols in Fig 2.9, the enhancements are found to decrease with increasing centre-of-mass energy, continuing the trend established at lower energies [67, 68]. The reduction of the strangeness enhancement factor with increasing $\sqrt{s}$ of the collision can be explained by thermal models as due to the reduction of the strangeness suppression in pp collisions (canonical suppression) [57].

[†]Reminder to the reader: soft processes are expected to be proportional to N_{part}.

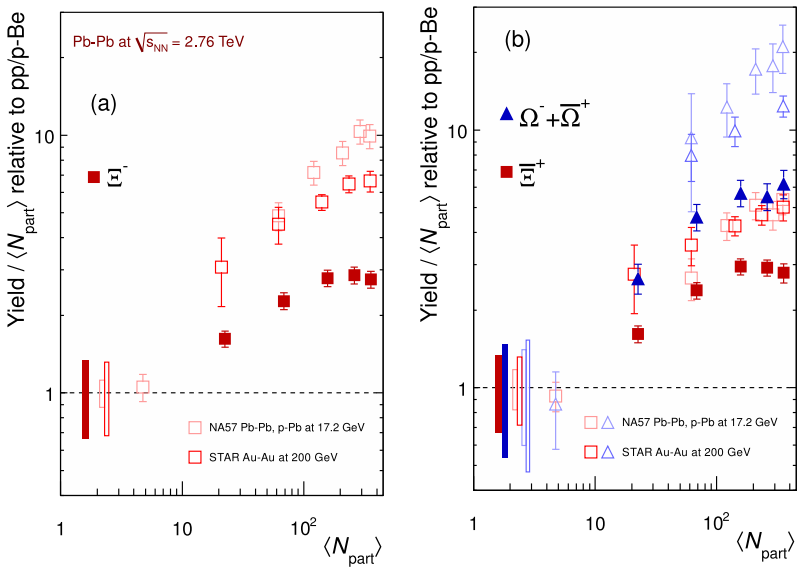

Figure 2.9: Enhancement of strange baryon (Ξ and Ω) production in the rapidity range $|y| < 0.5$ as a function of the mean number of participants $\langle \mathrm{N_{part}} \rangle$, showing LHC (ALICE, full symbols), RHIC [68] and SPS [67] (open symbols) data.

Collective flow from a hydrodynamic evolution picture

Collective flow is an unavoidable consequence of highly interacting systems, e.g the strongly-interacting medium created in heavy-ion collisions. Since the QGP is by definition a thermalized system of quarks and gluons, it has a thermal pressure. Thus the pressure gradients with respect to the surrounding vacuum cause the fireball to explode. The expansion and decoupling of the matter produced is understood with hydrodynamic models [69–73]. In these models, in order to study a large number of observables and correlation among them (e.g. particle p_{T} spectra, radial flow, elliptic flow, Hanbury Brown-Twiss correlations...), the fireball evolution is represented as a sequence:

Initial conditions
↓ are the input for the $\tau_{\mathrm{EQ}} \approx 0.8$–$1$ fm/c
Hydrodynamic evolution of the QGP
↓ which after hadronization is turned to $\tau_{\mathrm{ch}} \approx 10$ fm/c
Hydrodynamic evolution of a hadron gas
↓ up to the $\tau_{\mathrm{kin}} \approx 15$ fm/c
Kinetic freeze-out
↓ which is the condition before
Particle transport to the detectors

In this framework, the various time evolution stages of the A–A collisions (Sec. 1.2.1), are converted in kind of "wagons" including the description of the hydrodynamic expansion of the system.

Different assumptions have been considered in several hydrodynamic calculations for each step:

- A hydrodynamic picture is only applicable to a system in equilibrium, hence what happens before the system reaches the equilibrium (τ_{EQ}) has to be taken from other models. Two possible hypotheses are frequently used to define the initial conditions: Glauber models [74] or Colour Glass Condensate (CGC) approach [75].

- Viscosity can be considered or neglected (ideal fluid) in the hydrodynamic equations. Viscosity has been neglected in most applications of hydrodynamics to low $\sqrt{\mathrm{s_{NN}}}$ heavy-ion collisions. The comparison between hydrodynamic calculations results and experimental data suggests that the average value of the shear viscosity to entropy ratio η/s is small (QGP evolves like a perfect fluid) [28, 76].

- Equation of State (EoS) is used to close the system of equations given by hydrodynamics. EoS is the missing piece in the dynamic description of the system. If it is assumed that the expanding system stays in local thermodynamic equilibrium, the complicated deconfinement or hadronization process do not need to be known in microscopic detail; all that is necessary is the thermodynamic equation of state which is constrained by lattice calculations, see Sec. 1.1.1.

- A link to convert hydrodynamic quantities into particle spectra is mandatory to describe the freeze-out at the temperature $\mathrm{T_{kin}}$, when the elastic interactions stop and the particles become independent and fly to the detectors. This decoupling can be implemented in two different ways:

  - by truncating the hydrodynamic phase abruptly with the Cooper-Frye [77] algorithm,
  - by supplementing the hydrodynamic evolution of the system with a hadron cascade model (e.g. UrQMD [78]). These models are often called hybrid models.

The main component of the collective expansion in heavy-ion collisions comes from an isotropic source called *radial flow*. Moreover, in case of a spatially asymmetric collision zone, a contribution from azimuthal momentum space anisotropy must be considered. The latter is usually characterized by the coefficients of the azimuthal Fourier decomposition of the momentum distribution.

Among the coefficients, the one that is more frequently analysed is the second one, v_2, called *elliptic flow*. Observables related to the collective motion are important experimental tools to prove the assumption of equilibrium of the system and thus, to infer properties of the medium created in heavy-ion collisions such as η/s, $\tau_{\rm EQ}$, EoS...

Radial flow:

Thermal and collective properties of the system created in heavy-ion collisions can be studied through the transverse momentum distributions of identified hadrons. This observable encodes information about the collective transverse expansion (*radial flow*) and the kinetic freeze-out. Therefore, by measuring the $p_{\rm T}$ spectra of different hadron species, such as π, K and p, it is possible to estimate the average transverse expansion velocity $\langle\beta_{\rm T}\rangle$ and the temperature at the kinetic freeze-out, $\rm T_{kin}$.

The $p_{\rm T}$-differential particle spectra at low transverse momenta (i.e. $p_{\rm T} \lesssim 2$ GeV/c) can be considered as the superposition of a thermal Boltzmann distribution and a global velocity due to a collective motion. In this way, the spectra are well described by the hydrodynamics-motivated *blast-wave model* [79]. It makes the simple assumption that the particles are in local thermal equilibrium at a fixed kinetic freeze-out temperature $\rm T_{kin}$ and moving with a collective radial flow. The blast-wave function for the transverse mass spectra is:

$$\frac{d\rm N}{m_{\rm T}dm_{\rm T}} \propto \int_0^{\rm R} rdr\, m_{\rm T}\, I_0\left(\frac{p_{\rm T}\sinh\rho}{\rm T_{kin}}\right) K_1\left(\frac{m_{\rm T}\cosh\rho}{\rm T_{kin}}\right), \tag{2.9}$$

where I_0 and K_1 are the modified Bessel functions, $m_{\rm T} = \sqrt{p_{\rm T}^2 + m_0^2}$[‡] and the dependence on the velocity profile (ρ) is described by

$$\rho = \tanh^{-1}(\beta_{\rm T}). \tag{2.10}$$

In absence of a collective expansion (i.e. $\rho = 0$), as expected in pp collisions, Eq. 2.9 is reduced to:

$$\frac{d\rm N}{m_{\rm T}dm_{\rm T}} \sim m_{\rm T}K_1\left(\frac{m_{\rm T}}{\rm T_{kin}}\right) \tag{2.11}$$

which is approximated to an exponential $\sim {\rm e}^{-m_{\rm T}/\rm T}$, since $m_{\rm T}/\rm T > 1$, and should not depend on the particle mass. In a static fireball, all hadron spectra follow the same exponential distribution, $d^2{\rm N}/(m_{\rm T}dm_{\rm T}d{\rm y}) \sim m_{\rm T}^{1/2}{\rm e}^{-m_{\rm T}/T}$, and the fireball temperature can be immediately extracted from their slope. This effect is called $m_{\rm T}$-*scaling*.

Collective expansion breaks the $m_{\rm T}$-scaling at low $p_{\rm T}$ (i.e. $p_{\rm T} << m_i$). In this case, the shape of the spectrum of the particle species i can be described in a simplified

[‡] $p_{\rm T}$ spectra are related to $m_{\rm T}$ spectra as $\frac{d^2{\rm N}}{m_{\rm T}dm_{\rm T}} = \frac{d^2{\rm N}}{p_{\rm T}dp_{\rm T}}$

approach as:

$$\frac{d^2\mathrm{N}}{m_\mathrm{T} dm_\mathrm{T} dy} \sim \mathrm{e}^{-m_\mathrm{T}/\mathrm{T}_{slope,i}} \tag{2.12}$$

where $\mathrm{T}_{slope,i}$ is a parameter defined as:

$$\mathrm{T}_{slope,i} = \mathrm{T}_\mathrm{kin} + \frac{1}{2} m_i \langle \beta_\mathrm{T} \rangle^2 \ , \tag{2.13}$$

T_kin is the temperature of the thermal freeze-out and β_T is the collective transverse surface velocity of the medium.

The breaking of m_T-scaling in A–A collisions leads to different slopes of the p_T-spectra of different hadron species because $T_{slope,i}$ depends on m_i. The evolution of the spectra with the particle mass and the radial flow velocity β_T is shown in Fig. 2.10, where the proton curves have been highlighted for better understanding. In the figure it can be observed that:

- The steepness of the spectrum decreases with increasing hadron mass.
- The spectra at low p_T for each hadron species become less steep (harder) with increasing radial flow.

For sufficiently large hadron mass and flow velocity, the spectrum develops a "blast-wave peak" at non-zero p_T. The inverse slope of these spectra reflects a *blueshifted* freeze-out temperature, given by the hydrodynamic expansion of the system.

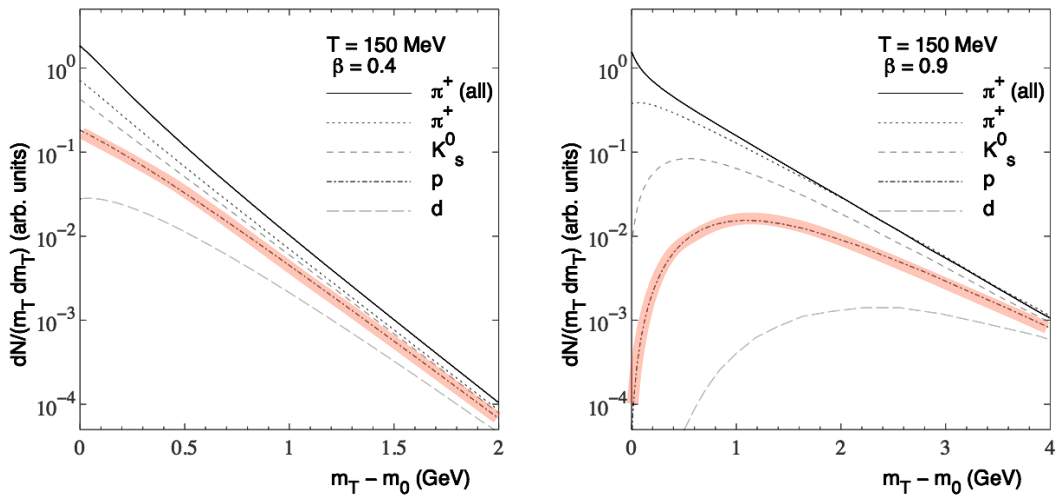

Figure 2.10: m_T spectra for various hadron species as a function of $m_\mathrm{T} - m_0$. The calculation assumes an infinitesimal thin shell of temperature T=150 MeV expanding with transverse velocity $0.4c$ (left) and $0.9c$ (right). The curve labelled "π^+(all)" includes also pions from resonance decays. [25].

The p_{T}-distributions of pions, kaons and protons measured by ALICE in central Pb–Pb collisions at $\sqrt{s_{\mathrm{NN}}} = 2.76$ TeV [62] compared to the results obtained by STAR [49] and PHENIX [80] collaborations in Au–Au collisions at $\sqrt{s_{\mathrm{NN}}} = 200$ GeV are reported in Fig. 2.11. For all hadron species the spectra measured at the LHC are significantly harder (less steep) than the spectra obtained by RHIC experiments. This is understood as an indication of a stronger radial flow at LHC energies. A similar interpretation holds when the particle p_{T}-distributions are studied as a function of the centrality of the collision [63]. In this case, the spectral shape is harder for central collisions with respect to peripheral ones, consistently with a collective motion which depends on the size of the system (the larger the system, the higher the collective flow) and on the density of particles in the fireball, which influences the amount of interactions among the constituents. In the same figure, ALICE results are compared to the predictions of various theoretical calculations based on a hydrodynamic approach [69–71]. Hybrid models which include a specific description of the hadronic phase (e.g. via hadronic cascade as implemented in HKM [70]) after the hydrodynamic phase give a reasonable description of the data.

The surface velocity $\langle\beta_{\mathrm{T}}\rangle$ and the thermal freeze-out temperature $\mathrm{T_{kin}}$ can be estimated from a simultaneous fit to the p_{T} spectra of different hadron species using the blast-wave function 2.9. The blast-wave fits do not replace full hydrodynamical calculations but, in spite of their limitation, they allow a fast comparison between hydrodynamical parameters of different colliding systems. It should be noted that from an individual fit to a single particle species, no physical meaning can be given to the blast-wave parameters, due to the strong correlation between them (i.e. different pairs of $\langle\beta_{\mathrm{T}}\rangle$ and $\mathrm{T_{kin}}$ lead to the same $\mathrm{T}_{slope,i}$, see Eq. 2.13). A simultaneous fit to p_{T} spectra of various particle species is therefore needed to constrain on the parameters and to extract reliable values for the radial flow and the kinetic freeze-out temperature of the fireball. The blast-wave fits to individual hadron species are used for the extrapolation to zero p_{T} in order to evaluate the average transverse momentum $\langle p_{\mathrm{T}}\rangle$ and the particle yield, see Sec. 7.

In Fig. 2.12 the values of $\langle\beta_{\mathrm{T}}\rangle$ and $\mathrm{T_{kin}}$ measured in Au–Au collisions at top RHIC energy and in Pb–Pb collisions at $\sqrt{s_{\mathrm{NN}}} = 2.76$ TeV at the LHC, from a simultaneous fit to the π, K and p spectra using the blast-wave function 2.9 are presented for different centrality intervals [63]. The results indicate that at LHC energies a stronger radial flow is established (i.e $\langle\beta_{\mathrm{T}}\rangle$ measured at the LHC is higher than at RHIC for the same centrality interval): this evidence can be explained with the higher energy density of the fireball created at higher $\sqrt{s}$ which leads to stronger pressure gradients.

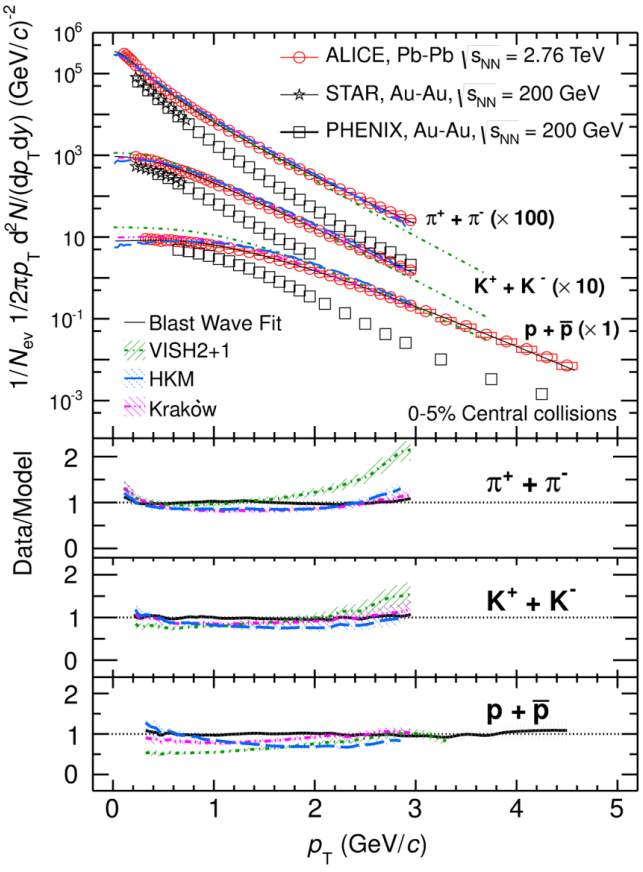

Figure 2.11: Particle p_{T}-spectra measured in central Pb–Pb collisions at $\sqrt{s_{\mathrm{NN}}} = 2.76$ TeV by ALICE [62] compared to results in Au–Au collisions at $\sqrt{s_{\mathrm{NN}}} = 200$ GeV [49, 80]. and to predictions from hydrodynamic calculations [69–71].

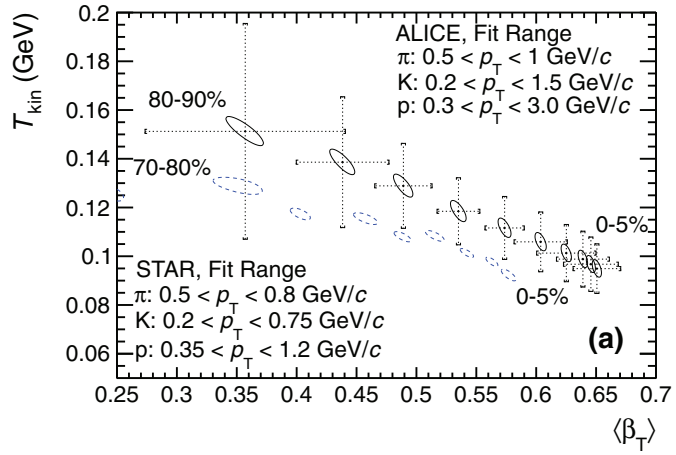

Figure 2.12: $\mathrm{T_{kin}}$ vs $\langle\beta_{\mathrm{T}}\rangle$ extracted via blast-wave fits at RHIC and at the LHC in different centrality intervals. One-sigma contour of the fit to LHC(RHIC) spectra are shown as solid(dashed) ellipses [63].

Anisotropic flow:

In non head-on collisions of spherical heavy nuclei (e.g. ^{208}Pb) or for any collision geometry using deformed nuclei (such as ^{238}U), the interaction zone of the two colliding nuclei is spatially anisotropic with an almond-like shape as shown in the left panel of Fig. 2.13. Due the pressure gradient, which is different along the two axes in the transverse plane, and in presence of a large number of re-scatterings of the produced particles in the medium[§], the spatial anisotropy is transformed into a momentum anisotropy of the final-state particles, see Fig. 2.13 right [28].

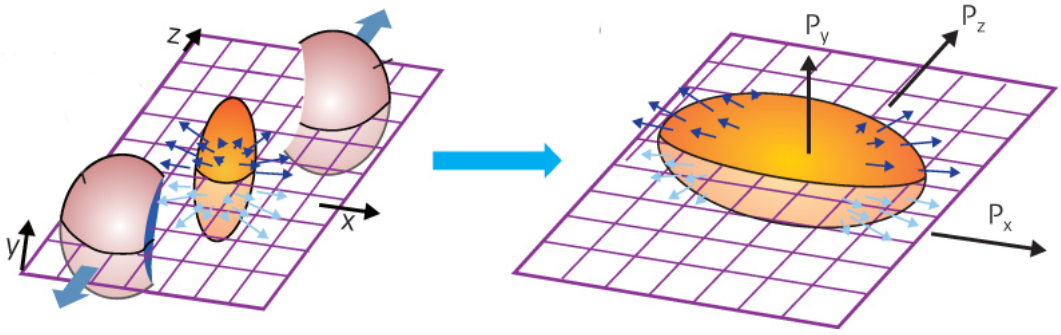

Figure 2.13: Left: Schematic of the collision zone between two incoming nuclei. The plane x-z is the reaction plane. Right: Anisotropy of final-state particle momenta, commonly quantified by the Fourier coefficients v_n.

The final-state particle azimuthal anisotropy can be quantified by studying the Fourier expansion of the azimuthal angle distribution of the produced particles with respect to the reaction plane. The reaction plane is defined by the impact parameter and the beam direction. The invariant triple differential distribution can be expressed as follow:

$$\mathrm{E}\frac{d^3\mathrm{N}}{d^3\mathbf{p}} = \frac{1}{2\pi}\frac{d^2\mathrm{N}}{p_\mathrm{T}dp_\mathrm{T}dy}(1 + 2\sum_{\mathrm{n}=1}^{\infty} v_\mathrm{n}\cos[\mathrm{n}(\phi - \psi_\mathrm{RP})]) \tag{2.14}$$

the sine terms vanish because of the system symmetry with respect to the reaction plane. In this Fourier expansion, E is the energy of the particle, ϕ the azimuthal angle, ψ_RP the reaction plane angle in the transverse plane and the coefficients:

$$\mathrm{v_n}(\mathrm{p_t}, \mathrm{y}) = \langle\cos[\mathrm{n}(\phi - \psi_\mathrm{RP})]\rangle \tag{2.15}$$

are the flow coefficients. In particular v_1, v_2 and v_3 are known as directed, elliptic and triangular flow respectively.

[§]Observation of azimuthal anisotropy is sign of multiple interactions, which eventually can lead the system to thermalization.

A non-zero v_2 is interpreted as an effect of an anisotropy in the flow velocity of the medium which undergoes a collective expansion as confirmed by the evidence of a strong radial flow. Assuming a smooth matter distribution in the colliding nuclei, the symmetry plane is the reaction plane, $\psi_n = \psi_{RP}$ and the odd Fourier coefficients are zero by symmetry. However, as consequence of fluctuations in the initial matter distribution the symmetry planes fluctuate event-by-event around the reaction plane. These fluctuations of the initial geometry are reflected in the final-state particle azimuthal anisotropy and lead to non-zero values also for odd harmonics (e.g. v_3 and v_5).

Experimental results of the flow coefficients, in particular v_2 and v_3 values, can be compared with the outcome of hydrodynamic calculations tuned to reproduce the radial flow. This provides a further test for the hydrodynamic description of the medium evolution. In Fig. 2.14 the p_T-differential v_2 for different particle species measured by two experiments at RHIC is compared with hydrodynamical predictions for a fluid with almost zero viscosity and critical temperature for the phase transition $T_c = 165$ MeV [81]. The model reproduces well RHIC measurements in the low-intermediate transverse momentum region ($p_T < 2$ GeV/c). At higher p_T a hydrodynamic approach cannot be applied since high p_T are more difficult to thermalize.

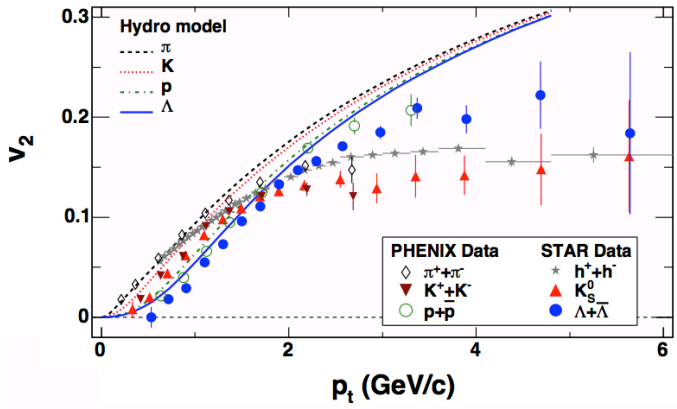

Figure 2.14: p_T-differential v_2 of identified π, K, p and Λ measured by STAR [82] and PHENIX [83] in semi-peripheral Au–Au collisions at $\sqrt{s_{NN}} = 200$ GeV compared to hydrodynamical calculations [81].

Figure 2.15 shows the p_T-differential elliptic flow coefficient, v_2, for several identified particle species measured by ALICE in Pb–Pb collisions at $\sqrt{s_{NN}} = 2.76$ TeV. From the upper panel we can observe a centrality dependence of v_2 (up to the 40–50% centrality interval) that reflects the increase of the initial spatial eccentricity ($\epsilon_x(b) = \frac{\langle y^2 - x^2 \rangle}{\langle y^2 + x^2 \rangle}$) of the overlap region of the colliding nuclei with increasing impact parameter. For more peripheral events (i.e. 50–60%), the magnitude of v_2 does not change significantly within the systematic uncertainties compared to the previous centrality interval. This might be originated, according to [84], by a convolution of different effects such as: the smaller lifetime of the fireball in peripheral compared to more central collisions, the contribution

of eccentricity fluctuations and of final state hadronic effects. At LHC energies, the p_{T}-integrated elliptic flow increases by $\approx 30\%$ for semi-peripheral collisions with respect to RHIC top energy. Since the p_{T}-differential v_2 is similar at the two energies, this $\approx 30\%$ increase is due to the higher $\langle p_{\mathrm{T}} \rangle$ of hadrons at the LHC, which is a consequence of the stronger radial flow and of the higher centre-of-mass energy.

From Fig. 2.15 lower panel, a clear mass ordering of v_2, already observed at RHIC [85] and attributed to the interplay between elliptic and radial flow [69], is seen for all centralities in the low p_{T} region (i.e. $p_{\mathrm{T}} \leq 2$ GeV/c), where at a given p_{T}, the higher is the hadron mass the lower is the value of v_2. For $p_{\mathrm{T}} > 2$ GeV/c, particles tend to group according to the number of constituent quarks (NCQ), i.e. mesons and baryons. This was suggested in a picture in which most of the hydrodynamical flow develops in the partonic stages of the system evolution and hadronization occurs mainly via quark coalescences mechanism [86, 87] in the intermediate p_{T} region [88]. However, while at RHIC energies, it was observed that the elliptic flow normalized to the number of constituents quarks (v_2/n_q) as a function of the particle kinetic energy normalized to the number of constituents quarks ($\mathrm{E_T}/n_q$) follows a common trend for all measured hadron species (NCQ-scaling)[¶] [85], ALICE data exhibit deviations from the NCQ-scaling at the level of $\pm$ 20% [89].

Crucial information about the anisotropic collective flow of the medium can be inferred also from two-particle correlation measurements. Indeed, this observable provides a method to measure the flow coefficients. Two-particle angular correlation measurements examine the distribution of final-state particle pairs by counting the number of pairs with the azimuthal separation $\Delta\phi = \phi_1 - \phi_2$ and the pseudo-rapidity separation $\Delta\eta = \eta_1 - \eta_2$. Depending in the p_{T} interval in which the particles are measured, correlation observables highlight different aspects of heavy-ion collisions including medium response to a high p_{T} trigger [90], bulk medium evolution [91], and the p_{T} dependent evolution of the system [92]. The first is called "hard ridge"[‖] since it analyses particle pairs selected by a high p_{T} trigger particle and lower p_{T} associated particles also in a "hard" region of the particle spectrum; triggered hard ridge measures the correlated yield of associated particles per jet trigger $(1/\mathrm{N}_{trig})d\mathrm{N}/d\phi d\eta$. The intention is to isolate jet quenching effects by specifically examining correlations of trigger particles in a high p_{T} range with associated particles in a lower p_{T} range. Measurements at lower p_{T}, as well as untriggered measurements, fall in the category of the "soft ridge" since all possible particle pairs contribute.

[¶]NCQ-scaling was interpreted as an evidence that coalescence is the dominant hadronization mechanism, at intermediate p_{T} [87].

[‖]The uses of "ridge" term to describe the long angular correlation will be introduced below.

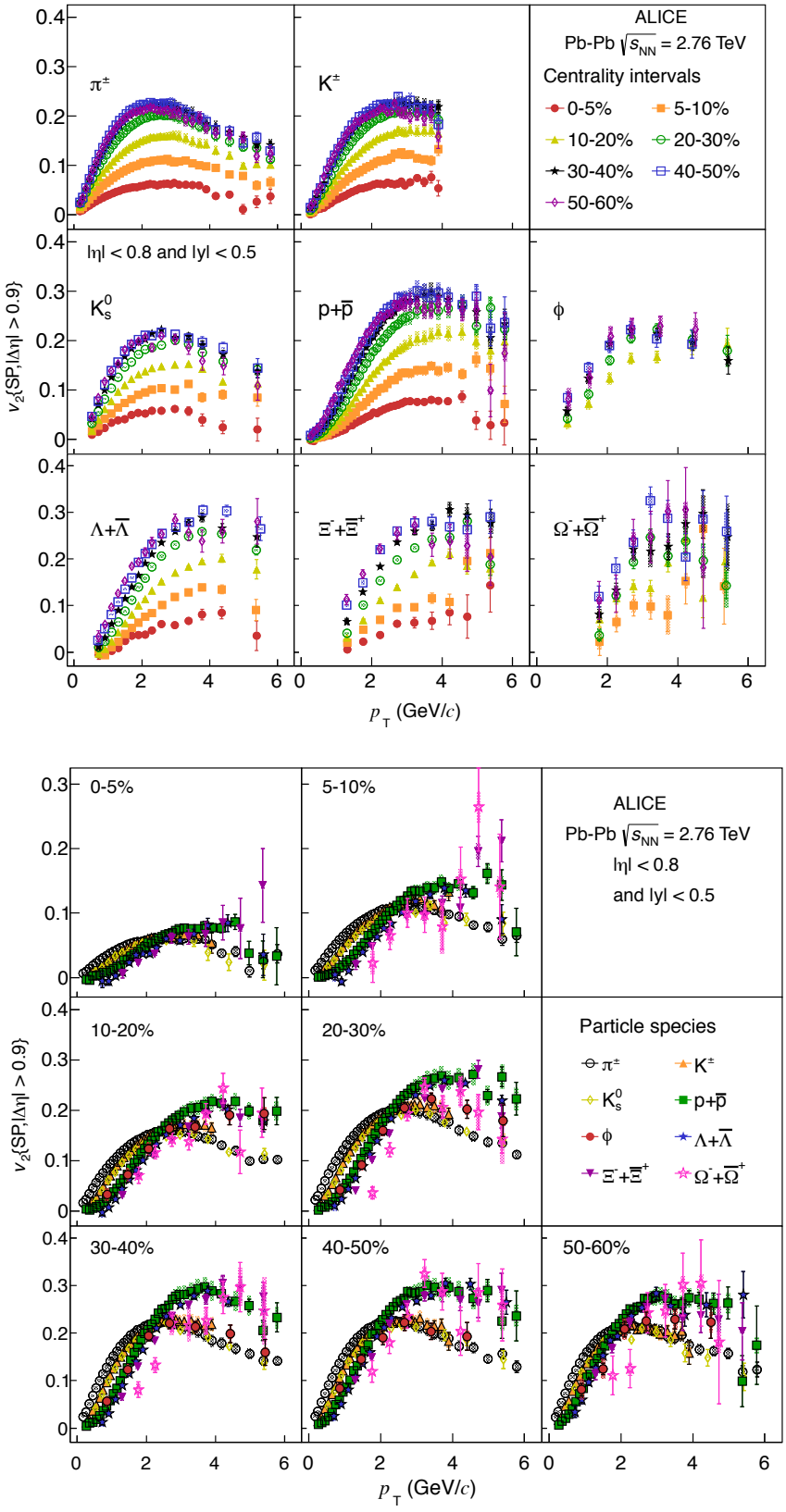

Figure 2.15: p_{T}-differential v_2 measured by ALICE in Pb–Pb collisions at $\sqrt{s_{\mathrm{NN}}} = 2.76$ TeV grouped by particle species (upper panel), centrality interval (lower panel) [89].

Two-particle angular correlations are characterized by a "near-side" peak centered at $\phi = \eta = 0$, due to the "near-side" jet (see Fig. 2.16), i.e. the "spray" of collimated particles coming from fragmentation of the high-energy parton in which the trigger hadron is produced. In addition, for pp and p–A collisions, an elongated structure (also like a ridge) at $\Delta\phi = \pi$ (away-side) spreading over a broad range in $\Delta\eta$ is observed (Fig. 2.16 (a)). This structure can be interpreted as due to back-to-back jet production or more generally momentum conservation. A modification of the jet-peak shape in the near side have been observed from correlation measurements in A–A collision with respect to the one seen in low multiplicity systems (i.e. pp and p–A collisions at RHIC energy). In A–A collisions, the away-side structure is modified by jet-quenching (Sec. 2.1.1) and hydrodynamic collective flow effects (and maybe also by jet-medium modifications [93, 94]).

In Fig. 2.16 the two-particle correlation results for d–Au and central Au–Au collisions at top RHIC energy are shown [95]. The near-side peak is similarly narrow in ϕ and η for low multiplicity systems like d–Au collisions at RHIC, Fig. 2.16 (a). However, a pedestal-like enhancement of the yield at small $\Delta\phi$ under the jet peak is observed in central Au–Au collisions, Fig. 2.16 (b). This structure, called "ridge" because of its resemblance to a mountain ridge, is broad and seemingly flat in η but shares the same narrow ϕ profile as the jet peak. This feature observed at RHIC was also later confirmed at the LHC in Pb–Pb collisions at $\sqrt{s_{NN}} = 2.76$ TeV. The observation of the ridge-like structure in A–A collisions is currently described as the results of the hydrodynamical evolution of the medium.

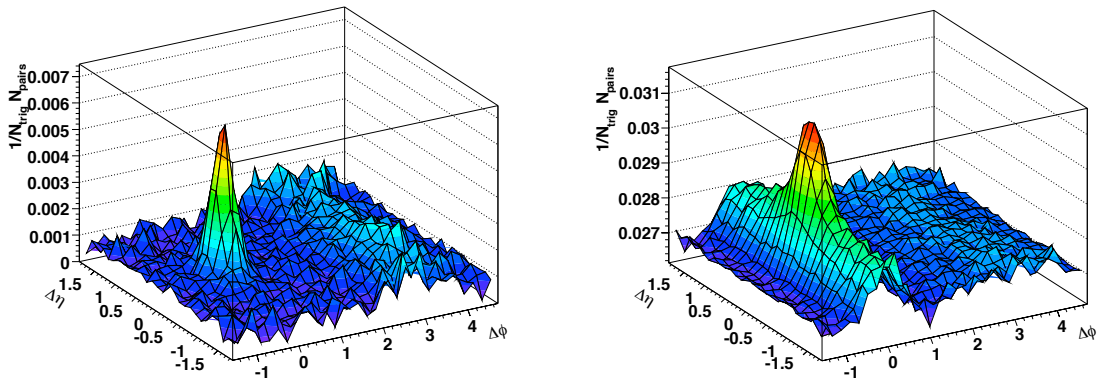

(a) (b)

Figure 2.16: Two-particle angular correlations ($\Delta\phi$,$\Delta\eta$) in d–Au (a) and 10% most central Au–Au (b) collisions at $\sqrt{s_{NN}} = 200$ GeV for $3 < p_T^{trig} < 6$ GeV/c and $2 < p_T^{assoc} < p_T^{trig}$ GeV/c [95].

The two-particle triggered azimuthal correlation (projection of the $\Delta\phi$, $\Delta\eta$ correlations along $\Delta\phi$) was measured by ALICE in the 1% most central Pb–Pb collisions at $\sqrt{s_{NN}} = 2.76$ TeV, for trigger particles in the range $2 < p_T < 3$ GeV/c and associated particles in $1 < p_T < 2$ GeV/c for pairs with $|\Delta\eta| > 1$. The results, reported in Fig. 2.17, show a clear doubly peaked correlation structure in the away-side centered opposite to the trigger particle. This feature has been observed at lower energies in broader centrality bins [93, 94], but only after subtraction of the contribution of the v_2 component. It has been interpreted as an evidence of jet-medium modification (i.e. Mach cones) [93, 94] or in analogy to the elliptic flow in the context of hydrodynamics due to the initial geometry fluctuations, particularly the "triangularity", leading to positive v_3 Fourier coefficient in the final-state particle azimuthal anisotropy [96, 97].

Since the flow coefficients v_2, v_3, v_4, v_5 had been measured by ALICE, the azimuthal triggered correlation data were compared to the azimuthal correlation shape expected from the measured v_n components (solid line in Fig. 2.17). The good agreement between both azimuthal correlations, shown in Fig. 2.17, indicates that these harmonics can provide a natural description of the observed correlation structure on the away side.

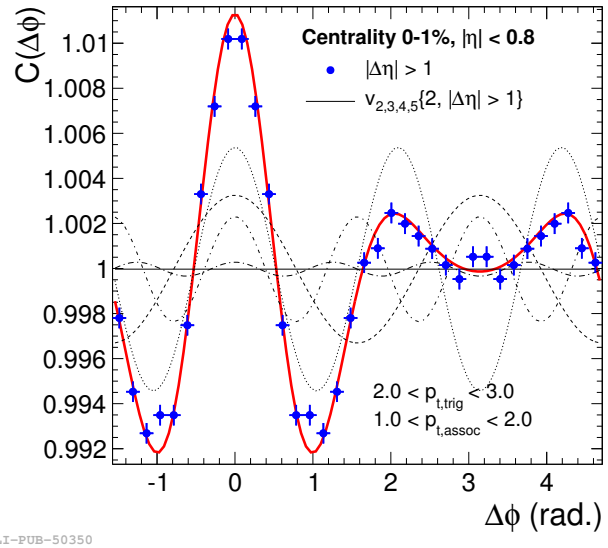

Figure 2.17: Two-particle azimuthal correlation, measured in $0 < \phi < \pi$ and shown symmetrized over 2π, between a trigger particle with $2 < p_T < 3$ GeV/c and associated particles with $1 < p_T < 2$ GeV/c for Pb–Pb collisions at $\sqrt{s_{NN}} = 2.76$ TeV in the 0–1% centrality class. The solid line shows the sum of the measured v_n (dashed line) [96].

Anisotropic flow coefficients are important measurements to constrain the fundamental properties of the matter created in A–A collisions, in particular the sound velocity and shear viscosity.

Hanbury Brown-Twiss (HBT):

Two-particle correlations depend on the average separation of particles at decoupling and therefore provide valuable spatial and temporal information on the medium evolution. Two-particle momentum correlation between pairs of identical particles are caused by quantum statistical effects. In the case of two identical bosons, for instance pions, this technique is known as Hanbury Brown-Twiss (HBT) interferometry. It is based on the idea that the observable $\mathbf{q} = \mathbf{p_1} - \mathbf{p_2}$ of identical bosons yields information on the average separation between emitters (HBT radius). The HBT radius $\mathbf{R}$ can be decomposed into (R_{out}, R_{side}, R_{long}), with the *out* axis pointing along the pair transverse momentum, the *side* axis perpendicular to it in the transverse plane, and the *long* axis along the beam [98]. The beam energy dependence of the HBT radii is reported in Fig. 2.18. The HBT radii are measured to increase with the collision energy: this means that the fireball formed in nuclear collisions at higher energies is hotter, lives longer, and expands to a larger size at freeze-out as compared to lower energies. Available model predictions are compared to the experimental data: an hydrodynamical approach is used in AZHYDRO [72], KRAKOW [71], and HKM [70]. The increase of the radii from RHIC to LHC energies is roughly reproduced by all four calculations, only two of them (KRAKOW and HKM) are able to describe the experimental R_{out}/R_{side} ratio.

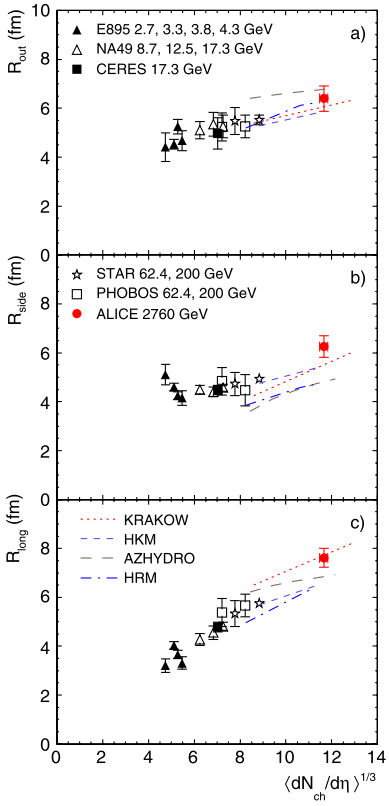

Figure 2.18: Pion HBT radii at $k_t = (|\mathbf{p}_{t,1} + \mathbf{p}_{t,2}|)/2 = 0.3$ GeV/c for the 5% most central Pb–Pb collisions at $\sqrt{s_{NN}} = 2.76$ TeV (red filled dot) and the radii obtained for central Au–Au and Pb–Pb collisions at lower energies at the AGS, SPS, and RHIC. Model predictions are shown as lines [98].

2.2 Cold Nuclear Matter effects

As discussed in Sec. 2.1, a strong jet quenching and a suppression of the yield of high-p_{T} hadrons in central Pb–Pb collisions relative to pp collisions at $\sqrt{s_{\mathrm{NN}}} = 2.76$ TeV have been observed at LHC. It is very important to check whether this behaviour of the nuclear modification factor is due to initial state effects, related to the fact that we are using nuclei as colliding particles, or to final state effects linked to the creation of a deconfined hot and dense system. Therefore, in order to disentangle the final state effects, one has to carefully estimate the initial state effects in an environment where the transition to a QGP phase is unlikely, e.g. in p–A collisions.

Cold Nuclear Matter (CNM) effects define the different phenomena which modify the production of particles in p–A collisions with respect to pp ones in the initial and in the final state. Since these phenomena are due to the presence of a nuclear environment they are presumed to be present both in A–A and in p–A collisions.

One of the initial state CNM effects is the so called k_{T}-*broadening* [99]. It is a consequence of the fact that before the inelastic interaction, partons of the projectile nucleon could have suffered *multiple elastic scatterings* in the target nucleus. These interactions lead to a small extra p_{T} component of the parton, which reflects in the p_{T}-distribution of the particles produced in the hard scattering of this parton, in the case of A–A or p–A collisions.

This k_{T}-broadening explains the observed *Cronin enhancement*, which was seen for first time in p–A collisions at Fermilab [100, 101]. This experimental observation is an increased yield in p–A collisions at intermediate p_{T} compared to binary scaled yield in pp collisions. Since this extra-k_T becomes less relevant with increasing hadron p_{T}, the Cronin enhancement should disappear as $p_{\mathrm{T}} \to \infty$. For the same reason it should become weaker as $\sqrt{s_{\mathrm{NN}}}$ increases. In the left panel of Fig. 2.19 the Cronin enhancement (R_{AA} larger than unity at intermediate p_{T}) is shown in d–Au collisions at top RHIC energy.

Another known initial state effect is the nuclear modification of the *parton distribution functions* (PDF) in a nucleus with respect to those of the proton. This modification depends on Bjorken x (see Appendix B for Bjorken scaling definition) and Q^2. In particular at low x (partons with $x < 10^{-2}$) a reduction of the PDFs is observed, usually called shadowing, as it is shown in the right panel of Fig. 2.19 [102]. In particular, the shadowing affects significantly the measured value of R_{AA} at low p_{T}. The shadowing region can be described phenomenologically by gluon saturation at small x.

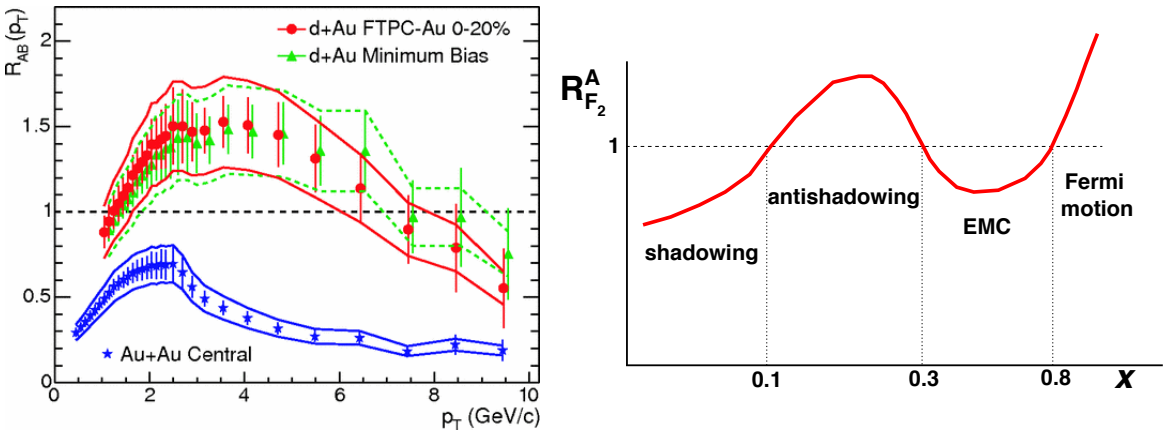

Figure 2.19: Left: R_{AA} of charged hadrons, measured in d–Au and central Au–Au collisions at $\sqrt{s_{NN}} = 200$ GeV, by STAR [104]. At intermediate p_T, a Cronin enhancement is observed in d–Au collisions. Right: $R^A_{F_2}$ as a function of Bjorken scaling variable x for a given fixed Q^2. $R^A_{F_2}$ is the variable commonly used to study nuclear modification effects. $R^A_{F_2}$ is defined as the nuclear structure function $F_2^A(x, Q^2)$ of nucleus A divided by the nucleon structure function for a free nucleon and normalized to the mass number of the nucleus A [102].

This approach predicts that the nuclei accelerated to near the speed of light, at RHIC and at the LHC, would reach an upper limit of gluon concentration that can be described in the framework of the Colour Glass Condensate (CGC) models [75, 103]. In this framework the initial conditions in p–A collisions are created by a hit of the projectile proton with a bunch of nucleons (a dense field of gluon) simultaneously instead of individual nucleon–nucleon interactions, making it harder for particles with a given momentum to be produced.

The measurement of identified particle spectra in p–Pb and pp collisions provides the reference for Pb–Pb collisions and is also helpful to understand the initial CNM effects. Furthermore, the Bjorken scaling variable x at the LHC can reach values about two orders of magnitude smaller than at RHIC. Thus, p–Pb collisions at the LHC allow for investigation of fundamental properties of QCD at very low fractional parton momentum x and very high density regime, where parton shadowing and novel phenomena like saturation, e.g. as implemented in CGC model, may appear [103].

2.2.1 p–Pb collisions at LHC: more than a simple reference

As already mentioned, the comparison of observables in p–A and A–A reactions has frequently been used to separate initial state effects from final state effects, since the former are present in both p–Pb and Pb–Pb collisions, while the latter are expected only in Pb–Pb.

The pseudo-rapidity density of particles created in p–Pb collisions at the LHC reaches values comparable to semi–peripheral Au–Au and Cu–Cu collisions at top RHIC energy [105]. Therefore the assumption that final state effects can be neglected in p–A collisions may no longer be valid, in particular as far as the establishment of a collective behaviour is concerned. This last statement was not really taken into account by the heavy-ion physics community until when the measurements at the LHC in p–Pb collisions at $\sqrt{s_{NN}}$ = 5.02 TeV revealed a surprising** near-side long-range "ridge" structure in two-particle angular correlations [106–108]. This phenomenon was previously seen first in Au–Au collisions at $\sqrt{s_{NN}}$ = 200 GeV and Pb–Pb collisions at $\sqrt{s_{NN}}$ = 2.76 TeV at RHIC and at the LHC respectively, but it was also detected by CMS in high multiplicity pp collisions at 7 TeV [109]. As was commented in Sec. 2.1.2, in A–A collisions the long-range correlations are understood as a consequence of the hydrodynamic expansion of the system and are used to determine its fluid properties [110].

Figure 2.20 summarizes CMS two-particle angular ($\Delta\eta$,$\Delta\phi$) correlation measurements in high multiplicity pp, p–Pb and Pb–Pb collisions at the LHC. The arrow shows the long-range (= expanding over a wide $\Delta\eta$ range) correlations at $\Delta\phi \approx 0$ (i.e. the ridge-like structure). A second ridge is observed at $\Delta\phi = \pi$. As this effect was seen in both pp and Pb–Pb collisions, a possible long-range structure in two-particle angular correlations was somehow expected also in p–Pb collisions. However, the amplitude of the ridge was completely unpredictable. In p–Pb collisions the ridge-like structure is much stronger than in pp collisions. In fact it is comparable to that observed in Pb–Pb collisions [106].

The same phenomenon was observed by the ALICE collaboration [107]. The angular correlation of pairs of charge particles reported by ALICE in p–Pb collisions at $\sqrt{s_{NN}}$ = 5.02 TeV for the lowest (60–100%, left top) and the highest (0–20%, left bottom) multiplicity classes are shown in the left side of Fig. 2.21. The per-trigger yields in $\Delta\phi$ on the near side and on the away side are similar for low-multiplicity p–Pb collisions and pp collisions at $\sqrt{s}$ = 7 TeV. Thus, in order to remove jet-like correlations and to quantify the change of the long-range angular correlations with the multiplicity, the data of the lowest (60–100%) class were subtracted from those of the highest (0–20%) one. The resulting distribution shows a new distinct excess structure in the correlation, which form two ridges, one in the near side ($|\Delta\phi| < \pi/2$) and one on the away side ($\pi/2 < \Delta\phi| < 3\pi/2$), Fig. 2.21 right.

**The most commonly used p–Pb event generators did not show long-range correlation phenomenon before it was discovered by CMS at the LHC in pilot run of p–Pb collisions at $\sqrt{s_{NN}}$ = 5.02 TeV.

This double-ridge structure in two particle correlations has been described satisfactory by two different categories of model. The first theory is based on final state effects, like hydrodynamic flow [111, 112]. The second type of models uses a CGC description [113] based on initial state non-linear gluon interaction. Therefore, further experimental information, as those obtained by p_{T}-distribution of identified particles at low and intermediate momentum and elliptic flow mass dependence studies from correlation measurements of different identified hadron species, may reveal the origin of the correlation observed in p–Pb collisions.

In fact, two-particle angular correlations between charged particles and identified hadrons have been measured in p–Pb collisions at $\sqrt{s_{\mathrm{NN}}} = 5.02$ TeV at the LHC [114]. The elliptic flow, extracted from these correlations and studied as a function of the p_{T}, show a clear mass ordering between the v_2 of pions and protons for high multiplicity event classes. In A–A collisions this observation is consistent with expectation from hydrodynamic model calculations. In other hand, identified hadrons spectra results measured with the ALICE detector in p–Pb collisions at $\sqrt{s_{\mathrm{NN}}} = 5.02$ TeV is the main subject of this thesis and will be discussed in Sec. 7.

Image from: `http://cms.web.cern.ch/news/unexplained-long-range-correlations-observed-ppb-collisions`.

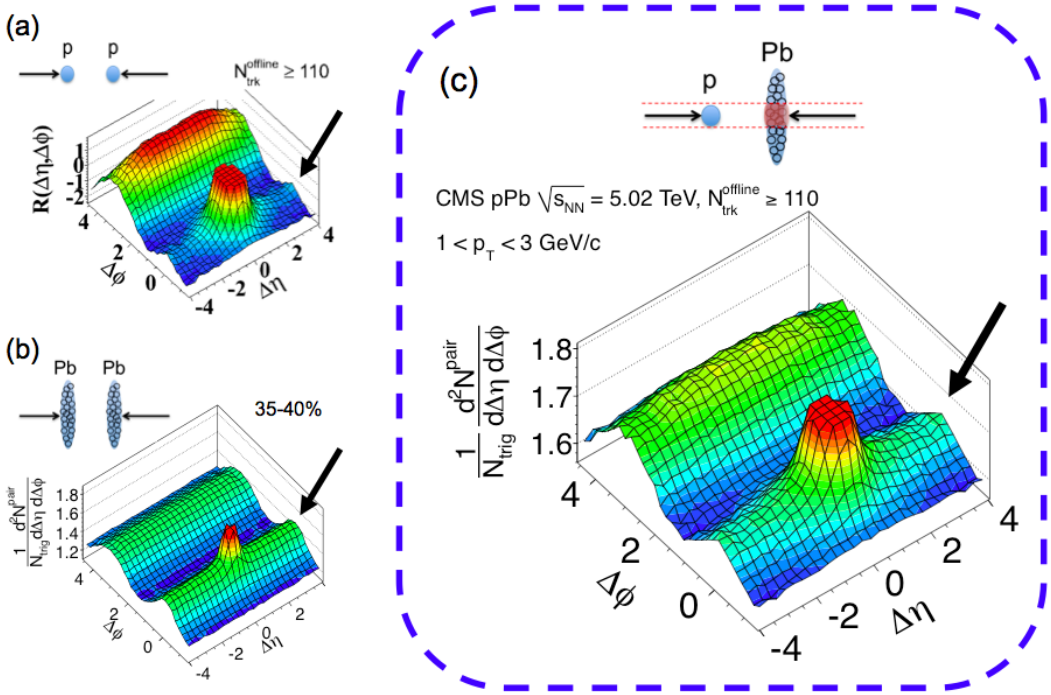

Figure 2.20: Two-particle correlation functions for 7 TeV pp (a), 2.76 TeV Pb–Pb (b), and 5.02 TeV p–Pb (c) collisions.

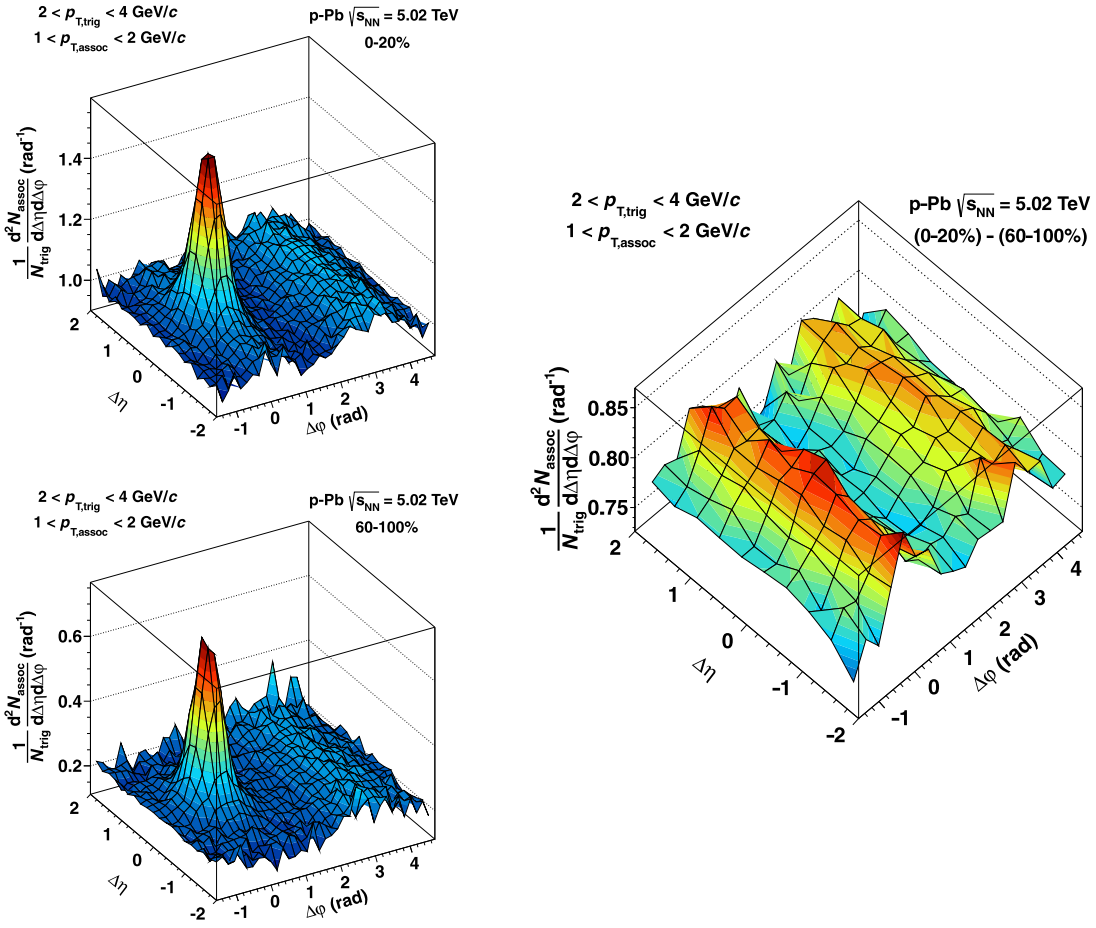

Figure 2.21: Left: Associated yield per trigger particle in $\Delta\phi$ and $\Delta\eta$ for pairs of charged particles with $2 < p_{t,trig} < 4$ GeV/c and $1 < p_{t,assoc} < 2$ GeV/c in p–Pb collisions at $\sqrt{s_{\rm NN}}$ = 5.02 TeV for the 0–20% (top) and 60–100% (bottom) event classes. Right: Same results for the 0–20% (top left) multiplicity class, after subtraction of the associated yield obtained in the 60–100% (bottom left) event class [107].

3 ALICE in the LHC world

In this Chapter, a brief introduction to the Large Hadron Collider (LHC) accelerator complex will be provided. Then, a detailed description of the ALICE detector layout will be given, with a specific focus in some subdetectors, which are employed in the measurement of p_{T} distributions of identified particles at mid-rapidity. In the following section the performance of trigger and background rejection in data acquisition processes are reported. The last part will be dedicated to the offline data processing framework used in ALICE, which include data simulation and reconstruction.

3.1 A Large Hadron Collider

The Large Hadron Collider (LHC) is a two ring superconducting accelerator complex installed underground at CERN, in the 26.7 km long tunnel of the former e^-e^+ collider (LEP) [115]. The LHC has been designed to collide hadrons at the centre-of-mass energy $\sqrt{s}$ per nucleon of 14 TeV and 5.5 TeV for pp and Pb–Pb collisions respectively. In order to reach these energies protons and nuclei are pre-accelerated before entering the LHC by lower-energy accelerator lines built in the last decades at CERN. A schematic view of the LHC system is shown in Fig. 3.1. Protons are extracted from a hydrogen tank and injected in a linear accelerator (Linac2) in which they reach an energy of 50 MeV. Then, they are accelerated up to 1.4 GeV in the Proton Synchrotron (PS)-Booster and injected in the PS which leads to the Super Proton Synchrotron (SPS). After the SPS, protons at 450 GeV are injected in the LHC accelerator ring. Ion acceleration is different in the initial steps. In particular, lead ions are extracted from a piece of isotopically enriched lead (^{208}Pb) heated up to 500 Celsius degrees using an electric field. Then, they are accelerated in a linear machine (Linac3) in which the ionization procedure is completed. Ions are then accumulated in a dedicated ion ring (LEIR) and later injected in the PS–SPS–LHC chain.

Four experiments take data simultaneously at different interaction points (IP) of the LHC collider. Two of them, CMS and ATLAS, are general purpose experiments mainly devoted to pp collisions and designed to study the SM predictions and to seek

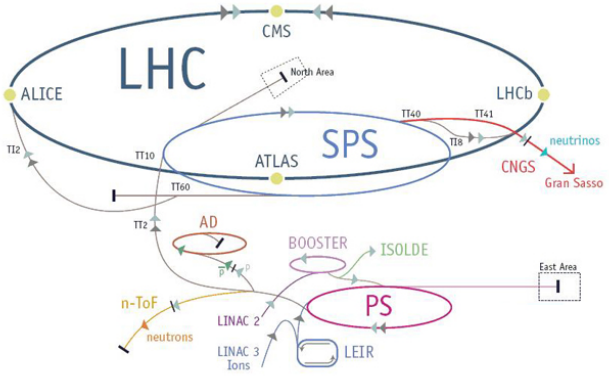

Figure 3.1: The full complex accelerator chain at CERN.

for possible physics beyond the SM. Actually, one of their main goals has been achieved when the Higgs boson signal was detected in pp collisions at $\sqrt{s} = 7$ and 8 TeV [11,12]. The third experiment, LHCb, is mainly focused on the study of CP asymmetries in processes that involve b-quarks production, while ALICE is the fourth experiment and it is optimized for the study of the physics of the QGP.

One important characteristic of the accelerator is the luminosity L which is related to the collision rate R, and it is defined in terms of the latter as

$$L = \frac{R}{\sigma_{int}} \tag{3.1}$$

where σ_{int} is the interaction cross section. One of the main requirements of the LHC, since the machine was designed to study rare processes, is the possibility to reach very high rate of interactions. Indeed, in November of 2012 the LHC reached a peak instantaneous luminosity of 7.7×10^{34} cm^{-2}s^{-1}, higher than the design luminosity of 10^{34} cm^{-2}s^{-1}. However, the ALICE design, optimized for nuclear collisions, requires a reduced luminosity in pp interactions, because the maximum pp interaction rate at which all ALICE detectors can be safely operated is around 700 kHz (including the contribution of both beam–beam and beam–gas collisions). The rate of Pb–Pb collisions in 2010 and 2011 was well below the ALICE limits, therefore this experiment was able to take data at the highest achievable luminosity, on the order of 10^{25} cm^{-2}s^{-1} in 2010 and 10^{26} cm^{-2}s^{-1} in 2011.

LHC provided pp collision at $\sqrt{s} = 900$ GeV in November 2009. In the period 2010–2013 LHC delivered pp collisions at $\sqrt{s} = 2.36$, 2.76, 7 and 8 TeV, Pb–Pb collisions at $\sqrt{s_{NN}} = 2.76$ TeV and p–Pb collisions at $\sqrt{s_{NN}} = 5.02$ TeV. These data-taking periods are summarized in Tab. 3.1 and they comprise the so-called LHC Run-1.

System	$\sqrt{s_{NN}}$ (TeV)	Year	Delivered L_{int}
pp	0.9	2009	19.6 μb^{-1}
		2010	0.31 nb^{-1}
	2.36	2009	0.87 μb^{-1}
	2.76	2011	46 nb^{-1}
		2013	129 nb^{-1}
	7	2010	0.5 pb^{-1}
		2011	4.9 pb^{-1}
	8	2012	9.7 pb^{-1}
Pb–Pb	2.76	2010	9 μb^{-1}
		2011	146 μb^{-1}
p–Pb	5.02	2012(Pilot)	1.5 μb^{-1}
		2013	14.8 nb^{-1}
Pb–p	5.02	2013	17.1 nb^{-1}

Table 3.1: Data taking periods during the LHC Run-1.

3.2 A Large Ion Collider Experiment – ALICE

ALICE is a general purpose heavy-ion experiment. It aims at studying the strongly interacting matter created in Pb–Pb collisions at the LHC. The goal is to get insight into the properties of QCD matter at high temperatures, where the system is expected to be in a quark gluon plasma state. Therefore, the ALICE detector has been optimized to study for the QGP properties and its collective dynamic evolution toward hadronization, as presented in Sec. 2. Its tracking and Particle IDentification (PID) systems are designed to cope with a huge particle multiplicity environment. The experiment has a high detector granularity, low material budget and good particle identification capabilities up to momenta of 20 GeV/c. The moderate magnetic field (B = 0.5 T) and the low material budget allow for track reconstruction down to low momenta, 80 MeV/c for pions.

3.2.1 ALICE apparatus

ALICE [116] consists of a *central barrel* system, covering the pseudo-rapidity region $|\eta| < 0.9$, a forward muon spectrometer and several forward detectors for trigger and multiplicity estimation. A schematic view of the ALICE apparatus is depicted in Fig. 3.2.

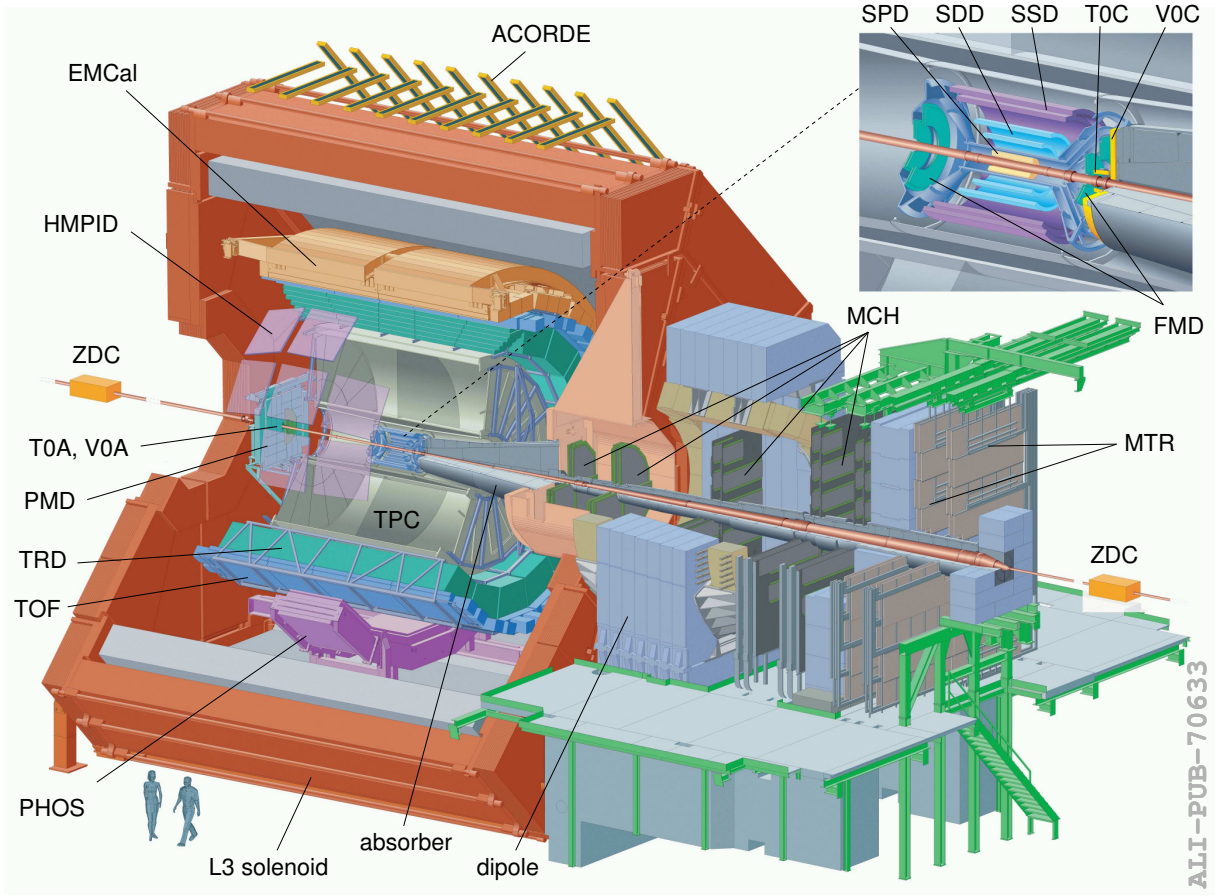

Figure 3.2: Schematic view of ALICE detector.

Detectors in the central barrel are embedded in the large solenoidal magnet of the former L3 experiment, which generates a magnetic field of B = 0.5 T parallel to the beam axis*. It is composed of the following detectors, all having cylindrical geometry and covering the full azimuth region: the Inner Tracking System (ITS) which is the innermost detector closer to the beam line and it consists of six layers of silicon detectors, the Time Projection Chamber (TPC) which is the main tracking detector, the Transition Radiation (TRD) for electron identification and the Time-Of-Flight (TOF) for charge particles identification. In addition other detectors with smaller acceptance are located at mid-rapidity: the High-Momentum Particle Identification Detector (HMPID), an array of Cherenkov detectors designed to identify high-momentum particles and two electromagnetic calorimeters, the PHOton Spectrometer (PHOS) and the ElectroMagnetic calorimeter (EMcal). PHOS is dedicated to the measurements of photons and neutral mesons while EMCAL is meant to enhance ALICE capabilities in jet studies.

*The global ALICE reference frame is: z-axis parallel to the beam axis, pointing opposite to the Muon Arm and, x and y-axis in the plane transverse to the beam direction.

At forward and backward rapidities, one can find the Forward Muon Spectrometer which detects muons in $-4 < \eta < -2.5$, a Photon-Multiplicity Detector (PMD) and the forward Multiplicity Detector (FMD) that is a silicon strip detector built to measure particle multiplicity. Two arrays of scintillator counters, the VZERO detectors, and two sets of neutron and proton calorimeters, the Zero Degree Calorimeters (ZDC) are located in each side of the IP in order to measure the event centrality in Pb–Pb and p–Pb collisions. VZERO detectors are also essential to provide the minimum bias trigger and to allow rejection of the beam–gas interaction. Other two Cherenkov counters, the T0 detectors are installed to measure the interaction time of the collision, used as starting time for the TOF detector and for background rejection. In the following paragraphs, a more accurate description of some subdetectors will be provided. A detailed description of the ALICE apparatus and its performance can be found in [116–118].

Inner tracking system

The ALICE Inner Tracking System (ITS) is composed of six cylindrical layers of silicon detectors located in the central barrel at radii $r \sim 4$, 7, 15, 24, 39 and 44 cm (Tab. 3.2). The innermost radius is the minimum allowed by the beam pipe radius of 3 cm. On the other hand, the outermost radius is constrained by the requirement of track matching from ITS to TPC and vice-versa. The two innermost layers are equipped with Silicon Pixel Detector (SPD). They are followed by two layers of Silicon Drift Detectors (SDD). The two outermost layers consist of double-sided strip detectors (SSD). This layout is depicted in Fig. 3.3. The four layers equipped with SDD and SSD also provide a measurement of the specific ionization energy loss dE/dx with a resolution $\sim 11\%$.

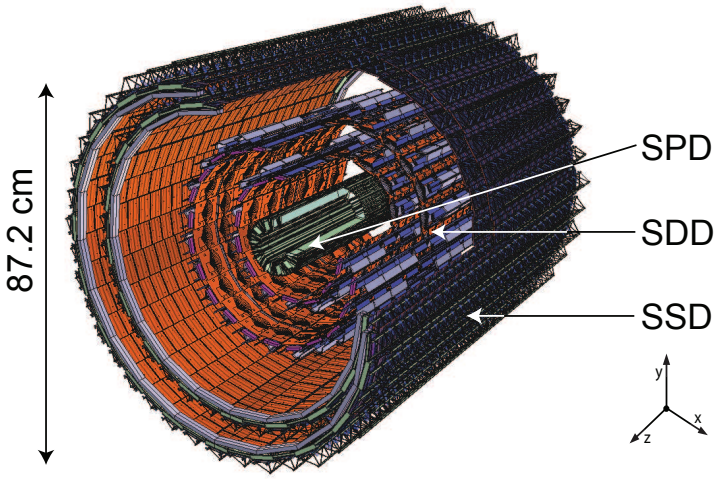

Figure 3.3: The ALICE Inner Tracking System (ITS)

The ITS is crucial to provide high spatial resolution (better than 100 μm) on the primary vertex of the collision, on the secondary vertices of particle decays such as hyperons, D and B mesons and on the track impact parameter, which is the distance to closer approach of a track to the primary vertex. Furthermore, ITS tracking information allows to improve the momentum and angle resolution for particles reconstructed by the Time Projection Chamber (TPC). This can be achieved only if multiple scattering is minimized. Therefore, the amount of material in the active volume must be reduced at a minimum: the thickness of the four outermost layers used for particle identification is approximately 300 μm and it is smaller (200 μm) for the two inner pixel layers. The detectors must overlap in order to cover the entire solid angle. The total of the radiation length for the full ITS is less than 8% X/X_0 for particles at $\eta = 0$. In addition, ITS can be also used as a stand-alone (sa) tracker to reconstruct and identify particles with low momentum (Sec. 5) that are deflected or decay before reaching the Time Projection Chamber (TPC), and to recover tracks crossing the dead regions of the TPC ($\sim 10\%$).

The ITS, as all the ALICE detectors, was designed to cope with a high multiplicity environment. Thus, the granularity is high enough to guarantee a high tracking efficiency, even in central Pb–Pb collisions at the nominal LHC energy where some models predicted up to 8000 charged particles per pseudo-rapidity unit at the time of the ALICE design. The layer dimensions along the beam axis [117], reported in Tab. 3.2, allow to cover a pseudo-rapidity range $|\eta| < 0.8$ for all vertices located within the standard fiducial region $|Z_{vertex}| \lesssim 10$ cm.

Layer	Type	r[cm]	$\pm z$[cm]	Active Area m^2
1	pixel	3.9	14.1	0.07
2	pixel	7.6	14.1	0.14
3	drift	15.0	22.2	0.42
4	drift	23.9	29.7	0.89
5	strip	37.8	43.1	2.09
6	strip	42.8	48.9	2.68

Table 3.2: Geometrical parameters of the six layers of the ALICE Inner Tracking System.

Time Projection Chamber

The TPC covers the pseudo-rapidity range $|\eta| < 0.9$ and it is the main tracking detector in the central barrel. It provides, together with the information from the ITS, charged particle track reconstruction, particle identification through the specific ionization energy loss dE/dx, and good two-track separation.

The TPC consists of a cylindrical field cage surrounding the ITS detector, filled with $\approx$ 90 m^3 of a gas mixture $Ne/CO_2/N_2$ (90/10/5), in which the ionization electrons are transported over a distance of up to 2.5 m on either side of the central electrode to the end-plates. The inner radius is r_{min} = 80 cm, set by the maximum acceptable particle density of 0.1 particle per cm^2 and the outer radius is r_{max} = 250 cm. The charge collected at the end-plate is proportional to the dE/dx of the particles in the gas with a resolution of about 5% and 6.8% for isolated track and high-occupancy environment (dN/dy = 8000) respectively. The dE/dx of the ALICE TPC as a function of the momentum together with the parametrized expected response for various particle species is reported in Fig. 3.4 left. The TPC allows hadron and nuclei identification over a wide p_{T} range. The relativistic rise at high momentum ($p > 4$ GeV/c) of the dE/dx can also be used to identify π, K and p at high p_{T} [119].

Time Of Flight

The TOF is an array of time of flight detectors, optimized to provide particle identification in the intermediate momentum region from 0.6 to 5(3) GeV/c for protons (pions and kaons). The pseudo-rapidity coverage is $|\eta| < 0.9$. The TOF detector design is based on the Multi-gap Resistive-Plate Chamber (MRPC) technology, which guarantees an intrinsic time resolution better than 60 ps and the possibility to cover large areas. The start time for the time-of-flight measurement can be determined from different methods, e.g. using the time-zero given by the T0 detector or using the measured times in the TOF itself. The whole device is inscribed in a cylindrical shell with an internal radius of 370 cm and an external one of 399 cm. The entire detector thickness correspond to 30% of a radiation length. The β–p TOF performance plot for p–Pb collisions at $\sqrt{s_{\mathrm{NN}}}$ = 5.02 TeV is reported in the right panel of Fig. 3.4.

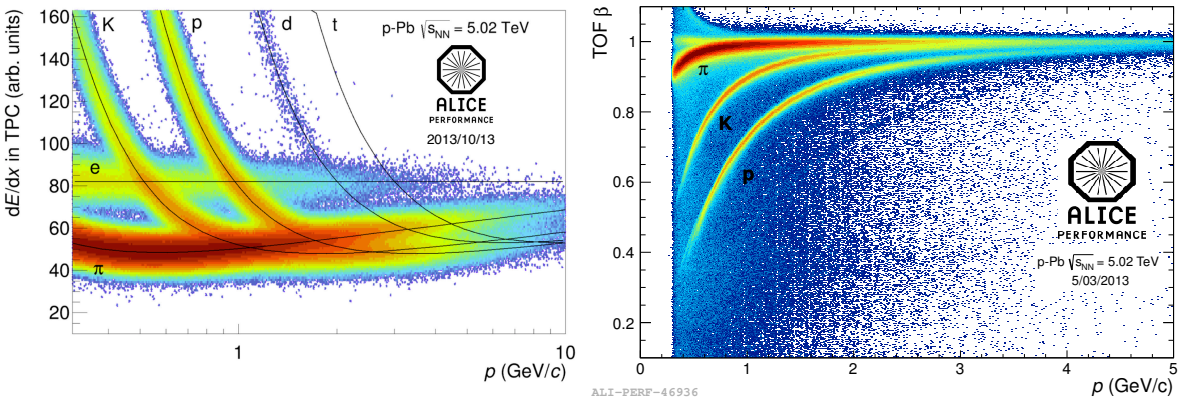

Figure 3.4: PID performance plot TPC (left) and TOF (right) detectors of ALICE.

VZERO

The VZERO detector is made of two arrays of scintillator counters located on each side of the interaction point: the VZERO-C is located at z = 90 cm distance from the detector centre along the beam axis on the Muon Spectrometer side while the VZERO-A detector is installed at 340 cm distance on the opposite side. The detectors cover the pseudo-rapidity ranges $-3.8 < \eta < -1.7$ (VZERO-C) and $2.8 < \eta < 5.1$ (VZERO-A). They are segmented into 64 elementary counters distributed in eight rings.

Together with the SPD, the VZERO detectors is used for minimum bias trigger selection. In addition, the measurement of the time difference between signals in the VZERO-A and VZERO-C detectors allows us to reject beam–gas interactions. Finally, since the amplitude in the VZERO detector is proportional to the particle multiplicity, this detector is also used to define centrality(multiplicity) event classes in Pb–Pb(p–Pb) collisions. The centrality of the collisions can be estimated via the multiplicity recorded in the event. It is evaluated from a Glauber fit to the distribution of the summed amplitudes in the VZERO scintillator tiles (Fig. 3.5).

T0

The T0 detector consists of two arrays of quartz Cherenkov detectors installed at 72.7 cm and 375 cm distance from the interaction point along the beam axis with pseudo-rapidity coverages of $-3.28 < \eta < -2.97$ and $4.61 < \eta < 4.92$ respectively. It is used to generate a start time (T0) for the TOF detector, to measure the vertex position (with a precision ± 1.5 cm) for each interaction and to provide a L0 trigger when the position is within the preset values.

3.3 Event selection: Trigger and Background rejection

ALICE physics event selection is performed using both, online (detector trigger) and offline procedures. The main goal of event selection is to tag good hadronic interactions with the highest possible efficiency, while rejecting the machine-induced and physical background.

3.3.1 Trigger

The trigger is handled by the Central Trigger Processor (CTP) of ALICE based on detector signals and information about the LHC filling scheme. The CTP evaluates

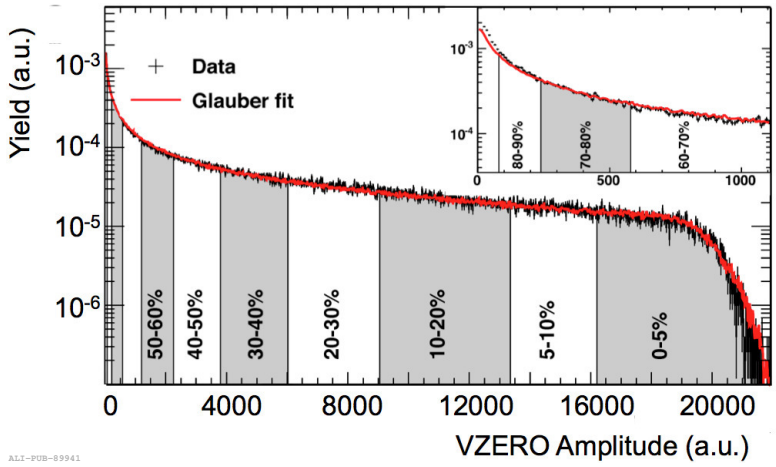

Figure 3.5: Distribution of VZERO amplitude in Pb–Pb collisions at $\sqrt{s_{NN}} = 2.76$ TeV. Red line represents the (Negative Binomial Distribution) NBD-Glauber fit to the distribution. [27]

trigger inputs from the trigger detectors every machine clock cycle ($\sim$ 25 ns) and provides *trigger signals* to readout detectors in case the trigger conditions are fulfilled. Information about the LHC filling scheme is used by the CTP to suppress the background. The bunch crossing mask (BCMask) provides the information as to whether there are bunches coming from both A-side and C-side, or one of them, or neither.

ALICE online Minimum Bias (MB) trigger have evolved during the Run1 data taking to accommodate the increasing luminosity. According to the period, the MB trigger was defined[†] using one of the following requirements:

- at least one hit in the SPD or in either of the VZERO arrays. (MB_{OR})
- VZERO signals on both A and C sides. (MB_{AND})

The high efficiency MB_{OR} was used at low luminosity. Once the luminosity and the background level increased, the high-purity MB_{AND} trigger became more advantageous. The rest of trigger types implemented in ALICE are *rare*-triggers. More details about trigger conditions in ALICE data taking can be found in Ref. [120].

3.3.2 Offline selection

The machine–induced background (MIB) is caused by beam interactions with the residual gas in the beam pipe (beam–gas) or by particles in the halo of the beam interacting with mechanical structures in the machine. These events can be rejected making use of the timing information from the VZERO or the ZDC detectors.

[†]In Pb–Pb collisions other MB implementations are used in high luminosity conditions.

The rejection is based on the fact that MIB caused by interactions of one of the beam upstream of the VZERO produce an "early" signal on the one of the VZERO counters as compared to the time corresponding to a collision in the nominal interaction point. This is shown in the left panel of Fig. 3.6, where background events accumulate mainly in two peaks (beam 1: -14.3, -8.3 ns and beam 2: 14.3, 8.3 ns) in the time sum-difference plane, well separated from the main (collision: 8.3, 14.3 ns) peak. With this method the MIB contamination is reduced to about 10%, depending on vacuum conditions and luminosity.

The second source of background is due parasitic collisions of main bunches with satellite bunches located a few radio-frequency (RF) buckets away from the main bunch. Main-satellite collisions occur at positions displaced by multiples of 2.5 ns/2·c = 37.5 cm, with respect to the nominal interaction point. These events are rejected using the correlation between the sum and the difference of times measured in the ZDC, as shown in Fig. 3.6 right. In the figure the large cluster in the middle corresponds to collisions between ions in the nominal RF bucket on both sides, while the small clusters along the diagonals (spaced by 2.5 ns in the time difference) correspond to collisions in which one of the ions is displaced by one or more RF buckets.

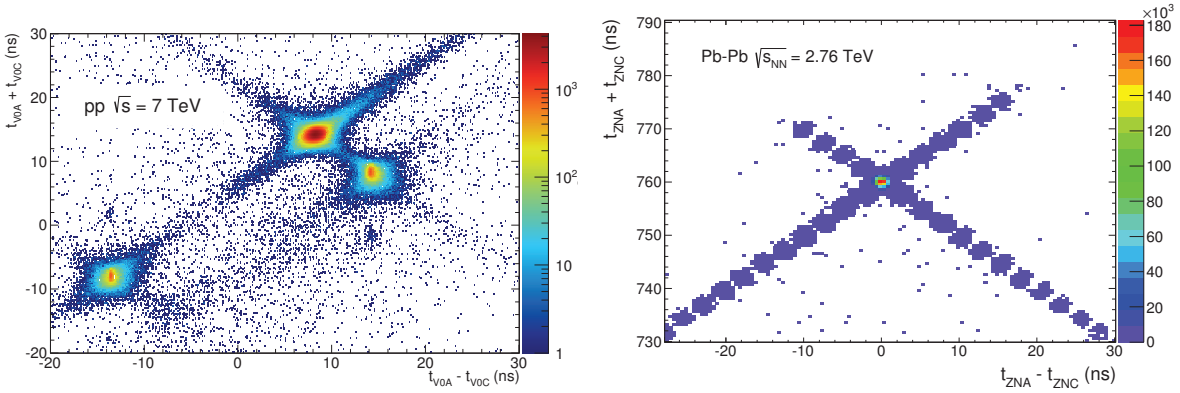

Figure 3.6: Correlation between the sum and the difference of times recorded by: VZERO(left) and neutron ZDCs in Pb–Pb collisions (right) on either side.

Additional background rejection can be implemented based on time information from T0 detectors. The T0 provides a vertex trigger defined as the coincidence between T0A and T0C, with the additional requirement that the difference in their signal times corresponds to an interaction happening within 30 cm from the nominal interaction point. The latter condition provides excellent rejection of beam–gas and satellite background. Indeed, a background contamination below 0.1% was obtained in p–Pb collisions at a luminosity of 10^{29} cm^{-2}s^{-1}.

3.4 ALICE offline framework

The ALICE offline framework consist of both AliRoot [121] and AliEn [122] frameworks. The first is an Object-Oriented (OO) framework based on Root [123], a software specifically designed to cope with huge amounts of data coming from high energy experiments. Root and AliRoot provide the packages to perform event generation, detector simulation, event reconstruction and data analysis. AliRoot in particular includes the geometry of the detectors of the ALICE apparatus and their response to the passage of particles. The data processing framework is schematically shown in Fig. 3.7.

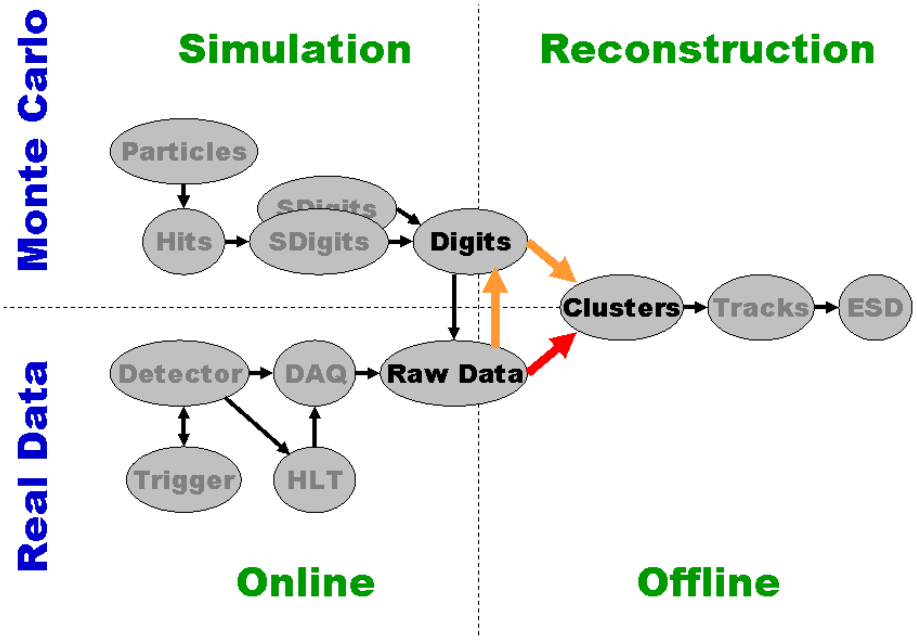

Figure 3.7: Data processing framework in ALICE.

3.4.1 Simulation

Event simulation is performed using Monte Carlo (MC) particle generators. In ALICE, the main generators used for pp collisions are PYTHIA [124] and HERWIG [125], which are based on theoretical QCD calculations based on a perturbative approach for high virtuality process and phenomenology description of the underlying event. The codes adopted for p–Pb and Pb–Pb collisions are mainly HIJING [126] and DPMJET [127]. The generated particles are then propagated through the detectors with MC transport programs, like Geant3 [128], Geant4 [129] and Fluka [130], which describe particle interaction with the material.

The results of this process are the positions and the energy deposit of each particle in the sensitive region of the detectors (*hits*). Reliable MC simulations demand a precise description of the detectors in terms of geometry and material composition. *Hits* are then transformed into *digits* via the simulation of the detector response. There are two type of *digits*, *summable digits* where low signal/noise thresholds are used, in order to preserve the possibility to add signals from other particles (event merging), and *digits*, where the real threshold is considered. Digits are usually stored in the format called *raw data*, which is specific for each detector. This format is identical to the one that is used by the acquisition systems during data taking and it is the starting point for the reconstruction of both Monte Carlo events and real data.

3.4.2 Reconstruction

Both real and simulated data use the same reconstruction procedure. The input to the reconstruction framework could be digits in ROOT TTree format or raw data. First, a local reconstruction of clusters/rec points is performed in each detector, which is followed by *track finding*. The detector cell that were fired by the same particle are grouped together into a cluster, whose coordinates and energy deposit are calculated and stored in the reconstructed points. The vertex position is firstly estimated using rec points in the SPD. The reconstructed points left by the particle on the tracking detectors are assigned to tracks by the tracking algorithm. Thus, the particle track kinematic is reconstructed. In ALICE a high track-finding efficiency is required for tracks down to $p_{\mathrm{T}} = 100$ MeV/c even at the highest track densities. Tracks are reconstructed in ITS, TPC and TRD detectors and then propagated to the outer detectors and matched with the reconstructed point in this detectors. The ITS allows to improve the momentum and angle resolution for the tracks reconstructed in the TPC and prolonged to the ITS.

In general, the reconstruction steps are:

Raw data
This is a digitised signal (ADC count) obtained by a sensitive pad of a detector at a certain time.

Rec Points
Reconstructed space points: this is the measurement of the position where a particle crossed the sensitive element of a detector (often, this is done by calculating the centre of gravity of the "cluster", which is a group of contiguous cells with signals above applied thresholds).

Tracks
Reconstructed tracks. A track is an helix defined by a set of five parameters (the curvature, two angles with respect to the coordinate axes, two positions) describing the trajectory of particles together with the corresponding covariance matrix estimated at a given point in space. The information of the detectors in which reconstruction occurred is also stored in the track together with the information of TOF, HMPID detectors when available.

The output of the reconstruction is the Event Summary Data (ESD), which is an array of AliESDtracks, an AliRoot class object. The AliReconstruction class provides a simple user interface to the reconstruction framework. The size of the ESD is about one order of magnitude lower than the corresponding raw data. The are further reduced into Analysis Object Data (AOD) which contain the information used for physics analyses.

ITS stand-alone tracking

In addition to the global procedure described above, the ITS can be used as a stand-alone tracker with a dedicated tracking algorithm [131]. In this way it is possible to reconstruct low momentum track of particles that decays before reaching the TPC, but also high momentum particles that pass through the dead zone of the TPC or decays between the ITS and the TPC. The interaction vertex is firstly estimated from the tracklets (= track segments) using reconstructed points in the SPD layers. The ITS stand-alone tracking algorithm is performed in two steps:

Track finding. In the inward track finding mode, of the ITS stand-alone tracking algorithm, the track seeding starts from the inner SPD layer and goes toward the external SSD layer. Search windows are defined by two quantities:

$$\lambda = \arctan\left[\frac{(z - z_V)}{\sqrt{(x - x_V)^2 + (y - y_V)^2}}\right], \quad \phi = \arctan\left[\frac{y - y_V}{x - x_V}\right] \tag{3.2}$$

where x_V, y_V and z_V are the coordinates of the primary vertex reconstructed with the SPD. For each pairs of clusters belonging to the same (λ, ϕ) window the track curvature is estimated using the vertex information. The expected position on the next layer is calculated and clusters are searched in a given $(\Delta\lambda, \Delta\phi)$ window. If the rec. point on a given layer is missing (because of a dead region or detector inefficiency) the seeding is prolonged to the following layer. A least 3 associated points are requested to form a candidate track. The track finding procedure is iterated increasing progressively the size of the window in order to reconstruct low

p_{T} tracks which are significantly bent in the magnetic field and deflected by multiple scattering.

The possibility of performing an inward track finding from the outer layers to the primary vertex is also implemented. The procedure is the same as in the case of the outward track finding but in opposite direction.

Track fitting. The fit of the tracks is done with the Kalman filter method also used in the global track (ITS+TPC) reconstruction [118]. The determination of the initial values of the track parameters for the track reconstructed with the ITS stand-alone algorithm, is done performing an helix fit on the primary vertex and the first two available points close to the vertex. The track is then fitted through the other associated point outward and then inward from the outer associated point to the primary vertex. If a track candidate have more than two associated points in the same layer the fit is performed using all the possible combinations and the points associated to the fit with the lowest χ^2 is chosen. As a last step, the track are re-fitted from the outer ITS layer to the primary vertex and the track parameters are stored in the object represented the track (AliESDtrack).

It is possible to distinguish two different sets of tracks reconstructed only with the ITS:

***ITSsa* tracks.** The ITS stand-alone tracking algorithm runs after the reconstruction of global tracks. Only ITS clusters whose were not attached to a global track are used in the ITS stand-alone reconstruction. This sample contains only tracks not reconstructed by the TPC. Therefore it is not a "complete" set of tracks but it is "complementary" to the ITS-TPC track sample.

***ITSpureSA* tracks.** The ITS stand-alone tracking algorithm runs using all available ITS clusters. This sample contains all the particle tracks in the event.

The relative p_{T} resolution for global tracks and ITS stand-alone tracks are shown in Fig. 3.8 as a function of p_{T}. The values have been extracted by Monte Carlo simulations. The p_{T} resolution for ITS stand-alone tracks is worse than ITS+TPC ones. At low p_{T} the resolution is about 5% for ITS stand-alone tracks and $\sim 0.6\%$ for global tracks. This is mainly due to the smaller level-of-arm and the limited number of points in the case of the ITS stand-alone tracking.

The resolution of the track impact parameter (d_0) has been studied separately for the transverse plane ($r\phi$) and the z components[‡]. The resolution is estimated from a

[‡]The ($r\phi$) plane corresponds to the (x, y), plane. z is the beam direction.

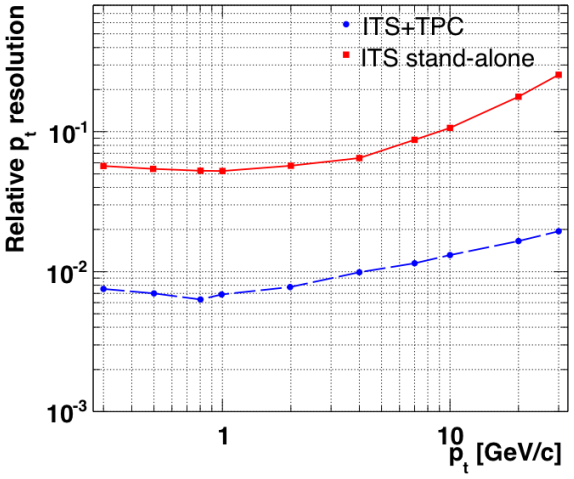

Figure 3.8: Relative p_{T} resolution for ITS stand-alone tracks and global tracks as a function of p_{T} [131].

Gaussian fit to the distribution of the considered component of the impact parameter. The resolution on $d_0(r\phi)$ and $d_0(z)$ obtained from Monte Carlo simulation for ITS stand-alone tracks and global tracks are compared in Fig. 3.9. The two tracking algorithms provide a similar resolution in the transverse plane, as expected, since the resolution is mainly given by the high precision points of the SPD layers. Along the beam direction a clear worsening of the resolution for ITS stand-alone tracking can be observed. In the ITS only the SDD detector provides a high precision measurement of the z coordinate, while for global tracking the larger level-of-arm of the TPC results in a better resolution at high p_{T}.

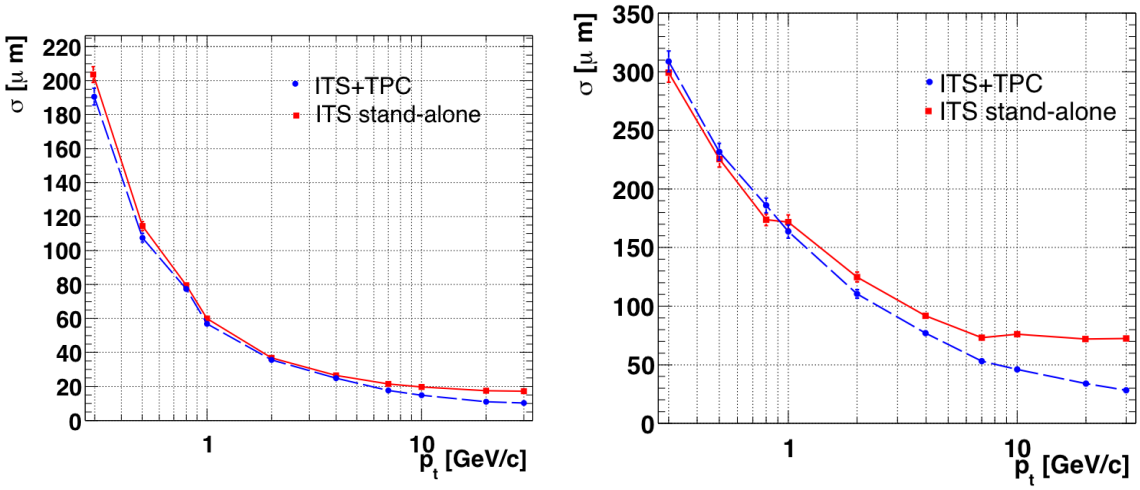

Figure 3.9: Track impact parameter resolution in the transverse plane (left) and along the beam direction (right) for ITS stand-alone tracks and global tracks as a function of p_{T} [131].

In addition, the resolution on $d_0(r\phi)$ for ITS stand-alone tracking is shown in Fig. 3.10 for π, K and p in pp data and Monte Carlo simulation. The impact parameter resolution is determined by two main contributions:

1. a momentum-independent contribution due to the spatial resolution of the detectors,

2. a momentum-dependent contribution due to multiple scattering.

Since multiple scattering angle depends on $1/\beta$, for low momenta, where this is the main contribution to the impact parameter resolution, the resolution itself depends on the particle species, being worse for heavier particles. The resolution in the data is well reproduced in the Monte Carlo simulation.

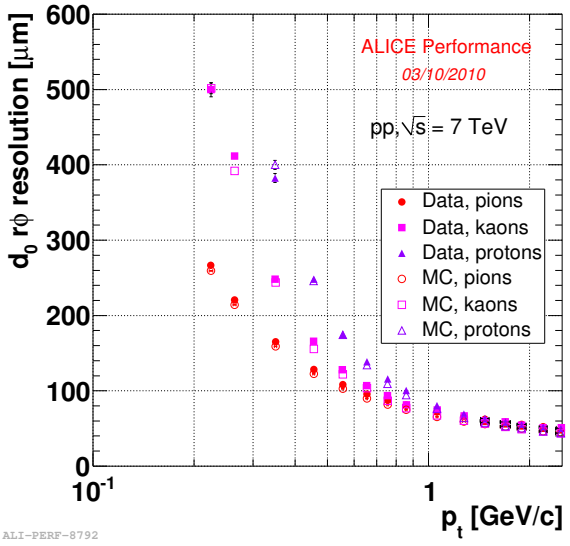

Figure 3.10: Transverse track impact parameter ($d_{0_{r\phi}}$) resolution as a function of p_{T} for the tracks reconstructed in the pp collisions at $\sqrt{s} = 7$ TeV by the ITS stand-alone and compared with the Monte Carlo simulation results.

3.4.3 Alien and the Grid

Large computing resources are demanded by high-energy experiments at the LHC to store and analyse huge amount of data. To cope with these requirements, a distributed computing is necessary, which is the Grid. The Grid [132] is an infrastructure that allows one to distribute computer resources across institutes and universities which take part in the project and it is organised in different levels or Tiers. Data coming from LHC experiments are stored in the CERN computing centre, the Tier–0. Copies of the collected data are then replicated in large regional computing centres (Tier-1), which also contribute in the event reconstruction and Monte Carlo simulation. Tier-2 centres are computing centres located in different institutions which do not have large storage capabilities but provide a large fraction of the computing resources for Monte Carlo simulations, data reconstruction and data analysis. The AliEn (ALIce Environment) framework has been developed with the aim of offering to the ALICE user community a transparent access to computing resources distributed through a single interface.

4

Bayesian approach for PID in the ALICE ITS

A key feature of the ALICE detector is the capability of particle identification (PID) in a wide momentum range, by means of various detectors which allow to separate different particle species in different kinematic regions (ITS, TPC, TOF, HMPID... [120]). An important contribution to the reconstruction and identification of charged particles is provided by the ITS, which allows to extend the tracking and PID capabilities down to very low p_{T} (≈ 80 MeV/c for pions), a region inaccessible with the other detectors. This is achieved by making use of a stand-alone (sa) analysis in which the ITS operates as a stand-alone tracker, with a dedicated tracking algorithm (Sec. 3.4.2) [131], and exploiting at best the advantage of its PID capabilities.

The four outermost layers of the ITS (equipped with SDD and SSD) provide measurements of the specific ionization energy loss (dE/dx) of particles as they pass through the detector. These informations are used together with the track momentum to identify the track. A precise parametrization of the dE/dx observed in SDD and SSD as a function of the particle momentum for the various particle species (denoted "response function") is required to define an effective PID algorithm for ITS stand-alone tracks. Different PID approaches based on the calculation of a truncated mean of the four dE/dx samples measured in the SDD and SSD layers have been used for pion, kaon and proton identification in the sample of ITS stand-alone tracks reconstructed in pp and Pb–Pb collisions [62, 63, 133]. Nevertheless, an improvement of the ITS PID performance can be obtained by implementing an approach which uses all the dE/dx samples to compute a per-layer probability of a given particle species. The probabilities of the four layers are then multiplied together and finally the probability of a given track to be a pion/kaon/proton is computed using the Bayes theorem.

In this Chapter, the results obtained during the first part of my Ph.D. activity will be presented. They include: a reliable parametrization of the SDD and SSD response functions for MC simulations and real data, the implementation of a track-by-track Bayesian approach to identify the reconstructed tracks and the comparison of its performance (i.e. efficiency and contamination) with other PID methods used in previous analyses.

4.1 Bayesian PID

In this section a track-by-track Bayesian PID approach implemented by the author will be described. The method has been used for the study of the p_{T}-spectra of identified π, K and p using the ITS stand-alone sample of tracks (Sec. 5).

The dE/dx signals measured in the SDD and SSD are parametrized as a function of the track momentum for all species with functions $f(s = dE/dx)$, also called detector response functions because of their dependence on the detector as well as on the particle momentum and species. These functions are related to the conditional probability density ($f_{N_i}(dE/dx|i,p)$) for a particle of type i, in a given momentum window $[p, p + \Delta p]$, to lose the quantity dE/dx of energy in the sensitive area of the detector. In fact, $f_{N_i}(dE/dx|i,p)$ functions for each track can be obtained dividing the response functions $f_{N_i}(s)$ by their area, where i means the species of the particle (namely π, K or p) and s is the dE/dx signal measured by a given SDD or SSD detector. Then, for a given track with momentum p, the conditional probability density function for a vector of signals

$$S \equiv \{s_{SDD1}, s_{SDD2}, s_{SSD1}, s_{SSD2}\} \tag{4.1}$$

is computed as the product of the corresponding normalized response functions of each layer:

$$R(S|i,p) = \prod_{SDD,SSD} f_{N_i}(s|i,p) \tag{4.2}$$

Finally, we make use of the Bayes' theorem in order to get the probability* for a track with a set of ITS signals S and momentum p of being of type i:

$$P(i|S,p) = \frac{R(S|i,p)\Pi(i)}{\sum_{t=e,\pi,K,p...} R(S|t,p)\Pi(t)} \tag{4.3}$$

where $\Pi(i)$ is the prior probability (also called only *prior*) for a particle to be of i type, i.e. is the relative abundance of the different particle species in the analysed sample of events. Once the Bayesian probability for each species (p, K, π, etc.) has been calculated for a given track, the PID may be performed by applying a selection criterion. In this work the *maximum probability* selection criterion is applied, i.e. the track is assigned an identity based on the species with the highest Bayesian probability.

*In a Bayesian framework the probability is interpreted as the degree of belief.

4.2 Response functions for PID signal in the ITS

The main particle species that can be separated based on their dE/dx in the ITS are pions, kaons and protons with momenta lower than 1 GeV/c[†]. For light nuclei the identification can be extended to higher momenta. Above these limits a particle identification based on the dE/dx in the ITS cannot be applied because the specific energy loss of π, K and p are very similar independently of the particle mass and the ITS resolution in the dE/dx does not allow to separate among species. At low momentum, PID analysis are extended down to the minimum momentum the considered hadron species must have in order to be reconstructed by the ITS stand-alone tracking algorithm.

In addition, it can be stressed that muons are excluded from PID method because their mass is very close to that of pions, thus the dE/dx of the two species is not distinguished experimentally. Also electrons with momenta higher than 200 MeV/c cannot be well identified since their specific ionization is similar to that of pions. However, an electron parametrization for $p < 200$ MeV/c is required to reduce the electron contribution to the pion contamination. The electron parametrization is obtained from a dedicated study of the ITS response for electrons. The procedure is done in an analogous way as for π, K and p.

For each track detected in the ITS, the measured cluster charges in the SDD and SDD are normalized to the path length, which is calculated from the reconstructed track parameters to obtain a dE/dx value for each SDD and SSD layer. The energy deposit is affected by fluctuations due to the small thickness of the material: in the case of the SDD and SSD, made of thin silicon layers of ~ 300 μm, the dE/dx follows the Landau asymmetric distribution with the most probable value (MPV) given by the Bethe-Bloch formula [134]. These fluctuations are folded with detector and electronic effects, i.e. an experimental resolution of the energy deposit, which leads to a Gaussian shape convoluted to the Landau.

4.2.1 Truncated mean approach

The Landau tail of such distributions complicates the separation of different hadron species. For this reason, a Gaussian distributed estimator is preferable. One way to reduce the effects of the asymmetric tail is to apply the *truncated mean* approach (also

[†]As will be presented in the next chapter: these limits depend on the requirement in the contamination from other species which is established specifically by each analysis.

called average dE/dx in this thesis): out of the four dE/dx samples the two higher energy signals are discarded and the remaining two are averaged with the same weight. A non negligible fraction of the reconstructed tracks is obtained using only 3 clusters in the SDD+SSD layers, due to modules excluded from the acquisition and to the presence of dead channels. For the tracks with only three clusters in the SDD and SSD layers, the truncated mean consists of a weighted average of the lowest (weight = 1) and the second lowest dE/dx samples (weight = 1/2). Tracks with less than three points in the SDD and SSD layers ($\lesssim 0.2\%$) are not recommended to be used in any analysis that exploits ITS PID.

In order to define the ITS response functions for the truncated mean, in each track momentum interval the distribution of the dE/dx values obtained with the truncated mean approach is fitted to a Gaussian distribution, assuming that the asymmetric tail at large dE/dx is reduced in the truncated average. The mean value of this distribution as a function of $\beta\gamma$ can be modelled with a Bethe-Bloch curve for large $\beta\gamma$, while it deviates from the Bethe-Bloch expectation for small $\beta\gamma$. This is mainly due to momentum and dE/dx resolution bias at low $\beta\gamma$[‡]. Therefore, the expected most probable value for the average dE/dx is calculated using the PHOBOS [135] parametrization of the Bethe-Bloch function for $\beta\gamma > 0.7$, complemented by a polynomial fit at low $\beta\gamma$:

$$dE/dx = \begin{cases} E_0\beta^{-1}(b + 2\ln\gamma - \beta^2)) & (\beta\gamma > 0.7) \\ \\ p_0 + p_1/\beta\gamma + p_2/(\beta\gamma)^2 + p_3(\beta\gamma)^3 & (\beta\gamma \leq 0.7) \end{cases} \tag{4.4}$$

where E_0, b, p_0, p_1, p_2 and p_3 are the free parameters, which are tuned on the measured or simulated data.

The truncated mean parametrization for real data and Monte Carlo simulations differ only by few percent. The response of the ITS and therefore the Bethe-Bloch truncated mean parametrization are the same for the various collision systems (pp, p–Pb and Pb–Pb) and energies. The distribution of the dE/dx (obtained using the truncated mean) as a function of the momentum for ITS standalone tracks in Pb–Pb collisions at $\sqrt{s_{NN}} = 2.76$ TeV and p–Pb collisions at $\sqrt{s_{NN}} = 5.02$ TeV, are shown in the Fig. 4.1 (a) and (b) respectively. They are compared to the parametrized response function for pions, kaons, and protons. The dotted line represents the expected energy loss of electrons in the ITS. It was obtained from an individual tuning made in an analogous way as for π, K and p.

[‡]When the track is fitted, π mass is assumed for each track, and also because we use the p at vertex which differs from the p at the considered SDD or SSD layer due to the energy lost while crossing the innermost ITS layers.

The relative resolution of the specific energy loss dE/dx resulting from the truncated mean, shown in Fig. 4.2, depends slightly on the number of ITS dE/dx samples attached to the tracks and does not show any significant trend with the transverse momentum of the track. The p_{T} variable has been chosen instead the of p in order to directly investigate the resolution as a function of the observable used in the p_{T} spectra analysis. The resolution is also found to be independent of the colliding system and similar in data an Monte Carlo simulations. It is evaluated by fitting the π peak in the dE/dx distribution in narrow[§] p_{T} intervals with a Gaussian function.

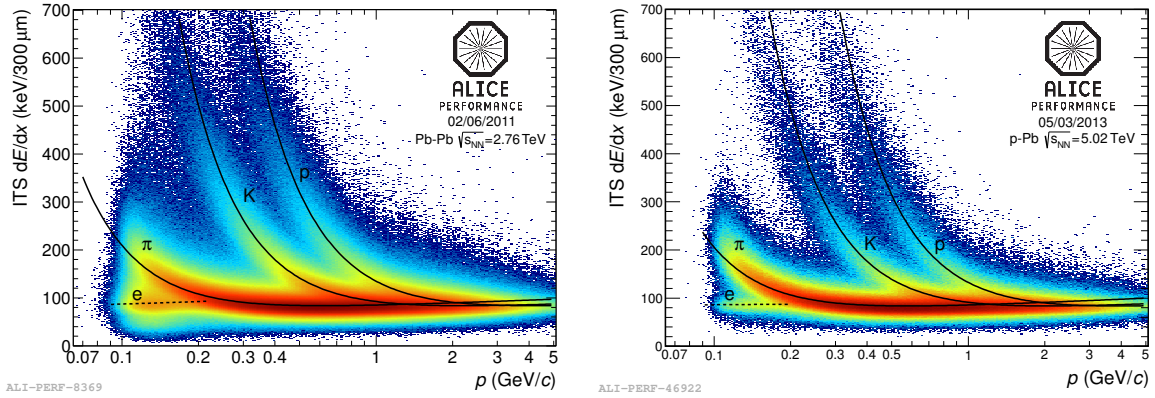

(a) **(b)**

Figure 4.1: Truncated mean dE/dx distribution as a function of the track momentum p in (a) Pb–Pb collisions at $\sqrt{s_{\mathrm{NN}}} = 2.76$ TeV and (b) p–Pb collisions at $\sqrt{s_{\mathrm{NN}}} = 5.02$ TeV. The Black lines are the tuned Bethe-Bloch parametrization.

The conditional probability density from the truncated mean approach can be obtained assuming a Gaussian shape for the ITS response function, and making use the parametrization mentioned above,

$$f_{N_i}(dE/dx|i,p) = \frac{1}{\sigma\sqrt{2\pi}} \exp\left(\frac{-(dE/dx_{meas} - dE/dx^{i,p}_{expect})^2}{2\sigma^2}\right) \tag{4.5}$$

where dE/dx_{meas} is the measured average dE/dx, $dE/dx^{i,p}_{expect}$ is the expectation value given by the Bethe-Bloch parametrization for particle species i and track momentum p and σ is the dE/dx resolution.

However, the small number of dE/dx measurements in the ITS (maximum 4) results in a residual Landau tail when the truncated mean approach is adopted. Therefore, the Gaussian assumption for the truncated mean response functions does not give a reliable estimation of the conditional probability densities. This can significantly affect the performance of the PID approach.

[§]narrow bins are needed to get negligible dependence on the momentum distribution in the bin.

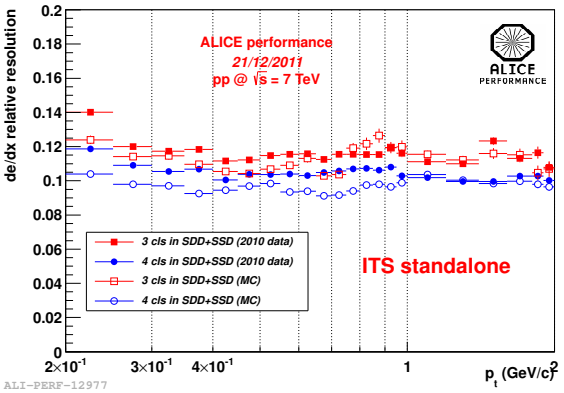

Figure 4.2: Truncated mean dE/dx relative resolution for ITSsa tracks as a function of p_{T} for data and Monte Carlo.

4.2.2 Parametrization of the single-layer ITS response functions

The truncated mean approach, despite its limitations, has been used by different PID methods in previous analyses of π, K and p spectra (e.g in pp collisions at $\sqrt{\mathrm{s}} = 900$ GeV [133] and Pb–Pb collisions at $\sqrt{\mathrm{s_{NN}}} = 2.76$ TeV [62, 63]) and it is used for ITS PID in other analyses. A possible solution, to improve the PID performance of the ITS by accounting better for the asymmetric tails of the Landau distribution, is to describe the dE/dx distribution in each of the four layers with PID capability with a convolution of a Gaussian and a Landau (Landau-Gauss) functions. Thus, the observed dE/dx is modelled with two contributions: the Landau function describes the ionization energy loss with its physical fluctuations and the Gaussian one represents the smearing of the signal due to the detector resolution (charge collection efficiency, diffusion during the drift, electronic readout effects and momentum resolution) [136].

With this approach, instead of using the truncated mean, we take all the dE/dx samples of each track, i.e. up to four signals (2 clusters in SDD and 2 clusters in SSD) rather than one are fitted. This should guarantee an improved performance with respect to the truncated mean approach because we are using all the available information from the ITS and also because any difference between the inter-calibration of SDD and SSD does not affect the PID performance as for the truncated mean. As mentioned above, the dE/dx distributions of the tracks of a given species in a given momentum range are fitted with a convolution of a Landau and a Gaussian function (Landau-Gauss).

The Landau-Gauss function has four free parameters (Landau-Gauss parameters): the width and the most probable value of the Landau distribution, the total area, and the width of the Gaussian function. As a first check, the Landau-Gauss parameters from fits to the layers equipped with the same detector type (e.g layer 3 and 4 both equipped with SDD) have been compared and it was found that their difference was below few percent ($< 2\%$). Since the detector response should not (or weakly) depend

on the layer on which it is mounted, we have merged the dE/dx distributions of the two layers equipped with the same type of detector to increase the statistics. Thus, the parametrization of the response functions has been done separately for SDD and SSD.

The ITS Landau-Gauss parametrization is performed in two steps:

1. The dE/dx distribution for each type of particle (π, K and p) in each detector and in several momentum intervals of width 32 MeV/c[¶] inside the interesting momentum range for ITS PID (0.1–1.6 GeV/c for pions, 0.2–1.6 GeV/c for kaons and 0.3–1.6 GeV/c for protons) were fitted with a Landau-Gauss function. The most probable value (MPV), the Landau width (Lwidth) and the Gaussian width (Gsigma) are extracted from the fit. The fit parameter representing the total area is neglected since the response functions are normalized to 1 because they should define a conditional probability.

2. Once the fits are performed, it is possible to plot the three parameters as a function of the track momentum p, separately for each particle species and detector type. Instead of storing all the three parameters for each detector type and momentum bin, these plots are fitted with *ad-hoc* functions, $f_{MPV}(p)$, $f_{Lwidth}(p)$, $f_{Gsigma}(p)$, for π, K and p and for the 2 detector types. The parameters used to define such ad-hoc functions are called ITS response function parameters and they allow us to compute the conditional probability for a track of momentum p to produce a given dE/dx signal in a given ITS layer under a given mass hypothesis (π, K, p). The ad-hoc functions $f_{MPV}(p)$, $f_{Lwidth}(p)$ and $f_{Gsigma}(p)$ for π, K and p that were used to obtain a good interpolation of data are:

$$f_{MPV}(p) = \begin{cases} \frac{A_{mp}}{p^2} + B_{mp}\ln(p) + C_{mp} & \text{for pions} \\ \\ \frac{A_{mp}}{p^2} + \frac{B_{mp}}{p}\ln(p) + C_{mp} & \text{for kaons and protons} \end{cases} \tag{4.6}$$

$$f_{Lwidth}(p) = \begin{cases} \frac{A_{lw}}{p^2} + \frac{B_{lw}}{p}\ln(p) + C_{lw} & \text{for pions} \\ \\ \frac{A_{lw}}{p^2} + B_{lw} & \text{for kaons and protons} \end{cases} \tag{4.7}$$

$$f_{Gsigma}(p) = \begin{cases} \frac{A_{gs}}{p^2} + B_{gs}\ln(p) + C_{gs} & \text{for pions} \\ \\ \frac{A_{gs}}{p^2} + \frac{B_{gs}}{p}\ln(p) + C_{gs} & \text{for kaons and protons} \end{cases} \tag{4.8}$$

[¶]This value is 3 (1) times larger the momentum resolution, which is 10 (6)%, for the ITS stand-alone tracks reconstructed with momentum $p \approx 0.1$ GeV/c ($p \gtrsim 0.6$ GeV/c). The dE/dx is $\sim$ flat (i.e. it does not vary strongly with the momentum) for $p \gtrsim 0.6$ GeV/c, so that it is safe considering, for ITS PID response studies, only one σ in the momentum range $0.6 < p < 1.6$ GeV/c.

The parameters $A_{mp,lw,gs}$, $B_{mp,lw,gs}$ and $C_{mp,lw,gs}$ allow to calculate the Landau-Gauss probability density function (pdf) starting from the track momentum and mass. The MPV functional form has been modelled by a "Bethe-Bloch" motivated function, $f_{MPV}(p)$. Individual fits to each particle species were chosen, instead a common fit to MPV as a function of $\beta\gamma$. This allows to account better for small deviations with respect to the "Bethe-Bloch", due to possible different biases in the determination of dE/dx and p for different species (Sec. 4.2.2). In general, we have tried to use the simplest function able to describe the data.

The same procedure is repeated on real and Monte Carlo simulated data, thus, two different sets of ITS response function parameters are extracted. In the case of data where the real particle species is unknown we have used a high purity sample of π, K and p of global tracks[‖] identified by the TPC and TOF to tune the ITS response functions. In the MC simulations, the Monte Carlo truth was used to define the particle identity, while the reconstructed momentum was used in the fits. These parameters are an intrinsic feature of the SDD and SSD detectors, therefore they should not change significantly run-by-run, at least if the cluster charge calibration and the readout conditions of SDD and SSD are the same, common also on pp, p–Pb and Pb–Pb, run-by-run.

Response functions in simulated data

The parametrization of the dE/dx (ITS response) is also required in MC simulated samples, to evaluate PID efficiency and contamination needed to correct the raw data.

The dE/dx distributions of π, K and p in narrow momentum intervals, have been obtained from $\sim$ 1.5 M events generated with Pythia6 with the Perugia0 tune. The simulation included a description of the detector conditions of the 2010 run with pp collisions at $\sqrt{s} = 7$ TeV. Each distribution was fitted with a Landau-Gauss function in the dE/dx range between 0.3 and 2 times its mean value. In order to obtain a reasonable fit, some checks on the histograms are performed before fitting. In particular, it was verified that the total number of entries is > 3000, that the maximum value of entries per bin in the histogram is > 80 and that there are not empty bins inside the range defined by one RMS distance from the maximum entry bin.

The results of the fits done for the SDD(SSD) detectors and for two momentum intervals, $0.192 < p < 0.224$ GeV/c and $0.704(1.216) < p < 0.736(1.248)$ GeV/c, are shown in Fig. 4.3 and 4.4(4.5). Let us remark that in the first ($0.192 < p < 0.224$ GeV/c) momentum interval the fits to protons and kaons are not possible because of lack of

[‖] Tracks reconstructed using both ITS and TPC clusters information. Global tracks have a different momentum resolution with respect ITSsa ones (see Sec. 3.4.2).

statistics. Indeed there are few reconstructed protons and kaons at low momentum because, due to their large mass, they have large energy loss in the silicon layers and consequently it may happen that they do not cross all the tracking system. In addition, a kaon/proton at low p will have lower β than a pion with the same p and will therefore suffer more multiple scattering making the reconstruction of its trajectory more difficult. From all fits it can be clearly seen that the Landau-Gauss distribution gives a good description of the dE/dx distributions in the ITS detector obtained in Monte Carlo simulations.

The parameters extracted from each Landau-Gauss fit were plotted as a function of momentum defined as the centre of the corresponding p interval, and afterwards they were fitted with the ad-hoc functions described above (see Fig. 4.6–4.11 for all the particle species).

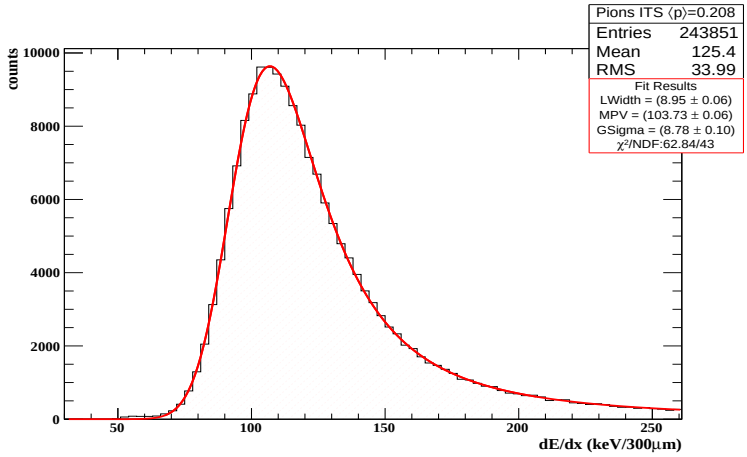

(a) Pions SDD

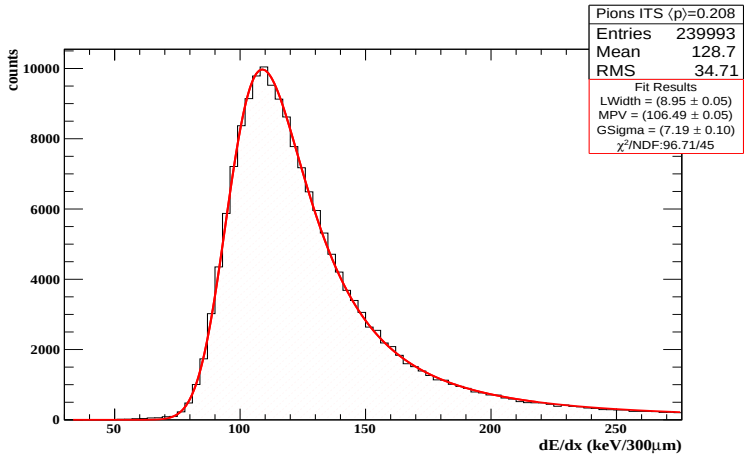

(b) Pions SSD

Figure 4.3: dE/dx distribution in the (a) SDD and (b) SSD detectors from MC simulated sample of pions with momentum $0.192 < p < 0.224$ GeV/c. The Landau-Gauss fit is superimposed (red curve).

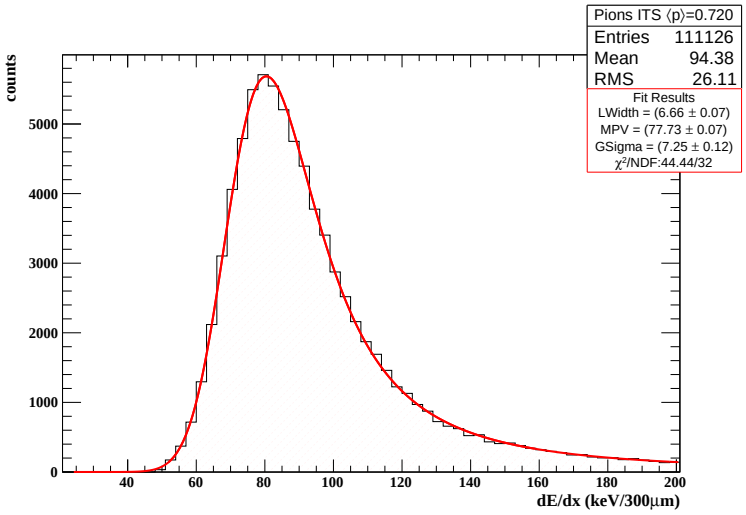

(a) Pions

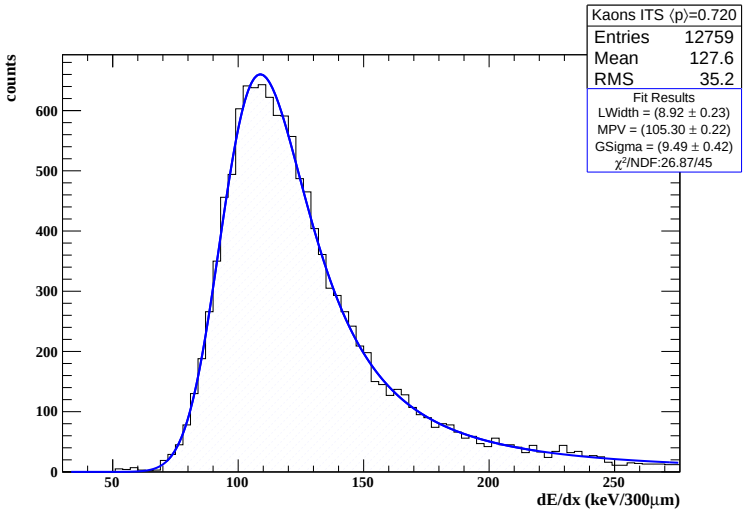

(b) Kaons

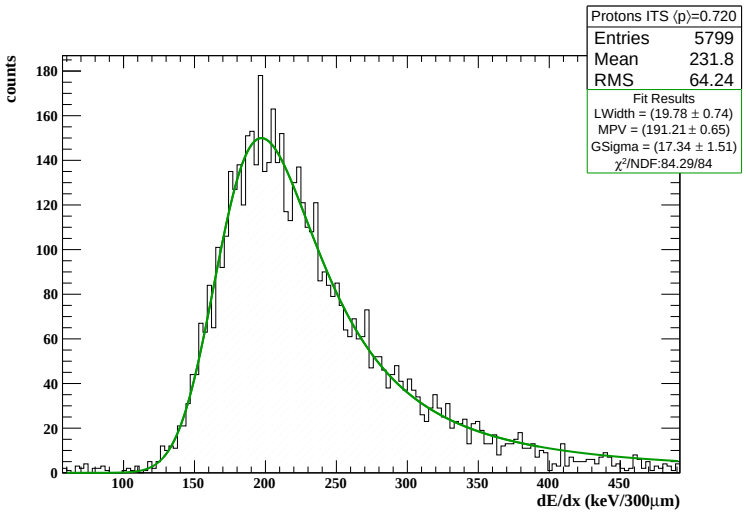

(c) Protons

Figure 4.4: dE/dx distribution in the SDD from MC simulated samples of (a) pions, (b) kaons and (c) protons with momentum $0.704 < p < 0.736$ GeV/c. The Landau-Gauss fit is superimposed.

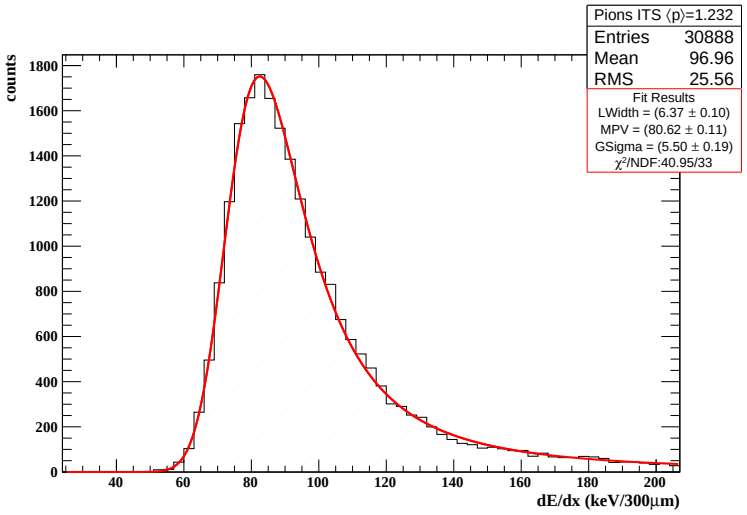

(a) Pions

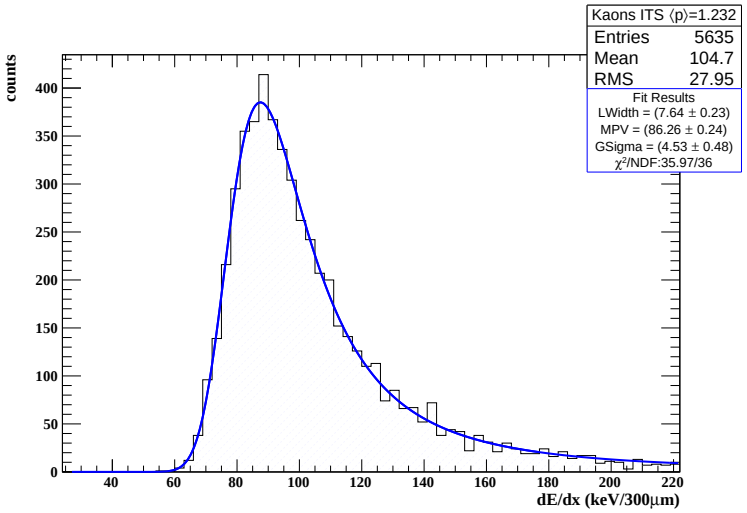

(b) Kaons

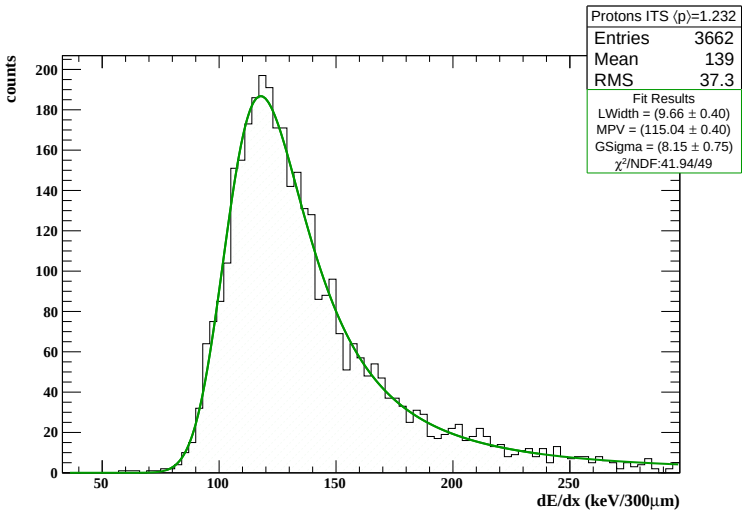

(c) Protons

Figure 4.5: dE/dx distribution in the SSD from MC simulated samples of (a) pions, (b) kaons and (c) protons with momentum $1.216 < p < 1.248$ GeV/c. The Landau-Gauss fit is superimposed.

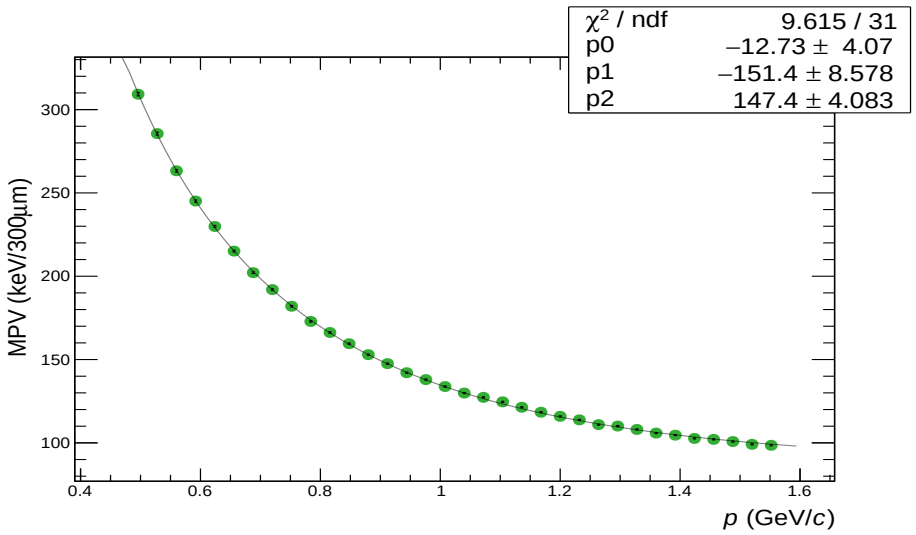

(a) MPV

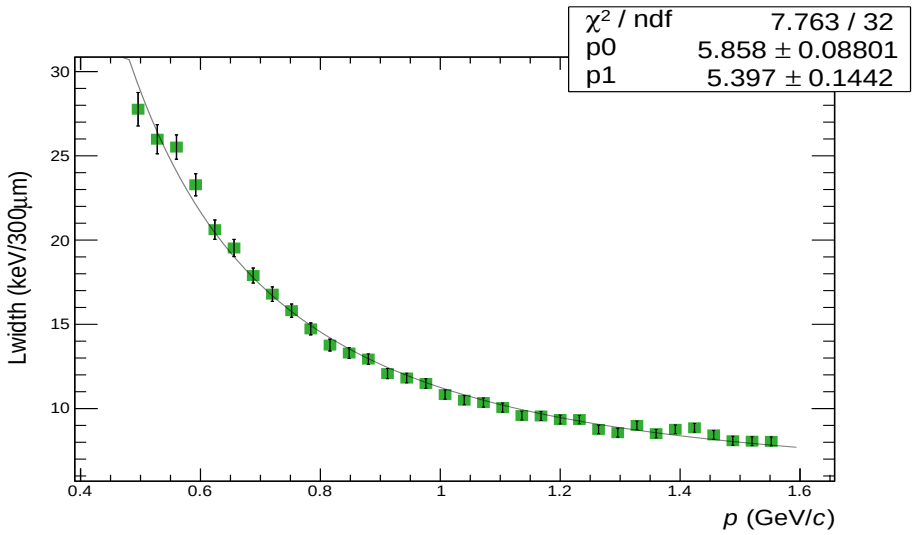

(b) Lwidth

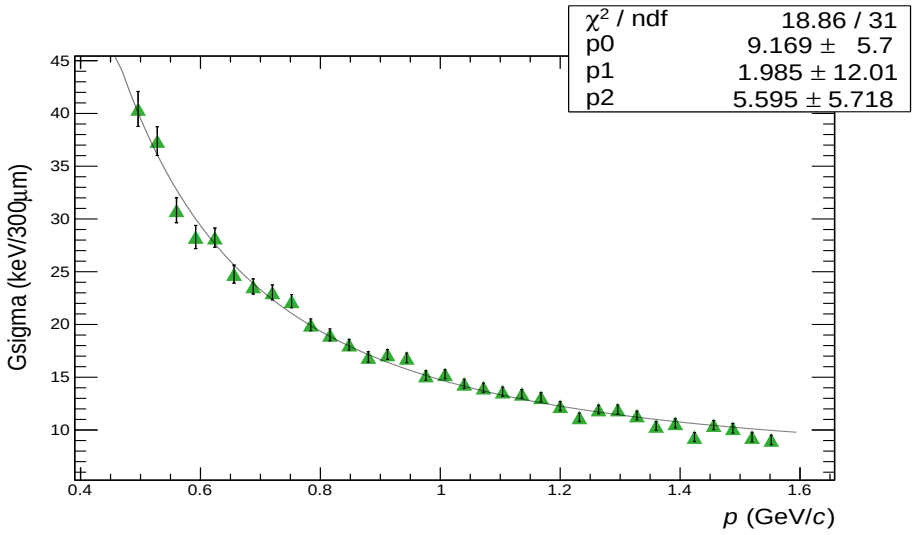

(c) Gsigma

Figure 4.6: Landau-Gauss fit parameters, (a) MPV, (b) Lwidth and (c) Gsigma, for SDD layers as a function of the momentum for protons in MC simulations.

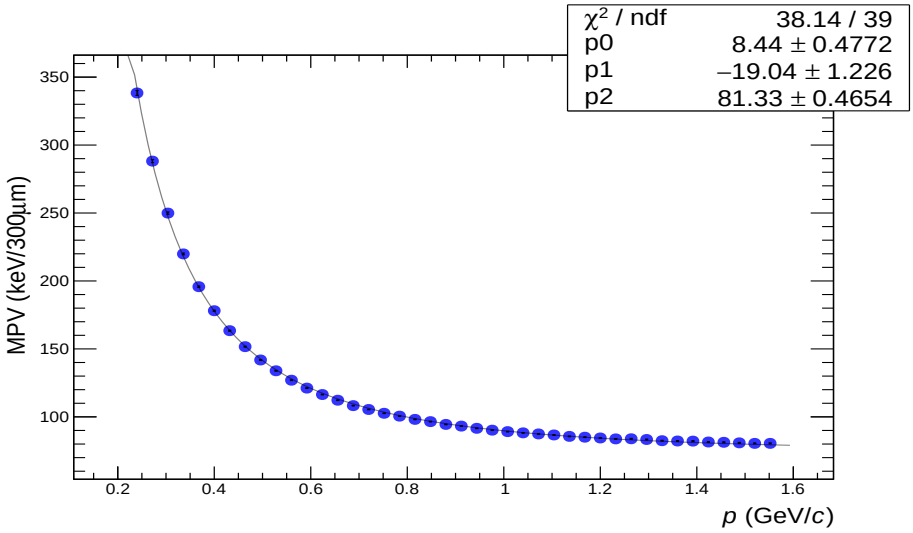

(a) MPV

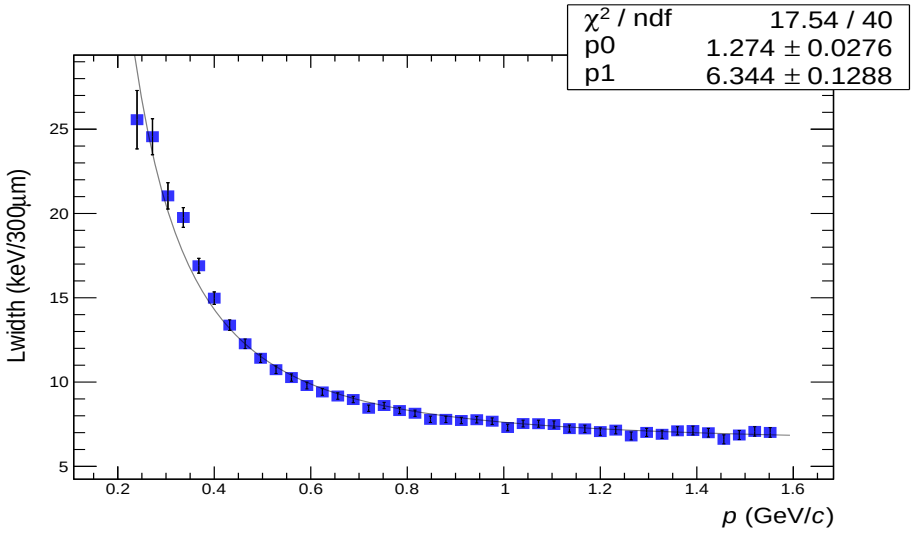

(b) Lwidth

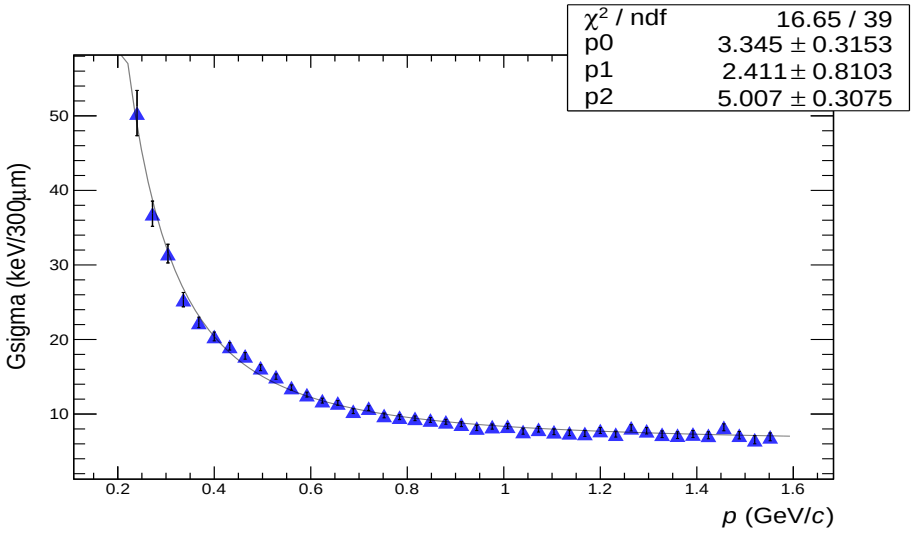

(c) Gsigma

Figure 4.7: Landau-Gauss fit parameters, (a) MPV, (b) Lwidth and (c) Gsigma, for SDD layers as a function of the momentum for kaons in MC simulations.

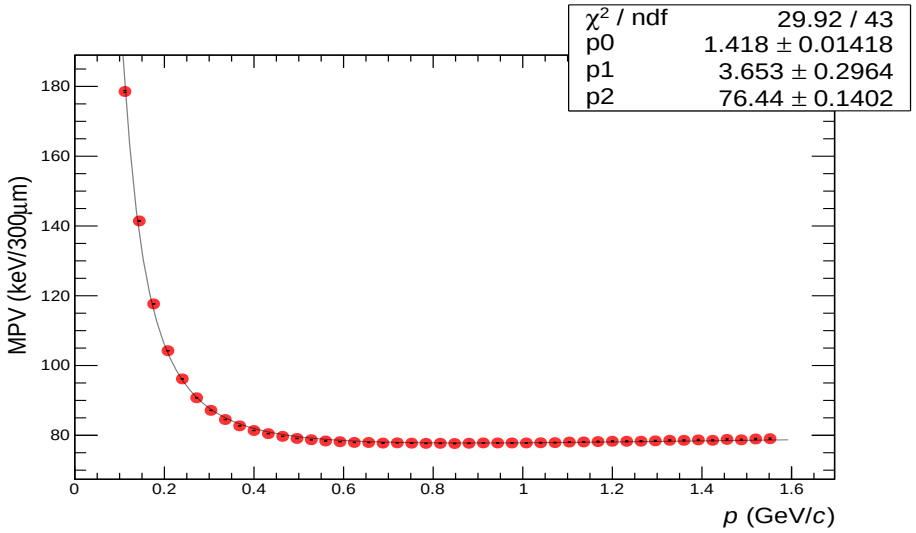

(a) MPV

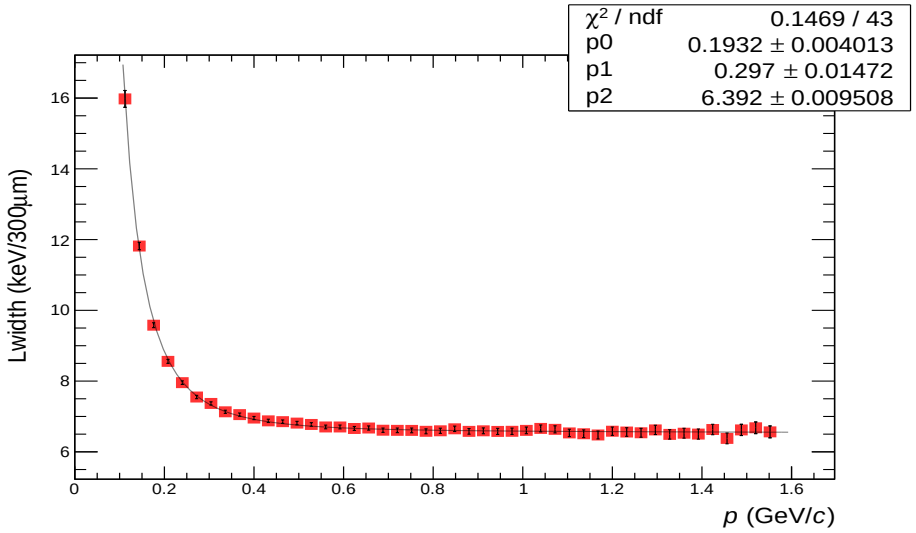

(b) Lwidth

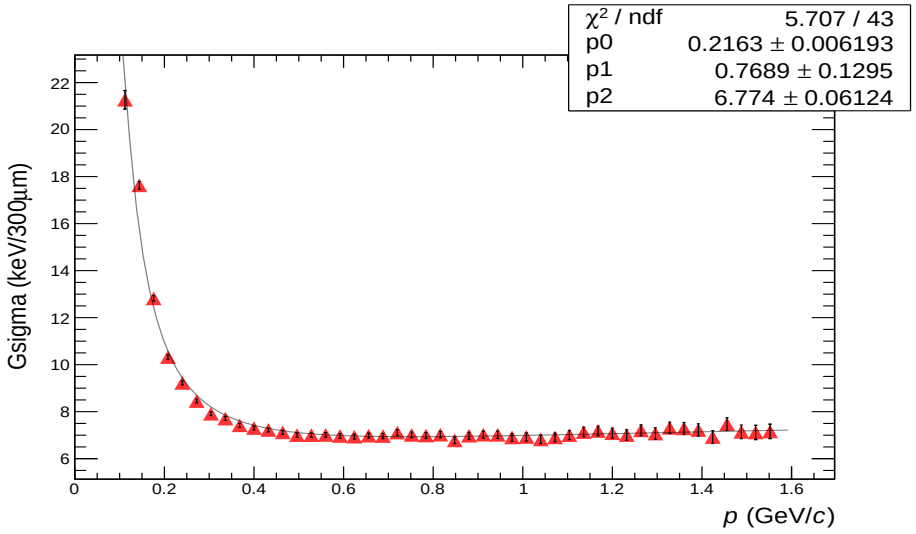

(c) Gsigma

Figure 4.8: Landau-Gauss fit parameters, (a) MPV, (b) Lwidth and (c) Gsigma, for SDD layers as a function of the momentum for pions in MC simulations.

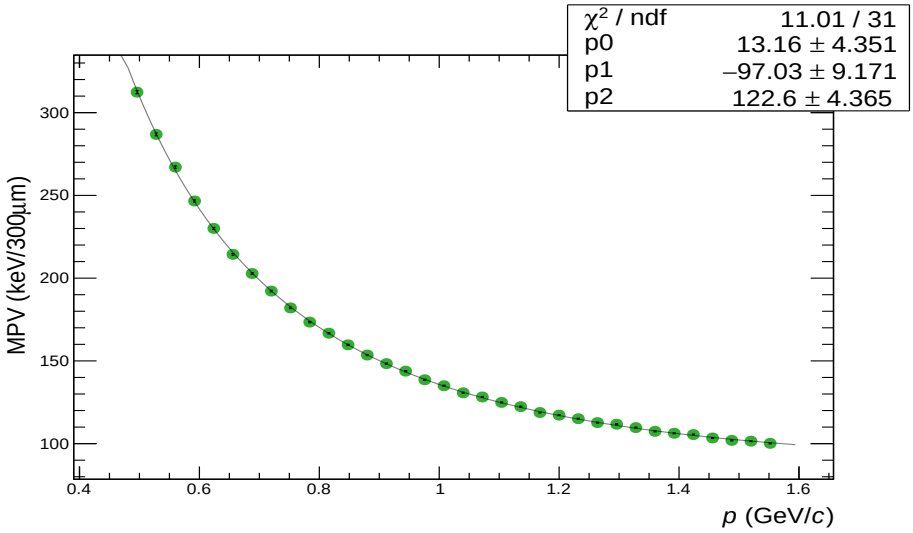

(a) MPV

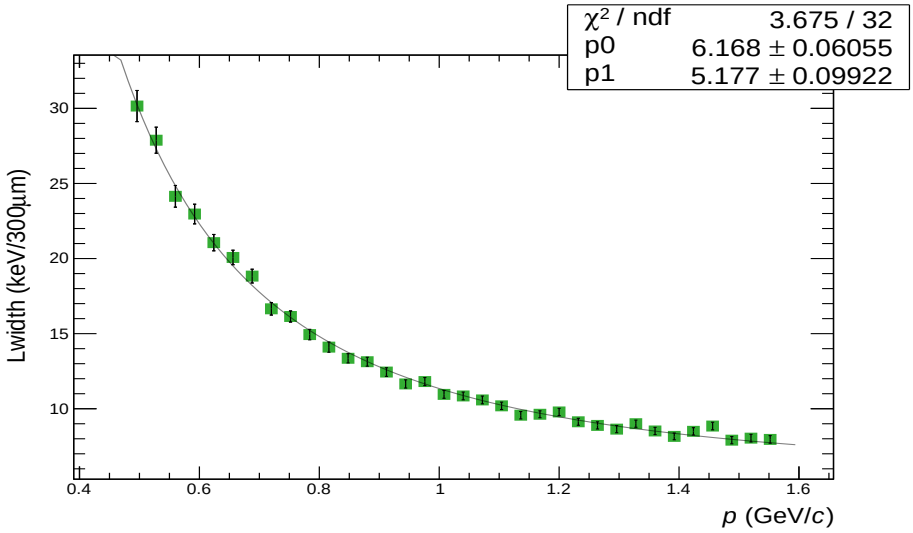

(b) Lwidth

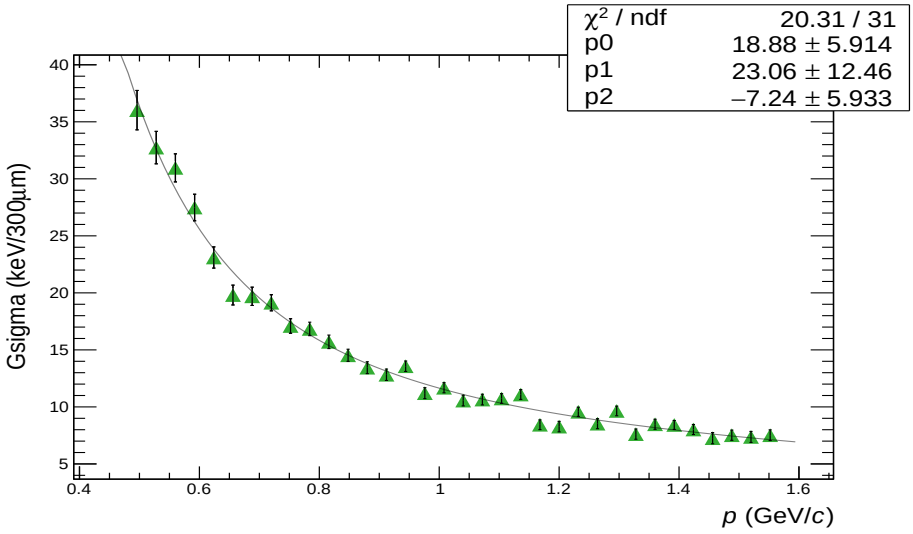

(c) Gsigma

Figure 4.9: Landau-Gauss fit parameters, (a) MPV, (b) Lwidth and (c) Gsigma, for SSD layers as a function of the momentum for protons in MC simulations.

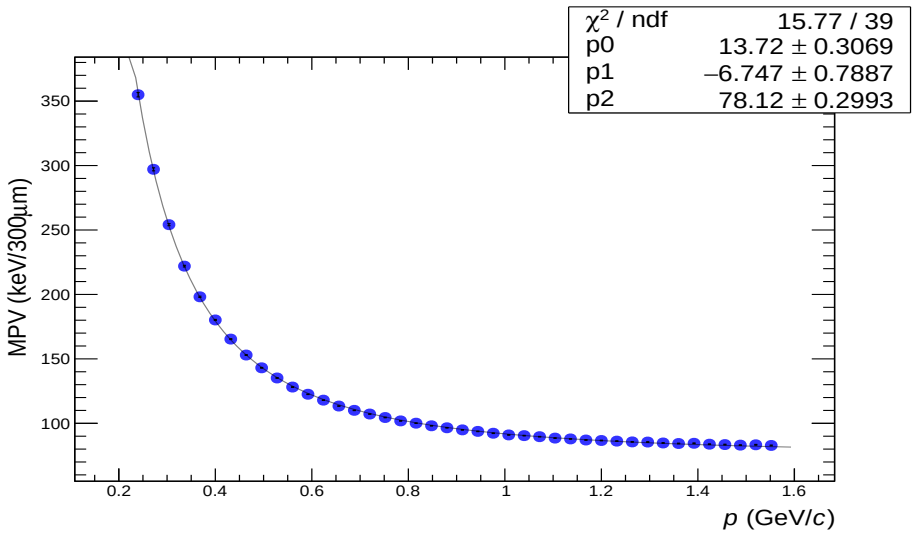

(a) MPV

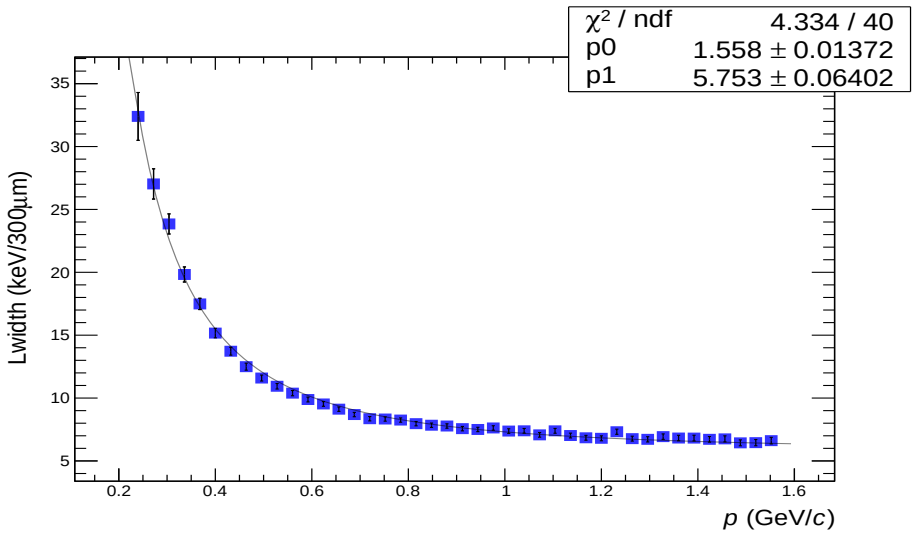

(b) Lwidth

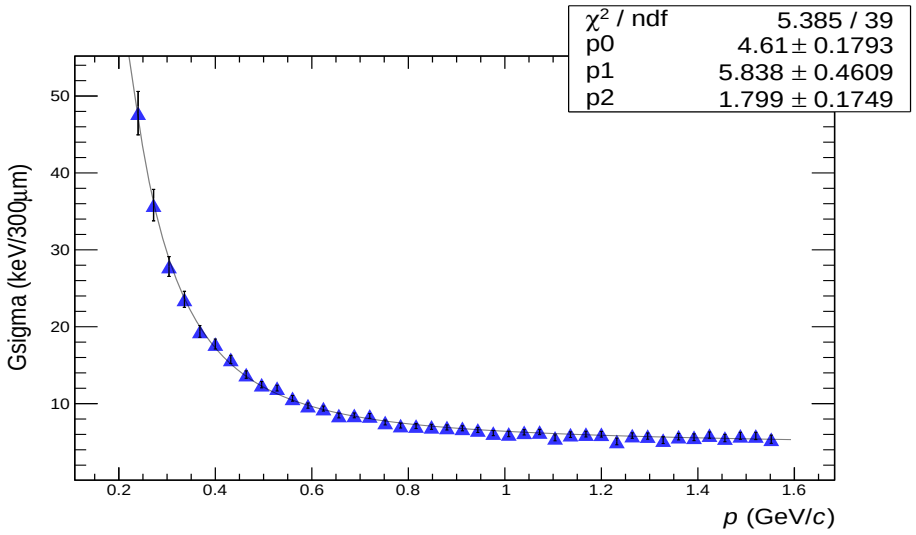

(c) Gsigma

Figure 4.10: Landau-Gauss fit parameters, (a) MPV, (b) Lwidth and (c) Gsigma, for SSD layers as a function of the momentum for kaons in MC simulations.

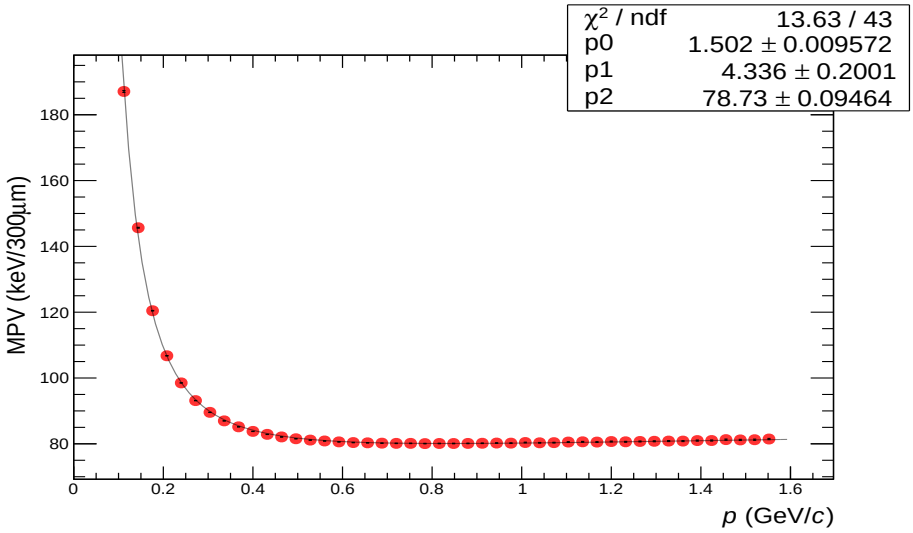

(a) MPV

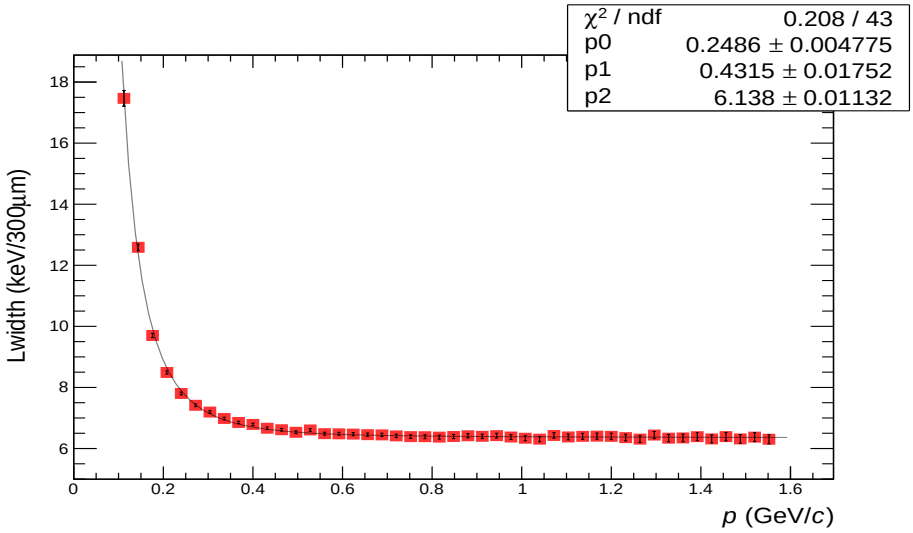

(b) Lwidth

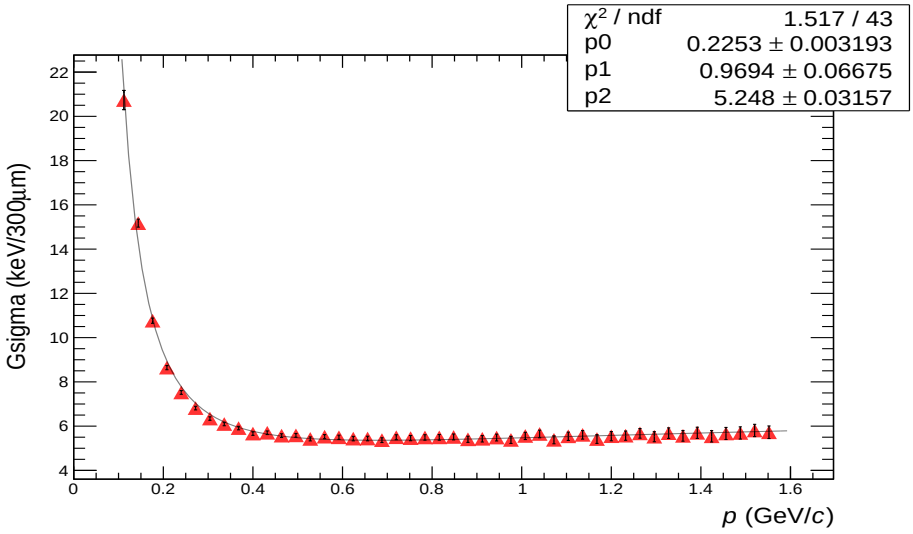

(c) Gsigma

Figure 4.11: Landau-Gauss fit parameters, (a) MPV, (b) Lwidth and (c) Gsigma, for SSD layers as a function of the momentum for pions in MC simulations.

Response functions in real data

For real data the Landau-Gauss parametrization of the ITS response functions has been performed following the same two steps done for simulated data. The difference is that in this case the track particle species is unknown, thus we used the information from other detectors to identify the track. The ITS dE/dx response are expected to be only slightly different for global and ITS stand-alone tracks due to the differences in the momentum resolution. Therefore a common parametrization can be used.

The choice was to use the TPC+TOF nσ technique. In this PID approach the identity of the track is assigned based on the number of sigma (nσ) separation between the measured dE/dx and time of flight and the expected signal for a given particle species with a given momentum. This approach was chosen for various reason:

1. It is a track-by-track PID approach.
2. It gives good PID performance in term of efficiency and purity for π, K and p in the momentum range $0.2 \lesssim p \lesssim 1.5$ GeV/c, since it combines TPC and TOF information (see Fig. 3.4)
3. Higher purity samples can be obtained by tightening the nσ cut.

There are several ways to use (or combine) TPC and TOF information. In order to assign an identity to each track and to create the ITS dE/dx distributions for each momentum bin, we proceed as following:

Tracks with TPC only signal: Tracks with momentum $p \leq 0.6$ GeV/c do not reach the TOF detector, so that time of flight information is missing and PID is based on TPC dE/dx only. For each track, the $\mathrm{n}\sigma_{\mathrm{TPC}}$ for the different particle species (π, K and p) hypothesis is calculated. The track is assigned as species i only if $\mathrm{n}\sigma^{\mathrm{i}}_{\mathrm{TPC}}$ is the lowest value among the three species and if $\mathrm{n}\sigma^{\mathrm{i}}_{\mathrm{TPC}} < \mathrm{n}\sigma_{\mathrm{cut}} = 1$, otherwise the track is not used.

Tracks with TPC and TOF signals: In case both TPC and TOF signals are available, a selection on the $\mathrm{n}\sigma^{\mathrm{i}}$ values from both detectors is applied. That means, $\mathrm{n}\sigma^{\mathrm{i}}_{\mathrm{TPC}}$ and $\mathrm{n}\sigma^{\mathrm{i}}_{\mathrm{TOF}}$ are required to be both the lowest among the TPC and TOF nσ of π, K and p and both values are required to be below $\mathrm{n}\sigma_{\mathrm{cut}}$.

Even with a tight $\mathrm{n}\sigma_{\mathrm{cut}} = 1$, a remaining contamination by other species has been observed (Fig. 4.12 and 4.13). For example in the momentum region where the electron dE/dx band in the TPC crosses that of kaons.

Therefore, the Landau-Gauss fit ranges were reduced with respect to those used for the parametrization of the simulated data and the momentum intervals where high contamination is observed, mainly in kaon and proton samples due to electron and pion contributions (see, Fig. 3.4), were discarded.

The π, K and p data samples used to tune the ITS PID response have been obtained from ~ 3 M events collected in 2010 with pp collisions at $\sqrt{s} = 7$ TeV and triggered with a minimum bias selection criterion (minimum bias trigger, see Sec. 3.3.1). Some examples of Landau-Gauss fits to each species for SDD(SSD) detectors and the $0.480(0.992) < p < 0.512(1.024)$ GeV/c momentum intervals are reported in Fig. 4.12(4.13). The contribution from contamination by other species (left bump) is clearly seen in kaon and proton histograms for the momentum intervals $0.480 < p < 0.512$ GeV/c and $0.992 < p < 1.024$ GeV/c respectively. In addition, the behaviour of the Landau-Gauss parameters of π, K and p are shown as a function of track momentum in Fig. 4.14–4.19.

The ITS response parameters obtained from real and simulated data are reported in Tab. 4.1.

			Simulated data			**Real data**		
			A	B	C	A	B	C
SDD	Proton	MPV	-12.73	-151.4	147.4	-2.753	-136.5	133.5
		Lwidth	5.858	5.397	–	5.393	4.793	–
		Gsigma	9.169	1.985	5.595	21.08	30.0	-4.265
	Kaon	MPV	8.44	-19.04	81.33	13.35	-8.146	74.82
		Lwidth	1.274	6.344	–	1.247	5.966	–
		Gsigma	3.345	2.411	5.007	4.649	6.21	5.832
	Pion	MPV	1.418	3.653	76.44	1.348	5.457	80.29
		Lwidth	0.1932	0.297	6.392	0.1526	0.2125	6.456
		Gsigma	0.2163	0.7689	6.774	0.2112	1.07	8.882
SSD	Proton	MPV	13.16	-97.03	122.6	9.856	-108.9	122.5
		Lwidth	6.188	5.177	–	5.61	4.315	–
		Gsigma	18.88	23.06	-7.24	37.12	65.45	-23.83
	Kaon	MPV	13.72	-6.747	78.12	18.71	4.229	71.27
		Lwidth	1.558	5.753	–	1.421	5.547	–
		Gsigma	4.61	5.838	1.799	6.208	10.35	1.885
	Pion	MPV	1.502	4.336	78.73	1.435	5.768	81.76
		Lwidth	0.2486	0.4315	6.138	0.2191	0.385	6.207
		Gsigma	0.2253	0.9694	5.248	0.1941	0.9167	6.712

Table 4.1: ITS response function parameters for π, K and p in MC simulations and real data. The Landau-Gauss parameters (MPV, Lwidth and Gsigma) are related to the parameters A, B and C through Eq. 4.6–4.8 as described in Sec. 4.2.2.

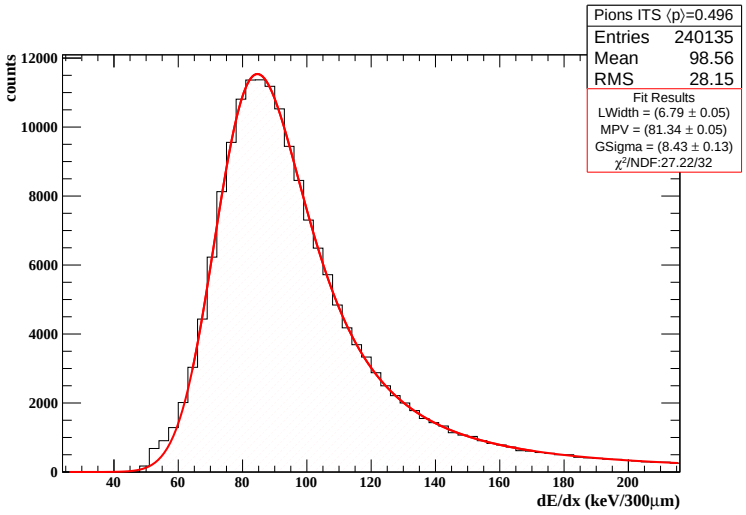

(a) Pions

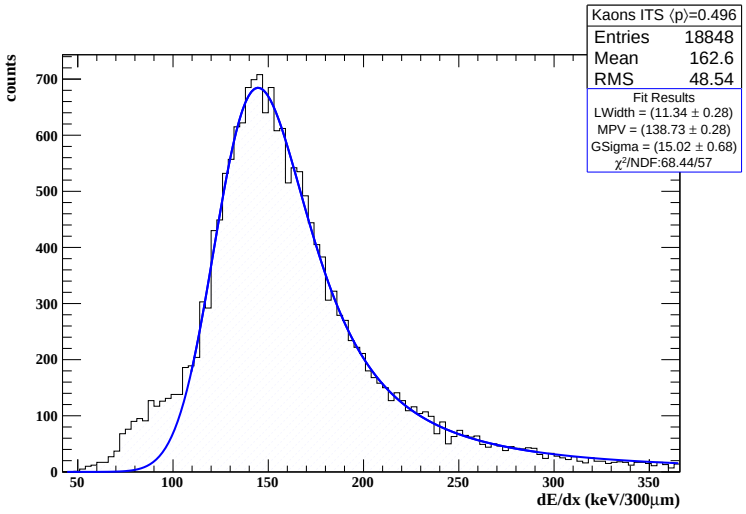

(b) Kaons

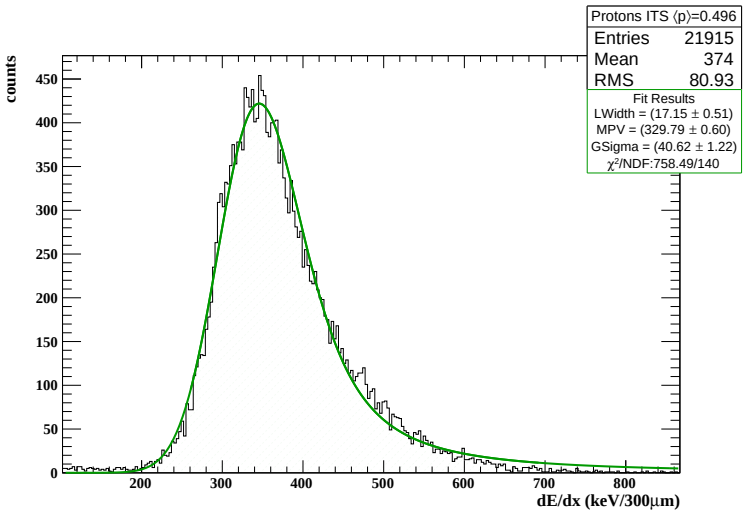

(c) Protons

Figure 4.12: dE/dx distributions in the SDD for (a) pions, (b) kaons and (c) protons with momentum $0.480 < p < 0.512$ GeV/c in pp collisions at $\sqrt{s} = 7$ TeV. The Landau-Gauss fit is superimposed. A bump in the left side of the kaon distribution due to contamination from other species is clearly visible.

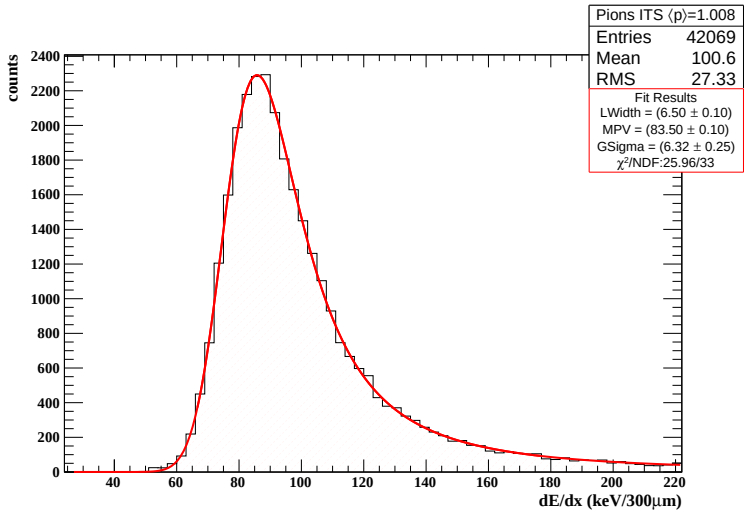

(a) Pions

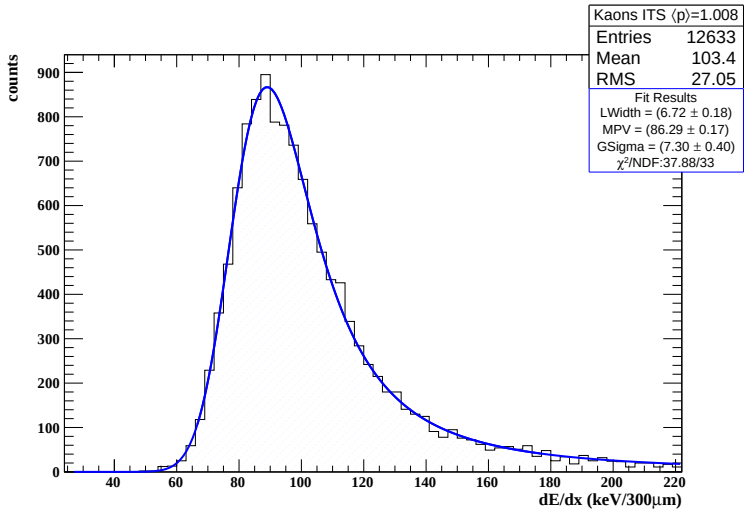

(b) Kaons

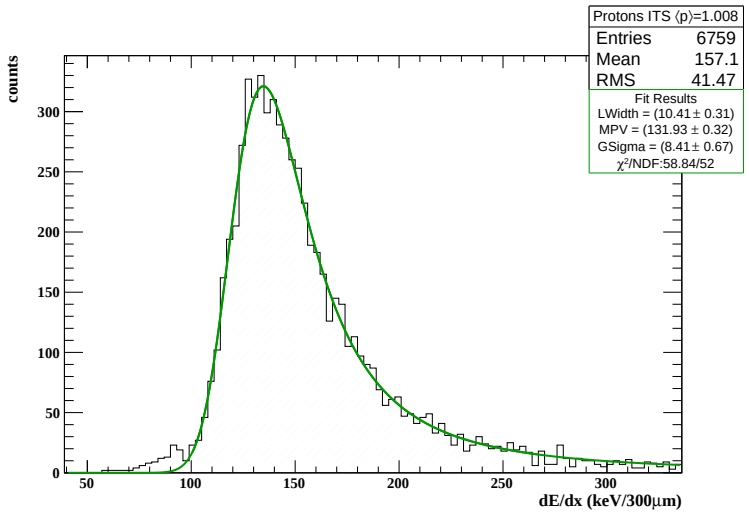

(c) Protons

Figure 4.13: dE/dx distributions in the SSD for (a) pions, (b) kaons and (c) protons with momentum $0.992 < p < 1.024$ GeV/c in pp collisions at $\sqrt{s} = 7$ TeV. The Landau-Gauss fit is superimposed. A bump in the left side of the proton distribution due to contamination from other species is visible.

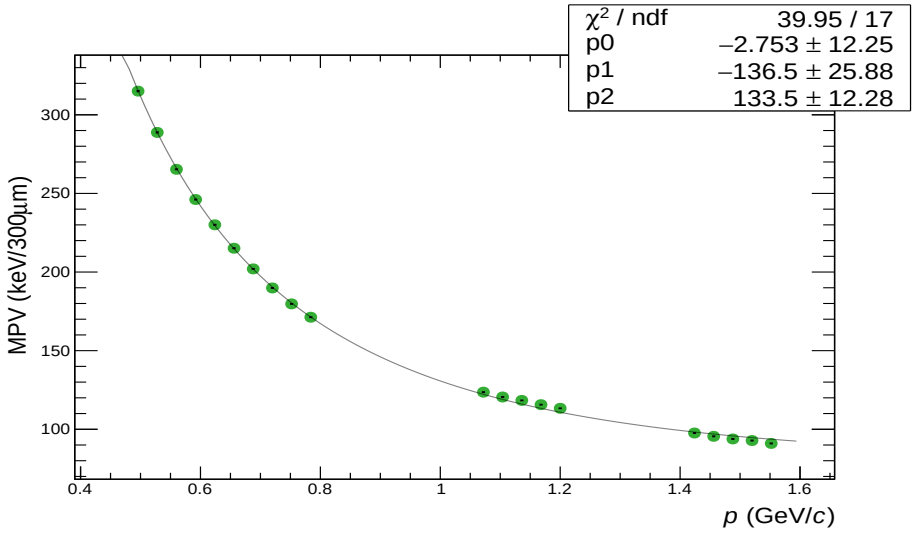

(a) MPV

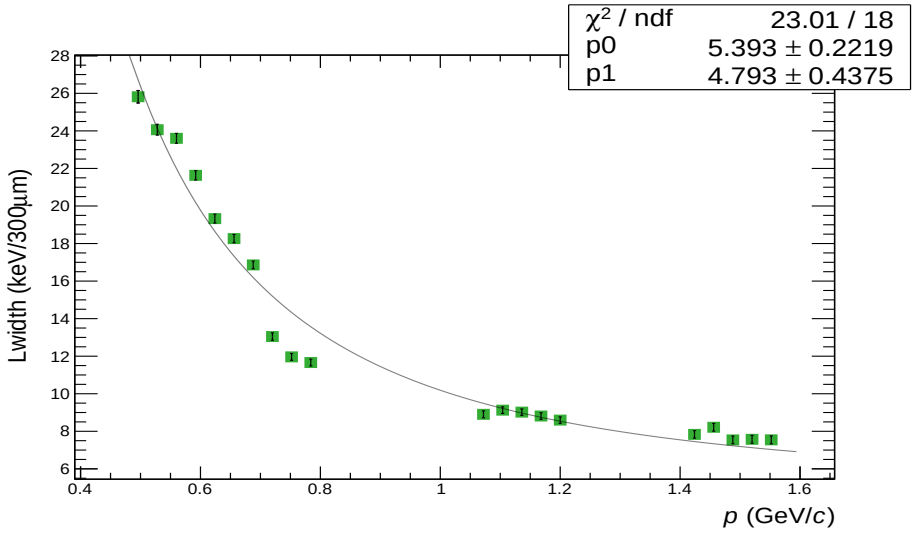

(b) Lwidth

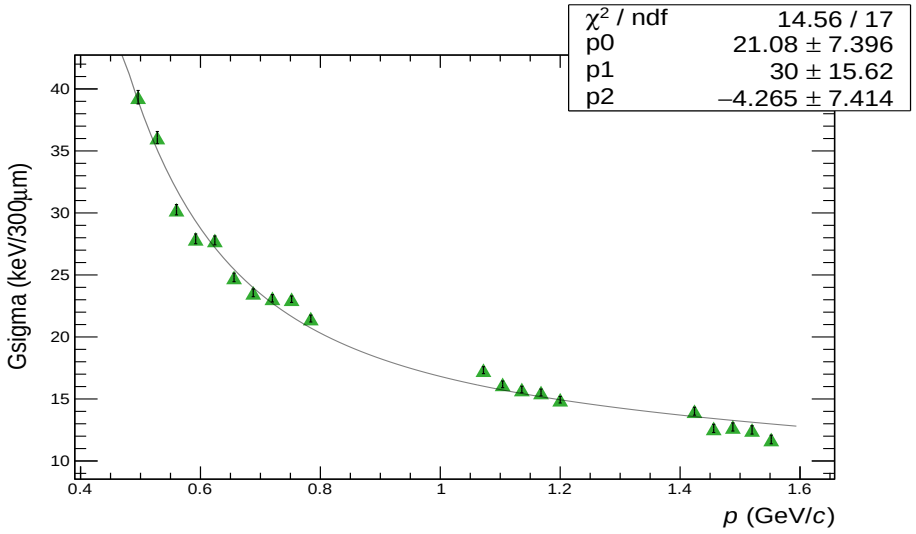

(c) Gsigma

Figure 4.14: Landau-Gauss fit function parameters, (a) MPV, (b) Lwidth and (c) Gsigma, as a function of the momentum for protons in the SDD detector for pp collisions at $\sqrt{s} = 7$ TeV.

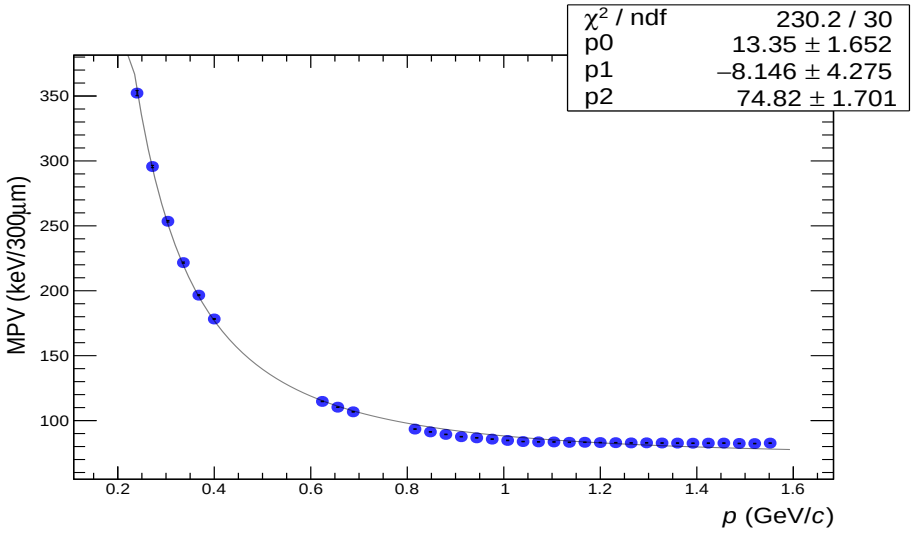

(a) MPV

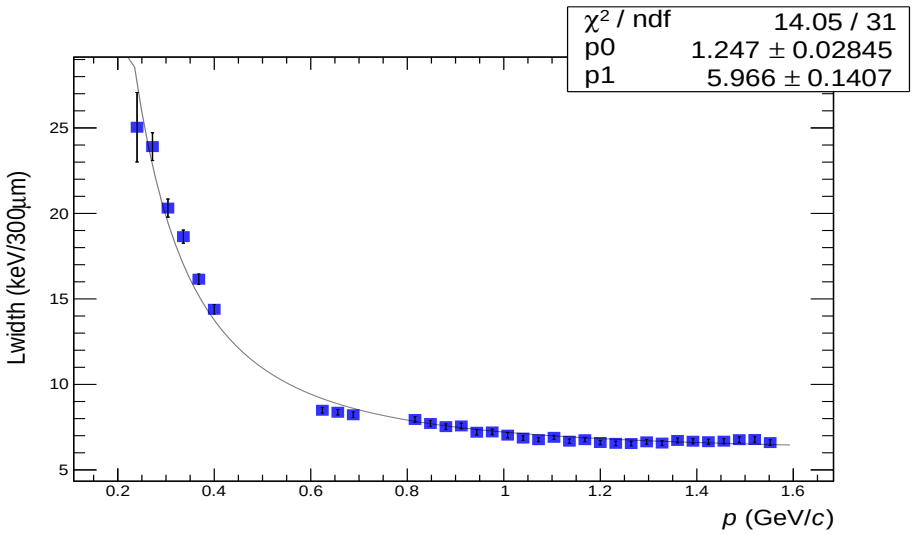

(b) Lwidth

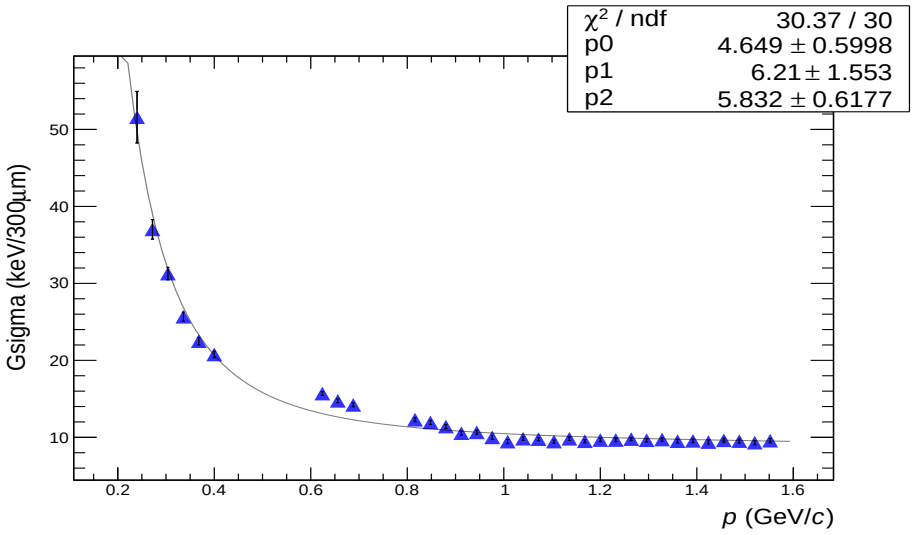

(c) Gsigma

Figure 4.15: Landau-Gauss fit function parameters, (a) MPV, (b) Lwidth and (c) Gsigma, as a function of the momentum for kaons in the SDD detector for pp collisions at $\sqrt{s} = 7$ TeV.

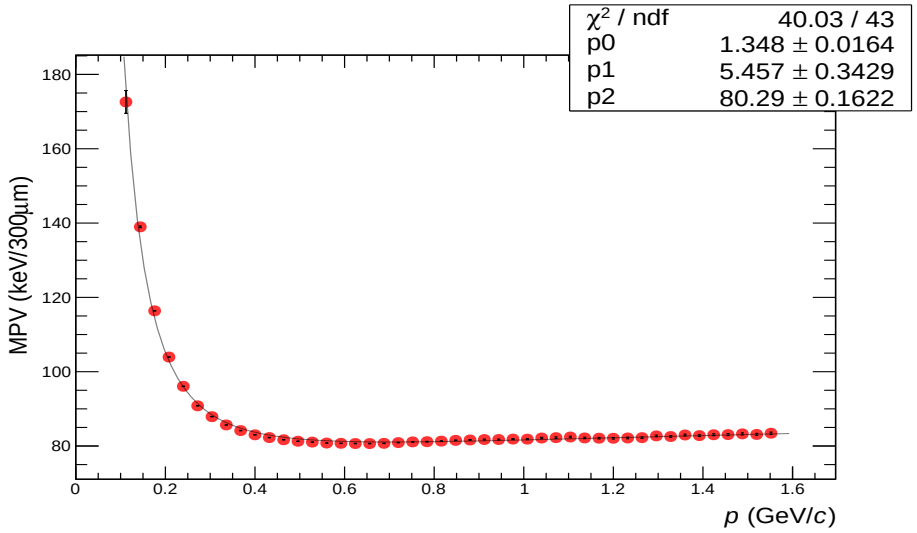

(a) MPV

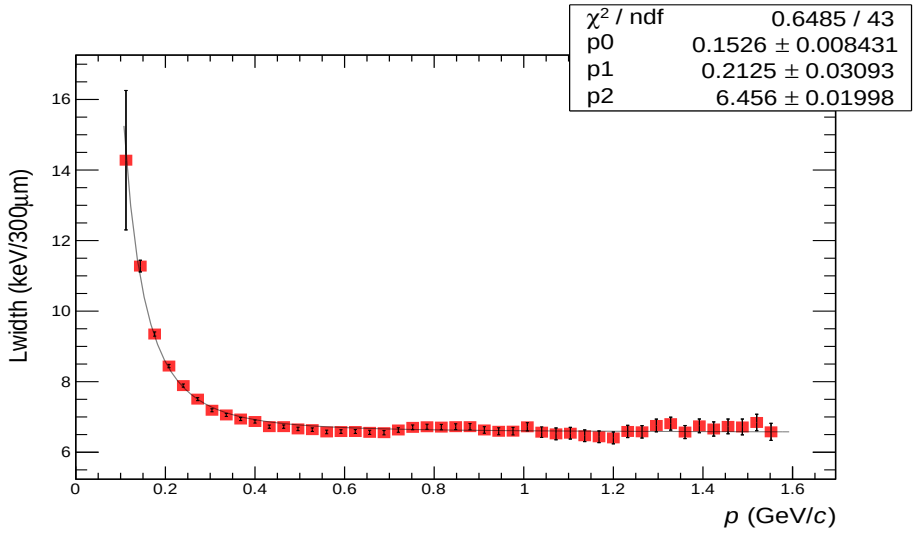

(b) Lwidth

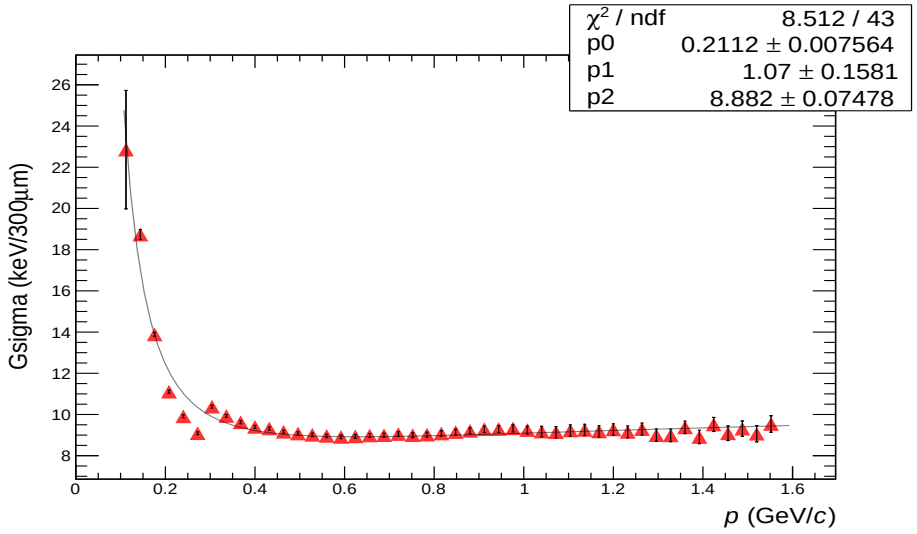

(c) Gsigma

Figure 4.16: Landau-Gauss fit function parameters, (a) MPV, (b) Lwidth and (c) Gsigma, as a function of the momentum for pions in the SDD detector for pp collisions at $\sqrt{s} = 7$ TeV.

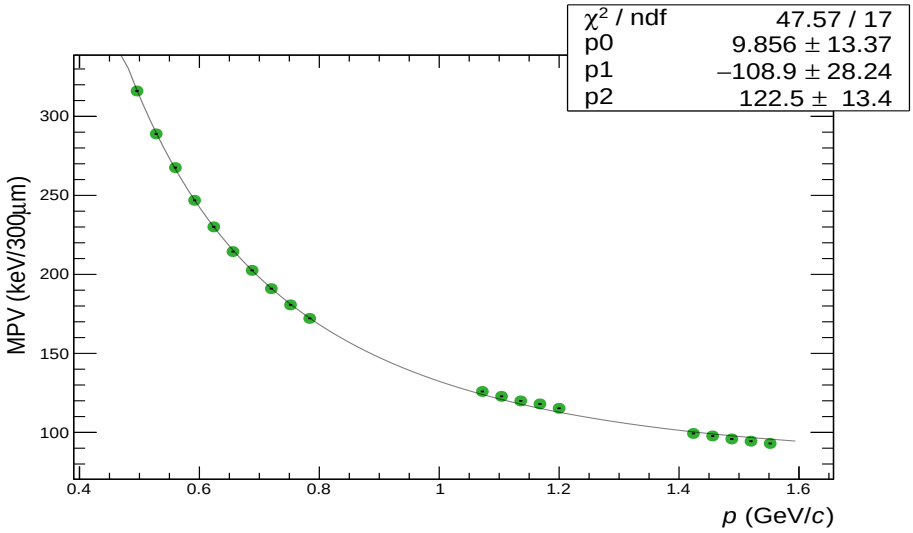

(a) MPV

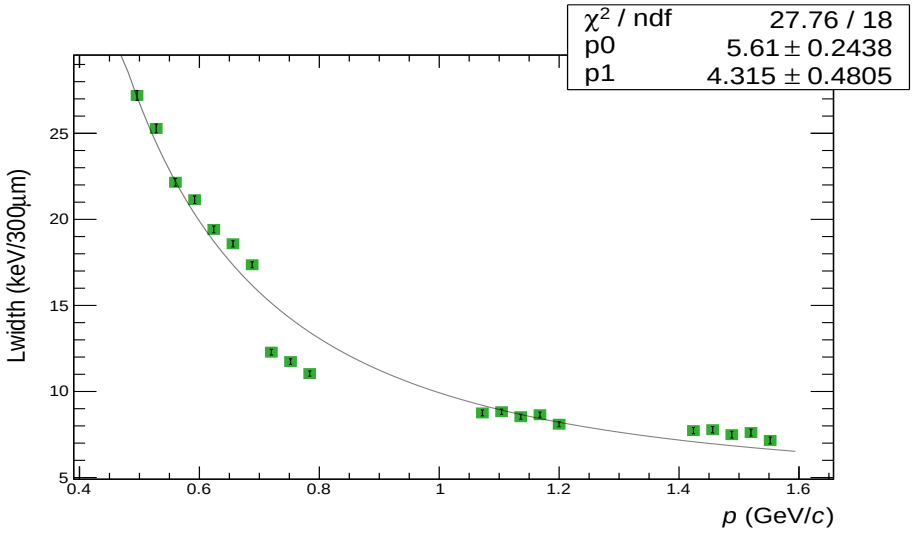

(b) Lwidth

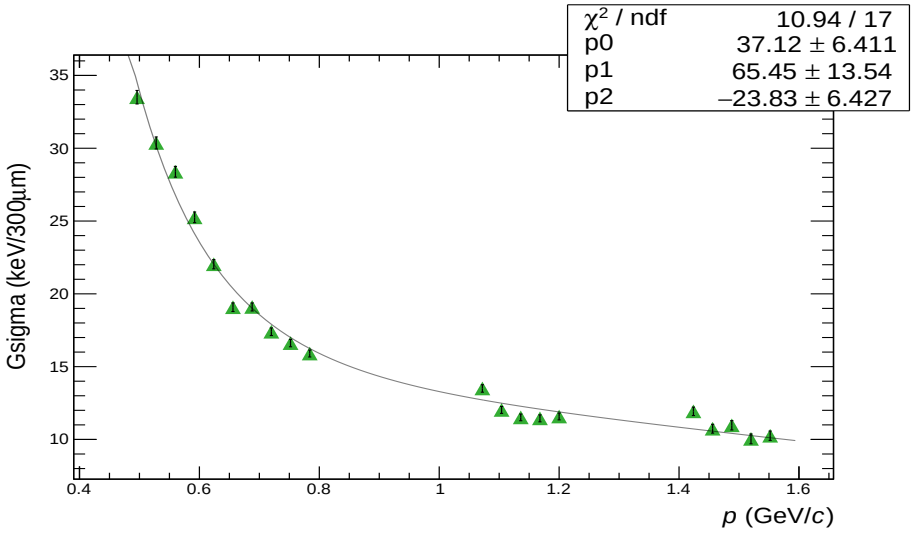

(c) Gsigma

Figure 4.17: Landau-Gauss fit function parameters, (a) MPV, (b) Lwidth and (c) Gsigma, as a function of the momentum for protons in the SSD detector for pp collisions at $\sqrt{s} = 7$ TeV.

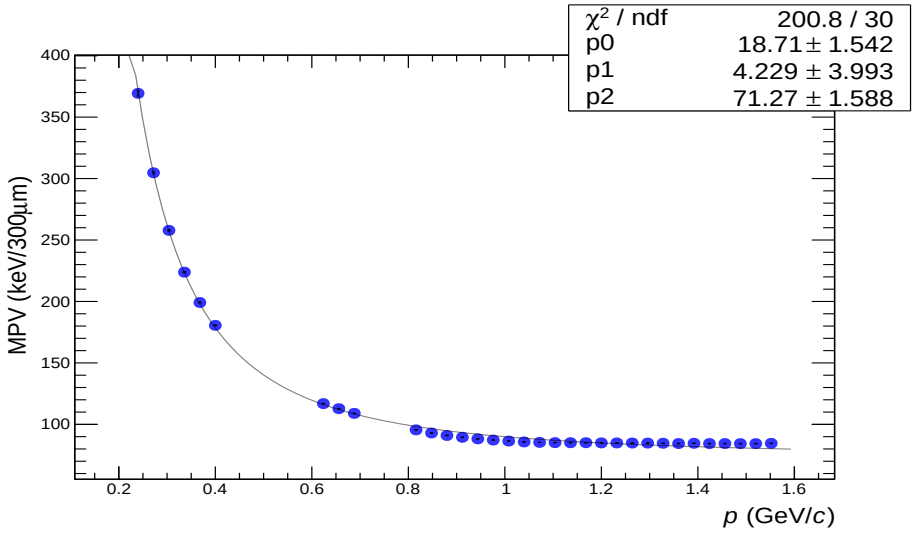

(a) MPV

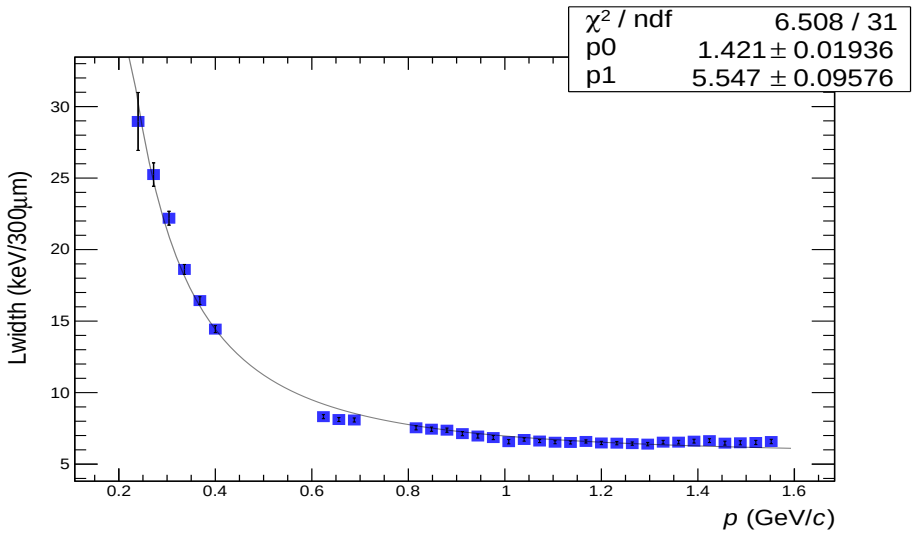

(b) Lwidth

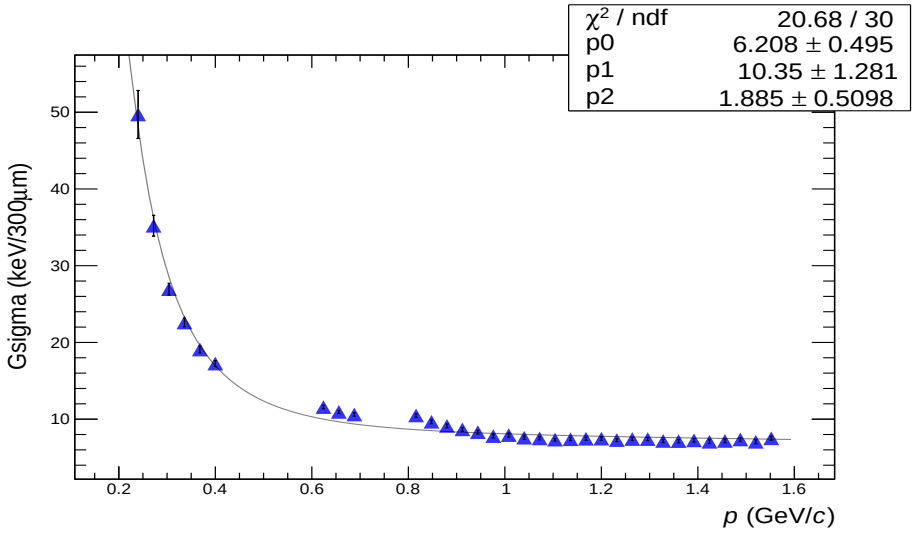

(c) Gsigma

Figure 4.18: Landau-Gauss fit function parameters, (a) MPV, (b) Lwidth and (c) Gsigma, as a function of the momentum for kaons in the SSD detector for pp collisions at $\sqrt{s} = 7$ TeV.

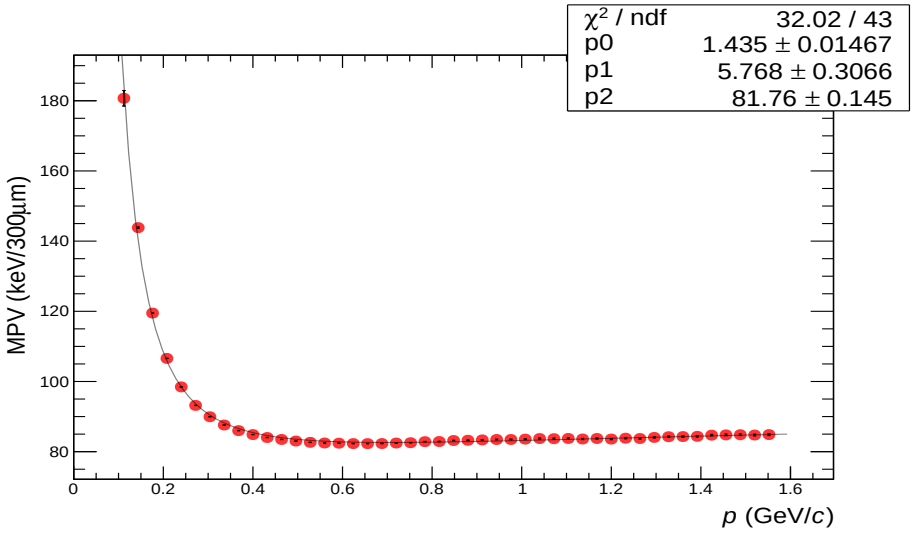

(a) MPV

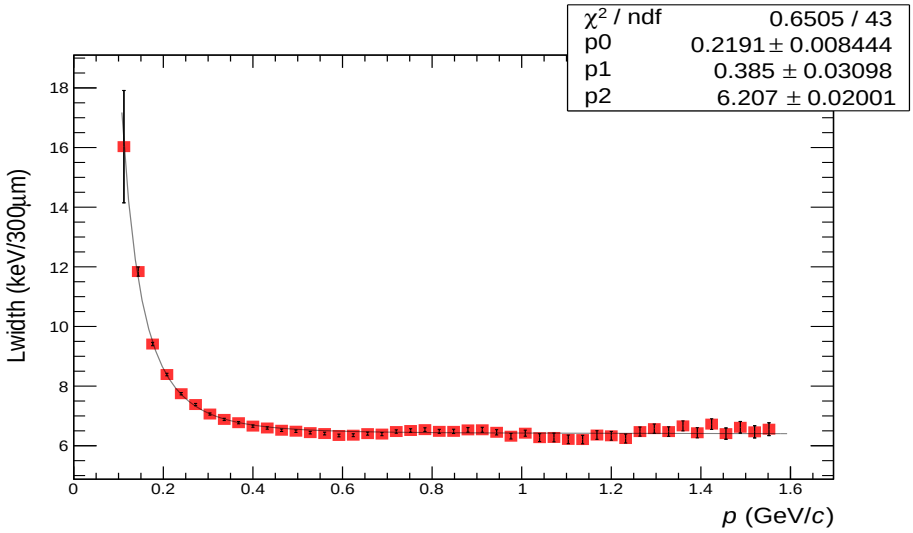

(b) Lwidth

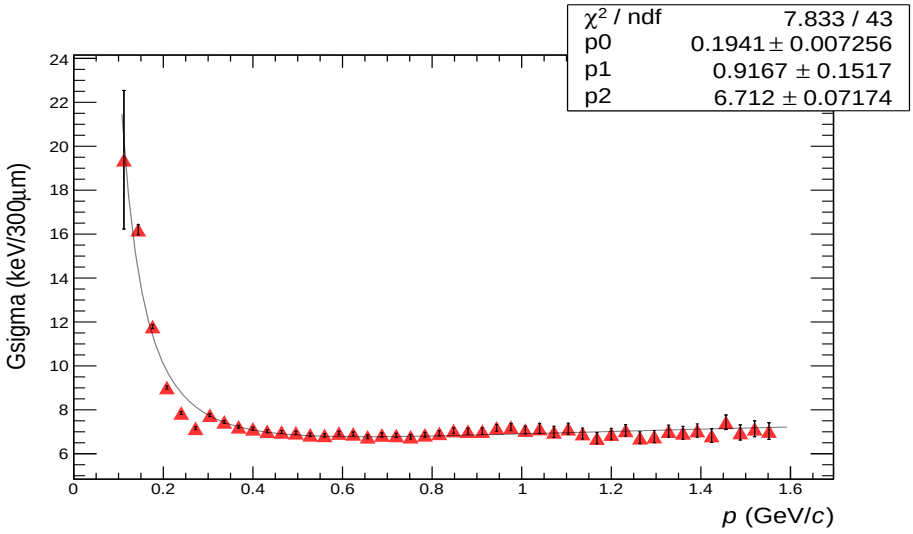

(c) Gsigma

Figure 4.19: Landau-Gauss fit function parameters, (a) MPV, (b) Lwidth and (c) Gsigma, as a function of the momentum for pions in the SSD detector for pp collisions at $\sqrt{s} = 7$ TeV

The MPV values obtained from the Landau-Gauss fits in the SSD detector, for simulated (a,b) and real (c,d) data of π, K and p, are reported in Fig 4.20 as a function of $\beta\gamma$ (a,c) and as a function of momentum (b,d). In addition, as a further check, the MPV values as a function of $\beta\gamma$ have been fitted with the same PHOBOS [135] parametrization of the Bethe-Bloch function, common for all three species, as done in the truncated mean approach. Furthermore, the species-dependent MPV parametrization fit results, with $f_{Lwidth}(p)$ from Eq. 4.6, for each particle species separately, are superimposed in panels (b,d).

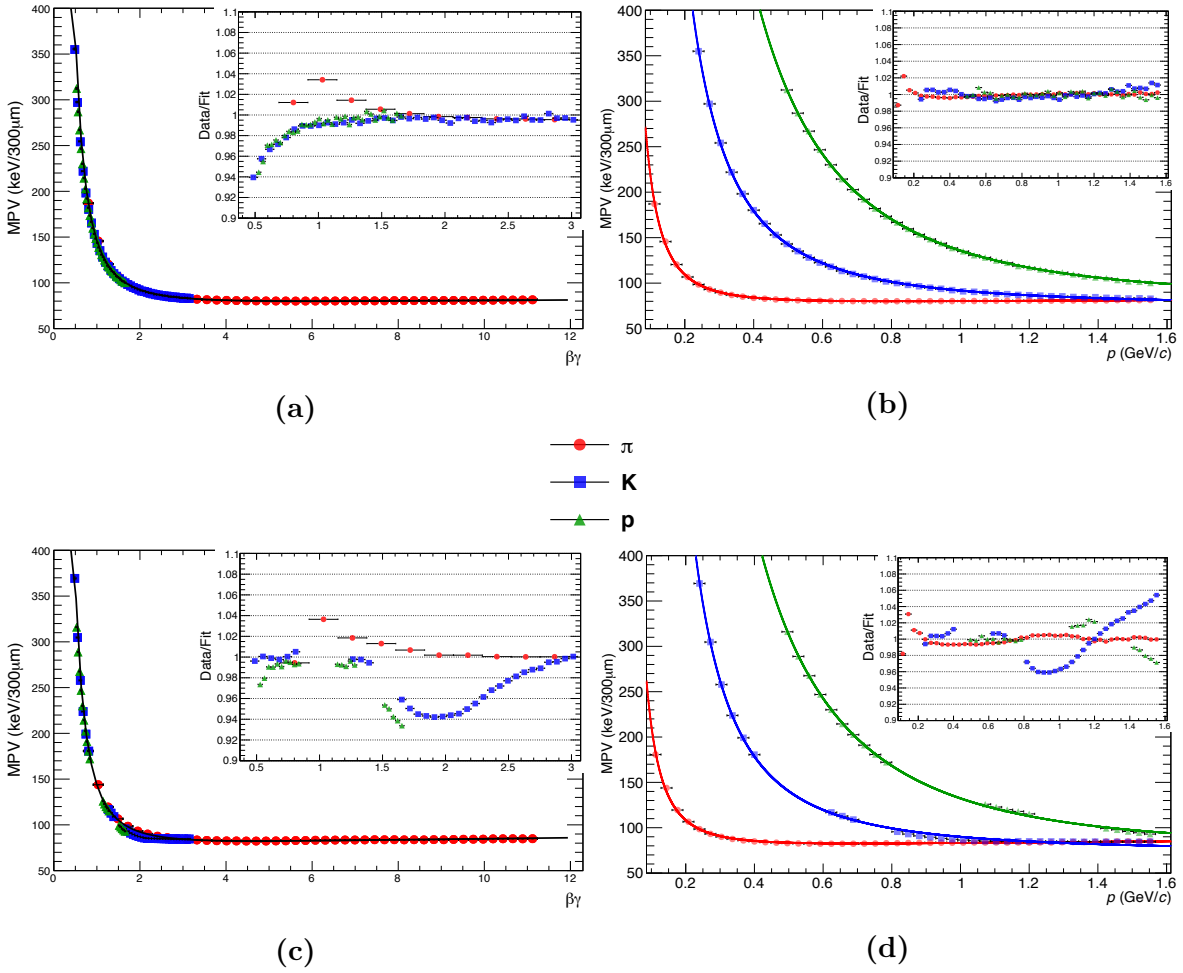

Figure 4.20: Landau-Gauss fit function MPV parameters in the SSD, for (a, b) simulated and (c, d) real samples of π, K and p, as a function of (a, c) $\beta\gamma$ and (b, d) p. The individual MPV parametrization fit, for each particle species, are superimposed (b, d). The MPV parameters as a function of $\beta\gamma$ (a,c) are fitted with a PHOBOS parametrization of the Bethe-Bloch function common to all species.

The MPV values of the Landau-Gauss fit functions as a function of $\beta\gamma$, for simulated and real sample of π, K and p, tend to lie on the same "Bethe-Bloch" curve (Fig 4.20).

However, small deviations ($\approx 5\%$) with respect to the common fit, using the PHOBOS Bethe-Bloch function, are observed as it can be seen in the insets of panels (a) (c) showing the ratio data/fit. This is due to momentum and dE/dx resolution bias at low $\beta\gamma$ ($\beta\gamma < 0.7$) for both real and simulated data. In the case of real data, a deviation from fit is observed also at high $\beta\gamma$ ($1 \lesssim \beta\gamma \lesssim 2$) for kaon and proton samples, and it is due to contamination from electron and pion misidentification. For this reason we have performed the MPV parametrization independently for each hadron species (Fig 4.20 right panels). It can be stressed that the effect of contamination in the kaon MPV values ($\approx 4\%$ data/fit discrepancy for $p > 0.8$) remains, even when the MPV parameters are fitted for each species separately.

Even though, in the ITS stand-alone PID analysis the real and simulated data are managed using two different parametrizations, a comparison between them gives an estimation on how well the MC simulation reproduces the real ITS PID response. The parametrization of the kaon response obtained for the SDD layers from simulated and real data samples are compared in Fig. 4.21.

The MPV and the Landau width parameters, from real and simulated samples, differ only by few percent with a maximum value of 6% for low and high momenta, respectively. The Gaussian widths in simulated samples differ by more than 10% (up to 30%), for $p > 0.6$ GeV/c, with respect to those in real data. The difference in the Gaussian width parameters could be due to the simulation of the electronic readout features, e.g. the electronic noise. In addition, the Gaussian and Landau widths are somehow correlated in the fit, therefore, in the parametrization of real data we get larger Gaussian width and narrower Landau width, with respect to the ones in simulated samples. As long as these parameters provide a good description of the distribution more reliable the PID probabilities are. A similar behaviour in the comparison of the Landau-Gauss parameters between real and simulated data is observed for the other particle species as well as for the SSD parametrization.

Electron parametrization

An ITS response parametrization for electrons is needed for the analysis of π, K and p spectra in order to reduce the contamination to pions a very low p_{T}. In addition, the possibility of separating electrons from pions at low p_{T} with the ITS could be useful for other analyses, for example to help to reduce the background to the low-mass di-electrons. The parametrization of electron dE/dx was obtained from the MC simulated sample using the same procedure described above, i.e using the Monte Carlo truth to select reconstructed ITS stand-alone electron tracks.

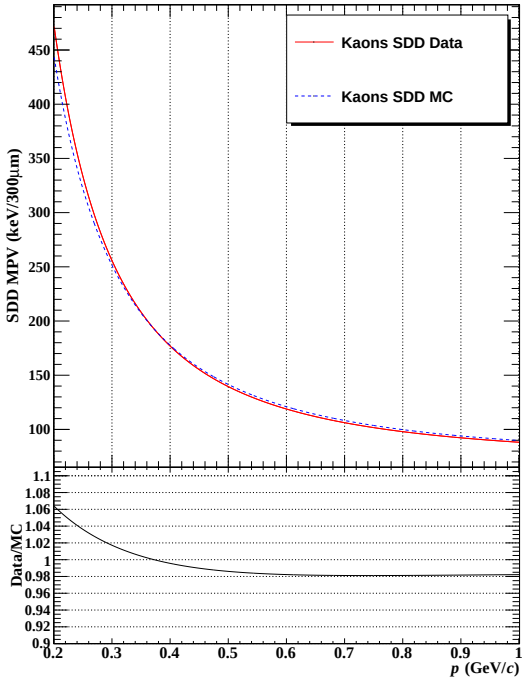

(a) MPV

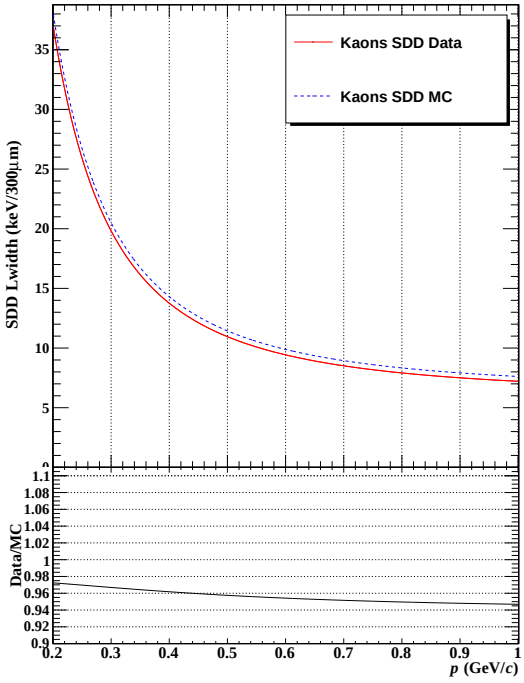

(b) Lwidth

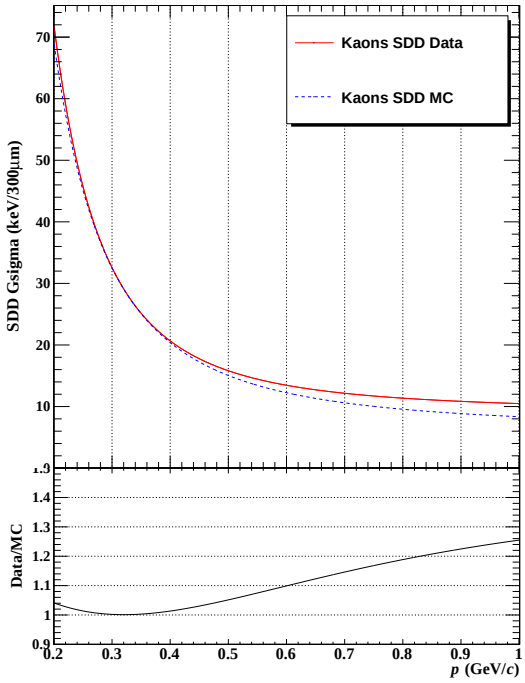

(c) Gsigma

Figure 4.21: Comparison of SDD response parameters, (a) MPV, (b) Landau width and (c) Gaussian sigma, for kaons in real and simulated data.

In the case of real data, since the isolation of a high purity and high statistics electron sample to tune the parametrization is challenging, the Monte Carlo based parametrization was used in the spectra analysis described in Sec. 5. Considering the overall good agreement between data and MC observed for π, K and p (see Fig. 4.21), the use of a simulated response function for electrons is justified and acceptable for the analysis of pions, kaons and protons where it is used to reduce the electron contamination, which is not large since electrons are about 2–3% of the total number of charged particles produced in the collision. If the Landau-Gauss parameters would wanted be used for electron identification, a more reliable description of the data sample is required.

Given the different nature of the energy loss for electrons (light charged particle) with respect to hadrons (heavy charged particle), it is expected that the ad-hoc functions used for π, K and p do not work for electrons. In the momentum region 0.1–1 GeV/c the electron most probable value dE/dx as a function of momentum is described by a linear function. So, all parameters are fitted with:

$$f_{MPV,Lwidth,Gsigma}(p) = \begin{cases} A^{e}_{mp,lw,gs} \times p + B^{e}_{mp,lw,gs} & \text{for electrons} \end{cases} \tag{4.9}$$

The results of the electron parametrization from simulated data for the SDD layers is shown in Fig. 4.22 and the fit results are reported in Tab. 4.2. In addition, the MPV ITS response parametrization for the simulated electron sample are compared in Fig. 4.23 with the ones obtained for pions, kaons and protons in simulated data. The plots show that electron identification is only feasible for reconstructed ITS stand-alone tracks with momentum below 0.2 GeV/c.

			MC simulations	
			A	B
SDD	Electron	MPV	0.2507	84.64
		Lwidth	0.02969	6.634
		Gsigma	-0.4338	8.225
SDD	Electron	MPV	0.2762	86.92
		Lwidth	0.06276	6.333
		Gsigma	0.1672	6.519

Table 4.2: ITS response function parameters for electrons in MC simulations. The Landau-Gauss parameters (MPV, Lwidth and Gsigma) are related to the parameters A and B through Eq. 4.9.

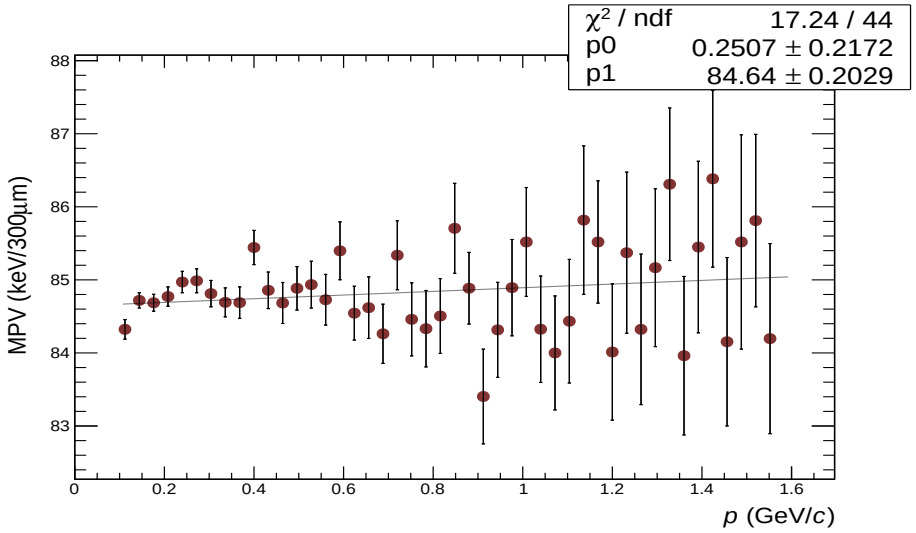

(a) MPV

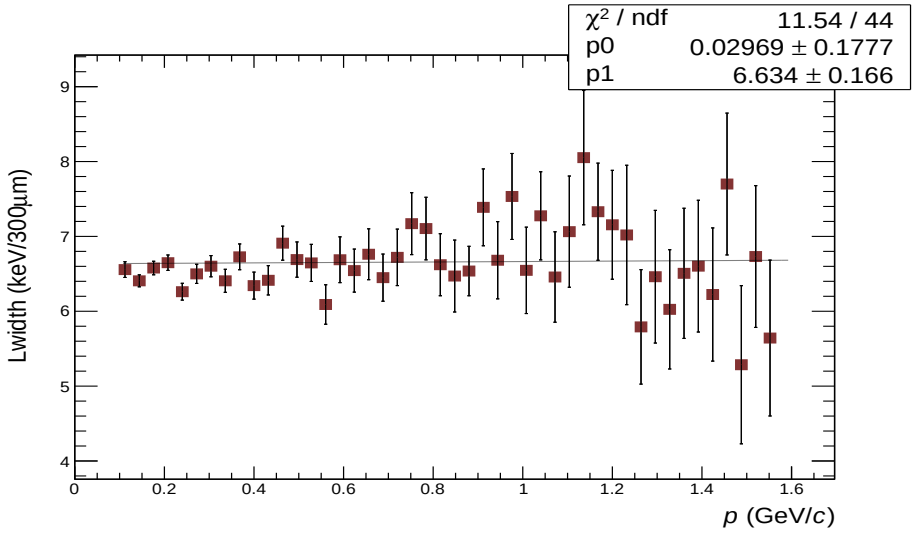

(b) Lwidth

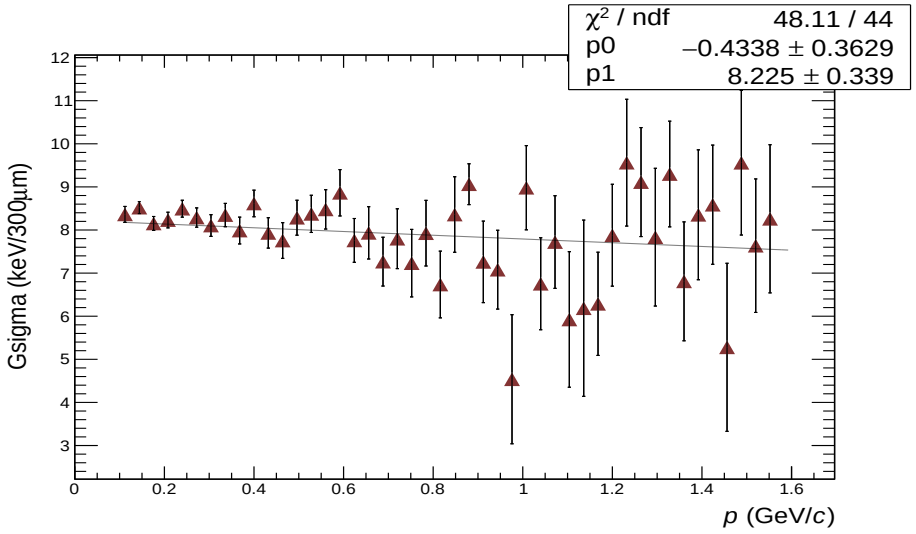

(c) Gsigma

Figure 4.22: Landau-Gauss fit parameters, (a) MPV, (b) Lwidth and (c) Gsigma, for SDD detectors as a function of the momentum for MC simulated electron sample.

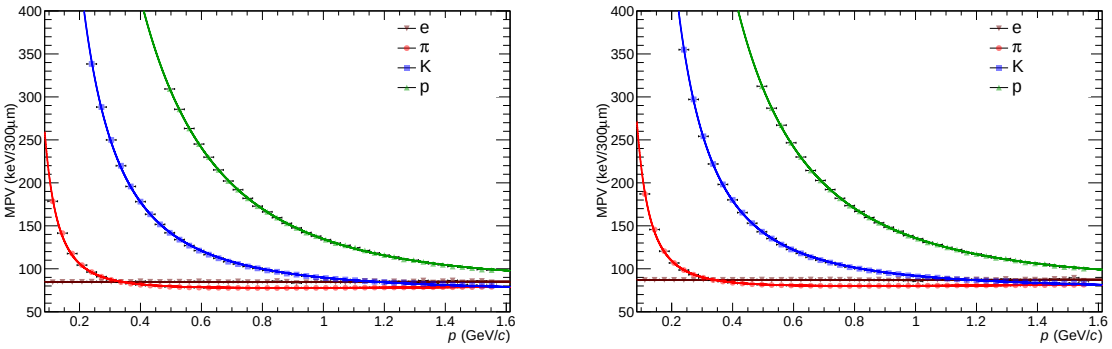

(a) SDD **(b)** SSD

Figure 4.23: Landau-Gauss fit MPV parametrization for (a) SDD and (b) SSD detectors as a function of the momentum for simulated electron, pions, kaons and protons samples.

4.2.3 Prior estimation

The prior probability represents our *prior* knowledge before the data are considered. For the purposes of PID this corresponds to the relative abundances of the various particle species in the sample which is analysed. Thus, the priors depend upon the collision type (pp, p–Pb, Pb–Pb...), the event selection, the selection cuts applied to the sample of analysed tracks and also on p_{T}, because of the different transverse momentum distributions of different hadron species.

In principle, the Bayesian PID approach can be seen as self-consistent if the same values of priors are used in the data analysis and in the determination of the efficiencies, and if the detector response functions are properly parametrized in data and Monte Carlo. In this sense, the priors do not need to be a perfect description of the real abundances and could e.g. even be the same for all species independently of p_{T} (*flat prior*), although better performances, in terms of efficiency and purity, are obtained if the priors are closer to reality.

In π, K and p spectra analysis, the corrections applied to the raw spectra for the PID efficiency and for the contamination from other species are based on Monte Carlo simulations. Therefore, we are sensitive to the different relative abundances of π, K and p in data and MC samples. For this reason, minimizing the contamination using a high purity PID approach is helpful to reduce the systematic uncertainties. On the other hand, the correction for PID efficiency should not depend on these difference in the particle species composition of data and MC samples.

Since the real relative abundance of particle species i as a function of p_{T} is unknown, a possible effective approach to get the prior probabilities for species i is to utilize an

iterative procedure. In this approach, flat priors are considered at the first step. Subsequently the relative abundances of the various particle species are computed making use of the Bayesian probability to identify the tracks. To each track an identity is assigned based on the species with the higher Bayesian probability. The resulting relative abundances are used as the new prior probabilities in next step. The iterations continue until the prior probabilities and the resulting relative abundances of π, K and p converge. That is,

$$\Pi(i; p_{\mathrm{T}}) = \lim_{iteration \to \infty} \frac{N_i}{N}\Big|_{p_{\mathrm{T}}} \tag{4.10}$$

where N is the total number of particles in the sample and N_i is the number of particles of species i. The prior probabilities obtained with this approach will be denoted as *MaxProb. prior*.

The prior probabilities for π, K and p as a function of p_{T} for different iterations are reported in Fig. 4.24 for the sample of ITS stand-alone tracks. The prior probability for each species has been obtained on a sample of pp collisions at $\sqrt{\mathrm{s}} = 7$ TeV which do not belong to the same data taking period used to build the Landau-Gauss ITS response functions.

In the plot we can observe that the prior probabilities for all species converge after $\sim$ 5–6 iterations. In addition, it is observed that a "zero-prior valley" is produced, mainly for kaons, in the p_{T} range where the kaons can not be separated from pions. This is consequence of the use of the maximum probability to assign identities to tracks in the calculation of the species relative abundances. This "zero-prior valley" affects the PID performance, and in particular the pion contamination, because all kaons in that p_{T} range, will be identified as pions using the Bayes formula.

An alternative possibility is to define the priors at each iteration using the Bayesian probability of each particle species i as weights:

$$\Pi(i; p_{\mathrm{T}})^{iteration\ j} = \sum_{k=1}^{N_{p_{\mathrm{T}}}} P(i|S)^{iteration\ j-1} \tag{4.11}$$

where $N_{p_{\mathrm{T}}}$ is the number of particles in a given transverse momentum interval and $P(i|S)^{iteration\ j-1}$ is the Bayesian probability for species i calculated with the priors $\Pi(i; p_{\mathrm{T}})^{iteration\ j-1}$ from the previous iteration. The prior probabilities obtained with this approach will be denoted as "weighted priors".

In Fig. 4.25 the prior probabilities for kaons and protons, normalized to the pion ones, from the two iterative approaches (Max. prob. and weighted) are shown as a function of p_{T}. In addition, the ratio of the raw yields N(K)/N(π) and N(p)/N(π)

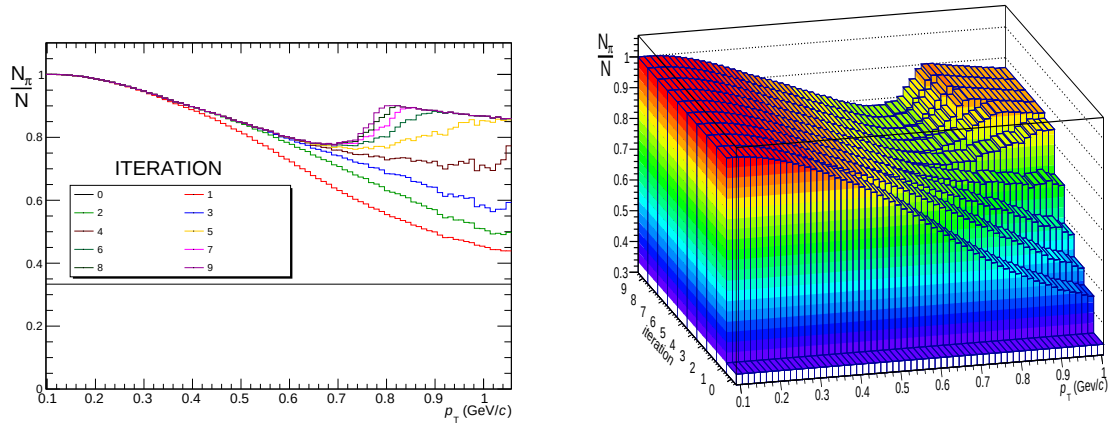

(a) Pion

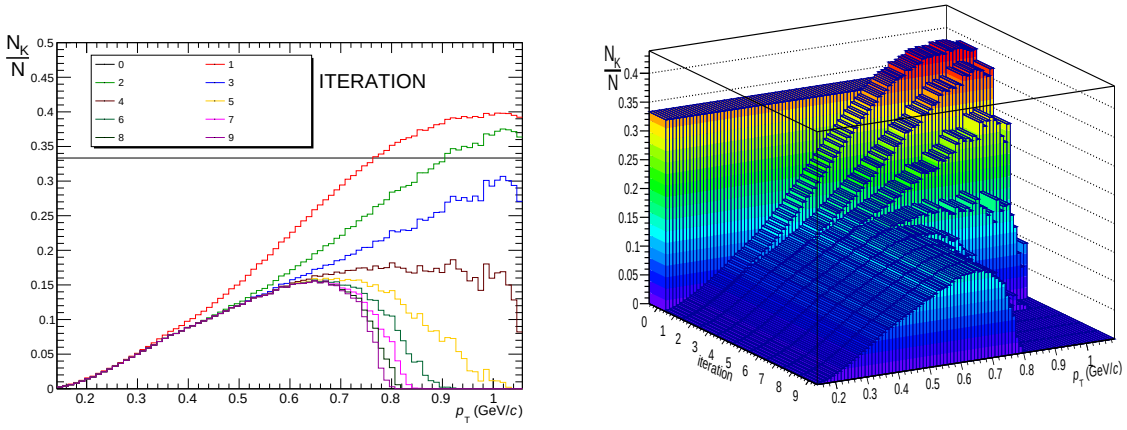

(b) Kaon

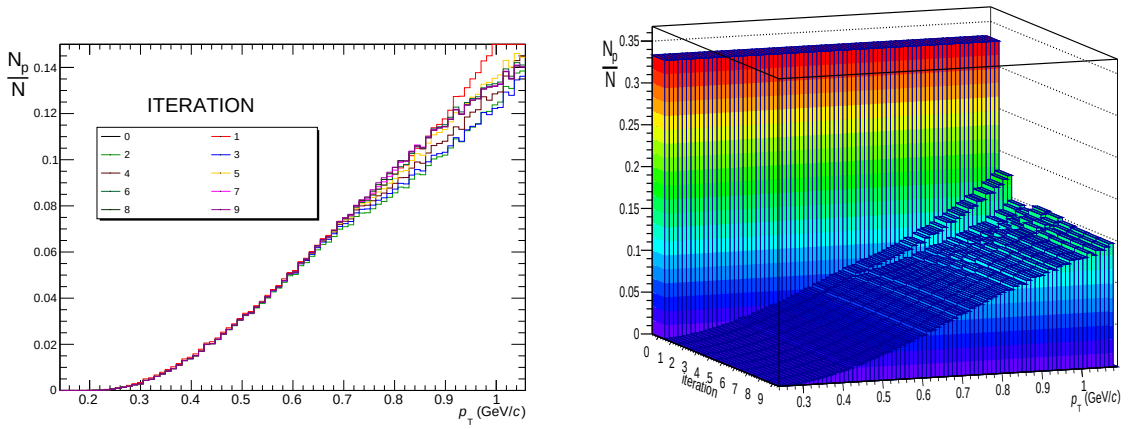

(c) Proton

Figure 4.24: Priors for (a) pions, (b) kaons and (c) protons as a function of p_{T} for different iterations for ITS stand-alone tracks.

as a function of p_{T} measured using an unfolding PID approach** in pp collisions at $\sqrt{s} = 7$ TeV are superimposed to the $\Pi(\mathrm{K})/\Pi(\pi)$ and $\Pi(\mathrm{p})/\Pi(\pi)$ prior ratio plots. It is observed that the results of both iterative procedures agree well with the relative abundances obtained in the data, at least in the transverse momentum range where the particle species can be separated. However, in the case where the Bayesian probabilities are used as weight to fill the particle distributions, the kaon priors tend to increase with an increasing slope with increasing p_{T}. Since π, K and p have equal conditional probabilities in the region where the ITS cannot separate them, the weighted prior probabilities tend asymptotically to 1. The weighted approach offers higher purity for pions and protons at high p_{T} independently on where the kaon identification is stopped. In the same way, we lose a bit of efficiency for pions and protons. The π, K and p spectra reported in Sec. 5 and Sec. 6 are obtained using priors from the results of the Bayesian weight iterative procedure.

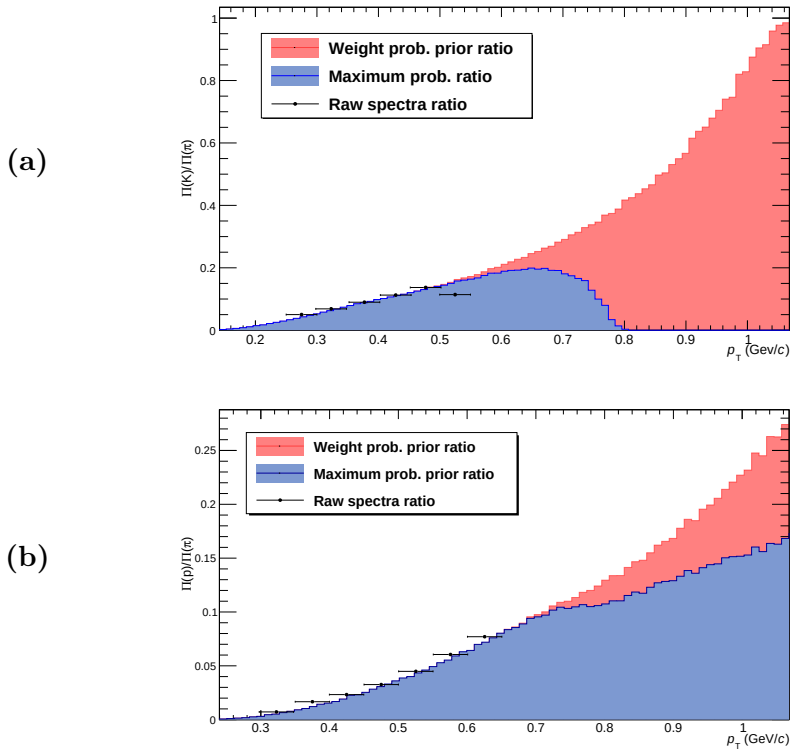

Figure 4.25: Prior probabilities for (a) kaons and (b) protons normalized to the pion ones obtained from both iterative procedures, see text. Ratio of raw spectra from ITSsa analysis using unfolding PID are superimposed.

**In the unfolding PID approach the raw yield is extracted from a multi-component fit to the dE/dx distribution in narrow p_{T} intervals. This approach was used in [133] and a detailed description can be found in [137]

4.3 ITS Bayesian PID performance

The Bayesian PID approach can be tested on simulated data and its performance can be compared with the other ITS PID approaches based on the truncated mean. In particular, for each species, the PID efficiency and the contamination from other species were studied. For each transverse momentum interval $[p_{\mathrm{T}}, p_{\mathrm{T}} \pm \Delta p_{\mathrm{T}}]$, the PID efficiency $\epsilon(i; p_{\mathrm{T}})$ and the contamination $\kappa(i; p_{\mathrm{T}})$ for the particle species i (with $i = \pi$, K and p) are defined respectively as:

$$\epsilon(i; p_{\mathrm{T}}) = \frac{N_{good}(i; p_{\mathrm{T}})}{N_{true}(i; p_{\mathrm{T}})} \quad \text{and} \quad \kappa(i; p_{\mathrm{T}}) = \frac{N_{fake}(i; p_{\mathrm{T}})}{N_{identified}(i; p_{\mathrm{T}})} \tag{4.12}$$

where $N_{true}(i; p_{\mathrm{T}})$ is the number of particles of type i in the considered p_{T} range, $N_{identified}(i; p_{\mathrm{T}})$ is the total number of tracks associated by the PID approach to the identity i. $N_{identified}(i; p_{\mathrm{T}})$ consist of particles correctly identified ($N_{good}(i; p_{\mathrm{T}})$) and particles tagged as i without being of type i ($N_{fake}(i; p_{\mathrm{T}})$). The purity is defined as:

$$\chi(i; p_{\mathrm{T}}) = \frac{N_{good}(i; p_{\mathrm{T}})}{N_{identified}(i; p_{\mathrm{T}})} = 1 - \kappa(i; p_{\mathrm{T}}). \tag{4.13}$$

In Fig. 4.27 the efficiency (closed symbols) and contamination (open symbols) for π, K and p are shown as a function of the transverse momentum of the reconstructed track. The performances were obtained using the Bayesian approach on a MC simulation anchored to the same runs used to determine the priors from real data. The Bayesian PID was implemented considering three different procedures:

Flat priors without electron PID: Equal prior values (1/3) have been used for π, K and p independently of track p_{T}. For other particle species (electrons, muons, deuterons...) the priors were set to 0.

Flat priors with electron PID: Equal prior values (1/4) have been used for e, π, K and p independently of p_{T}. For other particle species the priors were set to 0.

Iterative prior probabilities: Electron, π, K and p prior values obtained by the iterative procedure using the Bayesian probabilities as weight described above.

In all cases the parametrization of the ITS response functions with the Landau-Gauss reported in Sec. 4.2 was used. The identity of the track was assigned based on the species with the highest Bayesian probability. Additional checks on the performance of the Bayesian approach have revealed, that:

- Better PID performance, in terms of higher efficiency and higher purity, are achieved when the conditional probabilities are calculated based on the Landau-Gauss parametrization, instead the Gaussian ITS response for the truncated mean approach. The PID performance for kaons and protons as a function of p_{T} obtained for both cases are presented in Fig. 4.26.

- The PID performance does not change significantly ($< 1\%$), if the prior resulting from the iterative procedure in simulated samples are considered, instead of those from the iterative priors from real data.

(a) Kaons

(b) Protons

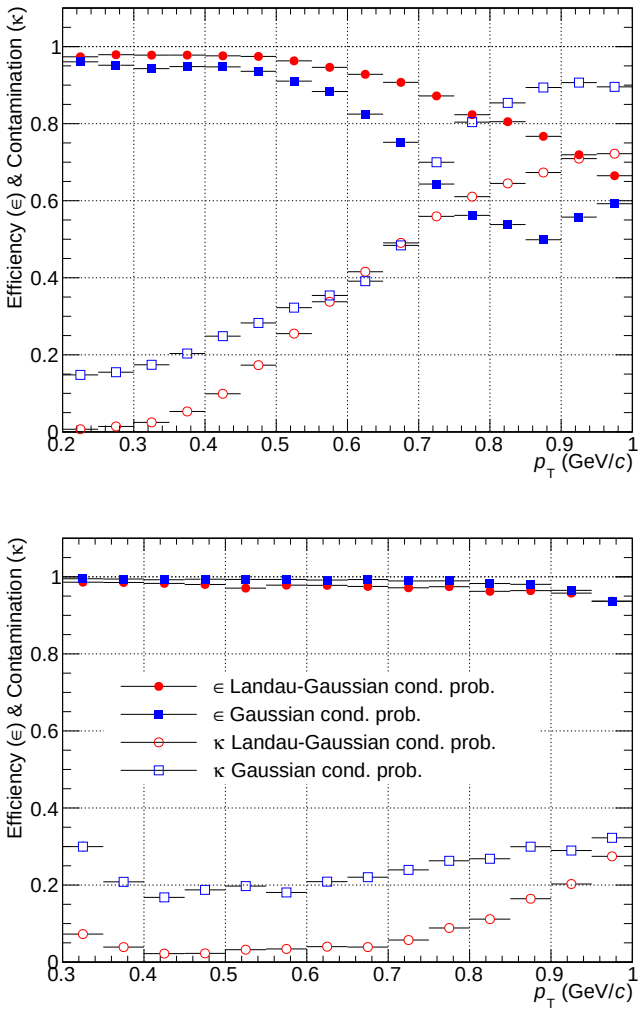

Figure 4.26: ITS Bayesian PID approach performance as a function of p_{T} for (a) kaons and (b) protons calculated with the conditional probabilities based on the Landau-Gauss parametrization (red circles) and on the Gaussian ITS response for the truncated mean approach (blue squared).

For pions at low transverse momentum a small contamination is observed when electron priors are set to zero (blue empty triangles). In order to remove it, we have included the electron parametrization discussed in Sec. 4.2.2 to calculate also the electron probability with the Bayes theorem. It can be observed, that the contamination in the pion bin at lowest p_{T} is reduced after adding the electron identification. However, if we compare the pion PID efficiencies in blue (flat prior without electron identification) and green (flat prior values with electron identification), Fig. 4.27, we can conclude that the use of electron PID causes a strong reduction of the PID efficiency for pions in the p_{T} region in which electron and pion dE/dx bands are superimposed.

In order to avoid this effect the iterative prior procedure was run using at the beginning equal priors for all species for $p_{\mathrm{T}} \leq 0.170$ GeV/c and "ad-hoc" prior values for electrons at higher momentum, considering that electrons are about few percent of the pions in that momentum range. The Bayesian performance using priors from an iterative procedure considering the electron prior equal to 2% of the pion one for $p_{\mathrm{T}} > 0.170$ GeV/c are reported in red.

As it can be seen in the plots in Fig. 4.27, the result of the PID performance depend on the prior probability. For pions, which represent about 80% of the produced particles, using the priors from the iterative procedure, the efficiency is high up to a high p_{T}, while the contamination remains low because it is due to kaons and protons which are less abundant. The usage of priors from the iterative procedure allows us also to reduce the contamination in the kaon and proton identified samples with respect to the flat prior case (e.g. kaon contamination is $< 30\%$ for $p_{\mathrm{T}} < 0.7$ GeV/c). Nevertheless, as soon as the efficiency in the identification of the pion decreases, the misidentified pions (few but with a high prior probability) can be tagged as protons or kaons, resulting in an enhancement of the contamination in protons and kaons. At the same time, the increase in the pion contamination leads to a decrease of the kaon and proton efficiencies.

In Fig. 4.28, the efficiency and contamination of π, K and p identified with the Bayesian approach with iterative priors are compared to those obtained with the method based on the truncated mean $\langle dE/dx \rangle$. In this second approach an identity is associated to each track based on the species whose expected mean dE/dx value (Eq. 4.4) is closer to the measured average dE/dx non explicit cut is applied on the distance between the measured and expected values in term on the number of σ, except for a lower band for pions defined at two times the experimental σ in order to reduce the contamination from electrons at low p_{T}. This PID approach was used to study the spectra of π, K and p at low p_{T} in Pb–Pb collisions at $\sqrt{s_{\mathrm{NN}}} = 2.76$ TeV [62, 63] and in pp collisions at $\sqrt{s} = 7$ TeV/c.

The performance of the method based on the truncated mean approach are very similar to the ones obtained from the Bayesian approach using flat priors, as it can be seen comparing Fig. 4.27 and Fig. 4.28. Therefore, the possibility to include the prior knowledge of the relative abundances of particle species in the analysed sample of tracks, guarantees to the Bayesian approach a better performance, especially in terms of contamination. For example, the kaon contamination is reduced by up to 20% with respect to the one obtained with the truncated mean approach. Since the PID efficiency and the contamination are somehow correlated, this effect in the contamination occurs at the price of a lower efficiency. Nevertheless, since PID contamination correction to the raw spectra, depends on the different relative π, K and p abundances in data and MC samples, while the PID efficiency does not, in the case of π, K and p spectra analyses a high purity PID approach with lower efficiency gives a more reliable PID correction factor than a more efficient one with high contamination. For this reason, the Bayesian approach was chosen to study the π, K and p spectra at low p_{T} in p–Pb collisions at $\sqrt{s_{\mathrm{NN}}} = 5.02$ TeV. The difference with respect to the results with the truncated mean cut approach is considered in the systematic uncertainties (Sec. 5.5).

(a) Pions

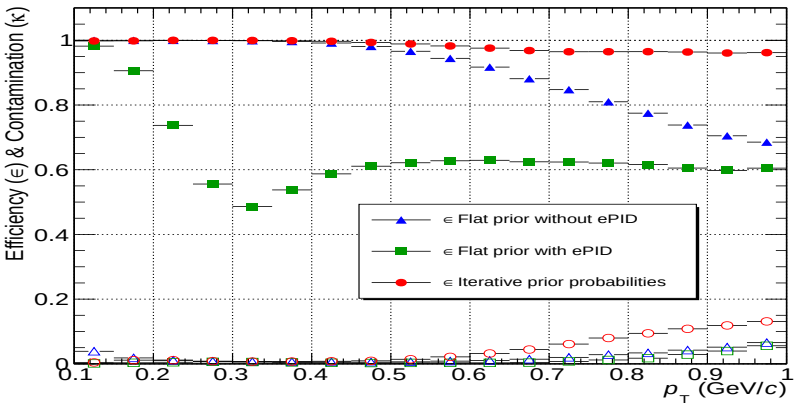

(b) Kaons

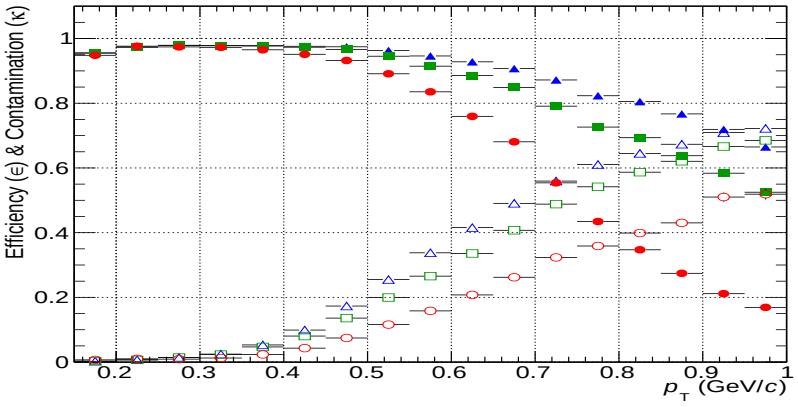

(c) Protons

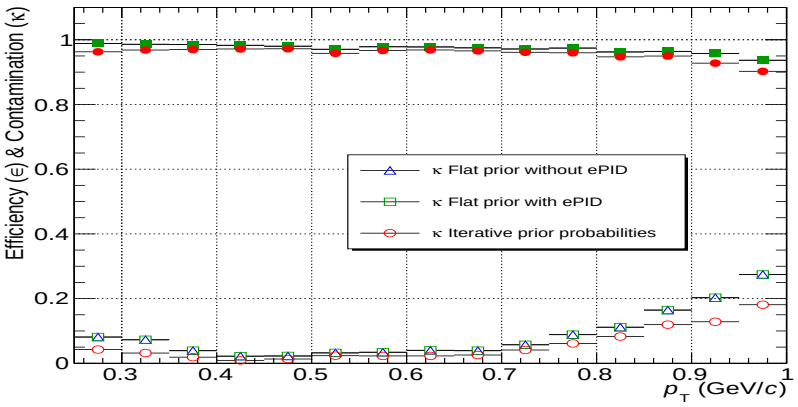

Figure 4.27: ITS Bayesian PID approach performance as a function of p_{T} for (a) pions, (b) kaons and (c) protons obtained with three different procedures: Flat priors without electron identification (blue triangles), Flat prior with electron identification (green squares) and Iterative prior probabilities (red circles).

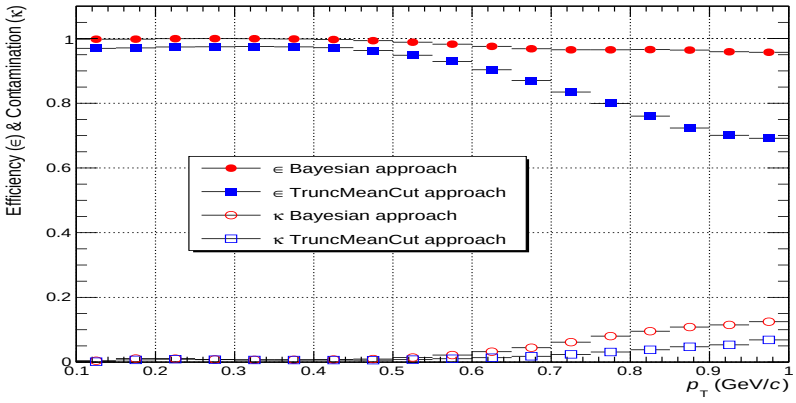

(a)

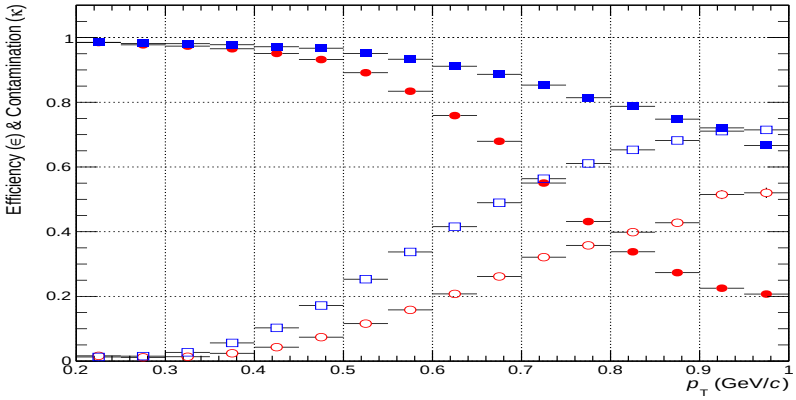

(b)

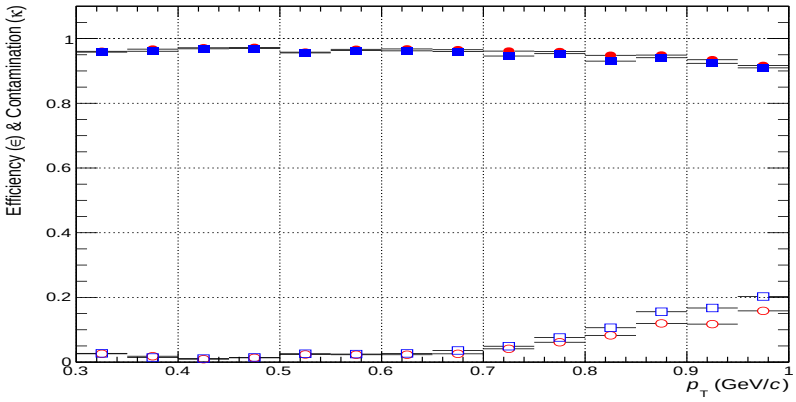

(c)

Figure 4.28: ITS PID performance obtained with the Bayesian approach (red circles), with iterative priors, and the truncated mean cut method (blue squares) for (a) pions, (b) kaons and (c) protons as a function of p_{T}.

5

π, K and p distributions in p–Pb collisions with the ITSsa analysis

The ITS stand-alone (sa) analysis allows us to extend the measurement of p_{T} spectra of identified hadrons down to 0.1, 0.2 and 0.3 GeV/c for π, K and p respectively. This guarantees a reduction of the uncertainties on the extrapolation of π, K and p yields down to $p_{\mathrm{T}} = 0$, and provide also a test of hydro/blast-wave model down to very low transverse momentum.

The low p_{T} reach of the ITSsa analysis, which depends on the particle species, is determined by the minimum momentum needed for a given hadron species in order to be reconstructed by the ITS stand-alone tracking algorithm. At high p_{T}, the analysis extends up the momentum at which a given hadron species can be separated from the others with high purity, i.e. up to the p_{T} values from which the uncertainty due to the contamination is acceptable ($\lesssim 2\%^{*}$). This means, for the Bayesian PID approach with iterative priors, up to $p_{\mathrm{T}} = 0.7$, 0.6 and 0.65 GeV/c for π, K and p respectively.

The π, K and p distributions, at higher transverse momenta, are obtained with other analyses (namely, TPCTOF and TOF analysis) based on the global track samples and using different PID approaches [62, 63, 133]. In particular, the TPCTOF analysis makes use of a 3σ cut on the dE/dx measured with the TPC and on the time of flight from the interaction vertex to the TOF. It allows us to identify π, K and p in the p_{T} ranges 0.2–1.5, 0.3–1.3 and 0.5–2.0 GeV/c, respectively. The TOF analysis is based on an unfolding approach that allows to measure π, K and p yields up to $p_{\mathrm{T}} = 3$, 2.5 and 4 GeV/c, respectively.

In this contest, the ITSsa analysis provides also a cross check of the TPCTOF analysis in the p_{T} region where the two analyses overlap. The measurements performed with the three independent analyses are finally combined to obtain the π, K and p distributions over a large momentum range. The TPCTOF and TOF analyses will be briefly described in Sec. 6 together with the combine procedure used for the combination of the three analyses.

*Which corresponds to a contamination $\lesssim 20\%$.

In this Chapter, a comprehensive overview of the π, K and p spectra analysis in p–Pb collisions at $\sqrt{s_{NN}} = 5.02$ TeV at the LHC, using the ALICE Inner Tracking System in stand-alone mode, will be reported. It includes a description of each step needed to measure the p_T distributions of primary particles[†]: event and track selection, the extraction of the raw yield, correction using Monte Carlo simulations and estimation of the systematic uncertainties.

5.1 Experimental conditions and event selection

The results presented in this thesis are obtained from a data sample collected during the LHC p–Pb run in the beginning of 2013. The two-in-one magnet design of the LHC imposes the same magnetic rigidity of the beams in the two rings, implying that the ratio of the beam energies is fixed to be exactly equal to the ratio of the charge/mass ratio of each beam. Protons at 4 TeV energy collided onto fully stripped $^{208}_{82}$Pb ions at 1.58 TeV per nucleon energy resulting in collisions at $\sqrt{s_{NN}} = 5.02$ TeV in the nucleon–nucleon centre-of-mass system (cms), which moves with a rapidity of $y_{NN} = -0.465$ in the direction of the proton beam, see Fig. 5.1.

The Fig. 5.2 illustrates in detail the integrated luminosity, collected by ALICE during the p–Pb data taking in 2013, for the minimum bias and rare-trigger running modes (Sec. 3.3.1). The number of colliding bunches was varied from 8 to 288. The total number of protons and Pb ions in the beams ranged from 0.2×10^{12} to 6.5×10^{12} and from 0.1×10^{12} to 4.4×10^{12}, respectively. The maximum luminosity at the ALICE interaction point was 5×10^{27} cm^{-2}s^{-1} resulting in a hadronic interaction rate of 10 kHz. The interaction region had a r.m.s. of 6.3 cm along the beam axis and about 60 μm in the direction transverse to the beam.

For the results presented in this thesis, a low-luminosity data sample has been analyzed where the event pile-up rate has been estimated to have negligible effects on the results. The LHC configuration was such that the lead beam circulated in the "counter-clockwise" direction, corresponding to the ALICE-A direction or positive rapidity as per the convention used in this thesis (Fig. 5.1). In the second part of the LHC p–Pb run the beam configuration was reverted (Pb–p), but we did not analyse those data. The ALICE collaboration has changed later the rapidity convention considering positive the p-going direction.

[†]Primary particles (π, K, p) are defined as prompt particles produced in the collision, including decay products, except those from weak decays of strange particles.

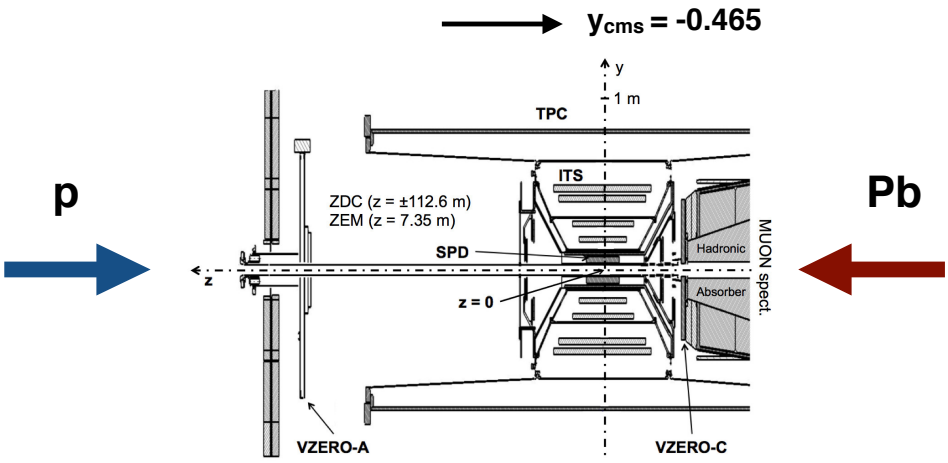

Figure 5.1: Schematic view of p–Pb collisions and ALICE frame system.

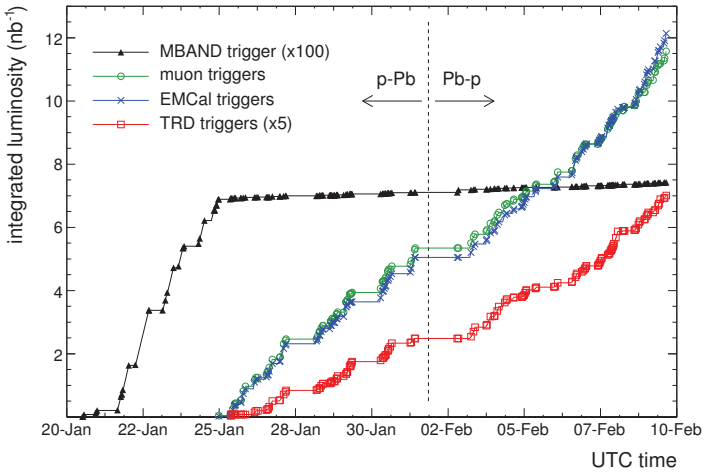

Figure 5.2: Integrated luminosity in the 2013 p–Pb run, collected by ALICE with the MB_{AND} and the rare-trigger mode (before and after January 25, respectively) [120].

5.1.1 Event selection

The event samples were collected with the minimum bias trigger MB_{AND} condition, i.e VZERO signals on both A and C sides, in order to remove contamination from single diffractive and electromagnetic events.

In addition, beam induced background events are removed using the offline event selection. The beam–gas interactions and the beam–halo interactions with materials of the apparatus (beam pipe, ...) are rejected using the timing information from the VZERO counters. In the offline analysis, the background is further suppressed by the time information recorded in the two neutron Zero Degree Calorimeters and in the T0 detectors (Sec. 3.3.2).

The primary vertex position is determined from the tracklets (= track segments) in the SPD [138] and from tracks reconstructed in the central barrel detector (global tracks). In the analysis, the vertex reconstruction from the global tracks is used if available, otherwise it falls back to the SPD vertex. Events without a reconstructed vertex are rejected. The events are further selected by requiring that the longitudinal position of the primary vertex is within ±10 cm from the detector centre, in order to cover the pseudo-rapidity range $|\eta_{lab}| < 0.8$ for the particles produced in the collision. In total from a sample of 15.3 M triggered events, which represent only a fraction of the collected p–Pb MB_{AND} data sample (run 195483 from the LHC13b period), about 12.5 M events passing the selection criteria were used.

In contrast to Pb–Pb collisions, in p–Pb collisions the geometry of the collision and the multiplicity in different pseudo-rapidity regions are not as well correlated. Therefore, the large multiplicity fluctuations together with the small range of participant nucleons available, generate a dynamical bias in the definition of centrality classes based on particle multiplicity [139].

In order to study the multiplicity dependence of particle production, a similar multiplicity estimator as that used for centrality estimation in Pb–Pb collisions [27] was considered. The selected event sample was divided into seven multiplicity classes (CC), based on cuts to the total charge deposited in the VZERO counter located in the Pb-going direction, which is the VZERO-A detector (V0A). The multiplicity percentiles have been evaluated from a NBD-Glauber fit to the distribution of the summed amplitudes of the signals in the VZERO-A scintillator tiles (Fig. 5.3). The NBD-Glauber fit result of considering a Glauber Monte Carlo model combined with a simple model for particle production. The same method was used in Pb–Pb collisions [27].

The corresponding fractions of the data sample in each class are summarized in Tab. 5.1. The mean charged-particle multiplicity ($\langle d\mathrm{N}/d\eta \rangle$) within $|\eta_{lab}| < 0.5$ corresponding to the different event classes are also listed in the table. These values are corrected for acceptance and tracking efficiency as well as for contamination from secondary particles. However, they are not corrected for trigger and vertex-reconstruction inefficiency, which is of the order of 2% for Non Single-Diffractive (NSD) events [138]. The same holds true for the p_{T} distributions, which are presented in this work.

The experimental data are normalized to the number of events passing the event selection criteria (including the vertex cut) in each multiplicity event class[‡]. In this work the minimum bias spectra are obtained by summing the spectra measured in all multiplicity classes (0–100%).

[‡]A systematic check for the effect of the vertex reconstruction efficiency will be discussed in Sec. 5.6.1

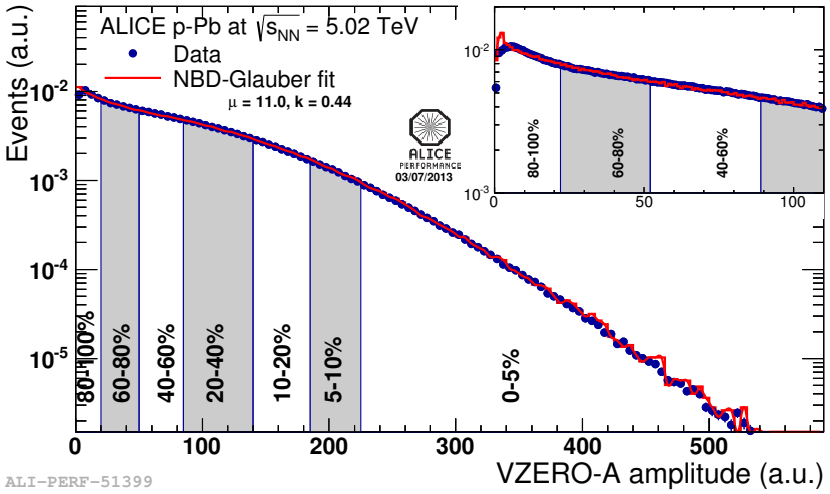

Figure 5.3: Distribution of the sum of amplitudes in the V0A scintillator counter (Pb-going) direction, as well as the NBD-Glauber fit. Multiplicity classes are indicated by vertical lines. The inset shows a zoom-in on the lower multiplicity events.

Event class	V0A range (arb. unit)	$\langle dN/d\eta \rangle\,|_{\|\eta_{lab}\|<0.5}$
0–5%	> 227	45 ± 1
5–10%	187–227	38.2 ± 0.8
10–20%	142–187	30.5 ± 0.7
20–40%	89–142	23.2 ± 0.5
40–60%	52–89	16.1 ± 0.4
60–80%	22–52	9.8 ± 0.2
80–100%	< 22	4.4 ± 0.1

Table 5.1: Definition of the event classes as fractions of the analysed event sample and their corresponding $\langle dN/d\eta \rangle$ within $|\eta_{lab}| < 0.5$ (systematic uncertainties only, statistical uncertainties are negligible).

5.1.2 Track selection

The tracks of the events that pass the selection criteria described in the previous section are selected applying different cuts. In ITSsa spectra analysis only ITSpureSA tracks are used. As discussed in Sec. 3.4.2 is a sample of tracks reconstructed using only the reconstructed points in the ITS. In order to select tracks with optimal determination of the trajectory parameters (and to reduce the contamination due to fake[§]), the tracks tagged as *ITSrefit* during the fitting steps of the ITS stand-alone tracking algorithm (see Sec. 3.4.2) are selected.

[§]Track reconstructed with at least one associated cluster not originated by the same particle.

Tracks are further selected by requiring at least one cluster in the SPD layers, to improve the resolution on the track impact parameter and to reduce contamination from secondary and fake tracks. In order to have the optimal PID performance, at least three clusters are required in the SDD and SSD layers. To further reduce the contamination from fake tracks and select high quality track sample a cut selection on the $\chi^2/\mathrm{N}_{ITSclusters}$ is applied. Finally, to reduce the contamination from secondary tracks, a p_T dependent cut on the transverse track impact parameter $d_0(xy) \leq 7\sigma_{d_{0xy}}(p_\mathrm{T})$ is applied. The resolution on the impact parameter $\sigma_{d_{0xy}}(p_\mathrm{T})$ is parametrized as $\sigma_{d_{0xy}} = 32.7 + 44.8/p_\mathrm{T}^{1.3}$ and as $\sigma_{d_{0xy}} = 36 + 43.9/p_\mathrm{T}^{1.3}$ for real and simulated data respectively.

The track cuts applied are summarized in Tab. 5.2. They have been tuned based on the experience of previous ITSsa spectra analysis in pp and Pb–Pb colliding systems.

Variable	Cut
$\mathrm{N}_{clusters}$ in SPD	≥ 1
$\mathrm{N}_{clusters}$ in SDD+SSD	≥ 3
$\chi^2/\mathrm{N}_{ITSclusters}$	≤ 2.5
$d_0(xy)$	$\leq 7\sigma_{d_{0xy}}(p_\mathrm{T})$

Table 5.2: Track cuts applied in the ITSsa spectra analysis.

Moreover, since ITS stand-alone tracking allows us to track down $p_\mathrm{T} = 100$ MeV/c and the description of the material budget in the Monte Carlo at large η is not completely satisfactory, only tracks within the region $|\eta_{lab}| < 0.8$ are accepted. An acceptance correction is then applied to compute the yield in $0 < \mathrm{y}_{cms} < 0.5$.

Rapidity selection

Since the p–Pb centre-of-mass system moved in the laboratory frame with a rapidity of $\mathrm{y_{NN}} = -0.465$, the nominal acceptance of the central barrel of the ALICE detector is not symmetric around mid-rapidity. This effect is more pronounced for heavier particles.

The acceptance for protons as a function of p_T and η_{lab} is shown in Fig. 5.4. As it can be seen, only with a small cut around mid-rapidity $|\mathrm{y_{cms}}| < 0.2$ the full p_T range can be covered. Alternatively, it is possible to apply an asymmetric cut around $\mathrm{y_{cms}}$ or around y_{lab}[¶].

[¶]A cut around y_{lab} is not really desirable, as it depends on the experimental conditions.

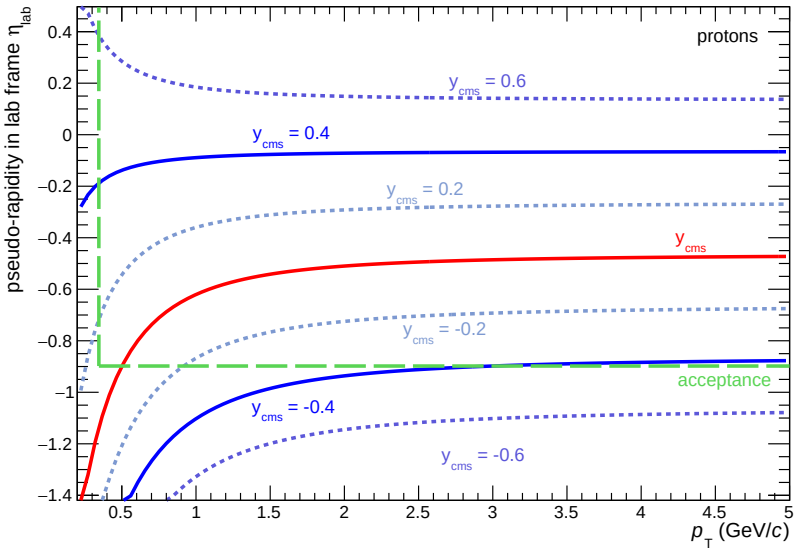

Figure 5.4: Acceptance of protons as a function of p_{T} and η_{lab}.

The analysis described in this thesis was performed in two different rapidity intervals:

- $0 < \mathrm{y}_{cms} < 0.5$ (**default**)
- $|\mathrm{y}_{\mathrm{cms}}| < 0.2$

The asymmetric range ($0 < \mathrm{y}_{cms} < 0.5$) has been chosen as the default one, because, as it can be seen in Fig. 5.4, a symmetric range around $\mathrm{y}_{\mathrm{cms}}$ would require to restrict the analysis at large $|\eta_{lab}|$, with a corresponding degradation of the TPC dE/dx performance [119].

The choice of the rapidity interval has a small effect on the interpretation of the data. Even if the rapidity distribution is not flat at mid-rapidity in p–Pb collisions, due to the asymmetric colliding system, the variations are smaller than 5% in the range $0 < \eta_{lab} < 1$ [138]. The asymmetric depends on the particle species and on the centrality (multiplicity) of the collisions. According to p–Pb simulations with the HIJING event generator, an extrapolation of the proton rapidity distribution from $|\eta_{lab}| < 0.8$ to $|\mathrm{y}_{\mathrm{cms}}| < 0.2$ or to $|\mathrm{y}_{\mathrm{cms}}| < 0.4$ assuming flat rapidity distribution would lead to a systematic bias on the yields of 0.7% and 1.3%. This is consistent with a similar study done with DPMjet simulations, shown in Fig. 5.5: the spectra in $|\mathrm{y}_{\mathrm{cms}}| < 0.2$ and $0 < \mathrm{y}_{cms} < 0.5$ differ by $\lesssim 2\%$. A comparison of the ITSsa analysis results obtained in the two different rapidity ranges is reported in Fig. 5.6. A similar result was obtained for other spectra analyses at higher p_{T}.

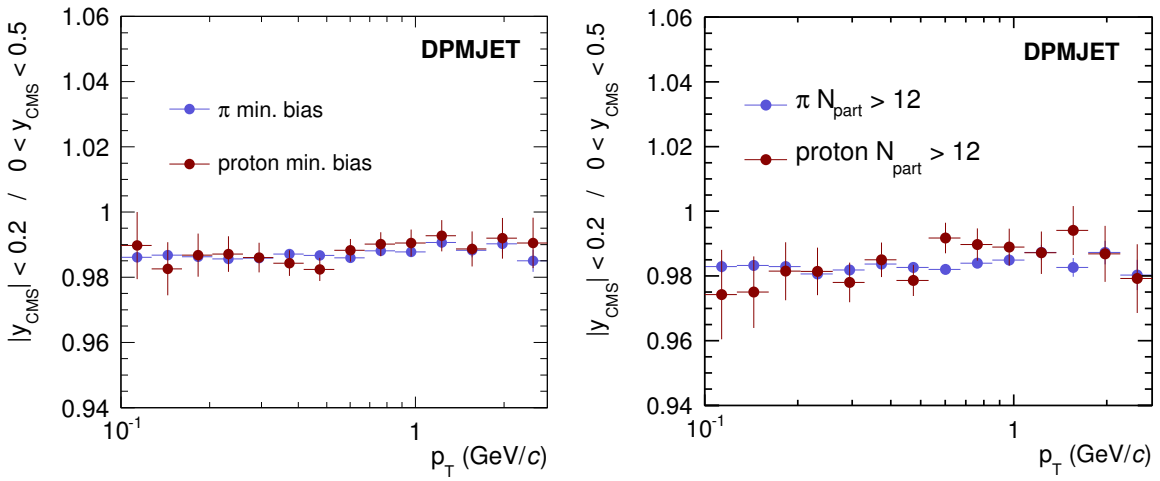

Figure 5.5: Ratio of spectra obtained in different rapidity regions with DPMjet for minimum bias (left) and central (right) collisions.

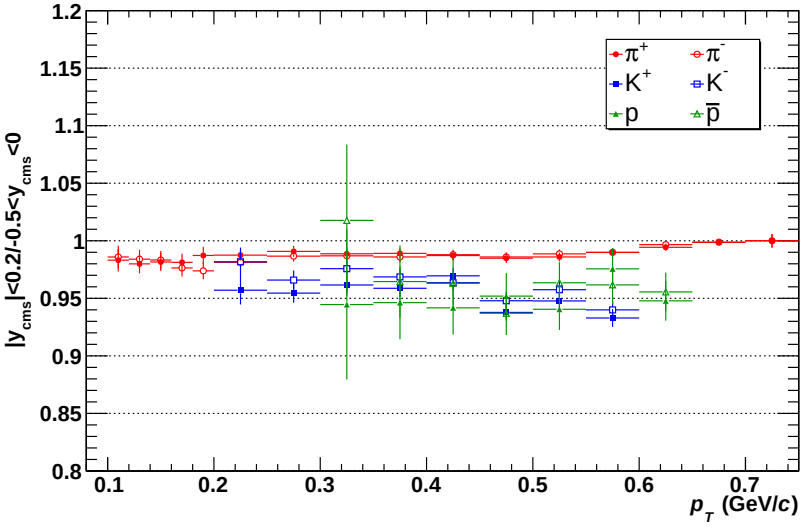

Figure 5.6: Results obtained with $|y_{cms}| < 0.2$ rapidity cut compared with default for ITSsa π, K and p spectra.

5.2 Particle identification

After the event and track selection, the track-by-track Bayesian PID approach using the Landau-Gauss parametrization of the dE/dx in each ITS layer as conditional probability (Sec. 4) is used to assign an identity (e, π, K or p) to each selected track.

For each track with momentum p, and with a set of three or four ITS $s = dE/dx$ signals, the global ITS conditional probability, $R(S = \{s_{k=1..N_{SDD+SSD}}\}|i)$, is estimated as a product of the conditional probabilities based on the normalized Landau-Gauss ITS

response function for each available layer. Thus, the probability for the track of being of type $i = e, \pi$, K or p is computed with the Bayes's theorem:

$$P(i|S, p, p_{\mathrm{T}}) = \frac{R(S|p, i)\Pi(i, p_{\mathrm{T}})}{\sum_{\mathrm{t=e,\pi,K,p}} R(S|p, t)\Pi(t, p_{\mathrm{T}})} \tag{5.1}$$

A particle is assigned the identity with the maximum Bayesian probability. The prior probabilities $\Pi(i, p_{\mathrm{T}})$ were estimated by the weighted iterative procedure as a function of p_{T} and the multiplicity event class. As discussed in Sec. 4.3, according Monte Carlo simulations the Bayesian approach using Landau-Gauss functions provides lower contamination than the PID methods baseed on the truncated mean of the dE/dx samples employed in previous ITSsa spectra analysis. This was the main reason to select the Bayesian as the default PID approach in this analysis. The contamination due to misidentification is corrected using Monte Carlo simulations.

5.2.1 Prior estimation

The priors for all four species were determined by an iterative procedure taking into account the following items for each multiplicity class:

1. We applied event and track selections described above.
2. Flat priors are used as initial value: $\Pi_0(\mathrm{e}) = \Pi_0(\pi) = \Pi_0(\mathrm{K}) = \Pi_0(\mathrm{p})$.
3. An "ad hoc" $\Pi(\mathrm{e})$ is forced[‖] in the region where electron-pion separation is not effective ($\Pi(\mathrm{e}) = 0.02 \times \Pi(\pi)$ for tracks with $p_{\mathrm{T}} > 160$ MeV/c).
4. The Bayesian probability $P(i|S, p, p_{\mathrm{T}})$ was used to fill (as weight) the p_{T} distribution for each particle species.
5. New priors were computed from the obtained particle abundances (particle ratios) and used as input for the next iteration step (10 iterations).
6. Priors are normalized, i.e. $\sum \Pi(\mathrm{t}) = 1$, at beginning of each iteration.
7. No MC information was used.

The resulting ratios $\Pi(\mathrm{K})/\Pi(\pi)$ and $\Pi(\mathrm{p})/\Pi(\pi)$ from the last iteration are shown in Fig. 5.7 as a function of p_{T} and the V0A amplitude percentile. The same priors extracted from data were used in the Monte Carlo simulations for the determination of the raw spectra correction factor.

[‖]Additional 1% of pion PID systematic uncertainty is considered due possible electron contaminations in the region $p_{\mathrm{T}} > 170$ MeV/c.

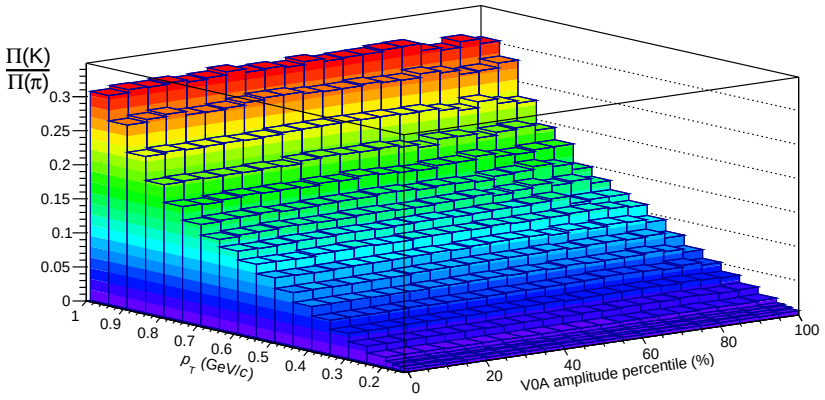

(a) Kaons

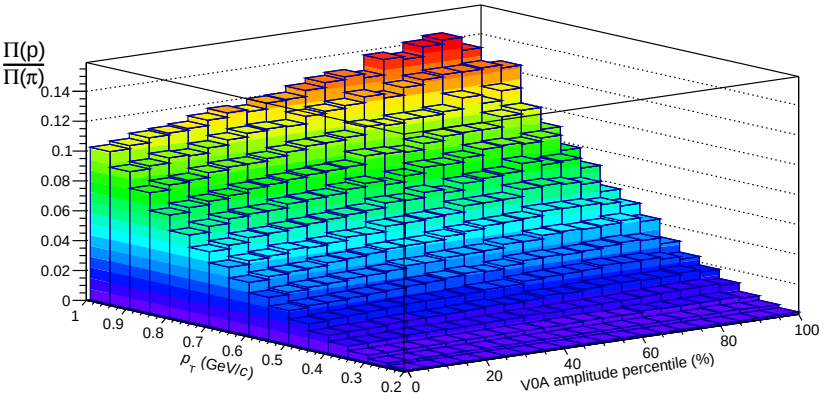

(b) Protons

Figure 5.7: Ratios of (a) kaon-to-pion and (b) proton-to-pion priors after 10 iterations as a function of p_{T} and multiplicity intervals.

5.3 Raw yield extraction

Once the identity is assigned to the track, the π, K and p raw yields are obtained counting the particles of a given species, in a given p_{T} and within the rapidity interval $0 < \mathrm{y}_{cms} < 0.5$. The minimum bias π, K and p raw spectra obtained with the ITSsa analysis for positive and negative charge sign separately are reported in Fig. 5.8. These yields represent only a fraction of the yields of produced particles due to various sources of inefficiency (e.g. detector acceptance, tracking efficiency...). In order to estimate the distributions of particles produced at mid-rapidity in p–Pb collisions different corrections must be applied.

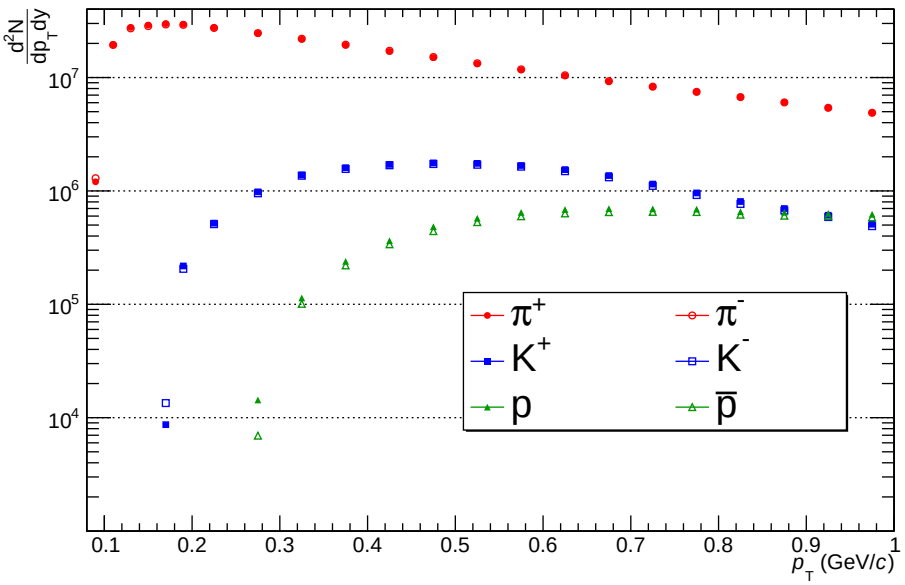

Figure 5.8: Raw π, K and p distributions in minimum bias p–Pb collisions at $\sqrt{s_{NN}} = 5.02$ TeV obtained with the ITSsa analysis.

5.4 Corrections

There are three main corrections applied to the raw π, K and p distributions. They will be discussed in detail in the following sections.

Summarizing, the p_T distribution of the hadron species i, is computed as:

$$\frac{d^2N_i}{dp_T dy} = 2 \times \frac{d^2N_i^{RAW}}{dp_T dy}\Big|_{0<y<0.5} \times \left\{\frac{d^2N_i^{RAW,MC}/dp_T dy}{d^2N_{Primaries,i}^{GEN,MC}/dp_T dy}\right\}^{-1} \times \left[\frac{(primaries/All)_{DATA}}{(primaries/All)_{MC}}\right]_i \quad (5.2)$$

the factor 2 is to normalize to unit of cms rapidity.

5.4.1 Tracking efficiency and PID corrections

To obtain the dN/dp_T of π, K and p correction should be applied for the detector acceptance, the tracking efficiency, including all event and track selection, the efficiency of PID and the contamination from misidentification. The correction values have been extracted from Monte Carlo simulations. A sample of about 13 M p–Pb collisions produced with the DPMjet event generator and propagated through the detector with the Geant3 transport code are used. The simulation included a detailed description of the detector conditions during the 2013 data taking with p–Pb collisions at $\sqrt{s_{NN}} = 5.02$ TeV.

The correction factor is computed as the ratio between the number of reconstructed tracks identified as species i using the Bayesian PID approach (regardless of the true identity of the track) and the total number of generated primary particles of species i after vertex and multiplicity selections.

$$\frac{d^2N_i^{RAW,MC}/dp_{\mathrm{T}}dy}{d^2N_{Primaries,i}^{GEN,MC}/dp_{\mathrm{T}}dy} \tag{5.3}$$

The denominator represents the spectrum of generated primary particles in the selected rapidity interval. The Monte Carlo correction factor is reported in Fig. 5.9 for all particle species in two multiplicity classes. At low p_{T}, the correction factor if different for π, K and p because the multiple scattering angle depends on $1/\beta$ for low momenta. Therefore, for a low momentum p, which leads to a low p_{T} because we are measuring at mid-rapidity**, the heavier particles suffer more multiple scattering making the reconstruction of its trajectory more difficult. In addition, about 30% of the correction applied to the raw spectra is caused by the track selection criteria.

No significant difference of the correction factor, which account for acceptance and efficiency, is observed between the highest and lowest multiplicity classes of events. The multiplicity dependence of the correction factor is also displayed in Fig. 5.10, where the ratio of the acceptance $\times$ efficiency in the 0–5% and 60–80% classes is shown. The variation with multiplicity is lower than 2% for all particle species. Therefore the minimum bias correction factor for a given particle species, which has a lower statistical uncertainty, was used to correct the raw spectra for all event classes. This variation of 2% was added in the systematic uncertainty on the tracking efficiency.

The factor of Eq. 5.3 includes the correction for the contamination due to misidentification of other species and for the contamination of secondary particles to the raw yield. Monte Carlo simulations are known to reproduce the measured particle relative abundances with an accuracy of $\sim 10\%$. Since the analysis is limited at high p_{T} at the momenta at which the contamination become $\gtrsim 15\%$, the effect of the different particle composition in data and Monte Carlo is smaller than 2% and it is considered in the PID systematic uncertainty.

An additional correction due to the different fraction of secondary particles in data and Monte Carlo simulations will be discussed later.

**Thus $p_{\mathrm{T}} \approx p$.

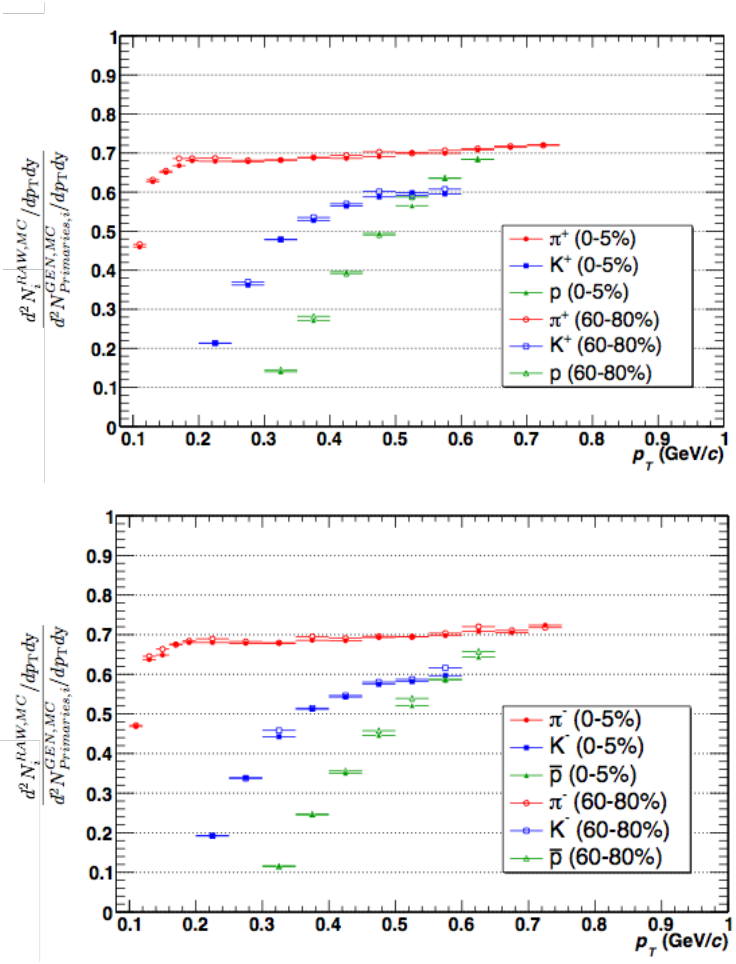

Figure 5.9: ITSsa correction factor for positive (left) and negative (right) charged particles in two multiplicity classes.

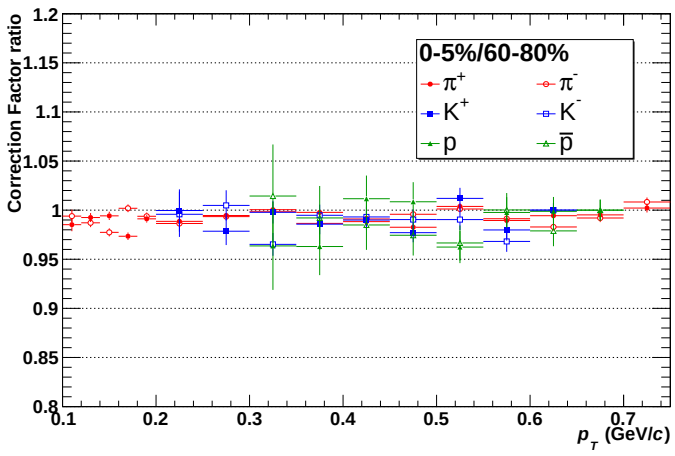

Figure 5.10: Ratio between ITSsa correction factors for high (0–5%) and low (60–80%) multiplicity collisions.

5.4.2 Correction for particle interactions in the transport code

The cross-section for interactions of negatively charger particles with the material, in the Geant3 versions used in the previous spectra analyses for different colliding system [62, 63, 133], are known to be larger than the experimentally measured ones, leading to a bias in the efficiency which is especially significant for K^- and $\bar{p}$. Since Geant4 and Fluka transport codes provide a description closer to the reality, as it is shown in Fig. 5.11 [140], a correction factor based on the comparison between Geant3 and Geant4/Fluka codes was applied to the efficiency shown in Fig. 5.9. These corrections as a function of p_T are shown in Fig. 5.12 for ITS stand-alone tracks.

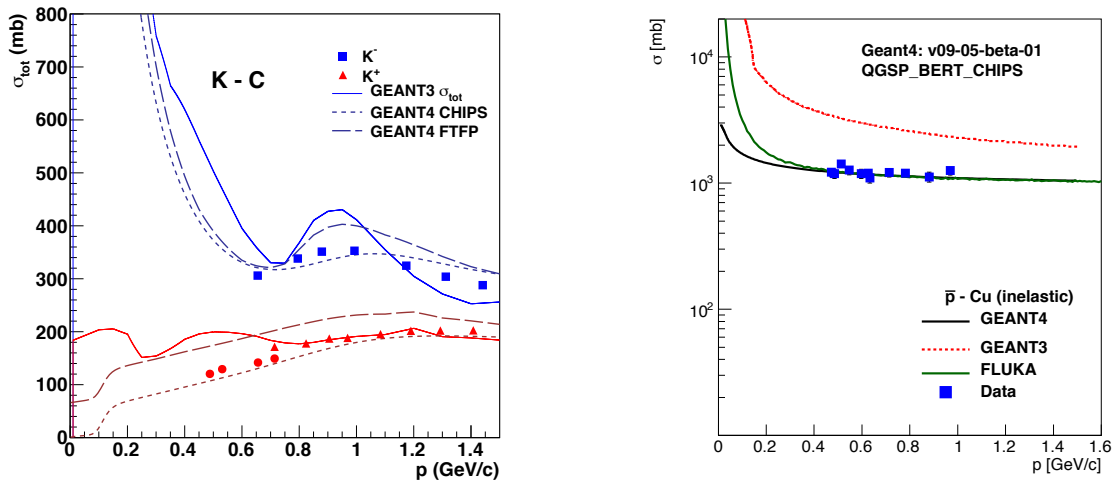

Figure 5.11: Comparison of K-C (left) and $\bar{p}$-Cu (right) cross sections, transport codes compared to data.

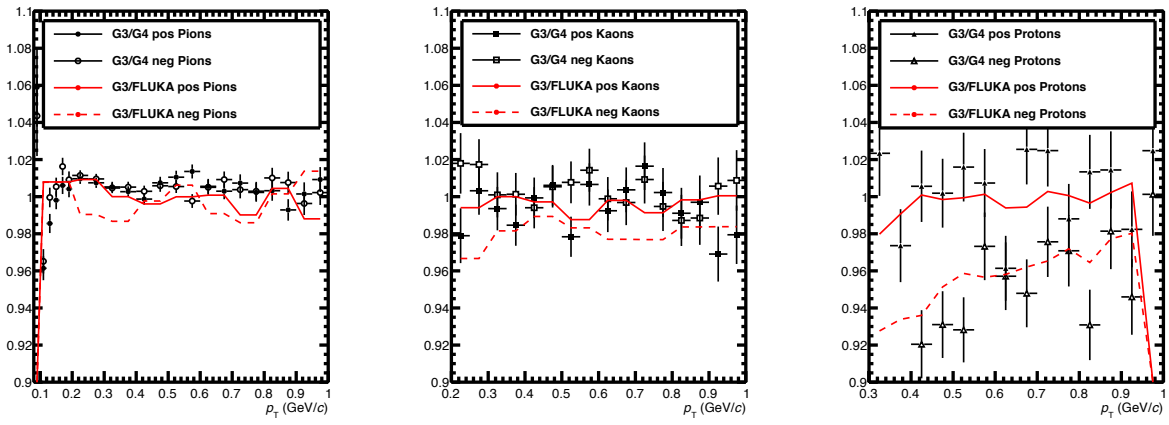

Figure 5.12: Geant3/Fluka and Geant3/Geant4 corrections as a function of p_T for ITS stand-alone tracks for pions (left panel), kaons (middle panel) and protons (right panel).

However, the Geant3 version used for the p–Pb analyses (v1-14-16) has been patched so that the anti-proton cross-section are properly reproduced. The patch is only applied to anti-protons, thus the correction reported in Fig. 5.12 are used for K^-. The correction calculated using Fluka is used to correct the data. As suggested by Fig. 5.12 Geant4 and Fluka agree within $\sim$ 2%. This difference has been included in the systematic uncertainty.

5.4.3 Subtraction of secondary particle contribution

Many of the particles produced in the collision are short-lived resonance states, which decay on time-scales of the order of 10^{-24} s. Their decay product are considered as part of the primary particle distributions. On the other hand, products from weak decays of strange particles are typically generated about 10^{-9} s after the collisions. The goal of the analysis is to measure the p_{T} spectra of primary π, K and p defined as particles produced in the collisions or in the decays of short lived particles except for the weak decays of strange particles. Therefore, the measured p_{T} spectra must be corrected for contributions due to feed-down from weak decays of strange hadrons. In addition, also secondary particles produced due to the interactions in the detector material must be subtracted.

The correction factor described in Sec. 5.4.1 has been defined in order to include a correction for secondary particle contamination. However, it has been verified by the ALICE experiment [141] that the yield of strange hadrons is not well reproduced in the Monte Carlo generators. As a consequence, a further correction is needed to account for different production of strange particle in data and in simulations.

The discrepancy on the fraction of secondary particles between data and simulation has been estimated using a data driven approach based on the distance of closest approach of reconstructed tracks to the primary vertex in the transverse plane (DCA_{xy}). The fraction of secondary particles in a given p_{T} interval is estimated by fitting the track DCA_{xy} distribution measured in the data with three different templates extracted from Monte Carlo simulations. These three templates are histograms that describe the DCA_{xy} distributions of primary particles, secondary particles from weak decay and secondary particles from interactions in the detector material. An example of fit to the DCA_{xy} distribution of protons is shown in Fig. 5.13 for a typical p_{T} interval. The fit is performed using the ROOT TFractionFitter class [123].

In the case of pions (π^+, π^-) and anti-proton ($\bar{\mathrm{p}}$) the contamination from secondary particles produced in the material is negligible and only the first two templates are used.

The same fit are performed to the DCA_{xy} distributions obtained from Monte Carlo simulations. Also in this case, the tracks are identified based on the Bayesian PID result, instead of the true Monte Carlo identity. From these fits we extract the ratio of secondary over primary particles in real and simulated data. The double ratio $(primaries/All)_{DATA}/(primaries/All)_{MC}$, which is shown in Fig. 5.14, is then used in the correction procedure to account for the different amount of primary and secondary particles in data and simulations. This correction was found to be independent of the multiplicity within the uncertainties provided by the TFractionFitter class.

The contribution of secondary particles to kaon yield is much smaller than for the other species. Thus, this additional correction factor is not needed and the usage of the fraction of primaries from the Monte Carlo generator leads to a small systematic uncertainty.

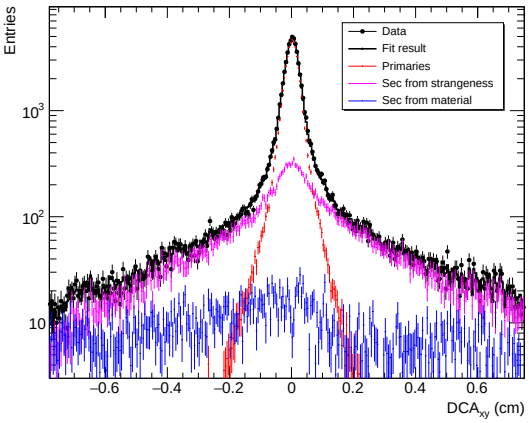

Figure 5.13: Fit to the data distribution of the distance of closest approach to the primary vertex in the transverse plane (DCA_{xy}) for protons in the p_{T} interval $0.50 < p_{\mathrm{T}} < 0.55$ GeV/c.

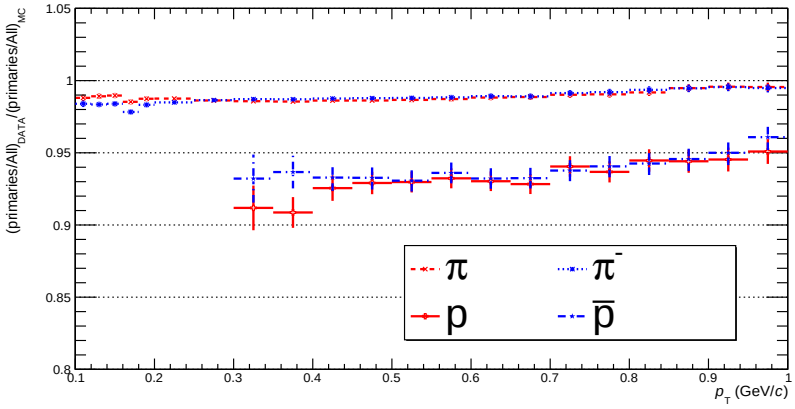

Figure 5.14: Double ratio $(primaries/All)_{DATA}/(primaries/All)_{MC}$ of secondary particle contribution in data and Monte Carlo simulations as a function of p_{T} for pions and protons (multiplicity integrated).

5.5 Systematic uncertainties

Systematic uncertainties in the tracking reconstruction and in the PID approach are mainly originated due to imperfect description in the Monte Carlo simulation:

- of the detector performance,
- of the track cut variables and
- of the relative abundances of π, K and p.

Additional unsatisfactory descriptions, in the simulation used to estimate the corrections applied to the raw spectra, of the material budget, of the "ExB effect"[††] and of the particle interactions with the material have been studied.

Since ITS stand-alone tracking efficiency was found to be independent of the multiplicity in p–Pb collisions, all systematic uncertainties described below are considered as independent of the multiplicity. Hence, they have been estimated based on checks applied to minimum bias spectra.

The systematic source considered in the ITSsa analysis, together with the checks performed in order to quantify them, are described in the following:

Tracking reconstruction:
This systematic uncertainty takes into consideration the imperfect description in the Monte Carlo simulation of the ITS stand-alone tracking reconstruction. It was estimated mainly by means of three mostly independent checks:

- varying track cuts:
  Different sets of cut combinations are checked, where all parameters were fixed while one was changed inside reasonable boundaries. The default selection is shown in **bold** font below.

  Distance of Closest Approach (DCA) cut: 7, 5, 10.
  The default selection $d_0(xy) \leq 7\sigma$ was varied to a tighter (5σ) and a looser (10σ) selection. The cut on the DCA_{xy} is done in order to reduce the fraction of secondary particles in the selected sample. By varying this cut we test the sensitivity of the analysis to the amount of secondary particles in the sample and to the description of the DCA_{xy} variable in the Monte Carlo.

[††] A shift of the cluster position in the SSD and the SDD due to the Lorentz force that acts on the electrons and holes as they drift through the sensors.

$\chi^2/\mathrm{N}_{\mathbf{ITSclusters}}$ **of the tracks: 2.5**, 5.
The χ^2/(# ITS clusters) track cut reduces the contamination from fake tracks. By varying it we check the description of the χ^2/(# ITS clusters) distribution of good and fake tracks in the simulation and the sensibility of the analysis to the fraction of fake tracks.

Number of ITS clusters: 1, 2 clusters in SPD & **at least 3**, 4 clusters in SDD+SSD.
The request of SPD points is used to reduce secondary particles and to improve the resolution on DCA_{xy}, while the request of at least 3 SDD+SSD points improve the ITS dE/dx resolution (i.e improve PID performance in term of efficiency and contamination). At the price of reducing the sample of selected tracks.

For all these cut variation the analysis was repeated and the corrected spectra were calculated using the corresponding efficiency from Monte Carlo simulation. The corrected spectra were compared with those with the default cuts. The ratio as a function of p_{T} for the different sets of cut combination is shown in Fig. 5.15 for all particle species. The maximum deviation among all the variation checks in a given p_{T} interval is used to quantify the contribution of the track selection cuts to the tracking reconstruction systematic uncertainty.

- check on the p_{T} dependence of the track reconstruction:
  This systematic effect is computed as the ratio of a mean tracking efficiency, weighted inside the p_{T} interval with the dN/dp_{T} in the data, and the value of the efficiency in the centre of the p_{T} interval. Tracking efficiency has been estimated by a linear interpolation using the p_{T} bin centre of the current and the immediately lower p_{T} intervals. This effects is considered in order to account for the steep slope of the tracking efficiency as a function of p_{T} (in the region of 0.1–0.2, 0.2–0.5 and 0.3–0.55 GeV/c for π, K and p respectively) and the bias (and resolution) effect on the reconstruction of the track transverse momentum. Indeed, for the calculation of the correction factor (Eq. 5.3), the ratio between reconstructed and generated results is performed, but the p_{T} bias is not present in the denominator. In addition, this systematic uncertainty study the dependence of the track reconstruction with the spectra shape of the Monte Carlo generated particles.

- pseudo-efficiency check:
  Ideally the sum of global tracks and the ITSsa ones has to be equal to the numbers of ITSpureSA tracks, (see Sec. 3.4.2 for definition of global, ITSsa

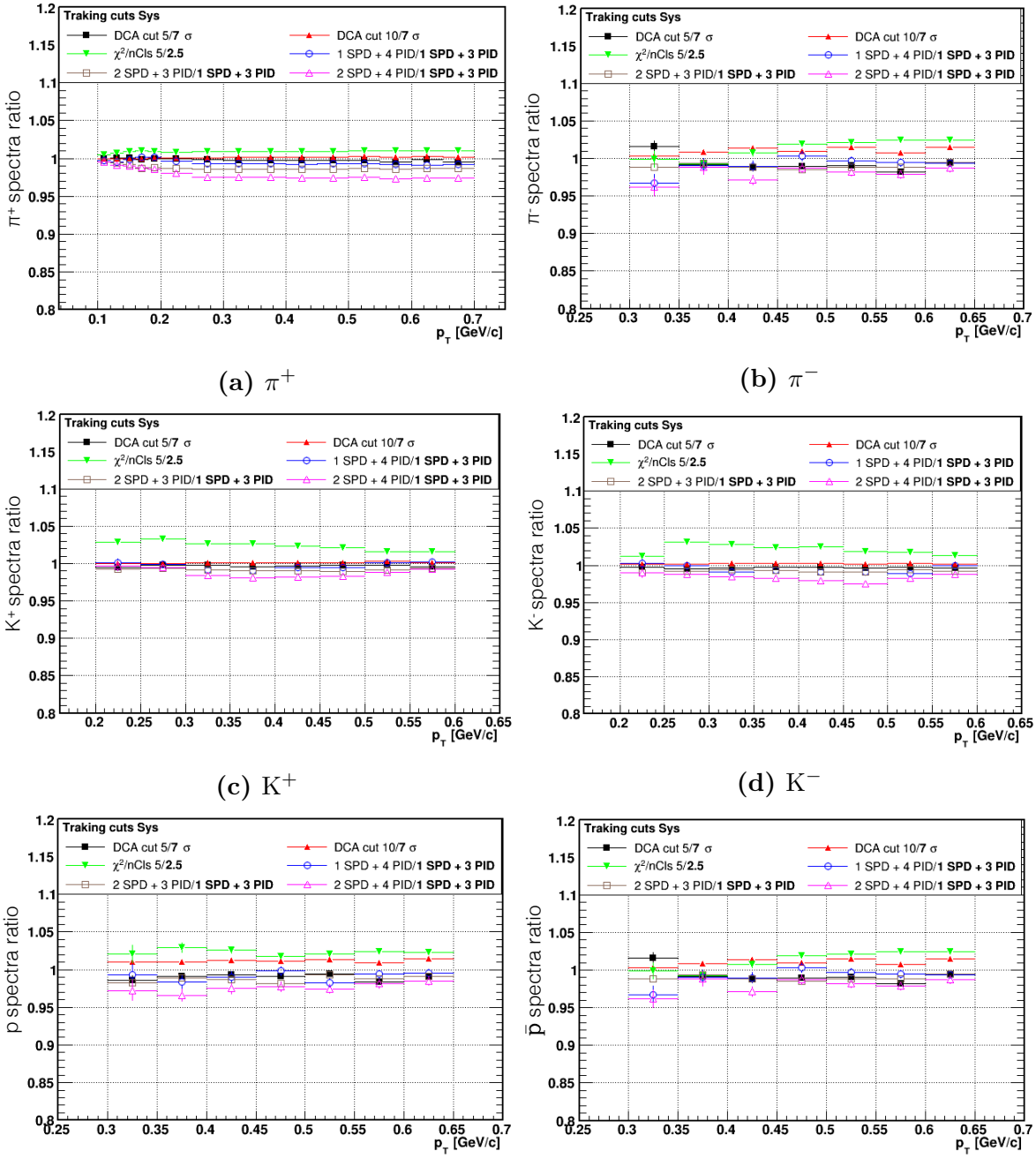

(a) π^+ (b) π^-

(c) K^+ (d) K^-

(e) p (f) $\bar{p}$

Figure 5.15: Systematic studies: Track selection cut checks.

and ITSpureSA tracks). A pseudo-efficiency on ITS pure stand-alone tracking algorithm can be measured by looking at matched tracks in the same phase-space region. A matched track means that we take a ITS+TPC (global) track and we match it with the corresponding ITSpureSA track. The match is done testing the compatibility of ϕ, η and p_{T} between the two tracks. The "pseudo-efficiency" is estimated as the fraction of global track matched to ITSpureSA ones. The Monte Carlo track matching efficiency is evaluated in the same way and the ratio from data/MC, which is $\sim 2\%$ in the p_{T} range where the ITSsa spectra analysis is applied ($p_{\mathrm{T}} < 0.7$), has been taken as a systematic contribution to the tracking efficiency. The results of the checks are reported in Fig. 5.16 for different multiplicity class.

The sum in quadrature of the three check results has been considered as the systematic uncertainty due to the imperfect description in the Monte Carlo simulation of the ITS stand-alone tracking reconstruction.

PID:
The results obtained with the Bayesian PID approach using iterative priors were compared to the obtained with the method based on a cut on the truncated mean $\langle dE/dx \rangle$ [62,63]. The ratio of the corrected spectra obtained from these two different PID approaches for the three particle species p–Pb collisions at $\sqrt{s_{\mathrm{NN}}} = 5.02$ TeV are reported in Fig. 5.17. The deviation of the ratio with respect to unity have been considered as a p_{T} dependent PID systematic uncertainties.

ExB effect:
This effect is not properly taking to account during the reconstruction and simulation. It has been observed from previous spectra analysis checks [62, 63] that the corrected spectra are different when the magnetic field is configured with opposite polarities. The same check in p–Pb spectra analysis results can not be repeated because the p–Pb data sample have been collected using only one magnetic field polarity. In any case, since the magnetic field is the same as in pp collision the effect should be the same. Therefore, the same uncertainty of 3% estimated by previous checks in pp and Pb–Pb collision has been assigned also to p–Pb case.

Description of the material budget in the Monte Carlo simulation:
The ITS stand-alone tracking efficiency was calculated using MC productions with different material budget. The ITS material budget was varied by $\pm$ 7.5%. This uncertainty is not dependent on collision system or on the centre-of-mass energy, therefore the same value evaluated in [133] is used.

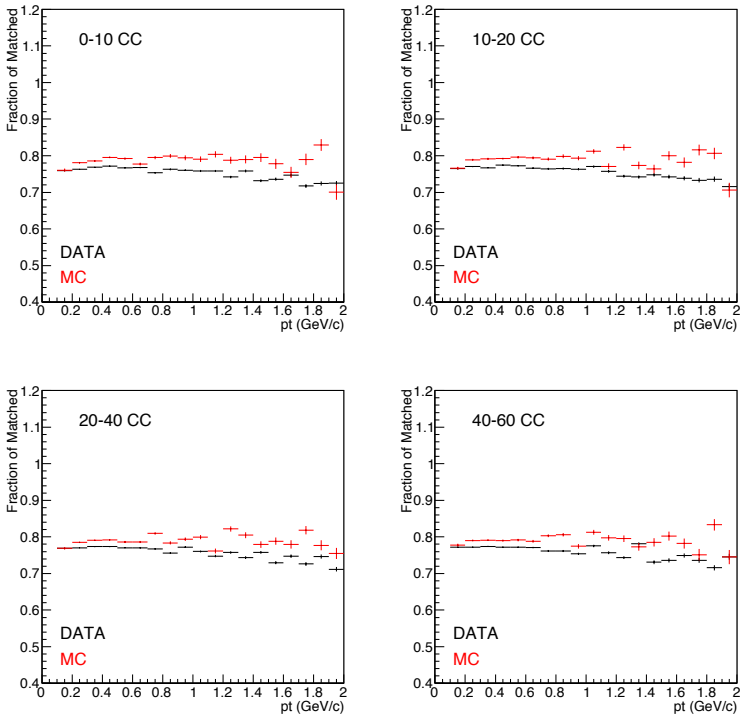

(a) Pseudo-efficiency results for different multiplicity event classes.

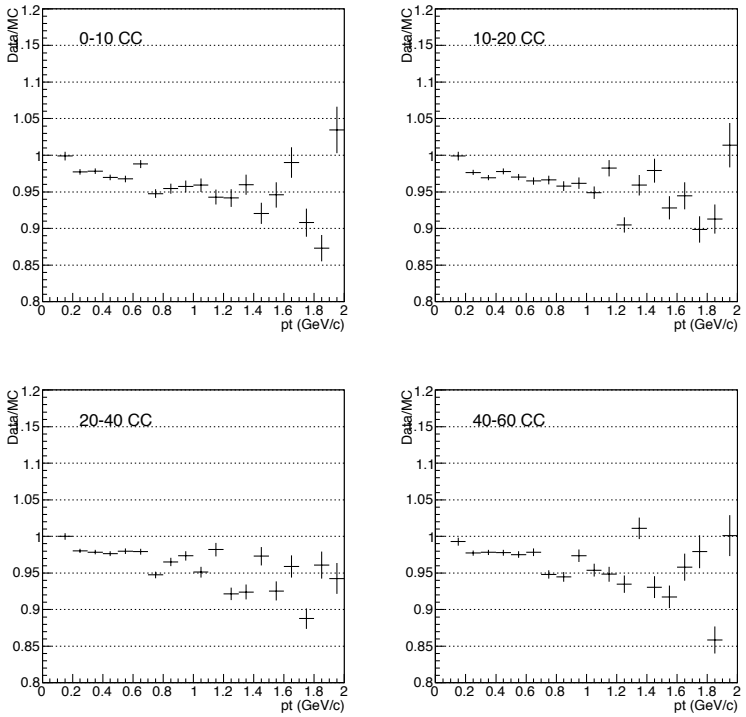

(b) Ratio Data/MC

Figure 5.16: Systematic studies: Pseudo-efficiency check.

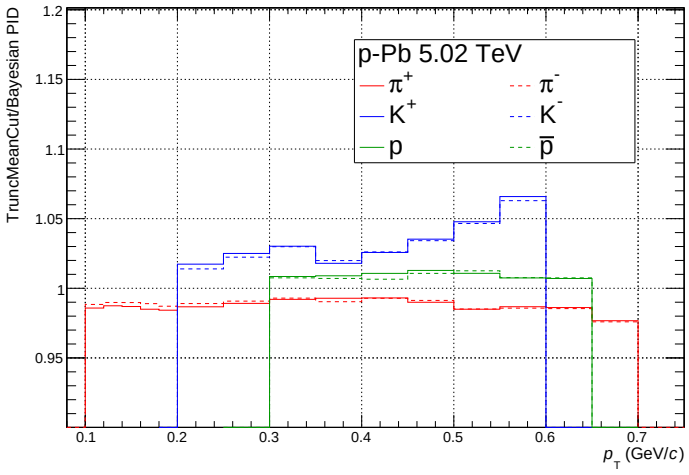

Figure 5.17: Ratio of the corrected spectra with two different PID methods check for π, K and p in p–Pb collisions at $\sqrt{s_{NN}} = 5.02$ TeV.

Geant/Fluka correction:
The difference from Geant4 and Fluka ($\sim 2\%$) for the kaon cross section with material has been considered as a systematic uncertainty. This systematic was applied for negative kaon only (see Sec. 5.4.2).

The main systematic source are summarized in Tab. 5.3. The total systematic uncertainty for the ITSsa analysis calculated as the sum in quadrature of the extracted value from each systematic source (in p_T interval) is reported in Fig. 5.18. The major contributor to the total systematic uncertainties is the systematic effects due to the stand-alone tracking in the ITS, except for kaons at high p_T where the PID systematics is the dominant one.

Source of systematic (lowest–highest p_T point)			
	$\pi^{\pm}$	$K^{\pm}$	p and $\bar{p}$
Track reconstruction	4.0–3.0%	5.0–3.5%	5.0–3.5%
PID procedure	1.0–3.0%	2.0–6.5%	1.5%
ExB	3.0%	3.0%	3.0%
Material budget	5.0–0.5%	2.5–0.5%	4.0–1.0%
Geant/Fluka Correction (K^- only)	–	2.0%	–

Table 5.3: Major ITS source of Systematic uncertainties.

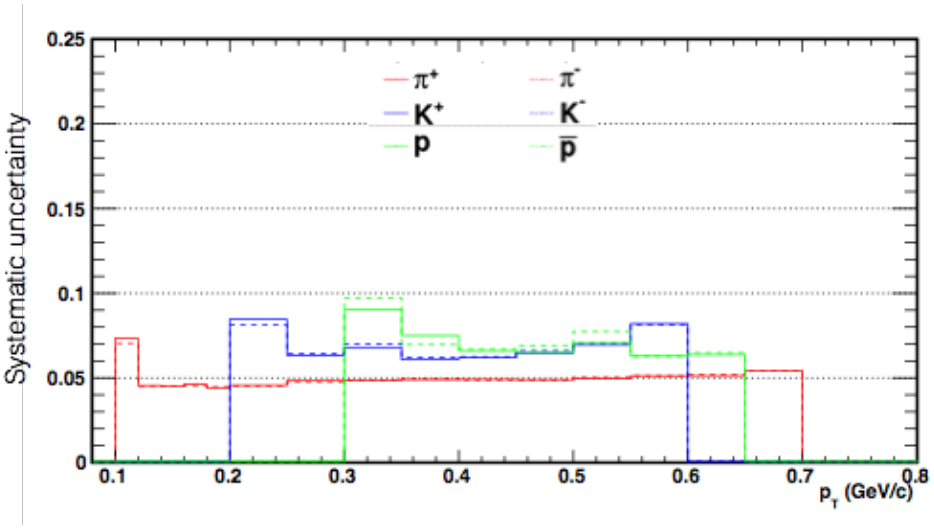

Figure 5.18: Total systematic uncertainty for π, K and p spectra.

5.6 Results

The p_{T} distributions of π, K and p in $0 < \mathrm{y}_{cms} < 0.5$ obtained with the ITSsa analysis in p–Pb collisions at $\sqrt{\mathrm{s}_{\mathrm{NN}}} = 5.02$ TeV are reported in Fig. 5.19 for different multiplicity classes. The boxes indicate the systematic uncertainties, the statistical ones are smaller than the symbols. The results will be discussed in Sec. 7 where they are reported in a broad p_{T} range.

In addition, the ratios of particle/anti-particle are shown in Fig. 5.20. Not all the parts of the systematic uncertainties of the spectra are relevant for the ratio uncertainties. Some of them cancel out, because they are the same for positive and negative particles, e.g. the systematic uncertainty obtained with the pseudo-efficiency check.

Only the systematic uncertainties due to the imperfect description in the simulation of the "ExB" effect and of the interactions with the detector material are propagated from the spectra measurement. The other parts of the total systematic uncertainties (boxes) for the particle ratios have been estimated on the measured ratio itself, without propagating the uncertainty from single p_{T} distribiutions. In this way the correlated systematic sources for particles and anti-particles are expected to cancel out. The statistical uncertainties are represented as bars.

The particle/anti-particle transverse momentum distributions are compatible within uncertainties. The latter is also valid for the full p_{T} range of the measured π, K and p distributions. For this reason, in Sec. 7, the spectra results are discussed for the summed charge states.

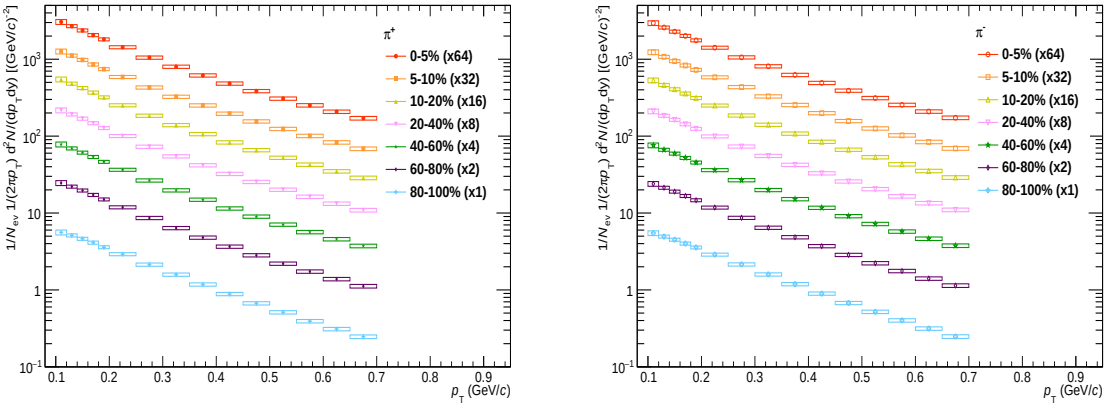

(a) Pions

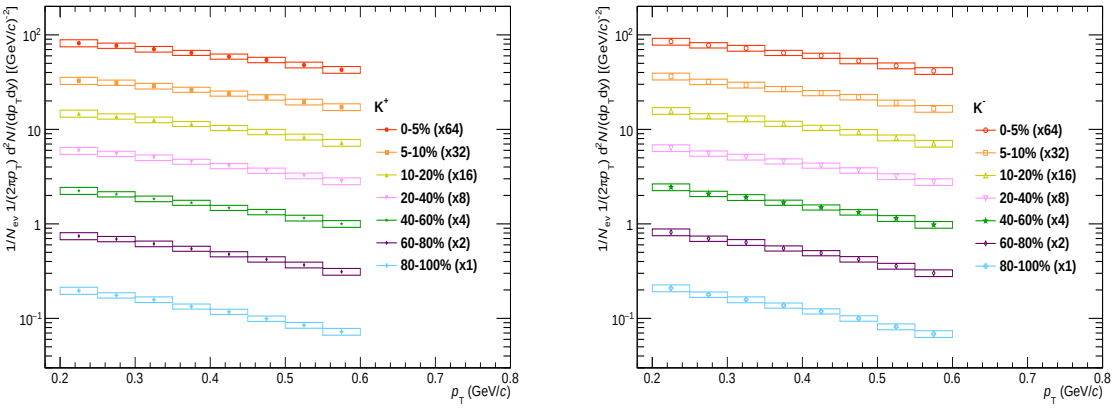

(b) Kaons

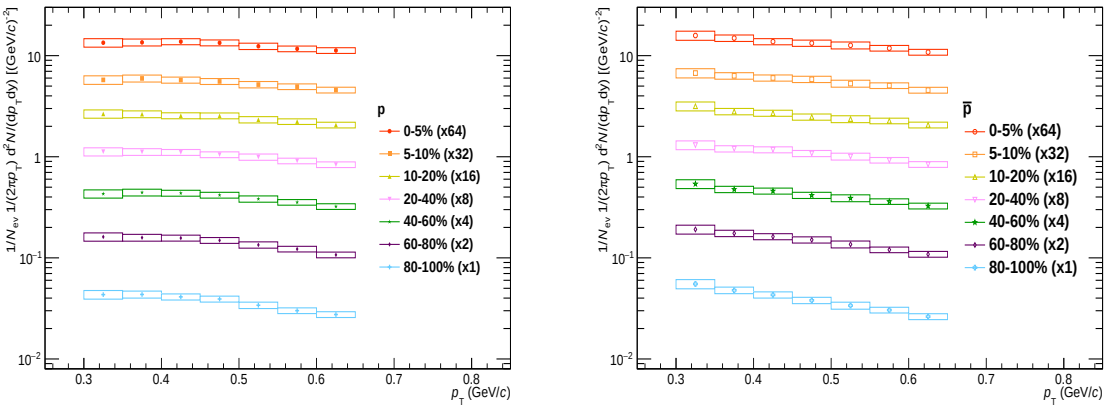

(c) Protons

Figure 5.19: Invariant p_{T}-differential yields of (a) pions, (b) kaons and (c) protons in different V0A multiplicity classes measured in the rapidity interval $0 < \mathrm{y}_{cms} < 0.5$. Top to bottom: central to peripheral; data scaled by 2^n factors for better visibility. The systematic uncertainties are shown as boxes, the statistical ones are smaller than the symbols.

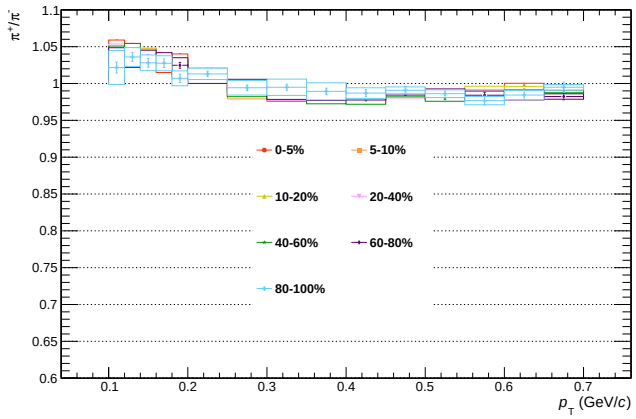

(a) Pions

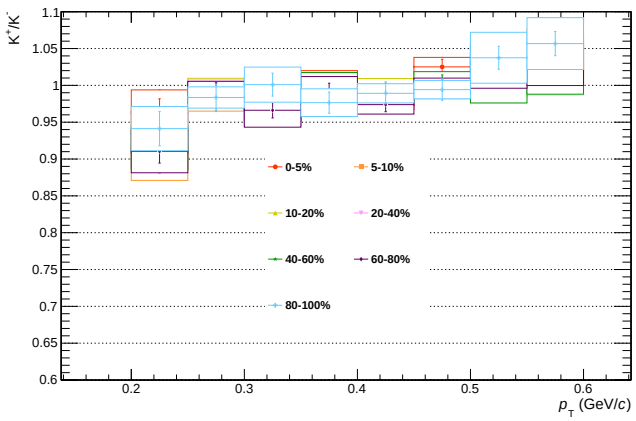

(b) Kaons

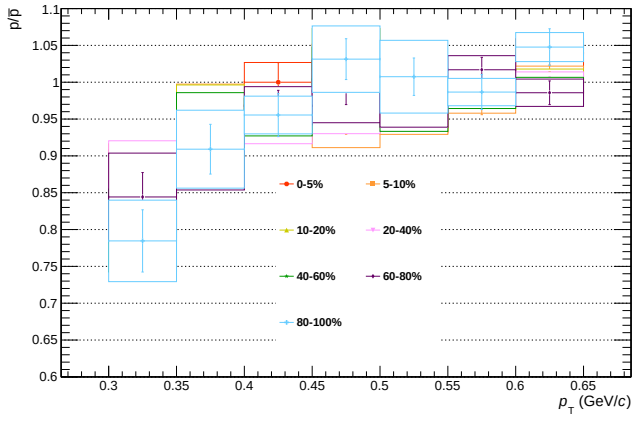

(c) Protons

Figure 5.20: Ratio of the negative to positive particle spectra in p–Pb collisions at $\sqrt{s_{NN}} =$ 5.02 TeV. The systematic uncertainties are shown as boxes and the statistical ones as bars.

5.6.1 Systematic check for vertex correction

In p–Pb collision the vertex reconstruction is not 100% efficient, which means that in a fraction of about 2%, mostly in the low multiplicity collision, the interaction vertex is not reconstructed. In the case of the analysis in multiplicity classes the vertex reconstruction inefficiency is more relevant for the low-multiplicity event classes, where the average multiplicity of produced particles is lower than that of pp minimum-bias collisions.

A systematic check on the vertex reconstruction efficiency is shown in Fig. 5.21 for positive pions. It has been studied from the ratio of the corrected spectra for vertex reconstruction efficiency and the spectra without this correction. As it can be seen the correction for vertex reconstruction efficiency is relevant for the lowest multiplicity bin (80–100%), where it can arrive up to 2%, and it is independent of p_{T}.

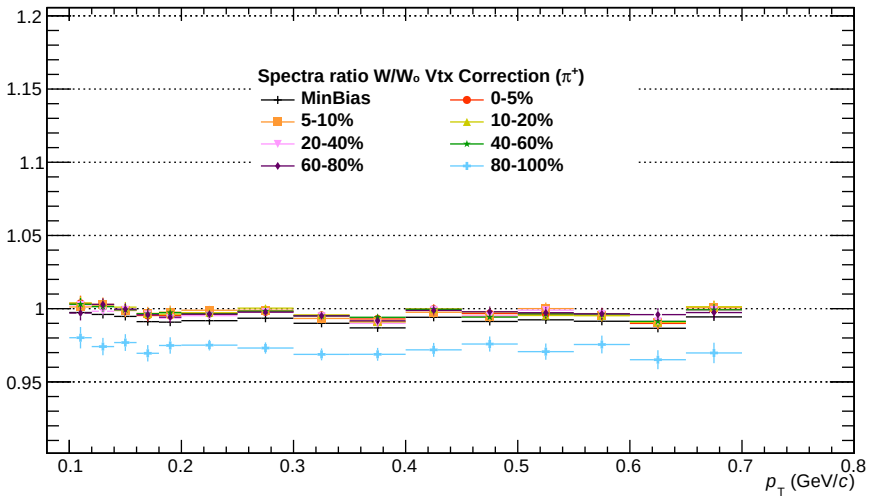

Figure 5.21: Ratio between the spectra with and without vertex reconstruction correction for positive pions in p–Pb collisions at $\sqrt{s_{\mathrm{NN}}} = 5.02$ TeV.

In this systematic check it is assumed that the vertex-finding probability is independent of the position of the collision vertex along the beam axis. The latter have been found to be not true and difference in the vertex reconstruction efficiency of 10% in the 80–100% multiplicity bin is observed between the collisions at $z = 0$ and collisions at $z = \pm 10$cm. The latter can introduce up to 10% systematic uncertainty, in the combined spectra reported in Sec. 7, due to the inefficiency of the vertex reconstruction.

6 Comparing and combining spectra

The combination of different detectors which use different PID techniques allows to the ALICE experiment the measurement of π, K and p spectra over a broad p_{T} range. Each method contributes to complementary but also partially overlapping p_{T} intervals. Those intervals are mainly determined by the PID capability of the detector which is used for particle identification. The endowment of the combine measurement is that each analysis is mostly independent, resulting in largely independent systematic uncertainties.

The following analyses are the ones used for the identification of $\pi^{\pm}$, $\mathrm{K}^{\pm}$, p and $\bar{\mathrm{p}}$ in the low-intermediate p_{T} range by the ALICE experiment:

ITSsa: ITS stand-alone analysis. It has been described in detail in the previous chapter using as example the analysis performed on the data sample of p–Pb collisions at $\sqrt{s_{\mathrm{NN}}} = 5.02$ TeV. The author has also carried out the ITSsa analysis, following the same procedure described in Sec. 5, to determine π, K and p distributions at low p_{T} in pp collisions at $\sqrt{s} = 2.76$ TeV. The ITSsa analysis is the only one which uses a different set of tracks, therefore the π, K and p distributions obtained with this analysis are completely uncorrelated, in terms of systematic uncertainty, with respect to the results of the other analyses.

TPCTOF: The TPCTOF combined measurement is done using global tracks, which are tracks reconstructed in TPC, prolonged to the ITS and propagated to the outer detectors (TOF, HMPID ...). Particles are identified on a track-by-track basis by applying a 3σ cut on the deviation between the measured PID signal (energy loss signal in the TPC and the measured time of flight in the TOF) and the expected value under a given mass hypothesis. For tracks without a matching hit in the TOF, only a 3σ cut on the dE/dx in the TPC is applied.

TOF: global tracks are used in this analysis. The identification is based on the time-of-flight measured by TOF. In order to extract π, K and p yields, the distribution of time of flight of tracks in a given p_{T} interval is fitted with the expected shapes of π, K and p time-of-flight distributions based on the knowledge of the TOF response function for different particle species.

In this chapter, the π, K and p spectra obtained with the ITSsa analysis are compared with the TPCTOF ones in p–Pb collisions at $\sqrt{s_{NN}} = 5.02$ TeV and pp collisions at $\sqrt{s} = 2.76$ TeV. The comparison is performed only with the TPCTOF because it is the analysis that has a broad overlapping p_T range with the ITSsa analysis and the TPCTOF and TOF results are compatible within systematic uncertainties. In addition, the combination procedure used to obtain the π, K and p spectra in a larger p_T range will be described.

6.1 p–Pb analysis

The p_T distributions of π, K and p in p–Pb collisions at $\sqrt{s_{NN}} = 5.02$ TeV with the ALICE detector have been obtained with the three different analyses described above. The momentum covered by each analysis are reported in Tab. 6.1.

Analysis	π range GeV/c	K range GeV/c	p range GeV/c
ITSsa	0.1–0.7	0.2–0.6	0.3–0.65
TPCTOF	0.2–1.5	0.3–1.3	0.5–2.0
TOF	0.5–3.0	0.5–2.5	0.5–4.0

Table 6.1: p_T ranges (GeV/c) covered by the different π, K and p spectra analyses in p–Pb collisions at $\sqrt{s_{NN}} = 5.02$ TeV.

The main sources of systematic uncertainties associated with the measurement of π, K and p spectra with the TPCTOF and TOF analyses are summarised in Tab. 6.2. They have been evaluated in a similar way as described for the ITSsa analysis in Sec. 5.5.

The uncertainties due to the subtraction for secondary particles were calculated varying the range of the DCA_{xy} fits inside a reasonable interval. Furthermore, the quality of the fit was controlled taking the ratio between the sum of the Monte Carlo templates (primary, weak decay and material) and the data.

The uncertainty on the energy loss correction was estimated by using a simulation with the material budget scaled by $\pm 7\%$. The contribution from hadronic interactions has been estimated, as described in Sec. 5.4.2, by comparing different transport codes (Geant3, Geant4 and Fluka). These systematic effects are not dependent on the collision energy and system, hence the same values found in previous analysis of Pb–Pb collisions were used. The tracking efficiency systematic uncertainty for global tracks was investigated by comparing different sets of tracks in data and Monte Carlo and by varying the quality selections. Its value has been taken from [34]. The uncertainty due

to TPCTOF PID procedure was estimated by varying the PID cuts between ±2 and ±4 σ (the standard was ±3σ). The systematic effect due to the yield extraction in the TOF analysis were calculated by varying the fit parameters by ±10%.

effect	$\pi^{\pm}$		$K^{\pm}$		p and $\bar{p}$	
p_T range (GeV/c)	0.2	3	0.3	2.5	0.5	4
correction for secondaries	1%	1%	negl.		4%	1%
material budget	3%	negl.	3%	negl.	3%	negl.
hadronic interation	2%	1%	3%	1%	6% 4%	1% ($\bar{p}$) negl. (p)
global tracking efficiency	4%		4%		4%	
multiplicity dependence	2%	negl.	5%	negl.	2%	negl.
p_T range (GeV/c)	0.2	0.65	0.3	0.6	0.5	0.8
TPC PID	1.5%		3.5%		2.5%	
p_T range (GeV/c)	0.5	3	0.5	2.5	0.5	4
TOF matching efficiency	4%	3%	5%	4%	5%	3%
TOF PID	1%	10%	2%	17%	2%	20%

Table 6.2: Main sources of systematic uncertainty for TPCTOF and TOF analyses in p–Pb collisions at $\sqrt{s_{NN}} = 5.02$ TeV.

6.1.1 Uncorrelated systematic uncertainties

Most of the sources of systematic uncertainties discussed in previous sections are strongly correlated across different multiplicity classes. This is illustrated for instance in Fig. 6.1: where a given variation of e.g. PID cuts is applied to the high and low multiplicity samples, the p/π ratio changes in the same direction for both multiplicity classes. The effect is relevant for the systematic uncertainties at high p_T.

In order to estimate the contribution to the systematic uncertainty uncorrelated among the multiplicity classes, the minimum bias results were used as a reference. For instance, in the case of p/π, the double ratios

$$\frac{\mathrm{p}/\pi_{[0-5\%]}}{\mathrm{p}/\pi_{[\mathrm{MB}]}} \quad \text{and} \quad \frac{\mathrm{p}/\pi_{[60-80\%]}}{\mathrm{p}/\pi_{[\mathrm{MB}]}} \tag{6.1}$$

were taken and the same systematic studies were repeated on the double ratios.

Systematic effects which are correlated between multiplicity intervals cancel in this ratio. The effect of applying the same PID variation mentioned above to the double ratios is shown in Fig. 6.2. Only a small difference is seen. This is assigned as the uncorrelated part across the multiplicity classes of the systematic uncertainty, due to the PID cut.

The same procedure is repeated for all the relevant sources of systematic uncertainty to get the systematic uncertainty uncorrelated among the multiplicity classes for the particle ratios and the $\langle p_{\mathrm{T}} \rangle$.

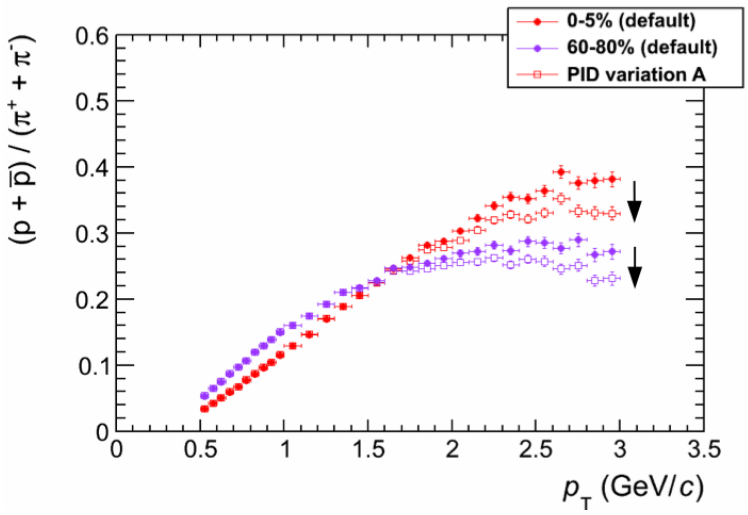

Figure 6.1: Effect of PID variation for the TOF analysis on the p/π ratio.

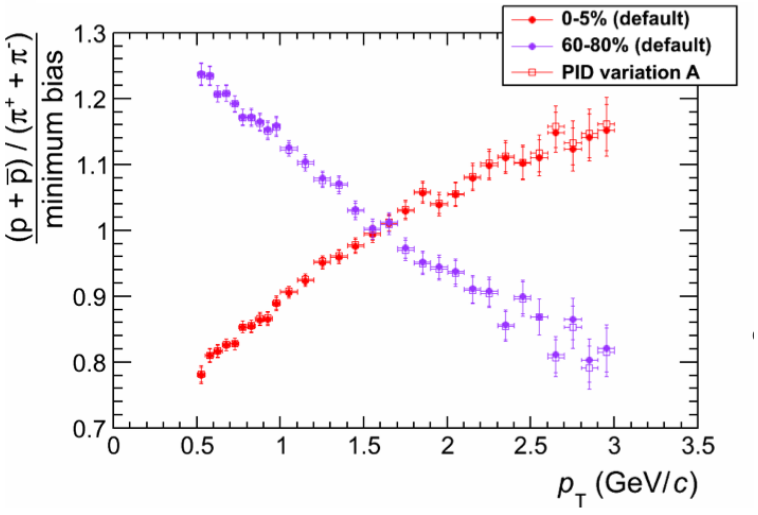

Figure 6.2: Effect of PID variation on the $(\mathrm{p}/\pi_{[0-5\%]})/(\mathrm{p}/\pi_{[MB]})$ and $(\mathrm{p}/\pi_{[60-80\%]})/(\mathrm{p}/\pi_{[MB]})$ double ratios in the TOF analysis.

6.1.2 Comparison of different analyses

As mentioned above, the TPCTOF is the only analysis which has an overlapping p_T range with the ITSsa analysis. The comparison between the ITSsa and TPCTOF spectra for $\pi^+ + \pi^-$, $K^+ + K^-$ and $p + \bar{p}$ in different V0A multiplicity bins are shown in Fig. 6.3, 6.4 and 6.5. The ratio between the spectra of the two analyses is reported in the lower panels of the figures.

In the ratio plots, the ITSsa systematic uncertainties are represented as shaded boxes while the bars indicate the TPCTOF systematic uncertainties. The two analyses are in very good agreement within their uncertainties in the overlapping p_T range for all the multiplicity classes and particle species.

6.2 pp collisions at $\sqrt{s}$ = 2.76 TeV

The π, K and p distributions in the low-intermediate p_T range have been measured in pp collisions at $\sqrt{s}$ = 2.76 TeV with the ALICE detectors. The data were collected using the minimum bias (MB_{OR}) trigger selection. The main goal of this measurement is to provide the reference spectra for the nuclear modification factor (R_{AA}) of identified hadrons in Pb–Pb collisions at $\sqrt{s_{NN}}$ = 2.76 TeV.

In addition to the analyses described in p–Pb collisions, the HMPID analysis has been used as bridge between the intermediate and the high-p_T spectra [119]. In this way the systematic uncertainties in the overlapping p_T interval covered by both HMPID and high-p_T analysis are reduced. The HMPID π, K and p analysis is based on the measurement of the Cherenkov angle θ in the HMPID detector to identify tracks reconstructed in TPC+ITS and matched to a hit in the HMPID. The yields of π, K and p are extracted using a statistical unfolding method. On the other hand, the high-p_T analysis allows us to extend the measurement of the π, K and p distributions up to p_T = 20 GeV/c. The analysis is performed based on the dE/dx of the global tracks in the relativistic rise regime of the TPC Bethe-Bloch (BB) curve, where the $\langle dE/dx \rangle$ separation between particles with different masses is nearly constant. The π, K and p yields are extracted by fitting a sum of four Gaussian functions (including electrons) to the dE/dx distribution in a given p interval. To reduce the degrees of freedom in the fits from 12 to 4, parametrizations of the BB ($\langle dE/dx \rangle$) and resolution (σ) curves as a function of $\beta\gamma$ are extracted first using tracks from identified particles. The particle yields in a p_T interval are obtained as the weighted average of the contributing momentum (p) intervals [119].

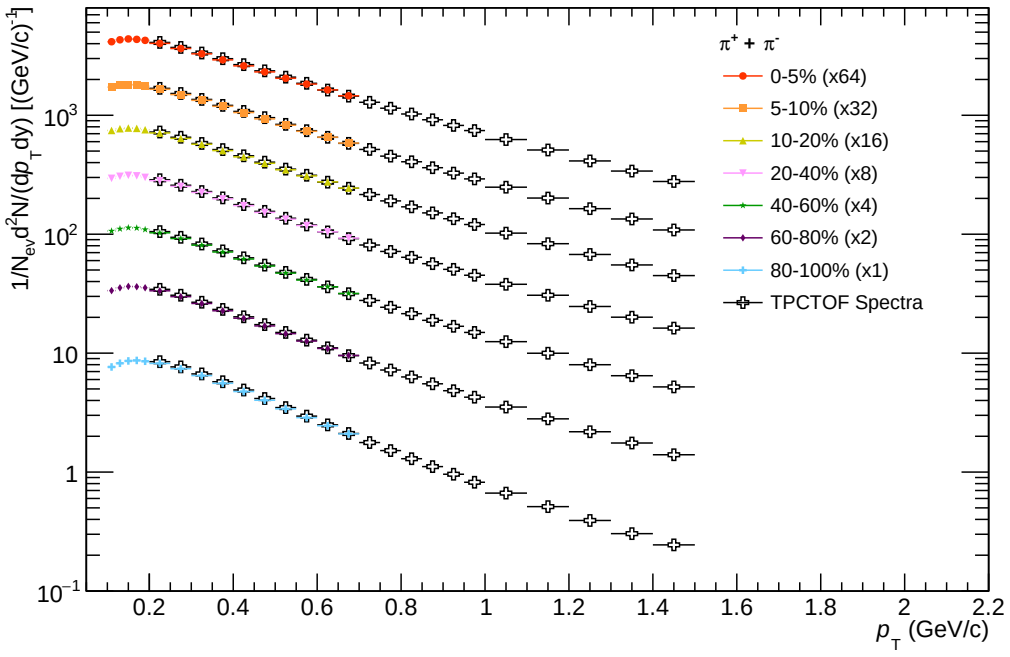

(a)

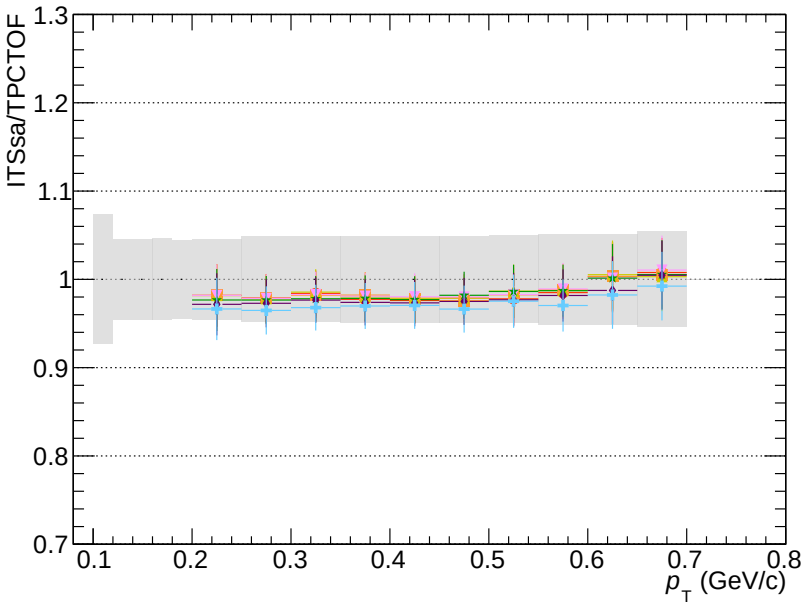

(b)

Figure 6.3: ITSsa and TPCTOF (a) spectra and (b) their ratio for $\pi^+ + \pi^-$ in different multiplicity classes. The ITSsa systematic uncertainties are shown as shade boxes in the lower panel while the bars indicate the TPCTOF systematic uncertainties.

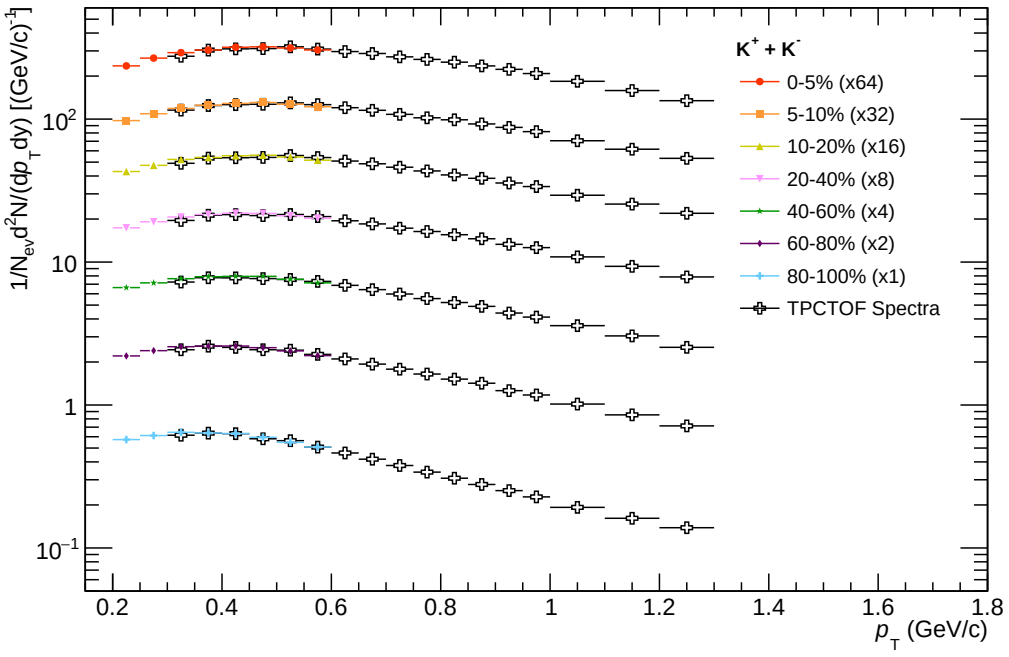

(a)

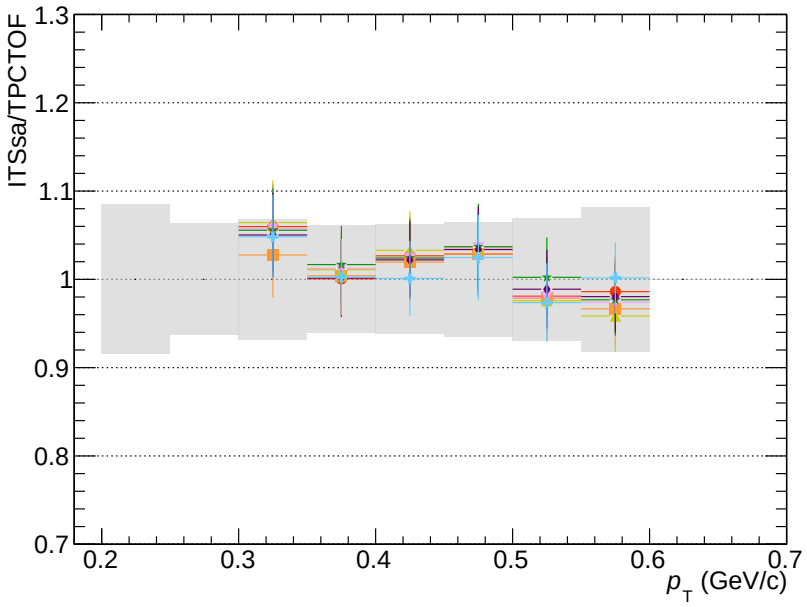

(b)

Figure 6.4: ITSsa and TPCTOF (a) spectra and (b) their ratio for $K^+ + K^-$ in different multiplicity classes. The ITSsa systematic uncertainties are shown as shade boxes in the lower panel while the bars indicate the TPCTOF systematic uncertainties.

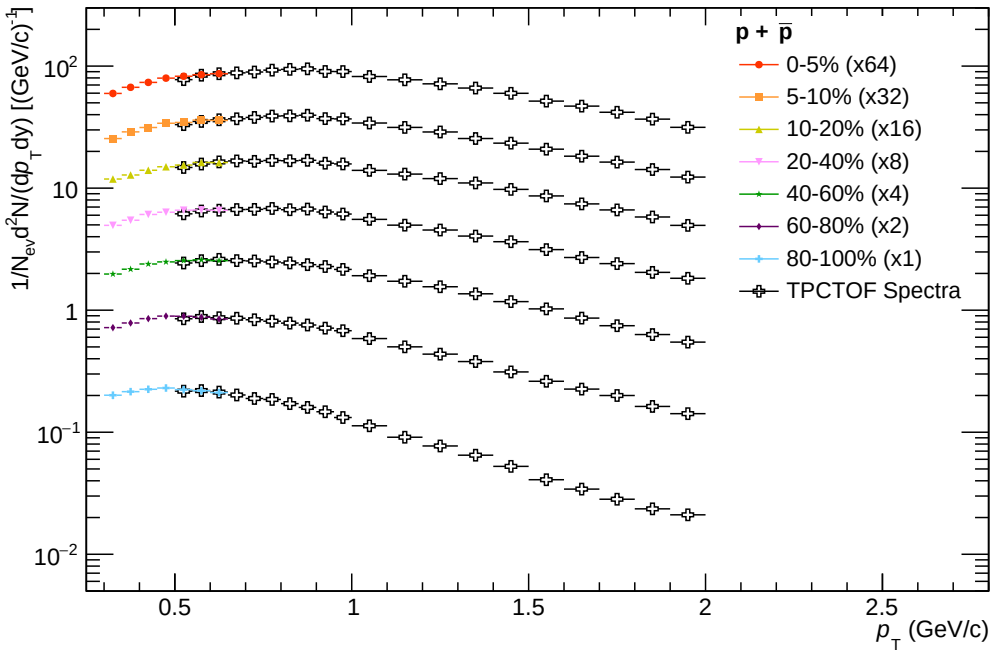

(a)

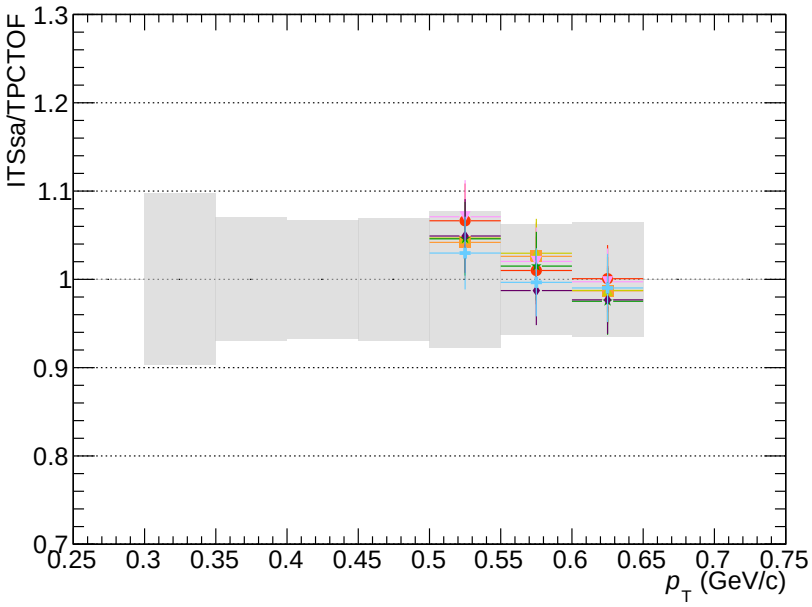

(b)

Figure 6.5: ITSsa and TPCTOF (a) spectra and (b) their ratio for $p + \bar{p}$ in different multiplicity classes. The ITSsa systematic uncertainties are shown as shade boxes in the lower panel while the bars indicate the TPCTOF systematic uncertainties.

The momentum ranges covered by the analyses in pp collisions at $\sqrt{s}$ = 2.76 TeV are shown in Tab. 6.3.

Analysis	π range GeV/c	K range GeV/c	p range GeV/c
ITSsa	0.1–0.7	0.2–0.55	0.3–0.6
TPCTOF	0.3–1.2	0.3–1.2	0.45–2.0
TOF	0.5–2.5	0.5–2.4	0.8–3.8
HMPID	1.5–4.0	1.5–4.0	1.5–6.0
High-p_{T} dE/dx	2.0–20	3.0–20	3.0–20

Table 6.3: p_{T} ranges (GeV/c) covered by the different spectra analyses in pp collisions at $\sqrt{s}$ = 2.76 TeV.

In Fig. 6.6 the four analyses used in the low-intermediate p_{T} range, ITSsa, TPCTOF, TOF and HMPID, normalized to the number of events after the physic selection are superimposed in log scale. The bars displayed in the plots are the total systematic uncertainties.

The single analyses were combined together to obtain the pion, kaon, and proton spectra over one p_{T} range using the procedure described in the next section. To check that all the analyses are compatible in the overlapping p_{T} regions and hence that they can be combined, we computed the ratios between them considering only the uncorrelated systematic uncertainties.

In Fig. 6.7, 6.8, 6.9 the ratios TPCTOF/ITSsa, TPCTOF/TOF and HMPID/TOF for pions (red), kaons (blue) and protons (green) are shown: filled markers refer to particles while open marker to anti-particles. As it can be seen, all these ratios are compatible with unity for all the particle species within uncertainties.

6.3 Combination of the spectra

The different analyses were combined together using a weighted mean procedure. In this procedure, the uncorrelated systematic uncertainties among analyses are used as weights. The correlated systematic uncertainties are added later to the combined result and summed in quadrature to the uncorrelated ones.

For instance, in pp collisions at $\sqrt{s}$ = 2.76 TeV the procedure is the following:

- The TPCTOF and the TOF spectra are combined using as weight their own systematics except the matching efficiency (common to both the analyses). We refer to this first combined spectra as TPCTOF+TOF. The uncorrelated uncertainties

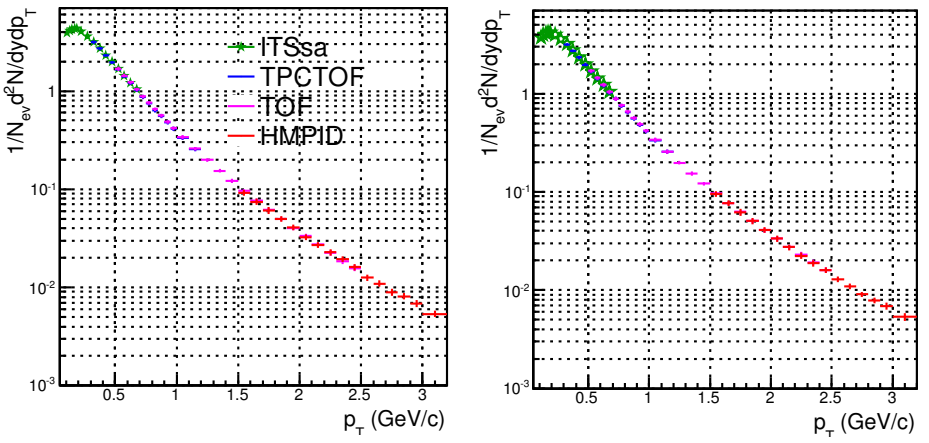

(a)

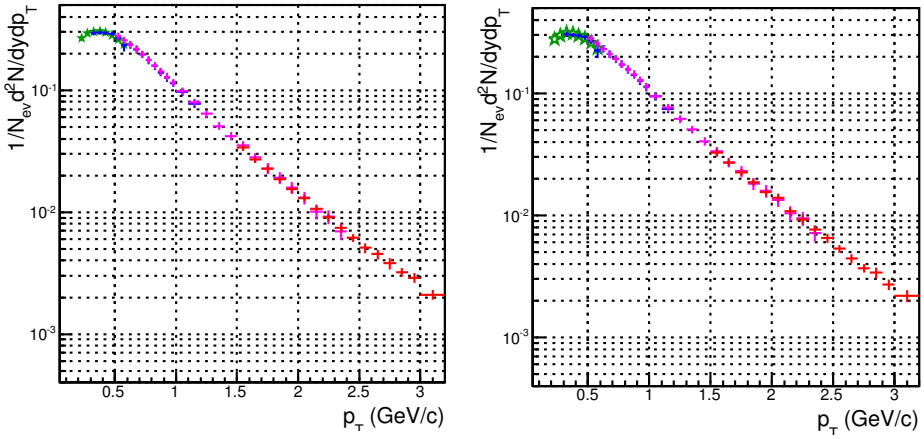

(b)

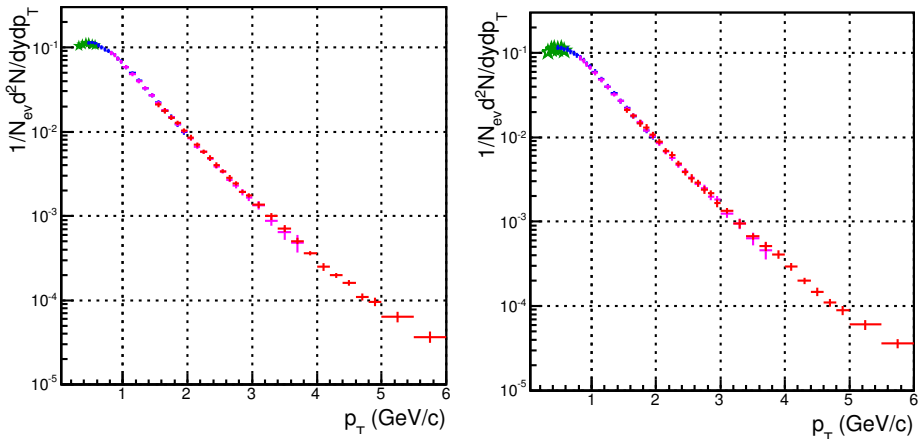

(c)

Figure 6.6: p_{T} distributions of (a) pions, (b) kaons and (c) protons for the four independent analyses used in the low-intermediate p_{T} range. Left column: particles. Right column: anti-particles.

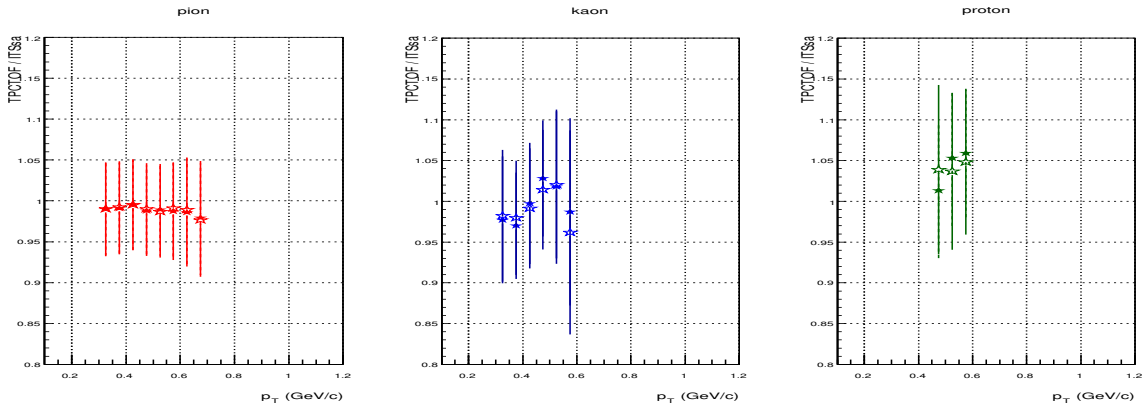

Figure 6.7: Ratio between TPCTOF and ITSsa analysis results. Left panel: pions, middle: kaons, right: protons. Filled markers for particles while open markers for anti-particles.

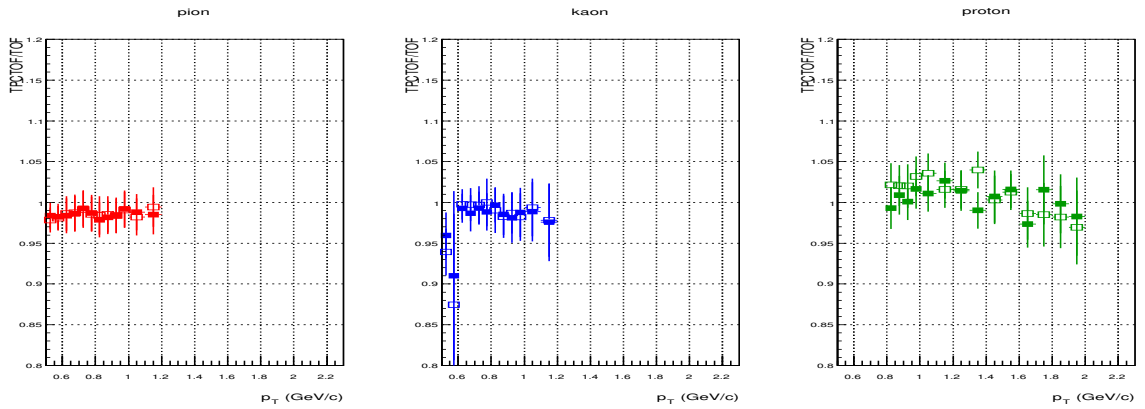

Figure 6.8: Ratio between TPCTOF and TOF analysis results. Left panel: pions, middle: kaons, right: protons. Filled markers for particles while open markers for anti-particles.

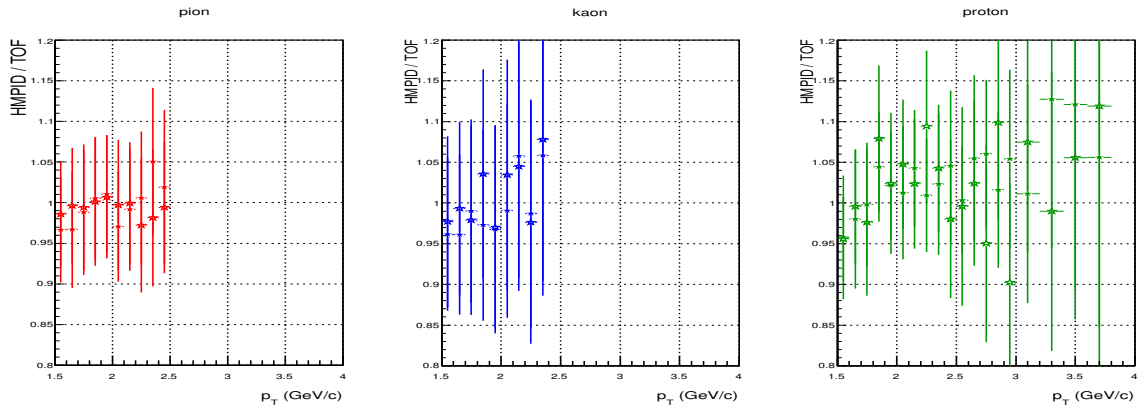

Figure 6.9: Ratio between HMPID and TOF analysis results. Left panel: pions, middle: kaons, right: protons. Filled markers for particles while open markers for anti-particles.

are propagated through the weighted-mean procedure to estimate the uncertainty of the TPCTOF+TOF combined spectra.

If $\frac{dN}{dp_{\mathrm{T}}}^{TPCTOF}$ and $\frac{dN}{dp_{\mathrm{T}}}^{TOF}$ are the yields for a given particle species in a given p_{T} interval, which are obtained from the TPCTOF and TOF analyses respectively, the weighted average TPCTOF+TOF yield and its uncorrelated systematic uncertainty are calculated as:

$$\frac{dN}{dp_{\mathrm{T}}}^{TPCTOF+TOF} = \frac{\frac{dN}{dp_{\mathrm{T}}}^{TPCTOF}/\sigma^2_{TPCTOF} + \frac{dN}{dp_{\mathrm{T}}}^{TOF}/\sigma^2_{TOF}}{1/\sigma^2_{TPCTOF} + 1/\sigma^2_{TOF}} \tag{6.2}$$

$$\sigma^2_{TPCTOF+TOF} = \left[\frac{1}{\sigma^2_{TPCTOF}} + \frac{1}{\sigma^2_{TOF}}\right]^{-1} \tag{6.3}$$

where σ_{TPCTOF} and σ_{TOF} are the uncorrelated systematic uncertainties of the TPCTOF and the TOF analysis, respectively.

- The systematic uncertainty on the matching efficiency are added in quadrature to the systematic uncertainties of the TPCTOF+TOF spectra (only in the region where the TOF is used)
- The TPCTOF+TOF spectra are combined with the HMPID ones using as weight their uncorrelated systematic uncertainties. We refer to this combined spectra as TPCTOF+TOF+HMPID.
- The tracking systematic uncertainty, the uncertainty on the material budget and that on the cross section with the material are added at this stage to the latter spectra since they are common to the three analyses.
- Finally the TPCTOF+TOF+HMPID spectra are combined to the ITSsa ones.

The same procedure is used for p–Pb collisions with the difference that only three analyses are averaged together since the HMPID results were not available.

With this method, the weights are only uncorrelated systematic uncertainties. The whole procedure is shown on Figure 6.10 for the analysis performed for pp collisions at $\sqrt{\mathrm{s}}$ = 2.76 TeV. Each step of the combination procedure is shown. In particular, each figure shows the ratios between the input spectra at a given step of the procedure and the combined spectra after this step. The coloured lines (not black) indicate the uncorrelated systematic uncertainties on the input spectra. The yellow areas show the systematic uncertainties which result from the combination of the input spectra. The black lines are the final systematic uncertainties after adding the correlated ones from the input spectra.

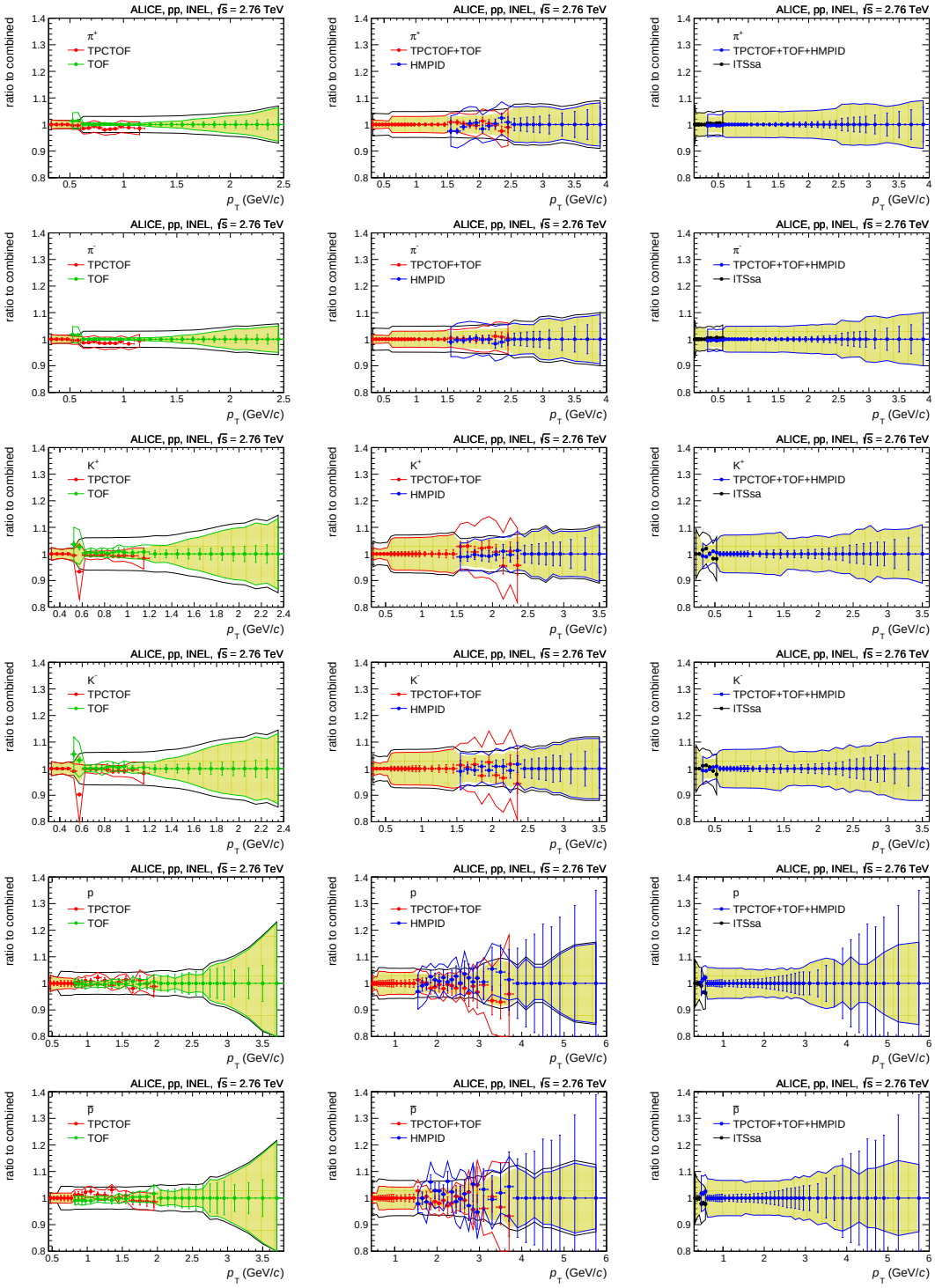

Figure 6.10: Procedure used to combine the spectra of different particles species. Each row is a given species. The first column shows the combination of TPCTOF and TOF spectra, the second column the combination with HMPID spectra and last column the average with the ITSsa to obtain the final result. The coloured lines (not black) indicate the uncorrelated systematic uncertainties of the input spectra. The yellow areas show the systematic uncertainties which result from the combination of the input spectra. The black lines are the final systematic uncertainties after adding the correlated ones.

7

Multiplicity dependence of pion, kaon and proton production in p–Pb collisions

The transverse momentum distributions of identified hadrons, like π, K and p, encodes information about the collective radial flow velocity ($\langle\beta_{\rm T}\rangle$) and the kinetic freeze-out temperature ($\rm T_{kin}$) of the medium created in A–A and p–A collisions. In this chapter, the results from p–Pb collisions at $\sqrt{\rm s_{NN}} = 5.02$ TeV are presented in different multiplicity classes, as defined in Sec. 5.1.1. The π, K and p distributions have been measured in different $p_{\rm T}$ ranges using three mostly independent analyses:

- ITSsa
- TPCTOF
- TOF

The $p_{\rm T}$ range used by each analysis have been summarised in Tab. 6.1. The spectra for each particle species over a broad $p_{\rm T}$ range are obtained by combining together the results from the individual analyses. The procedure used for the combination has been described in Sec. 6.3. Since the $p_{\rm T}$ distribution of positive and negative particles have been found to be compatible within uncertainties over the full measured $p_{\rm T}$ range, the results will be reported for the sum of particles and anti-particles. As described in Sec. 6.1.1, the study of the systematic uncertainties was repeated for the different multiplicity intervals in order to separate the contributions uncorrelated among different multiplicity bins (depicted as shaded boxes in the figures).

7.1 $p_{\rm T}$ distributions of primary π, K and p

The measured $\pi^{\pm}$, $\rm K^{\pm}$ and $\rm p(\bar{p})$ $p_{\rm T}$ distributions for different multiplicity classes in p–Pb collisions at $\sqrt{\rm s_{NN}} = 5.02$ TeV are reported in Fig 7.1 for the sum of particle and anti-particle states (from [142]). The spectra have been measured in the rapidity interval $0 < \rm y_{\it cms} < 0.5$ in the centre-of-mass system (cms). The fits with the blast-wave function

(Eq. 2.9) to the individual spectra are represented as dashed lines. These fits are used to extrapolate the spectra down to zero and to high p_{T} (see Sec. 7.2).

The shape of the p_{T} distributions evolves with the multiplicity of the collision, becoming harder as the multiplicity increases. This effect is mostly pronounced for protons. They also show an increase of the slope at low p_{T} ($p_{\mathrm{T}} \lesssim 0.5$ GeV/c) of the spectra with respect to the high p_{T} range, similar to the one observed in Pb–Pb collisions at $\sqrt{s_{\mathrm{NN}}} =$ 2.76 TeV [62, 63].

The stronger multiplicity dependence of the proton spectra is evident when the ratios $\mathrm{K}/\pi = (\mathrm{K}^+ + \mathrm{K}^-)/(\pi^+ + \pi^-)$ and $\mathrm{p}/\pi = (\mathrm{p} + \bar{\mathrm{p}})/(\pi^+ + \pi^-)$ are calculated as a function of p_{T}, the results are shown in Fig. 7.2 for the 0–5% and 60–80% multiplicity classes (left panel). The ratios are compared to the results in Pb–Pb collisions at $\sqrt{s_{\mathrm{NN}}} = 2.76$ TeV measured at mid-rapidity for 0–5% and 80–90% centrality classes (right panel). The systematic uncertainties are shown as empty boxes. As discussed in Sec. 6.1.1 they are strongly correlated across the multiplicity intervals, in particular at high p_{T}. The fraction of the uncertainty uncorrelated among multiplicity intervals is displayed as a shaded box (which is smaller than the marker size). The same study on the uncorrelated and correlated systematic uncertainties in Pb–Pb collisions data is not available.

The K/π ratio shows a weak evolution (considering only the shaded boxes uncertainties) with the multiplicity in p–Pb collisions. This behaviour is similar to that observed in Pb–Pb collisions. On the other hand, the p/π ratio exhibits a significant enhancement with increasing multiplicity at intermediate $p_{\mathrm{T}} \sim 3$ GeV/c, qualitatively reminiscent of that measured in Pb–Pb collisions. The Pb–Pb results are generally explained in terms of collective flow or hadronization via quark recombination [143–145]. The magnitude of the enhancement differs significantly between p–Pb and Pb–Pb results. For instance, the maximum of the ratio p/π reaches ~ 0.8 in the 5% most central Pb–Pb collisions, but only ~ 0.4 in the higher multiplicity p–Pb events. The maximum value of the p/π ratio observed in p–Pb high-multiplicity collisions is comparable with the corresponding ratio in the 60–70% centrality class in Pb–Pb collisions but differs somewhat in shape at lower p_{T}. The value of $\mathrm{d}N_{ch}/\mathrm{d}\eta$ in the 0–5% multiplicity class of p–Pb collisions (45 ± 1) is a factor ~ 1.7 lower than the one in the 60–70% class for Pb–Pb collisions [50]. A similar enhancement of p/π ratio in high multiplicity d–Au collisions has also been reported for RHIC energies [146].

It is worth noticing that the ratio of p/π as a function of the charged-particle density ($\mathrm{d}N_{ch}/\mathrm{d}\eta$) in a given p_{T} interval follows a power-law behaviour: $\frac{\mathrm{p}}{\pi} = A \times [\mathrm{d}N_{ch}/\mathrm{d}\eta]^B$, left panel of the Fig. 7.3, where the coefficient A and B depend on the chosen p_{T} interval. As it can be seen, the same trend is also observed in Pb–Pb collisions. The values

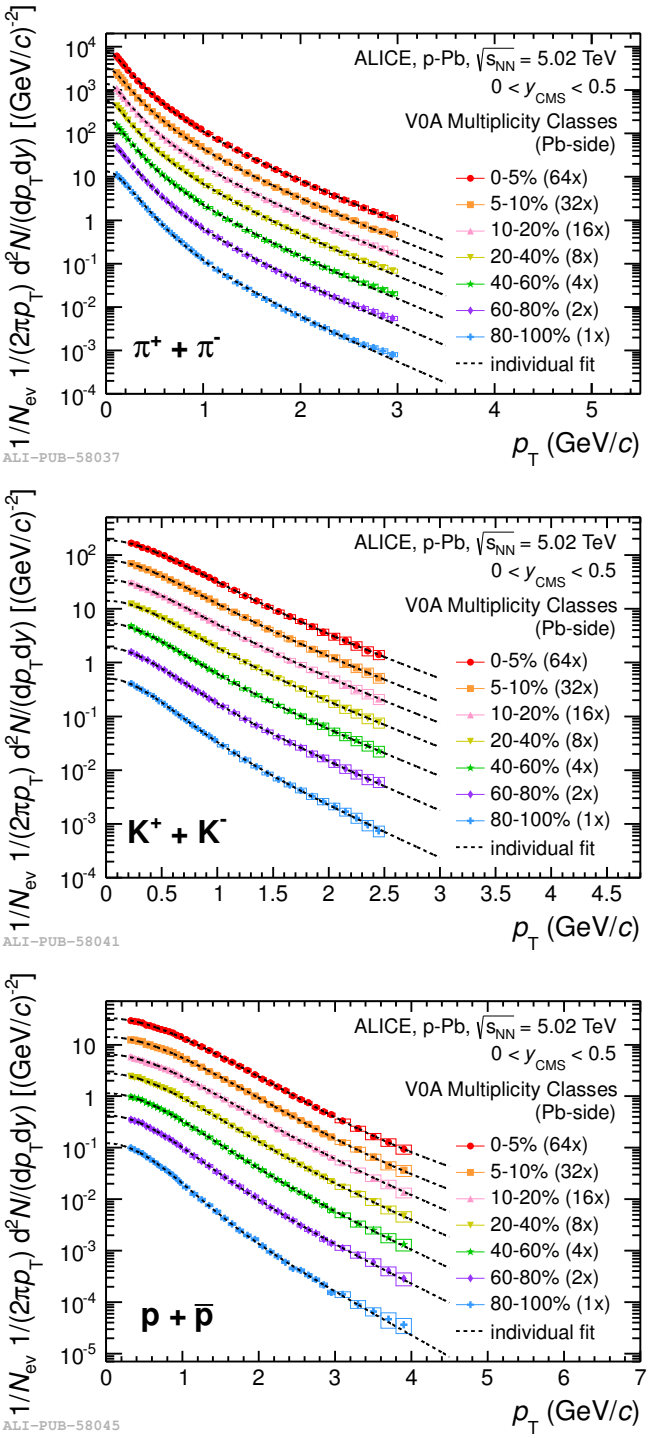

Figure 7.1: Invariant p_{T}-differential yields of $\pi^{\pm}$, $\mathrm{K}^{\pm}$ and $\mathrm{p}(\bar{\mathrm{p}})$ (sum of particle and anti-particle states) measured in $0 < \mathrm{y}_{cms} < 0.5$ in different V0A multiplicity classes. Top to bottom: high to low multiplicity; data scaled by factors of 2^n for better visibility. Statistical (bars) and full systematic (boxes) uncertainties are plotted. Dashed curves: blast-wave fits to each individual distribution. (from [142])

of exponent of the power-law, B, are shown as a function of p_{T} for p–Pb and Pb–Pb collisions in the right panel of Fig. 7.3. Their values in the two collision systems are found to be compatible. The same feature is also observed in the $\Lambda/\mathrm{K}^0_{\mathrm{S}}$ ratio in p–Pb and Pb–Pb collisions as well as in pp collisions at $\sqrt{\mathrm{s}} = 7$ TeV, as it can be seen in Fig. 7.4.

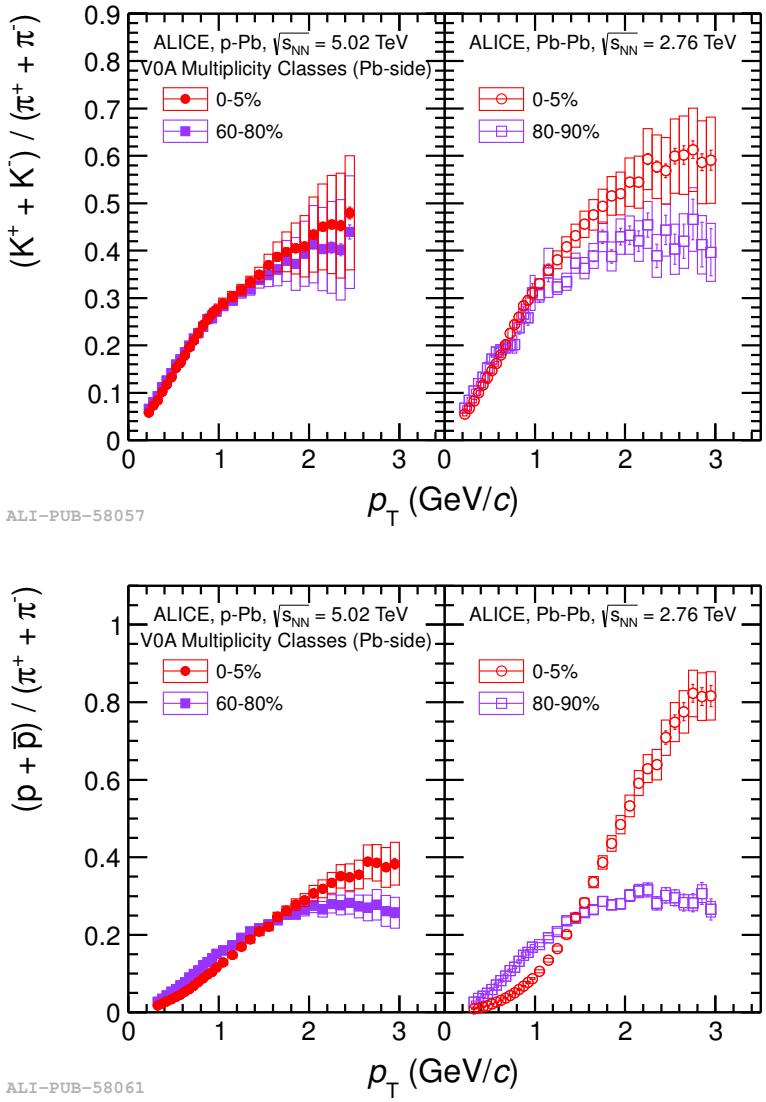

Figure 7.2: Ratios $\mathrm{K}/\pi = (\mathrm{K}^+ + \mathrm{K}^-)/(\pi^+ + \pi^-)$ and $\mathrm{p}/\pi = (\mathrm{p} + \bar{\mathrm{p}})/(\pi^+ + \pi^-)$ as a function of p_{T} in two multiplicity classes measured in the rapidity interval $0 < \mathrm{y}_{cms} < 0.5$ (left panels). The ratios are compared to results in Pb–Pb collisions measured at mid-rapidity, shown in the right panels. The empty boxes show the total systematic uncertainty; the shaded boxes indicate the contribution uncorrelated across multiplicity bins (not estimated in Pb–Pb). (from [142])

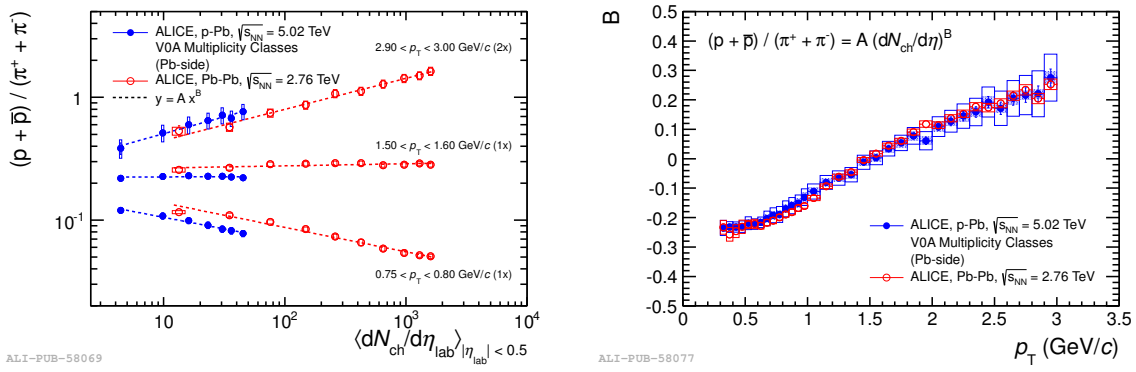

Figure 7.3: Left: p/π ratio as a function of $\mathrm{d}N_{ch}/\mathrm{d}\eta$ in three p_{T} intervals in p–Pb (measured in $0 < \mathrm{y}_{cms} < 0.5$) and Pb–Pb collisions (measured at mid-rapidity). The dashed lines show the corresponding power-law fit. Right: Exponent of the power-law fit to the p/π ratio as a function of p_{T} in p–Pb and Pb–Pb collisions. The empty boxes show the total systematic uncertainty; the shaded boxes indicate the contribution uncorrelated across multiplicity bins (not estimated in Pb–Pb).(from [142])

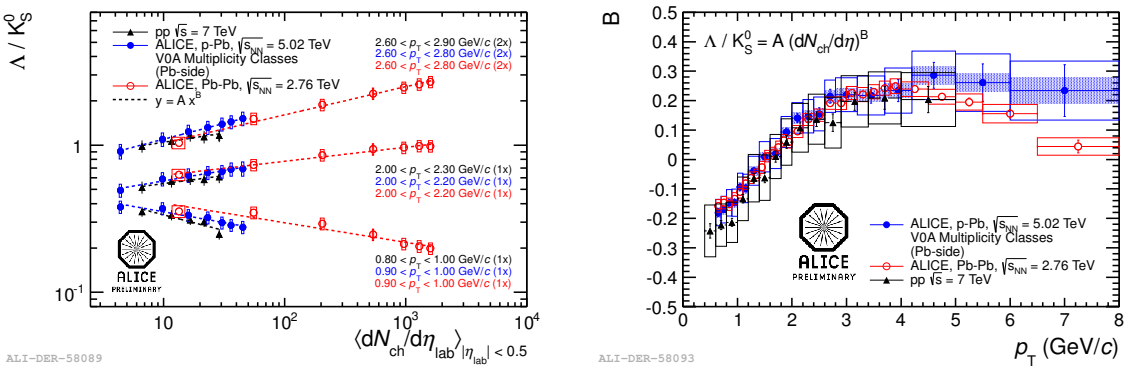

Figure 7.4: Left: $\Lambda/\mathrm{K}^0_{\mathrm{S}}$ ratio as a function of $\mathrm{d}N_{ch}/\mathrm{d}\eta$ in three p_{T} intervals in p–Pb and Pb–Pb collisions. The dashed lines show the corresponding power-law fit. Right: Exponent of the power-law fit to the $\Lambda/\mathrm{K}^0_{\mathrm{S}}$ ratio as a function of p_{T} in p–Pb and Pb–Pb collisions. The empty boxes show the total systematic uncertainty; the shaded boxes indicate the contribution uncorrelated across multiplicity bins (not estimated in Pb–Pb) [142]. The preliminary results in pp collisions at $\sqrt{\mathrm{s}} = 7$ TeV are superimposed (black markers).

The observations reported in this chapter are not strongly dependent on the actual variable used to select multiplicity classes (total charge deposited in the VZERO-A detector). The TOF analysis was repeated considering alternative approaches for the multiplicity estimation, such as using the total charge in both VZERO-A and VZERO-C detectors, the energy deposited in the ZNA (which originates from neutrons of the Pb nucleus) and the number of clusters in the SPD layers of the ITS detector (CL1).

The result from all multiplicity estimators reveal very similar trends. In the cases where the largest deviation is observed, the p/π ratio is essentially the same in the lowest multiplicity events and it is $\sim 15\%$ ($\sim 5\%$) higher (lower) at $p_{\rm T} \sim 3$ GeV/c for the result with the ZNA (CL1) estimator in the 60–80% class. Part of this difference is due to the mild correlation of events at forward and central rapidity (e.g. the lowest multiplicity class selected with ZNA leads to a larger multiplicity at mid-rapidity than the corresponding class selected with the VZERO-A).

7.2 $\langle p_{\rm T} \rangle$ and $p_{\rm T}$-integrated yields

In order to evaluate the average transverse momentum $\langle p_{\rm T} \rangle$ and the $p_{\rm T}$-integrated yields of π, K and p, the data in the measured $p_{\rm T}$ range are extrapolated down to zero and to high $p_{\rm T}$ (up to 10 GeV/c). Among several parametrizations tested, the blast-wave function (Eq. 2.9) gives the best description of the data over the entire measured $p_{\rm T}$ range. As it was discussed in Sec. 2.1.2, from the individual fits to a particle species distributions, no physical meaning can be extracted from the blast-wave parameters, due to the strong correlations between them. The individual blast-wave fit function are represented by dashed lines in Fig. 7.1.

Thanks to the good PID and tracking performance of the ALICE experiment at low $p_{\rm T}$, the fraction of yield contained in the extrapolated $p_{\rm T}$ region is small: about 8% (9%), 10% (12%) and 7% (13%) for $\pi^{\pm}$, $\rm K^{\pm}$, p and $\bar{\rm p}$ respectively for high (low) multiplicity events. Other fit functions [49] (Boltzmann, $m_{\rm T}$-exponential, $p_{\rm T}$-exponential, Tsallis–Levy, Fermi–Dirac, Bose–Einstein), are used to compute the systematic uncertainty due to the extrapolation. For those functions that did not give a satisfactory description of the data over the full measured $p_{\rm T}$ range, the fit has been performed in a narrower $p_{\rm T}$ range. The resulting systematic uncertainty on the integrated yields and on the $\langle p_{\rm T} \rangle$ due to the extrapolation is about 2% for π, K and p, in all multiplicity classes.

The mean transverse momentum $\langle p_{\rm T} \rangle$ as a function of $\mathrm{d}N_{ch}/\mathrm{d}\eta$ is shown in Fig. 7.5 for different hadron species. The results for the Λ (sum of particles and anti-particles) and $\rm K^0_S$ are superimposed to the π, K and p ones [142]. The $\langle p_{\rm T} \rangle$ increases with the multiplicity, at a rate which is stronger for heavier particles. In addition, for a given multiplicity class, a larger $\langle p_{\rm T} \rangle$ is observed for larger mass hadron species. A similar mass ordering is also observed in pp [147] and Pb–Pb [63] collisions.

In Fig. 7.6, the kaon-to-pion (left) and the proton-to-pion (right) ratios of the $p_{\rm T}$-integrated yields ($\mathrm{d}N/\mathrm{dy}$) are shown as a function of the multiplicity and compared to the Pb–Pb results at the LHC [63] and Au–Au and d–Au results at RHIC [49,80,146,148].

While the p/π ratio shows no evolution from low multiplicity (peripheral) to high multiplicity (central) collisions, a small increase is observed in the K/π ratio, if the bin-to-bin correlations of the uncertainties are considered. A similar rise is observed in Pb–Pb, Au–Au and d–Au collisions and for the Λ/π ratio in p–Pb, Pb–Pb and Au–Au collisions [142, 149]. This is typically attributed to a reduced canonical suppression of strangeness production in larger freeze-out volumes [150].

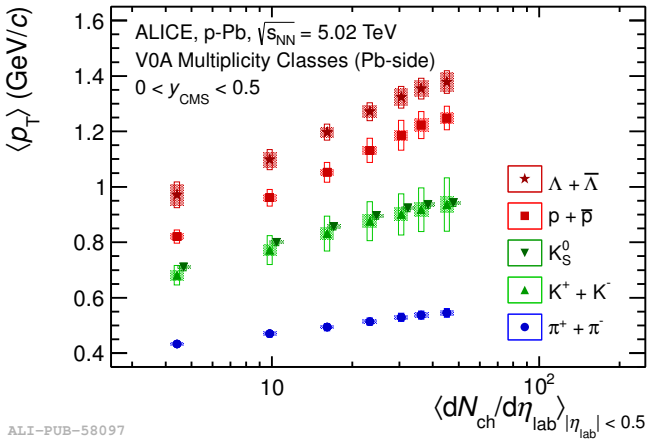

Figure 7.5: Mean transverse momentum $\langle p_{\mathrm{T}} \rangle$ as a function of $\mathrm{d}N_{ch}/\mathrm{d}\eta$ in each V0A multiplicity class for different hadron species. The $\mathrm{K}^0_{\mathrm{S}}$ points are shifted horizontally for visibility. The empty boxes show the total systematic uncertainty; the shaded boxes indicate the contribution uncorrelated across multiplicity bins.

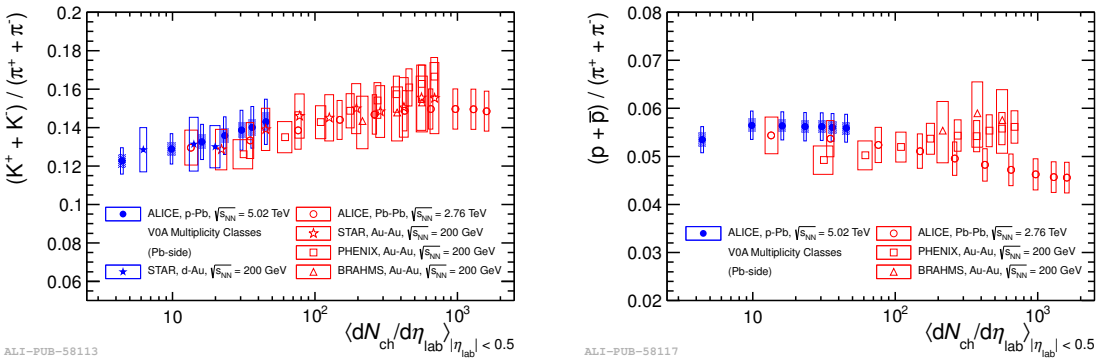

Figure 7.6: Particle yields $\mathrm{d}N/\mathrm{dy}$ of kaons (left) and protons (right) normalized to pion yields as a function of $\mathrm{d}N_{ch}/\mathrm{d}\eta$ in each V0A multiplicity class measured in the rapidity interval $0 < \mathrm{y}_{cms} < 0.5$. The values are compared to mid-rapidity results obtained from Pb–Pb collisions at the LHC [63] and Au–Au and d–Au collisions at RHIC [49, 80, 146, 148]. The empty boxes show the total systematic uncertainty; the shaded boxes indicate the contribution uncorrelated across multiplicity bins (not estimated in Pb–Pb)

7.3 Blast-wave fit

In the hydrodynamic picture of heavy ion collisions, discussed in Sec. 2.1.2, the flattening of the hadron spectra and its mass ordering find their natural explanation in the collective expansion of the strongly interacting system [25]. The hydrodynamical evolution of the system can be studied in a blast-wave framework with a simultaneous fit to all particle species for each multiplicity class. This framework assumes that the particles are in local thermal equilibrium at a fixed kinetic freeze-out temperature $\mathrm{T_{kin}}$ and moving with a collective radial flow. Since $\mathrm{d}N/p_{\mathrm{T}}\mathrm{d}p_{\mathrm{T}} = \mathrm{d}N/m_{\mathrm{T}}\mathrm{d}m_{\mathrm{T}}$, where the transverse mass m_{T} is defined as $\sqrt{p_{\mathrm{T}}^2 + m^2}$, then the blast-wave function of Eq. 2.9 describes the p_{T} spectra as:

$$\frac{1}{p_{\mathrm{T}}}\frac{\mathrm{d}N}{\mathrm{d}p_{\mathrm{T}}} \propto \int_0^{\mathrm{R}} r dr\, m_{\mathrm{T}}\, I_0\left(\frac{p_{\mathrm{T}}\sinh\rho}{\mathrm{T_{kin}}}\right) K_1\left(\frac{m_{\mathrm{T}}\cosh\rho}{\mathrm{T_{kin}}}\right), \tag{7.1}$$

where the velocity profile ρ is described by

$$\rho = \tanh^{-1}\left(\beta_{\mathrm{T}}\right) = \tanh^{-1}\left(\left(\frac{r}{\mathrm{R}}\right)^{\mathrm{n}}\beta_s\right) \tag{7.2}$$

and the average transverse velocity

$$\langle\beta_{\mathrm{T}}\rangle = \frac{\int_0^{\mathrm{R}}\beta_s\left(\frac{r}{R}\right)^{\mathrm{n}} r\mathrm{d}r}{\int_0^{\mathrm{R}} r dr} = \frac{2\beta_s}{\mathrm{n}+2}. \tag{7.3}$$

Here, I_0 and K_1 are the modified Bessel functions, r is the radial distance from the centre of the fireball in the transverse plane, R is the radius of the fireball at the kinetic freeze-out time, $\beta_{\mathrm{T}}(r)$ is the radial profile of the transverse expansion velocity, β_s is the transverse expansion velocity at the surface, n is the exponent of the velocity profile and $\mathrm{T_{kin}}$ is the kinetic freeze-out temperature.

The $\langle\beta_{\mathrm{T}}\rangle$ and $\mathrm{T_{kin}}$ parameters can be extracted from a simultaneous fit to all particle species under consideration. The free parameters in the fit are $\mathrm{T_{kin}}$, $\langle\beta_{\mathrm{T}}\rangle$ and n which are common to all particle species and a normalization parameter which is species dependent.

Figure 7.7 shows the blast-wave simultaneous fits performed to the p_{T} distributions of π, K and p in p–Pb collisions at $\sqrt{\mathrm{s_{NN}}} = 5.02$ TeV for the 0–5% and 60–80% multiplicity classes. The fit presented in this work is performed in the same p_{T} ranges as for Pb–Pb collisions at $\sqrt{\mathrm{s_{NN}}} = 2.76$ TeV in [62,63]. The p_{T} ranges used in the fit are 0.5–1 GeV/c, 0.2–1.5 GeV/c and 0.3–3 GeV/c for $\pi^{\pm}$, $\mathrm{K}^{\pm}$ and $\mathrm{p}(\bar{\mathrm{p}})$ respectively. They have been defined according to the available data at low p_{T} and based on the agreement with the data at high p_{T}, justified considering that the assumptions underlying the blast-wave

model are not expected to be valid at high p_{T}. In addition, the pions at low p_{T} are known to have a large contribution from resonance decays. Including the $\mathrm{K}^0_{\mathrm{S}}$ and $\Lambda(\bar{\Lambda})$ spectra in the fit causes a negligible difference in the fit parameters.

The ratio of the measured spectra to the simultaneous fits are shown in the bottom panel of Fig. 7.7. The discrepancy observed for pions at low p_{T} is due to the large contribution from resonances to the pion spectrum. The parameters determined by a simultaneous fit in a limited p_{T} range are not able to predict the full shape. The deviation of the fit from the pions and protons spectra are similar in both multiplicity classes, while for the kaons case, the discrepancies increase with the multiplicity. The fit is worse in p–Pb than in Pb–Pb collisions [62, 63].

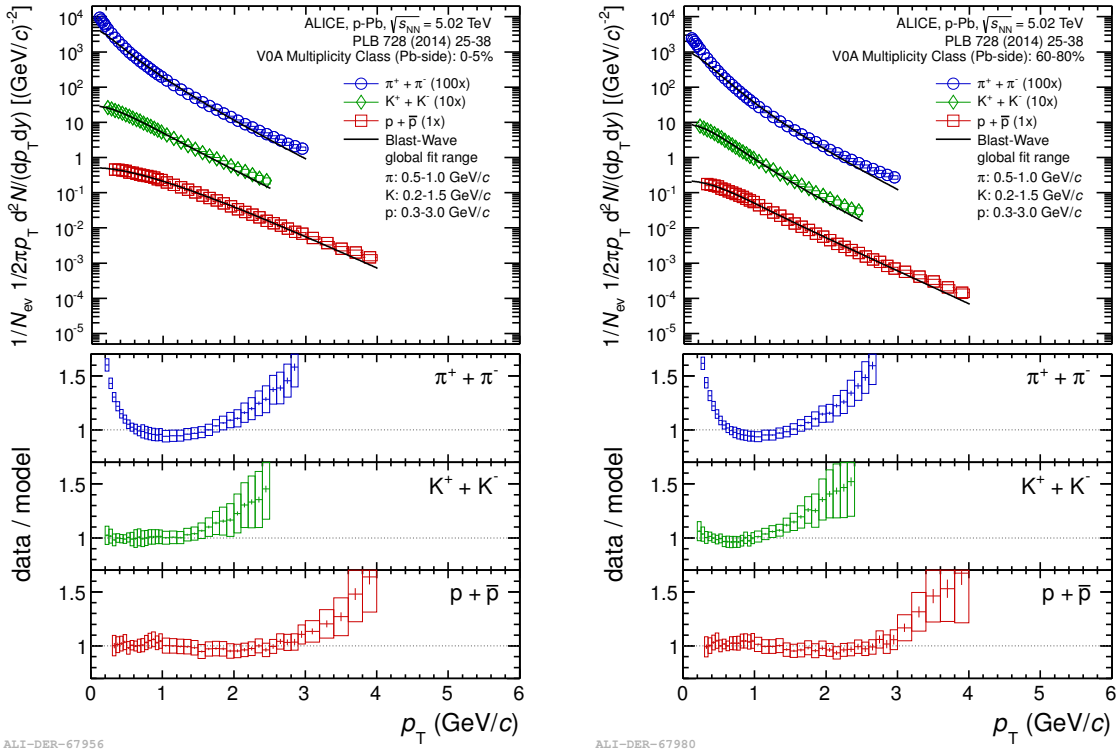

Figure 7.7: Simultaneous blast-wave fit to the $\pi^{\pm}$, $\mathrm{K}^{\pm}$ and $\mathrm{p}(\bar{\mathrm{p}})$ spectra in the fit ranges 0.5–1 GeV/c, 0.2–1.5 GeV/c and 0.3–3 GeV/c respectively, for 0–5% (left) and 60-80% (right) multiplicity classes for p–Pb collisions at $\sqrt{\mathrm{s_{NN}}} = 5.02$ TeV.

It is well know, moreover, that the fit parameters depend substantially on the p_{T} range used in the fit [62, 63]. For this reason, these fits by no means replace a full hydrodynamical calculation. However, in spite of this limitation, the blast-wave model still provides a handy way to compare the transverse momentum distributions and their evolution in different collision systems.

The resulting parameters of the simultaneous blast-wave fit, also including K^0_S and $\Lambda(\bar{\Lambda})$ in the p_T range 0–1.5 GeV/c and 0.6–3 GeV/c respectively, are reported in Tab. 7.1 and are shown in Fig. 7.8 as a function of multiplicity. Similarly as observed for Pb–Pb collisions, variations of the fit ranges lead to large shifts ($\sim 10\%$) of the fit results (correlated among multiplicity classes). The first uncertainty in Tab. 7.1 includes the effect of the bin-by-bin uncertainties, which is represented as the shaded region in Fig. 7.8. The systematic uncertainties on the fit parameters due to the fit stability, which were estimated as done in [62, 63] for Pb–Pb data, are also reported. These total systematic uncertainties include the effect of the variation of the lower fit bound for pions (to test the effect of resonance feed-down) and the sensitivity to different particle species (i.e., excluding K^0_S and lambdas or pions ...). They are asymmetric and they are represented as coloured lines in Fig. 7.8.

Event class	$\langle\beta_T\rangle$	T_{kin}(GeV/c)	n	χ^2/NDF
0–5%	$0.547 \pm 0.006^{+0.01}_{-0.02}$	$0.143 \pm 0.005^{+0.01}_{-0.01}$	$1.07 \pm 0.03^{+0.08}_{-0.09}$	0.27
5–10%	$0.531 \pm 0.006^{+0.01}_{-0.03}$	$0.147 \pm 0.005^{+0.01}_{-0.01}$	$1.14 \pm 0.03^{+0.1}_{-0.2}$	0.33
10–20%	$0.511 \pm 0.007^{+0.01}_{-0.03}$	$0.151 \pm 0.005^{+0.02}_{-0.01}$	$1.24 \pm 0.04^{+0.2}_{-0.2}$	0.36
20–40%	$0.478 \pm 0.007^{+0.02}_{-0.03}$	$0.157 \pm 0.005^{+0.02}_{-0.01}$	$1.41 \pm 0.05^{+0.2}_{-0.2}$	0.35
40–60%	$0.428 \pm 0.009^{+0.03}_{-0.03}$	$0.164 \pm 0.004^{+0.02}_{-0.02}$	$1.73 \pm 0.07^{+0.2}_{-0.4}$	0.43
60–80%	$0.360 \pm 0.009^{+0.04}_{-0.02}$	$0.169 \pm 0.004^{+0.02}_{-0.02}$	$2.40 \pm 0.1^{+0.2}_{-0.6}$	0.54
80–100%	$0.260 \pm 0.009^{+0.03}_{-0.01}$	$0.166 \pm 0.003^{+0.02}_{-0.01}$	$3.90 \pm 0.3^{+0.1}_{-0.7}$	0.84

Table 7.1: Results of the combined blast-wave p–Pb fit of $\pi^{\pm}$, $K^{\pm}$, K^0_S, $p(\bar{p})$ and $\Lambda(\bar{\Lambda})$ in the fit ranges 0.5–1 GeV/c, 0.2–1.5 GeV/c, 0–1.5 GeV/c, 0.3–3 GeV/c and 0.6–3 GeV/c, respectively. The first (symmetric) uncertainty is due to the effect of point-to-point uncertainties in the fit. The second (asymmetric) uncertainty is due to the dependence of the parameters on the fit ranges and the hadron species included in the fit.

As it can be seen in Fig. 7.8, the parameters in p–Pb collisions show a similar trend as a function of multiplicity as the ones obtained in Pb–Pb collisions. Within the limitations of the blast-wave model, this observation is consistent with the presence of radial flow in p–Pb collisions. At similar $dN_{ch}/d\eta$ the values of T_{kin} are similar for the two systems, whereas the $\langle\beta_T\rangle$ values are significantly higher in p–Pb collisions.

While in Pb–Pb collisions high multiplicity events are obtained through multiple soft interactions, in p–Pb collisions the high multiplicity selection biases the sample towards harder collisions [152]. This could explain the larger $\langle\beta_T\rangle$ parameter obtained from the blast-wave fits. In addition, under the assumption of a collective hydrodynamic expansion, a larger radial expansion velocity in p–Pb collisions has been suggested as a consequence of stronger radial gradients in [153].

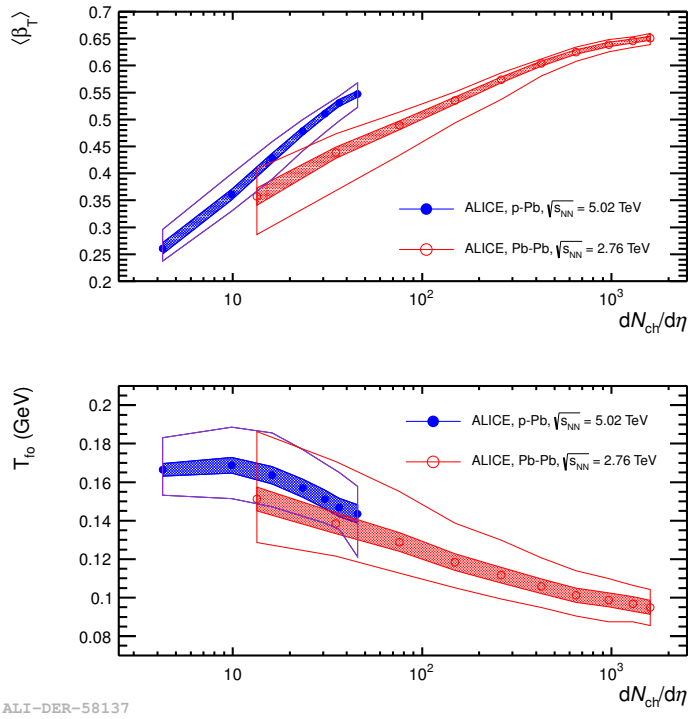

Figure 7.8: Combined blast-wave fit parameters, $\langle\beta_{\mathrm{T}}\rangle$ (top) and $\mathrm{T_{kin}}$ (bottom), as a function of $\mathrm{d}N_{ch}/\mathrm{d}\eta$ in p–Pb and Pb–Pb collisions. The same p_{T} range of the fit to π, K and p spectra are used in both collision system. The fit to the p–Pb data are performed considering also $\mathrm{K^0_S}$ and Λ spectra.

Other processes not related to hydrodynamic collectivity could also be responsible for the observed results. This is illustrated in Fig. 7.9, which shows the results obtained by applying the same fitting procedure to transverse momentum distributions from the simulation of pp collisions at $\sqrt{\mathrm{s}} = 7$ TeV with the PYTHIA8 event generator (tune 4C) [124], a model not including any collective expansion of the system. PYTHIA8 events are divided into several classes according to the charged-particle multiplicity at mid-rapidity $|\eta_{lab}| < 0.3$, namely $N_{ch} < 5$, $5 \leq N_{ch} < 10$, $10 \leq N_{ch} < 15$, $15 \leq N_{ch} < 20$ and $N_{ch} \leq 20$. The fit results are shown for PYTHIA8 simulations performed both with and without enabling the colour reconnection mechanism [154,155]. Colour reconnection mechanism consists on colour string formations between final partons from independent hard scatterings. This mechanism is necessary in PYTHIA tunes to describe the evolution of $\langle p_{\mathrm{T}}\rangle$ with multiplicity in pp collisions [152]. With colour reconnection the evolution of PYTHIA8 transverse momentum distributions follows a similar trend as the one observed for p–Pb and Pb–Pb collisions at the LHC, while without colour reconnection it is not as strong. This generator study shows that other final state mechanisms, such as colour reconnection, can mimic the effects of radial flow [156].

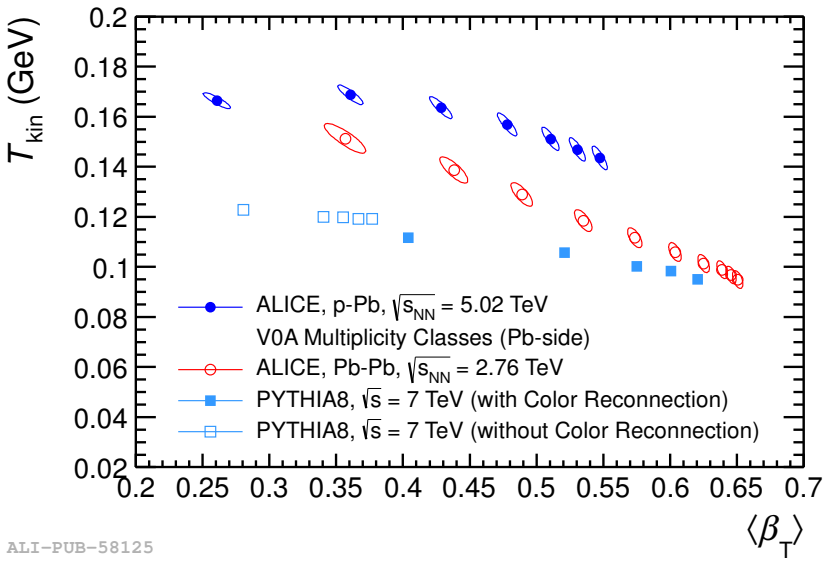

Figure 7.9: Blast-wave fit parameters in p–Pb collisions at $\sqrt{s_{NN}} = 5.02$ TeV for different multiplicity classes compared to Pb–Pb results for different centralities and MC simulations from PYTHIA8 with and without colour reconnection. Charged-particle multiplicity increases from left to right. Uncertainties from the global fit are shown as correlation ellipses. (from [142])

7.4 Model comparison

The π, K and p spectra together with the Λ and K^0_S ones, measured in p–Pb collisions at $\sqrt{s_{NN}} = 5.02$ TeV for the 5–10% V0A multiplicity classes, are compared in Fig. 7.10 with calculations from the DPMJET, Kraków [71] and EPOS LHC 1.99 v3400 [157] models. The QCD-inspired DPMJET [127] generator, which is based on the Gribov-Glauber approach, treats soft and hard scattering processes in an unified way. It has been found to successfully reproduce the pseudo-rapidity distribution of charged particles in Non-Single Diffractive (NSD) p–Pb collisions at the LHC as reported in [138]. On the other hand, it cannot reproduce the p_T distribution [34] and the $\langle p_T \rangle$ of charged particles [152]. In the Kraków hydrodynamic model, fluctuating initial conditions are implemented based on a Glauber model using a Monte Carlo simulation. The expansion of the system is calculated event-by-event in a $3+1$ dimensional viscous hydrodynamic approach and the freeze-out follows statistical hadronization in a Cooper–Frye formalism. In the EPOS model, based on "parton-based Gribov Regge theory", the initial hard and soft scatterings create "flux tubes" which either escape the medium and hadronize as jets or contribute to the bulk matter, described in terms of hydrodynamics. The version of the model used here implements a simplified treatment of the collective expansion [157].

The transverse momentum distributions in the 5–10% multiplicity class are compared to the predictions by Kraków for $11 \leq \mathrm{N_{part}} \leq 17$, since the $\mathrm{d}N_{ch}/\mathrm{d}\eta$ from the model matches best with the measured value in this class. DPMJET and EPOS events have been selected according to the charged-particle multiplicity in the pseudo-rapidity interval covered by the VZERO-A detector in order to match the experimental selection.

DPMJET distributions are softer than the measured ones and the model overpredicts the production of all particle species for p_{T} lower than about 0.5–0.7 GeV/c and underpredicts it at higher momenta. At high p_{T}, the spectra shapes of pions and kaons are rather well reproduced for p_{T} above 1 and 1.5 GeV/c respectively, even though the yield in this p_{T} region is underestimated by a factor of ~ 2 for pions and ~ 2.5 for kaons.

Final state effects may be needed in order to reproduce the data. In fact, the Kraków model reproduces reasonably well the spectral shapes of pions and kaons below transverse momenta of 1 GeV/c where hydrodynamic effects are expected to be relevant if a collective expansion is established. The observed deviations for pions and kaons at higher momentum ($p_{\mathrm{T}} \gtrsim 1$ GeV/c) could be explained in a hydrodynamic framework as due to the onset of a non-thermal component. EPOS can reproduce the pion and proton distributions within 20% over the full measured p_{T} range, while larger deviations are seen for kaons and lambdas. The yield and the shape of the p_{T} distributions of protons are rather well described by both Krakóv and EPOS models. In contrast to a similar comparison for Pb–Pb collisions, where the Kraków calculation for the pion and kaon yields are in a good agreement with the data [62, 63], they seems to be overestimated in p–Pb collisions. It is interesting to notice that when final state interactions are disabled in EPOS, the description of many pp and p–Pb observables worsens significantly [157].

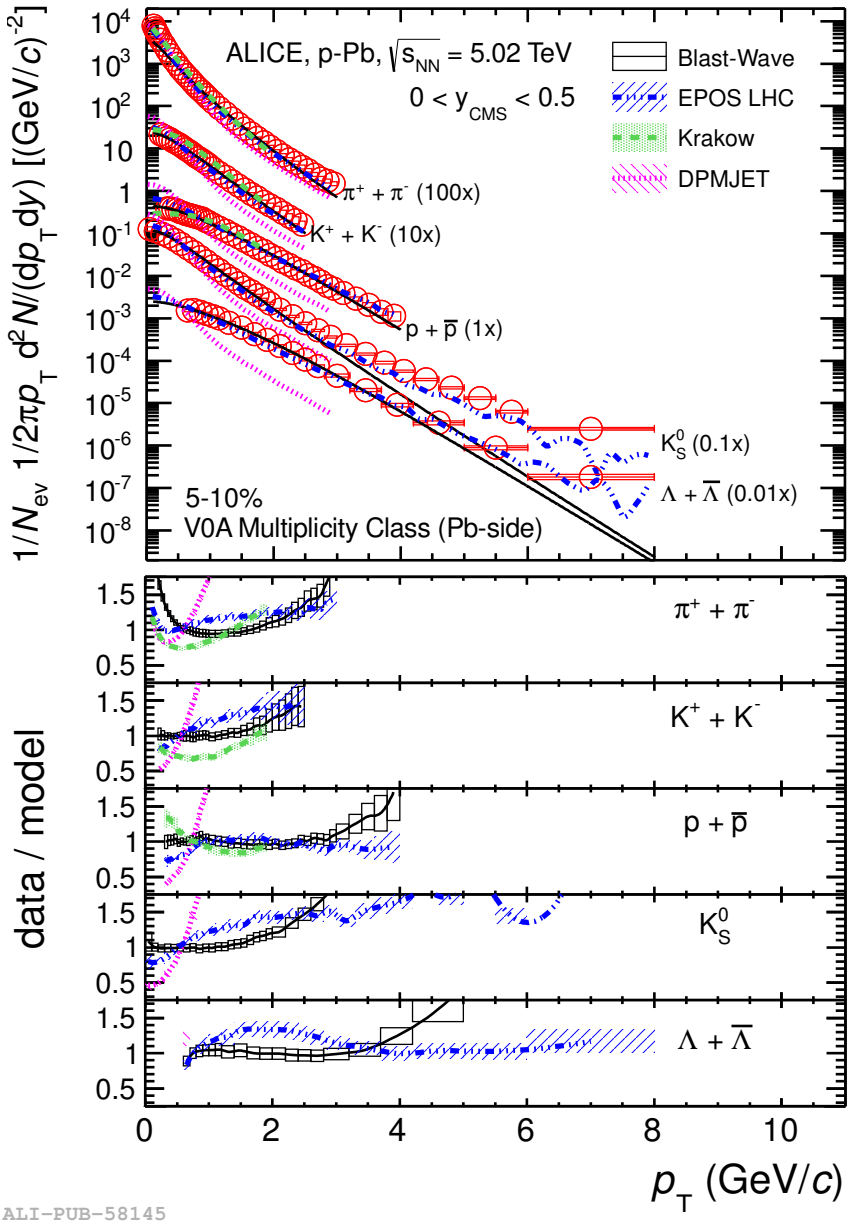

Figure 7.10: $\pi^{\pm}$, $K^{\pm}$, $p(\bar{p})$, $\Lambda(\bar{\Lambda})$ and K^0_S p_T distributions in the 5–10% V0A multiplicity class measured in the rapidity interval $0 < y_{cms} < 0.5$ compared to the several model calculations. (from [142])

8 Conclusions

The present thesis was focused on the measurement of the transverse momentum distributions of identified charged hadrons (π, K and p) in p–Pb collisions at $\sqrt{s_{NN}} = 5.02$ TeV using the Inner Tracking System (ITS) of ALICE. A particle identification approach based on the Bayes theorem was developed and used for this analysis. In contrast to previous ITS particle identification methods, where a truncated mean approach was used, in the Bayesian one, all four specific energy loss (dE/dx) samples measured in the two SDD and two SSD layers are taken into account. Each dE/dx distributions of the four outermost layers of the ITS are well described by a convolution of a Landau and a Gaussian function. The parametrizations of these functions as a function of momentum for different particle species were performed for real and simulated data. In the case of real data, were the particle identity is unknown, the TPC and TOF particle identification capabilities were used to select high purity samples of π, K and p. The prior probabilities for each particle species in the Bayes formula were obtained through an iterative procedure starting from equal priors for all particles species. From Monte Carlo simulation it is found that this Bayesian approach provides higher purity, at a cost of lower efficiency, compared with other PID approaches used in previous π, K and p spectra analyses. The analysis of π, K and p production was performed using tracks reconstructed with the ITS stand-alone algorithm, and identified track-by-track using this Bayesian approach. Thanks to the ITSsa analysis the π, K and p momentum distributions were extended down to very low p_{T} ranges. The π, K and p yields at low p_{T} obtained using the ITS in a stand-alone mode were compared and combined with spectra from other analyses (TPCTOF and TOF).

The combined π, K and p spectra over the full measured p_{T} range in the $0 < y_{cms} < 0.5$ rapidity interval have been reported for different V0A multiplicity classes. The p_{T}-distributions show a clear evolution with multiplicity, similar to the pattern observed in high-energy pp and heavy-ion collisions. In the heavy-ion collisions case, this behaviour is usually attributed to collective flow. The results from the simultaneous blast-wave fit to the π, K and p spectra are consistent with the presence of radial flow expansion in p–Pb collisions. However, other final state mechanisms, such as colour reconnection, can

mimic the effect of the collective radial expansion. Finally, it is observed that models incorporating a hydrodynamical expansion in the final state (Kraków & EPOS) give a better description of the data.

Bibliography

[1] E.V. Shuryak. *Phys. Rev.*, 61:71, 1980.

[2] BNL URL. `http://www.bnl.gov/`.

[3] CERN URL. `http://www.bnl.gov/`.

[4] BNL URL. `http://www.bnl.gov/rhic`.

[5] S.L. Glashow. *Nucl. Phys.*, 20:579, 1961.

[6] S. Weinberg. *Phys. Rev. Lett.*, 19:1264, 1967.

[7] A. Salam. *Elementary Particle Theory*. Svartholm, Almquist and Wiksells, 1968.

[8] S. Glashow, J. Iliopoulos, and L. Maiani. *Phys. Rev. D*, 2:1285, 1970.

[9] P.W. Higgs. *Phys. Rev. Lett.*, 13:508, 1964.

[10] P.W. Higgs. *Phys. Rev. Lett.*, 145:1156, 1966.

[11] ATLAS Collaboration. *Phys. Lett. B*, 716:1, 2012.

[12] CMS Collaboration. *Phys. Lett. B*, 716:30, 2012.

[13] H. Kastrup and P Zerwaas. *QCD 20 yrs later*. World Scientific, Singapore, 1993.

[14] J. Beringer et al. (Particle Data Group). *Phys. Rev. D*, 86:010001, 2012.

[15] D.J. Gross and F. Wilczek. *Phys. Rev. Lett.*, 30:1343, 1973.

[16] H. Politzer. *Phys. Rev. Lett.*, 30:1346, 1973.

[17] F. Karsch. Lattice results on qcd thermodynamics. 2001. `arXiv:hep-ph/0103314v1`.

[18] A. Chodos, R. L. Jaffe, K. Johnson, C. B. Thorn, and V. F. Weisskopf. *Phys. Rev. D*, 9:3471–3495, 1974.

[19] S. Hands. *Contemp. Phys.*, 42:209–225, 2001.

[20] P. Jacobs and X. N. Wang. *Prog. Part. Nucl. Phys.*, 54:443–534, 2005.

[21] Laszlo P. Csernai. *Instroduction to Relativistic Heavy Ion Collisions*. Jonh Wiley & Sons, 1994.

[22] J. C. Collins and M. J. Perry. *Phys. Rev. Lett.*, 34:1353, 1975.

[23] F. Karsch and E. Laermann. Thermodynamics and in-medium hadrons properties from lattice qcd. 2008. `arXiv:hep-lat/0305025v1`.

[24] F. Karsch and E. Laermann. *Phys. Rev. D*, 50:6954, 1994.

[25] U. Heinz. Concept of heavy-ion physics. 2004. `arXiv:hep-ph/0305025v1`.

[26] K. Rajagopal. *Comments Nucl. Part. Phys. A*, 2:120, 2002. `arXiv:hep-ph/0009058`.

[27] ALICE Collaboration. *Phys. Rev. C*, 88:044909, 2013.

[28] R. Snelling. Elliptic flow: A brief review. *New J. Phys.*, 13:055008, 2011.

[29] J. W. Cronin et al. *Phys. Rev. D*, 11:3105, 1975.

[30] ALICE Collaboration. *Phys. Lett. B*, 696:30–39, 2011.

[31] PHENIX Collaboration. *Phys. Rev. C*, 69:034910, 2004.

[32] STAR Collaboration. *Phys. Rev. Lett.*, 91:172302, 2003.

[33] CMS Collaboration. *Eur. Phys. J. C*, 72:1975, 2012.

[34] ALICE Collaboration. *Phys. Rev. Lett.*, 110:082302, 2013.

[35] STAR Collaboration. *Nucl. Phys. A*, 757:102, 2005.

[36] ATLAS Collaboration. *Phys. Rev. Lett.*, 105:252303, 2010.

[37] CMS Collaboration. *JHEP*, 05:063, 2012.

[38] S. Wicks, W. Horowitz, M. Djordjevic, and M. Gyulassy. *Nucl. Phys. A*, 783:493, 2007.

[39] N. Armesto, A. Dainese, C.A. Salgado, and U.A. Wiedemann. *Phys. Rev. D*, 71:054027, 2005.

[40] T. Matsui and H. Satz. *Phys. Lett. B*, 178:416, 1986.

[41] M. C. Chu and T. Matsui. *Phys. Rev. D*, 37:1851, 1988.

[42] ALICE Collaboration. *Phys. Lett. B*, 734:314–327, 2014.

[43] PHENIX Collaboration. *Phys. Rev. C*, 84:054912, 2011.

[44] Yunpeng Liu, Zhen Qu, Nu Xu, and Pengfei Zhuang. *Phys. Lett. B*, 678(72), 2009.

[45] Xingbo Zhao and Ralf Rapp. *Nucl. Phys. A*, 859(114-125), 2011.

[46] ALICE Collaboration. *Phys. Rev. Lett.*, 105:252301, 2010.

[47] CMS Collaboration. *JHEP*, 1108:141, 2011.

[48] ATLAS Collaboration. *Phys. Lett. B*, 710:363–382, 2012.

[49] STAR Collaboration. *Phys. Rev. C*, 79:034909, 2009.

[50] ALICE Collaboration. *Phys. Rev. Lett.*, 106:032301, 2011.

[51] J.D. Bjorken. *Phys. Rev. D*, 27:1, 1983.

[52] A. Andronic, P. Braun-Munzinger, and J. Stachel. *Nucl. Phys. A*, 722:167, 2006. `nucl/th/0511071`.

[53] F. Becattini et al. *Eur. Phys. J. C*, 35:243–258, 2004.

[54] J. Cleymans et. al. *Phys. Rev. C*, 57:3319, 1998.

[55] M. Petran, J. Letessier, V. Petracek, and J. Rafelski. *Phys. Rev. C*, 88(3), 2013.

[56] J. Rafelski and B. Muller. *Phys. Rev. Lett.*, 56:2334, 1986.

[57] A. Tounsi and K. Redlich. `hep-ph/0111159`.

[58] F. Becattini. Strangeness production in relativistic heavy ion collisions. In *QGP school, Torino.*, 2011.

[59] P. Braun-Munzinger and J. Stachel. *Phys. Lett. B*, 490:196–202, 2000.

[60] A. Andronic, P. Braun-Munzinger, K. Redlichd, and J. Stachel. *Nucl. Phys. A*, 904-905:535c–538c, 2013.

[61] A. Andronic, P. Braun-Munzinger, and J. Stachel. *Phys. Lett. B*, 673(2):142–145, 2009.

[62] ALICE Collaboration. *Phys. Rev. Lett.*, 109:252301, 2012.

[63] ALICE Collaboration. *Phys. Rev. C*, 88:044910, 2013.

[64] M. Floris. *Nucl. Phys. A*, 931:103–112, 2014.

[65] Anthony R Timmins (for the STAR Collaboration). *J. Phys. G: Nucl. Part. Phys.*, 36:064006, 2009.

[66] ALICE Collaboration. *Phys. Lett. B*, 728:216–227, 2014.

[67] NA57 Collaboration. *J. Phys. G*, 32:427, 2006.

[68] STAR Collaboration. *Phys. Rev. C*, 77:044908, 2008.

[69] C. Shen, U. W. Heinz, P. Huovinen, and H. Song. *Phys. Rev. C*, 84:044903, 2011.

[70] Y. Karpenko and Y. Sinyukov. *J. Phys. G*, 38:124059, 2011.

[71] P. Bozek. *Phys. Rev. C*, 85:034901, 2012.

[72] E. Frodermann, Rupa Chatterjee, and Ulrich Heinz. *J. Phys. G: Nucl Part. Phys.*, 34:2249–2254, 2007.

[73] L. Del Zanna et al. Relativistic viscous hydrodynamics for heavy-ion collisions with echo-qgp. *Eur. Phys. J. C*, 73:2524, 2013.

[74] M. Rybczyn ski and W. Broniowski. *Phys. Rev. C*, 84:064913, 2011.

[75] F. Gelis et al. The color glass condensate. 2010. `arXiv:1002.0333v1`.

[76] P. Huovinen and P.V. Ruuskanen. Hydrodynamic models for heavy ion collisions. *Annu. Rev. Nucl. Particle Science*, 56, 2006.

[77] F. Cooper and G. Frye. *Phys. Rev. D*, 10:186–189, 1974.

[78] S. Bass et al. *Prog. Part. Nucl. Phys.*, 41:255–369, 1998.

[79] E. Schnedermann, J. Sollfrank, and U.W. Heinz. *Phys. Rev. C*, 48:2462–2475, 1993.

[80] PHENIX Collaboration. *Phys. Rev. C*, 69:034909, 2004.

[81] (). P. Huovinen. Tc =165 mev, tf =130 mev, eos=q. *private communication*, 2004.

[82] STAR Collaboration. *Phys. Rev. C*, 72:014904, 2005. `arXiv:nucl-ex/0409033`.

[83] PHENIX Collaboration. *Phys. Rev. Lett.*, 91:182301, 2003.

[84] S. A. Voloshin. *Nucl. Phys. A*, 715:379, 2003. `nucl-ex/0210014`.

[85] STAR Collaboration. *Phys. Rev. Lett.*, 92:052302, 2004.

[86] V. Greco, C. M. Ko, and P. Levai. *Phys. Rev. C*, 68:034904, 2003.

[87] D. Molnar and S. A. Voloshin. *Phys. Rev. Lett.*, 91:092301, 2003.

[88] Huichao Song, Steffen Bass, and Ulrich W. Heinz. *Phys. Rev. C*, 89:034919, 2014.

[89] ALICE Collaboration. 2014. `arXiv:1405.4632`.

[90] STAR Collaboration. *Eur. Phys. J. C*, 62:265–269, 2009.

[91] STAR Collaboration. *J.Phys.G35:104090,2008 J.Phys.G35:104090,2008 J. Phys. G*, 35:104090, 2008.

[92] CERES collaboration. *Nucl. Phys. A*, 811:179–196, 2008.

[93] PHENIX Collaboration. *Phys. Rev. C*, 78:014901, 2008.

[94] STAR Collaboration. *Phys. Rev. C*, 82:024912, 2010.

[95] M Bombara. Two-particle correlations with star. *J. Phys.: Conf. Ser.*, 110:032003, 2008.

[96] ALICE Collaboration. *Phys. Lett. B*, 708:249, 2012.

[97] ATLAS Collaboration. *Phys. Rev. C*, 86:014907, 2012.

[98] ALICE Collaboration. *Phys. Lett. B*, 696:328–337, 2011.

[99] Xin-Nian Wang. *Phys. Rev. C*, 61:064910, 2000.

[100] et al. D. Antreasyan. *Phys. Rev. D*, 19:764, 1979.

[101] et al. P. B. Straub. *Phys. Rev. Lett.*, 68:452, 1992.

[102] N. Armesto. `arXiv:hep-ph/0604108v2`.

[103] Larry McLerran and Raju Venugopalan. Computing quark and gluon distribution functions for very large nuclei. *Phys. Rev. D*, 49:2233, 1994.

[104] STAR Collaboration. *Phys. Rev. Lett.*, 91:072304, 2003.

[105] PHOBOS Collaboration. *Phys. Rev. C*, 83:024913, 2011.

[106] CMS Collaboration. *Phys. Lett. B*, 718:795–814, 2013.

[107] ALICE Collaboration. *Phys. Lett. B*, 719:29–41, 2012.

[108] ATLAS Collaboration. *Phys. Rev. Lett.*, 110:182302, 2013.

[109] CMS Collaboration. *JHEP*, 91, 2010.

[110] Rudolph C Hwa and Xin-Nian Wang. *Quark Gluon Plasma 4*. World Scientific, Singapore.

[111] P. Bozek and W. Broniowski. *Phys. Lett. B*, 718:1557–1561, 2013.

[112] Berndt Müller Guang-You Qin. *Phys. Rev. C*, 89:044902, 2014.

[113] K. Dusling and R. Venugopalan. *Phys. Rev. D*, 87:094034, 2013.

[114] ALICE Collaboration. *Phys. Lett. B*, 726:164–177, 2013.

[115] CERN URL. The large hadron collider. `http://public.web.cern.ch/public/en/LHC/LHC-en.html`.

[116] ALICE Collaboration. The alice experiment at the cern lhc. *JINST*, 3:S08002, 2008.

[117] ALICE Collaboration. Alice: Physics performance report, volume i. *J. Phys. G: Nucl Part. Phys.*, 30:1517, 2004.

[118] ALICE Collaboration. Alice: Physics performance report, volume ii. *J. Phys. G: Nucl Part. Phys.*, 32:1295, 2006.

[119] ALICE Collaboration. *Phys. Lett. B*, 736:196–207, 2014.

[120] ALICE Collaboration. Performance of the alice experiment at the cern lhc. *International Journal of Modern Physics A*, 29(24):1330044, 2014.

[121] ALICE Offline framework. Aliroot. `http://aliceinfo.cern.ch/Offline`.

[122] ALICE. Alien. `http://alien.cern.ch`.

[123] R. Brun and F. Rademakers. *Nucl. Instrum. Meth. A*, 389:81–86, 1997. `http://root.cern.ch`.

[124] R. Corke and T. Sjostrand. Interleaved parton showers and tuning prospects. *J. High Energy Phys.*, 1103:032, 2011.

[125] G. Marchesini et al. *Comput. Phys. Commun.*, 67:465, 1992.

[126] Xin-Nian Wang and Miklos Gyulassy. *Phys. Rev. D*, 44:3501, 1991.

[127] J. Ranft. *Phys. Rev. D*, 64:51, 1995.

[128] R. Brun et al. Geant detector description and simulation tool. 1994.

[129] S. Agostinelli et al. Geant4 a simulation toolkit. *CERN-IT-20020003*, 2003.

[130] Frasso et al. Fluka. `http://www.slac.stanford.edu/econf/C0303241/proc/papers/MOMT004.PDF`.

[131] E. Crescio, A. Dainese, M. Masera, and F. Prino. Performance of the its stand-alone tracker in pp collisions. *ALICE-INT 2009-046*, 2009.

[132] P. Saiz et al. *Nucl. Inst. Meth. A*, 504:437–440, 2003.

[133] ALICE Collaboration. *Eur. Phys. J. C*, 71:1655, 2011.

[134] L. Landau. *J. Phys. USSR*, 8:201, 1944.

[135] PHOBOS Collaboration. *Phys. Rev. C*, 75:024910, 2007.

[136] et. al. B. Alessandro. Charge collection in the silicon drift detectors of the alice experiment. *JINST*, 5:P02008, 2010.

[137] E. Biolcati. *Distribution of hadrons identified with the Inner Tracking System of the ALICE experiment for p–p data.* PhD thesis, Turin University, 2011.

[138] ALICE Collaboration. *Phys. Rev. Lett.*, 110:032301, 2013.

[139] ALICE Collaboration. *arXiv:1412.6828v1*, 2015.

[140] P. Christakoglou and M. Oldenburg. Estimation of the systematic uncertainties in $\bar{\text{p}}$-p measurements. *ALICE-INT-2008-010*, 2008.

[141] ALICE Collaboration. *Phys. Lett. B*, 712:309–318, 2012.

[142] ALICE Collaboration. *Phys. Lett. B*, 728:25–38, 2014.

[143] R. Fries and et. al. *Phys. Rev. Lett.*, 90:202303, 2003.

[144] P. Bozek. Hydrodynamic flow from rhic to lhc. 2011. `arXiv:1111.4398v1`.

[145] B. Muller, J. Schukraft, and B. Wyslouch. *Annu. Rev. Nucl. Particle Science*, 62:361–386, 2012.

[146] PHENIX Collaboration. *Phys. Rev. C*, 88:024906, 2013.

[147] CMS Collaboration. *Eur. Phys. J. C*, 72:2164, 2012.

[148] BRAHMS Collaboration. *Phys. Rev. C*, 72:014908, 2005.

[149] STAR Collaboration. *Phys. Rev. Lett.*, 108:072301, 2008.

[150] J. Sollfrank, F. Becattini, K. Redlich, and H. Satz. Canonical strangeness enhancement. *Nucl. Phys. A*, 638:399c–402c, 1998.

[151] J. Letessier and J. Rafelski. Strangeness chemical equilibrium in qgp at rhic and cern lhc. *Phys. Rev. C*, 75:014905, 2007.

[152] ALICE Collaboration. *Phys. Lett. B*, 727:371–380, 2013.

[153] Edward Shuryak and Ismail Zahed. High multiplicity pp and pa collisions: Hydrodynamics at its edge. *Phys. Rev. C*, 88:044915, 2013.

[154] P.Z. Skands and D. Wicke. Non-perturbative qcd effects and the top mass at the tevatron. *Eur. Phys. J. C*, 52:133–140, 2007.

[155] H. Schulz and P. Skands. Energy scaling of minimum-bias tunes. *Eur. Phys. J. C*, 71:1644, 2011.

[156] A. Ortiza, P. Christiansen, E. Cuautle, I. Maldonado, and G. Paic. Color reconnection and flow-like patterns in pp collisions. *Phys. Rev. Lett.*, 111:042001, 2013.

[157] T. Pierog, Iu. Karpenko, J. M. Katzy, E. Yatsenko, and K. Werner. Epos lhc : test of collective hadronization with lhc data. `arXiv:1306.0121v2`.

A kinematics

Some of the most common kinematic variables in heavy-ion collisions are reviewed in this appendix.

Lorentz transformation

The energy E and 3-momentum $\mathbf{p}$ of a particle of mass m form a 4-vector $p = (E, \mathbf{p})$, being $p^2 = E^2 - |p|^2 = m^2$. The velocity of the particle is $\beta = \mathbf{p}/E$. The energy and momentum $p^{'} = (E^{'}, \mathbf{p}^{'})$ viewed from a frame moving velocity β_f are given by

$$\begin{pmatrix} E^{'} \\ p^{'}_{||} \end{pmatrix} = \begin{pmatrix} \gamma_f & -\gamma_f\beta_f \\ -\gamma_f\beta_f & \gamma_f \end{pmatrix} \begin{pmatrix} E \\ p_{||} \end{pmatrix}, \; p^{'}_{\mathrm{T}} = p_{\mathrm{T}} \tag{A.1}$$

where $\gamma_f = 1/\sqrt{1-\beta_f^2}$ is the Lorentz factor and $p_{T(||)}$ is the component of $\mathbf{p}$ transverse(longitudinal) to β_f. Other 4-vector, such as the space-time coordinates transforms in the same way. The scalar product of two 4-momenta $p_1 p_2 = E_1 E_2 - \mathbf{p}_1\mathbf{p}_2$ is invariant (independent of the frame).

Lorentz contraction An observer moving with respect to an object will get a measurement of the size contracted along the direction of motion by the factor

$$l' = l\sqrt{1-\beta^2} \tag{A.2}$$

Consequently, two colliding heavy-ion at ultra-relativistic energies see one to each other as saucers in their direction of motion.

Kinematic variables in HIC

Since the c.m. frame of the two colliding partons in heavy-ion collisions is *a priori* undetermined with respect to the lab frame, the scattering polar angle θ in these two frames is not a good observable to describe theory and the experiment. It would be thus more desirable to seek for kinematic variables that are invariant under unknown longitudinal boosts.

Transverse momentum and the azimuthal angle: Since in HIC the beam direction is usually the z-axis, variables involving only the transverse components are

invariant under longitudinal boosts. It is thus convenient to write the Lorentz-invariant phase-space element in the cylindrical coordinate as

$$\frac{d^3\vec{\mathbf{p}}}{E} = dp_x dp_y \frac{dp_z}{E} = p_{\mathrm{T}} dp_{\mathrm{T}} d\phi \frac{dp_z}{E}, \tag{A.3}$$

where ϕ is the azimuthal angle about the z-axis, and

$$p_{\mathrm{T}} = p_x^2 + p_y^2 = p \sin\theta \tag{A.4}$$

is the transverse momentum.

Rapidity and pseudo-rapidity: The most commonly used longitudinal variable is the rapidity y of a particle of momentum p^μ define as

$$y = \frac{1}{2} \ln\left(\frac{E + p_z}{E - p_z}\right) = \frac{1}{2} \ln\left(\frac{1 + \beta_z}{1 - \beta_z}\right) \tag{A.5}$$

With the introduction of rapidity y, the four-momentum can be rewritten as

$$p^\mu = (E_T \cosh y, p_{\mathrm{T}} \cos\theta, p_{\mathrm{T}} \sin\theta, E_T \sinh y), E_T = \sqrt{p_{\mathrm{T}}^2 + m^2} \tag{A.6}$$

and the phase-space element then can be expressed as

$$\frac{d^3\vec{\mathbf{p}}}{E} = p_{\mathrm{T}} dp_{\mathrm{T}} d\phi \frac{dp_z}{E} = p_{\mathrm{T}} dp_{\mathrm{T}} d\phi dy = E_T dE_T d\phi dy. \tag{A.7}$$

In the massless limit, $E \approx |\vec{p}|$, so that

$$y \to \frac{1}{2} \ln\left(\frac{1 + \cos\theta}{1 - \cos\theta}\right) = \ln\cot\frac{\theta}{2} \equiv \eta \tag{A.8}$$

where η is the pseudo-rapidity, which has one-to-one correspondence with the scattering polar angle $\pi \geq \theta \geq 0$ for $-\infty < \eta < \infty$. Since y as well as η is additive under Lorentz transformation in $z-$axis, the different in rapidity $\Delta y = y_2 - y_1 = y_2^{'} - y_1^{'}$ is invariant in the two frames.

B
Bjorken scaling x

The variable x known as Bjorken scaling variable represents in the limit of infinite momenta the fraction of the nucleon momentum carried by a parton. In the limit of $\mathrm{m} \to 0$, the 4-momenta of two colliding partons can be written as:

$$\tilde{\mathrm{p}_1} = (x_1, 0, 0, x_1)\frac{\sqrt{\mathrm{s}}}{2} \qquad \tilde{\mathrm{p}_2} = (x_2, 0, 0, -x_2)\frac{\sqrt{\mathrm{s}}}{2} \tag{B.1}$$

where $\sqrt{\mathrm{s}}$ is the centre-of-mass energy of the two colliding nucleons and $x_{1,2}$ are the Bjorken variables for the two partons. In case of a leading order process (e.g. gluon fusion $\mathrm{gg} \to \mathrm{Q\bar{Q}}$) which leads to the creation of a $\mathrm{Q\bar{Q}}$ pair, the invariant mass squared of the quark-antiquark system can be written as $\mathrm{M}^2_{\mathrm{Q\bar{Q}}} = \mathrm{s}x_1x_2$ and the rapidity as $\mathrm{y}_{\mathrm{Q\bar{Q}}} = \frac{1}{2}\ln\frac{x_1}{x_2}$. Solving the 2-equation system, it can be easily found that:

$$x_{1,2} = \frac{\mathrm{M}_{\mathrm{Q\bar{Q}}}}{\sqrt{\mathrm{s}}}\mathrm{e}^{\pm \mathrm{y}_{\mathrm{Q\bar{Q}}}} \tag{B.2}$$

In the central rapidity region $\mathrm{y} = 0$ thus:

$$x_1 = x_2 = \frac{\mathrm{M}_{\mathrm{Q\bar{Q}}}}{\sqrt{\mathrm{s}}} \tag{B.3}$$

The consequence of Eq. B.3 is that larger values of centre-of-mass energies allow us to investigate the region characterized by smaller x.